Development of the Multi-Purpose Airborne Sensor Carrier MASC-3 and Turbulence Measurements in the Atmospheric Boundary Layer

DISSERTATION

der Mathematisch-Naturwissenschaftlichen Fakultät

der Eberhard Karls Universität Tübingen

zur Erlangung des Grades eines

Doktors der Naturwissenschaften

(Dr. rer. nat.)

vorgelegt von

ALEXANDER RAUTENBERG

aus Göppingen

Tübingen

2019

Gedruckt mit Genehmigung der Mathematisch-Naturwissenschaftlichen Fakultät der Eberhard Karls Universität Tübingen.

Tag der mündlichen Qualifikation: 19. Dezember 2019

Dekan:	Prof. Dr. Wolfgang Rosenstiel
1. Berichterstatter:	Prof. Dr. Jens Bange
2. Berichterstatter:	Prof. Dr. Burkhard Wrenger

Abstract

This thesis deals with measurements in the atmospheric boundary layer, which is the lowest part of the earth's atmosphere. Here, life takes place. Stably stratified turbulence regimes in the atmospheric boundary layer and the wake aerodynamics of wind energy converters are investigated. These topics have one key element in common. The in-situ 3D wind vector measurement is crucial for a deeper understanding. Simplified algorithms to estimate the wind speed and direction are commonly used and the applicability in different meteorological conditions, as well as uncertainties and the temporal resolution are investigated. Fixed-wing unmanned aircraft systems using a multi-hole probe in combination with an inertial navigation system are capable of measuring the high resolution 3D wind vector on turbulent scales. Turbulent fluxes of heat and momentum can be estimated. Remaining uncertainties and error sources, such as the influence of a varying airspeed of the UAS during the measurements, or operational constraints due to the calibration of the multi-hole probe, are investigated, quantified and improved. The design and development of the third mark of the Multi-Purpose Airborne Sensor Carrier (MASC-3) is also a major part of this thesis and aims to improve the wind measurement, to gain endurance, to allow operations under an enlarged range of environmental conditions and to enable easy implementation of further sensors. A close comparison of the measurements of MASC-3 with established measurement systems, finally allows validation of the turbulent 3D wind vector measurement. MASC-3 in combination with a meteorological measurement tower and a Sodar system, is used for investigating the interactive nature of the stable boundary layer over homogeneous terrain in polar conditions. The wake of wind energy converters is investigated and the measurements of MASC-3 are able to capture the detaching tip vortices and resolve the complex nature of the flow field in a new and revealing manner.

Zusammenfassung

Diese Doktorarbeit beschäftigt sich mit naturwissenschaftlichen Untersuchungen in der atmosphärischen Grenzschicht, die den untersten Teil der Atmosphäre und unseren Lebensraum darstellt. Turbulenz in stabilen Grenzschichten und der Nachlauf von Windenergieanlagen werden untersucht und weisen Gemeinsamkeiten auf. Dabei ist die Messung des in-situ 3D Windvektor entscheidend für ein tieferes Verständnis. Es werden vereinfachende Algorithmen für Windgeschwindigkeit und -richtung und deren Anwendbarkeit bei unterschiedlichen meteorologischen Bedingungen, sowie Unsicherheiten und die zeitliche Auflösung untersucht. Unbemannte Flächenflugzeuge, die eine Mehrlochsonde und ein Navigationssystem verwenden, sind in der Lage den 3D Windvektor hochauflösend bis hin zu turbulenten Skalen zu messen. Turbulente Flüsse von Wärme und Impuls können so berechnet werden. Bestehende Unsicherheiten und Fehlerquellen, wie der Einfluss der veränderlichen Relativgeschwindigkeit des unbemannten Flugzeugs zur gemessenen Windgeschwindigkeit, oder die operationellen Einschränkungen aufgrund der Kalibrierung der Mehrlochsonde werden untersucht, quantifiziert und verbessert. Weitere, große Bestandteile der Doktorarbeit sind sowohl das Design als auch die Entwicklung des Multi-Purpose Airborne Sensor Carrier der dritten Generation (MASC-3). Ziele sind eine verbesserte Windmessung, eine größere Reichweite, die Einsatzfähigkeit bei unterschiedlichen meteoroligischen Bedingungen und eine einfache Implementation von neuen Sensoren. MASC-3 wird in Kombination mit meteorologischen Messmasten und Sodar Systemen eingesetzt, um die Windvektormessung zu validieren und die interaktiven Eigenschaften von stabilen, polaren Grenzschichten zu erforschen. Die Messungen des MASC-3 sind außerdem in der Lage, die ablösenden Blattspitzenwirbel von Windenergieanlagen zu erfassen und damit die komplexen Strömungseigenschaften auf eine neue, aufschlussreiche Art und Weise aufzulösen.

Danksagung

Mein Dank gilt allen, die mich in den Jahren meiner Arbeit an der Universität Tübingen unterstützt haben. Insbesondere möchte ich mich bedanken bei:

- Meinem Doktorvater Prof. Dr. Jens Bange. Er hat mir die Möglichkeit gegeben in seiner Arbeitsgruppe diese Promotion zu verfassen und mich in allen Belangen unterstützt und beraten. Außerdem konnte ich viele Kontakte knüpfen und einen regen Austausch mit Kollegen pflegen. Für die Möglichkeiten, die uneingeschränkte Unterstützung in jeder Lage, die stets guten Ratschläge und das viele Erlernte bin ich ihm sehr dankbar.
- meinen Kollegen in der Arbeitsgruppe Umweltphysik. Vielen Dank für die Unterstützung und die Zusammenarbeit!
- allen Studenten, die mir bei der Entwicklung und Wartung von MASC, bei der Datenanalyse und Programmierung und bei der Forschung geholfen haben. Ihr wart eine tragende Säule für diese Promotion. Vielen Dank!
- bei unserem Modellbauer Martin Schempp für seine herausragenden Fertigkeiten.
- bei den Kollegen des Projekts ISOBAR.
- bei meinen Co-Autoren, mit denen ich die Publikationen realisieren konnte.
- bei meiner Frau Katrin. Danke für die Geduld und Unterstützung!
- bei Prof. Dr. Jens Bange und Prof. Dr. Burkhard Wrenger für die Begutachtung dieser Arbeit.

Contents

Chapter 1

List of Publications

This thesis is presented as an integrated accumulation of three peer-reviewed publications. All three manuscripts have been published in peer-reviewed journals.

1.1 Peer-reviewed publications, first author

I **Rautenberg, A.**; Graf, M.; Wildmann, N.; Platis, A.; Bange, J. Reviewing Wind Measurement Approaches for Fixed-Wing Unmanned Aircraft, Atmosphere 2018, 9(11), 422.

II **Rautenberg, A.**; Allgeier, J.; Jung, S.; Bange, J. Calibration Procedure and Accuracy of Wind and Turbulence Measurements with Five-Hole Probes on Fixed-Wing Unmanned Aircraft in the Atmospheric Boundary Layer and Wind Turbine Wakes, Atmosphere 2019, 10(3), 124.

III **Rautenberg, A.**; Schön, M.; zum Berge, K.; Mauz, M.; Manz, P.; Platis, A.; van Kesteren, B.; Suomi, I.; Kral. S.T.; Bange, J. The Multi-Purpose Airborne Sensor Carrier MASC-3 for Wind and Turbulence Measurements in the Atmospheric Boundary Layer. Sensors 2019, 19(10), 2292.

1.2 Peer-reviewed publications, co-author

- El Bahlouli A, **Rautenberg A**, Schön M, zum Berge K, Bange J, Knaus H: (2019) Comparison of CFD Simulation to UAS Measurements for Wind Flows in Complex Terrain: Application to the Winsent Test Site. Energies 12(10).

- Knaus H, **Rautenberg A**, Bange J: (2017) Model Comparison of two Different Non-hydrostatic Formulations for the Navier-Stokes Equations Simulating Wind Flow in Complex Terrain. Journal of Wind Engineering and Industrial Aerodynamics 169:290–307.

- Knaus H, Hofsäß M, **Rautenberg A**, Bange J: (2018) Application of Different Turbulence Models Simulating Wind Flow in Complex Terrain: A Case Study for the Windfors Test Site. Computation 6(3).

- Kral ST, Reuder J, Vihma T, Suomi I, O'Connor E, Kouznetsov R, Wrenger B, **Rautenberg A**, Urbancic G, Jonassen MO, et al. (2018) Innovative Strategies for Observations in the Arctic Atmospheric Boundary Layer (ISOBAR) - The Hailuoto 2017 Campaign. Atmosphere 9(7).

- Mauz M, **Rautenberg A**, Platis A, Cormier M, Bange J: (2019) First Identification and Quantification of Detached Tip Vortices behind Wind Energy Converter using Fixed-wing Unmanned Aircraft System. Wind Energy Science 4(3):451–463.

- Schulz C, Hofsäß M, Anger J, **Rautenberg A**, Lutz T, Cheng PW, Bange J: (2016) Comparison of Different Measurement Techniques and a CFD Simulation in Complex Terrain. Journal of Physics: Conference Series 753:082,017.

1.3 Conference contributions, oral presentations

- **Rautenberg A**, Wildmann N, Smith J, Bange J (2015a) Investigation of the flow over an escarpment with regard to wind-energy research using small remotely piloted aircraft. In: 11th EAWE PhD Seminar on Wind Energy, Stuttgart, Germany, 23- 25 September 2015, EAWE, URL https://www.eawe.eu/index.php/events

- **Rautenberg A**, Wildmann N, Smith J, Bange J (2015b) Investigation of the flow over an escarpment with regard to wind-energy research using small remotely piloted aircraft. In: 15th EMS Annual Meeting/12th ECAM, Sofia, Bulgaria, 7- 11 September 2015, URL https://www.ems2015.eu/ems2015_programme_book.pdf

- **Rautenberg A**, Anger J, Hofsäß M, Schulz C, Bange J (2016a) Comparing in-situ measurements of small remotely piloted aircraft with lidar measurements in complex terrain. In: ISARS 2016, 18th International Symposium for the Advancement of Boundary-Layer Remote Sensing, Varna, Bulgaria, 6-9 June 2016, URL: http://isars2016.org/isars/sites/storm.cfd.meteo.bg.isars/files/Programme30May2016.pdf

- **Rautenberg A**, Graf M, Wildmann N, Bange J (2016b) Verbesserungen der Wind- und Turbulenzmessung mit UAV. In: DACH2016, Die Fach- und Fortbildungstagung für Meteorologie im deutschsprachigen Raum, Berlin, Germany, 14-16 March 2017, URL http://meetingorganizer.copernicus.org/DACH2016/DACH2016-123.pdf

- **Rautenberg A**, Wildmann N, Anger J, Schulz C, Bange J (2016c) Investigation of the flow in complex terrain with regard to wind-energy research using the small remotely piloted aircraft masc. In: 16th EMS Annual Meeting, Trieste, Italy, 12–16 September 2016, vol 13, URL https://www.ems2016.eu/EMS2016_programme_book.pdf

- **Rautenberg A**, Wildmann N, Anger J, Schulz C, Bange J (2016d) Investigation of the flow in complex terrain with regard to wind-energy research using the small remotely piloted aircraft masc. In: ISARRA, 4th Conference of the International Society for Atmospheric Research using Remotely-piloted Aircraft, Toulouse, France, 23-25 May 2016, URL http://www.isarra.org/wp-content/uploads/2018/11/ISARRA2016_SA5_2_Rautenberg_Complex_Terrain.pdf

- **Rautenberg A**, Graf M, Bange J (2017) Comparing common wind measurement algorithms of remotely piloted fixed-wing aircraft. In: ISARRA, 5th Conference of the International Society for Atmospheric Research using Remotely-piloted Aircraft, Oban, Scotland, 22-24 May 2017, URL http://www.isarra.org/?page_id=490

- **Rautenberg A**, Kral ST, Reuder J, Vihma T, Suomi I, O'Connor E, Kouznetsov R, Wrenger B, Rautenberg A, Urbancic G, Jonassen MO, Bange J, et al.15 (2018c) Wind and turbulence measurements with masc during the isobar campaign 2017. In: Polar 2018, Where the Poles come together, A SCAR & IASC Conference, Davos, Switzerland, 15-26 June 2018, URL http://www.professionalabstracts.com/polar2018/programme-polar2018.pdf

- **Rautenberg A**, Kral ST, Reuder J, Vihma T, Suomi I, O'Connor E, Kouznetsov R, Wrenger B, Rautenberg A, Urbancic G, Jonassen MO, Bange J, et al. (2018d) Wind and turbulence measurements with rpa during the isobar campaign. In: 2nd Baltic Earth Conference 2018, The Baltic Sea Region in Transition, Helsingor, Denmark, 11-15 June 2018, URL `https://d-nb.info/1164170147/04`

- **Rautenberg A**, Kral ST, Reuder J, Suomi I, Vihma T, Wrenger B, Bange J (2019b) Wind- und Turbulenzmessung in stabiler Grenzschicht mit kleinen unbemannten Luftfahrzeugen während zweier ISOBAR Kampagnen im nördlichen Finnland. In: DACH2019, Die Fach- und Fortbildungstagung für Meteorologie im deutschsprachigen Raum, Garmisch-Partenkirchen, Germany, 18-22 March 2019, URL `https://www.dach2019.de/DACH2019-abstracts.pdf`

Chapter 2

Introduction

The atmospheric boundary layer (ABL) is the lowest part of the earth's atmosphere where we live and breath. The weather influences our daily live and occurs typically only in the lowest 10 km which is the troposphere. Unlike the quiet stratosphere above, the troposphere inherits ubiquitous instabilities creating precipitation that waters the crops, provides freshwater, generates dispersion and dilution of our pollutants and provides the potential to generate wind energy. The ABL is the part of the troposphere where the influence of the earth's surface is apparent. The interaction between the surface and the air occurs mechanically and thermally by the friction between the wind and the ground surface and by the solar radiation, causing turbulence. Three basic classifications of the ABL can be defined. The convective boundary layer (CBL), a neutrally stratified boundary layer and a stable boundary layer (SBL). The driving forces of specific turbulence regimes can be sub-classified and parameterized for each thermal stratification. Understanding stably stratified turbulence in the ABL remains at the forefront of geophysical turbulence research and the dynamics are still in a state of discovery as some couplings between the driving forces continue to resist a generic description (Sullivan et al., 2016). The study of Fernando and Weil (2010) provides a recent review of persisting problems, stating that the

modeling of commonly sought meteorological and air quality indicators often rely heavily on details of the SBL. Further, greater emphasis is needed on the interactions of SBL processes and the resulting modification of heat, mass, and momentum fluxes. The study concludes, that the SBL remains the least understood element of the atmospheric boundary layer. In order to strengthen the understanding, measurements are irreplaceable. Climate change is humanity's biggest challenge in the future and prognostic climate models also depend on the parameterization of SBL regimes.

The main tool for this thesis is the unmanned aircraft system (UAS) with the name Multi-Purpose Airborne Sensor Carrier (MASC). One major part of this work was the participation in intensive measurement campaigns for the project called Innovative Strategies for Observations in the Arctic Atmospheric Boundary Layer (ISOBAR). The two main campaigns took place over sea ice at the western shore of Hailuoto island in the northern Bothnian Bay on the coast of Finland. The main motivation for the ISOBAR project is to develop and apply a new and innovative observation strategy for the stably stratified boundary layer that is based on meteorological UAS, ground-based in-situ and remote-sensing profiling systems (Kral et al., 2018).

Another major part of this thesis involves research of wind energy converters (WEC), which are an important contribution to the evolution towards sustainable energy resources. The meteorological conditions in the vicinity of WEC, wind farms and their interacting flow field, influence the power generation (Emeis, 2018) and large potential for optimizations remains unused. Especially the smaller structures of the wake aerodynamics downstream of WEC were of interest for this thesis (Mauz et al., 2019). Numerical models face challenges to resolve both at the same time, the small scale turbulence which is caused for example by detaching tip vortices of the rotor blades and the larger scales of atmospheric turbulence caused for example by the stratification of the ABL or by the complex flow dynamics in wind farms (Sanderse et al., 2011; Platis et al., 2018). Measuring the wake aerodynamics for com-

parisons with models and analyzing the dynamics of the small scale turbulence with fixed-wing UAS is a brand-new and very promising approach.

Although the requirements for the UAS measurements differ to some extent when measuring the wake dynamics of a WEC and the turbulence regimes of a SBL, the key requirement of measuring the turbulent 3D wind vector is the same. The high resolution in-situ 3D wind vector measurement with fixed-wing UAS using a multi-hole probe in combination with an inertial navigation system (INS) and the analysis of turbulent flow and the derivation of turbulence quantities can be applied to both subjects. UAS are relatively easy to deploy and can be operated with minimal logistical overhead, are cost effective, can operate in a wide range of environmental conditions and can deliver highly valuable and high quality data. Further developments regarding remaining uncertainties and error sources such as the influence of a varying airspeed of the UAS during the measurements, or operational constraints due to intensive calibration efforts of the multi-hole probe, were important findings for the scientific merit of the presented work and the drawn conclusions. The further development of MASC to it's third mark MASC-3 was also a major part of this thesis.

2.1 In-situ Wind Speed and Direction Measurements

MASC is operated by the environment-physics group at the Center for Applied Geo-Science (ZAG), University of Tübingen, and was the central tool to study the ABL in this thesis. During the ISOBAR campaigns it was used to measure the 3D wind vector, air temperature, and water vapor. A fast fine wire thermometer (Wildmann et al., 2013)) and a five-hole flow probe with an inertial navigation system (INS) (Van den Kroonenberg et al., 2008), allow measurements of small turbulent fluctuations of the in-situ three dimensional wind vector and temperature and thus estimations of heat and

momentum fluxes can be derived. Not only for the processes in a SBL, the wind speed and direction estimation is crucial for the interpretation of the phenomena under investigation. Also because the other utilized UAS during the ISOBAR campaigns make use of these algorithms, this thesis deals in the first place with the commonly used wind speed and direction estimation algorithms for UAS in order to investigate the capabilities of the algorithms. The focus was on the applicability under different meteorological conditions, the influence of flight patterns and the quantification of uncertainties. This was published in the first study of this thesis with the title "Reviewing Wind Measurement Approaches for Fixed-Wing Unmanned Aircraft" (Rautenberg et al., 2018).

The common method for measuring the 3D wind vector from any research aircraft is the multi-hole probe algorithm (MHPA), using a multi-hole probe in combination with the measured attitude, position, and velocity of the aircraft. The wind vector $\vec{w}$ is the orientation and magnitude of the airflow. A non-stationary observer (e.g., an UAS) sees the relative velocity $\vec{u}$ only, and from a fixed point of view (e.g., the Earth coordinate system), the observer is moving with a resulting velocity $\vec{v}$ that is the sum of $\vec{u}$ and $\vec{w}$. This fundamental relation is the basis of all wind measurement techniques with fixed-wing aircraft. The wind vector $\vec{w}_g$ in the geodetic coordinate system is the difference between $\vec{v}_g$ and $\vec{u}_g$. The wind vector $\vec{w}_g$ is calculated according to, e.g., Bange (2009) using

$$\vec{w}_g \;=\; \vec{v}_g \;+\; \mathbf{T}_{gb}\left(\vec{u}_b \;+\; \vec{\Omega}_b \times \vec{L}\right) \tag{2.1}$$

with the true airspeed vector $\vec{u}_b$ in the body-fixed coordinate system of the aircraft, and the transformation matrix $\mathbf{T}_{gb}$ in the geodetic coordinate system. The vector of angular body rates $\vec{\Omega}_b$ and its lever arm $\vec{L}$ describe the effect due to the spatial separation between INS and the multi-hole probe and can be neglected (Lenschow, 1970), since the lever arm $\vec{L}$ is only a few centimeters in the UAS. The attitude is measured with an inertial measurement unit (IMU), position, and velocity of the aircraft using a global navigation satellite

system (GNSS). The combination of both systems, usually supplemented by an extended Kalman filter (EKF), is called an INS. By calibration, the pressure readings of the individual holes of the multi-hole probe are used to estimate the true airspeed vector $\vec{u}_b$. The MHPA is used with manned aircraft, as published by Lenschow (1970), among others, and was adapted for the UAS called Mini Aerial Vehicle (M^2AV) by Van den Kroonenberg et al. (2008), which is the parent version of MASC. Beside the direct 3D wind vector measurement with the MHPA, simplifications such as the pitot tube algorithm (PTA) and the no-flow-sensor algorithm (NFSA) exist. The PTA only requires a pitot-static tube and a standard INS, measuring aircraft attitude (Euler angles) and position. Even less complex is the NFSA, which only requires a global navigation satellite system to estimate wind speed and wind direction. These algorithms require temporal averaging and are compared to the direct approach with the MHPA.

2.2 Multi-hole Probe Algorithm

With MASC, the turbulent flux of momentum and heat is estimated with the eddy covariance technique. With the Reynolds averaging rules, the variables are split into mean $\overline{X}$ and turbulent parts and the covariance Cov_{XY} of two variables X and Y is

$$\mathrm{Cov}_{XY} = \frac{1}{N-1}\sum_{i=1}^{N}(X_i-\overline{X})(Y_i-\overline{Y}). \tag{2.2}$$

The vertical kinematic eddy heat flux is calculated with $\mathrm{Cov}_{wT_{\mathrm{pot}}}$ and the vertical kinematic eddy moisture flux with Cov_{wq} and the vertical kinematic eddy flux of momentum with Cov_{wu} and Cov_{wv} over the number of data points N of the measurement (Stull, 2012). The statistical covariances of the vertical wind vector component w with the potential temperature T_{pot}, the moisture q and the horizontal wind vector components u and v is used to estimate the turbulent flux of heat and momentum. The measurement of the 3D wind vector components and the temperature with a temporal

resolution of $\approx$ 30 Hz is one fundamental requirement in order to reliably estimate turbulent fluxes. Beside turbulent fluxes, the application of MASC for research in the field of WEC also requires such high temporal resolution and is a major part in this thesis. Even expensive numerical simulations imply high uncertainties for the flow field around a WEC, since it is challenging to combine precise blade aerodynamics on the small scales with atmospheric dynamics on the larger scales (Cormier et al., 2018). Especially smaller structures in the wake of wind turbines are poorly resolved in numerical models and not well understood. The measurement of the in-situ 3D wind vector with MASC allows for verification and validation of numerical models and increases the understanding of the complex wake dynamics in front of and behind WEC. Especially the smaller structures like the detaching tip vortex helix that propagates downstream the WEC are not well represented in the models. MASC flights from the HeliOW (Hubschrauber-Einsätze in Offshore-Windparks) campaigns were therefore used to analyze the 3D wind vector measurement with MASC in highly non-stationary flow, downstream of WEC. Analyzing the 3D wind vector measurement using MASC and the MHPA in moderate turbulence regimes during the ISOBAR campaigns with homogeneous terrain and stably stratified boundary layers as well as the extreme turbulence behind WEC, lead to the questions posed in the second publication with the title "Calibration Procedure and Accuracy of Wind and Turbulence Measurements with Five-Hole Probes on Fixed-Wing Unmanned Aircraft in the Atmospheric Boundary Layer and Wind Turbine Wakes" (Rautenberg et al., 2019a). Uncertainties when calculating turbulence statistics from the time series of the 3D wind vector measurements or analyzing highly transient features in the wake of a WEC are partly unknown for the MHPA. In order to reliably quantify small momentum and heat fluxes that distinguish between important features of a SBL or to quantify the vortex strength of a detached tip vortex in the wake of a WEC and compare it with numerical models, the uncertainties of the MHPA

with UAS are not yet analyzed sufficiently. One assumption of the MHPA is, that the airspeed during the calibration of the multi-hole probe in the wind tunnel equals the airspeed during the measurement. Differences between the airspeed during the calibration and during the measurement can be attributed to differences in the Reynolds Number with the probe's tip diameter as characteristic length. Such differences are unavoidable and a method to account for these differences opens up further possibilities, increases the flexibility for the operations, and allows to quantify the uncertainties related to the calibration of the multi-hole probe. Further influences on the 3D wind vector measurement with MHPA, such as the accuracy and temporal resolution of the INS, were also discussed and analyzed. The influence of the temporal resolution of other inherited quantities in the MHPA, such as Euler Angles and GNSS velocities of the vehicle were yet only partly addressed. Last but not least, the airframe and the aerodymnamical properties of the UAS influence the reactions of the UAS to changes in the wind field and correlate, and are proportional to the momentum and the aerodynamic drag of the UAS. Moreover, the individual flight-mechanical behavior influences the reaction of the UAS. An influence on the turbulence measurements itself must be expected. An aircraft with low drag, reacts less on changes in the wind field than a lightweight UAS with aerodynamic and flight mechanical properties that are susceptible to interaction with the turbulence.

2.3 The Multi-Purpose Airborne Sensor Carrier MASC-3

After analyzing the common algorithms for wind speed and direction measurements in the ABL and focusing on remaining uncertainties with the MHPA and MASC, the third mark of the Multi-Purpose Airborne Sensor Carrier, was developed and build. MASC-3 aimed to improve the wind measurement, to gain endurance, to allow operations under an enlarged range

of environmental conditions and to enable easy implementation of further sensors. The influence on the 3D wind vector measurement by the flow field around the aircraft was minimized by the new airframe of MASC-3 which features a pusher engine in the very back (behind the tail unit) of the UAS as well as a forward-spaced and streamlined sensor hat, where the five-hole probe was mounted (Figure 2.1).

The flight guidance and the autopilot are also of major importance for the 3D wind vector measurement, since the attitude of the UAS, as well as the GNSS vehicle velocities, are directly inherited in the calculations. A steady and precise flight of MASC-3 is implemented by the Pixhawk 2.1 “Cube” autopilot. The fuselage and the installed sensor hat allow for different payloads, making MASC-3 versatile for many scenarios. The standard payload includes an INS, a five-hole probe, a fine wire platinum resistance thermometer (FWPRT) and further temperature, surface temperature and humidity sensors. The software architecture runs on a Raspberry Pi 3, which allows an easy implementation of future sensors. The developed post-processing software MADA provides a standardized quality control of the gathered data within minutes after the flight experiment and enables comprehensive quick-looks of mean values and turbulence statistics of the flight experiment. During the second ISOBAR campaign ”Hailuoto-II”, measurements in the vicinity of a meteorological measurement tower were used to validate the turbulent 3D wind vector measurements with MASC-3. Subsequently the turbulence regimes during transition phases of the SBL were analyzed and accompanied with SODAR measurements. The findings were published in the third article with the title "The Multi-Purpose Airborne Sensor Carrier MASC-3 for Wind and Turbulence Measurements in the Atmospheric Boundary Layer" (Rautenberg et al., 2019b).

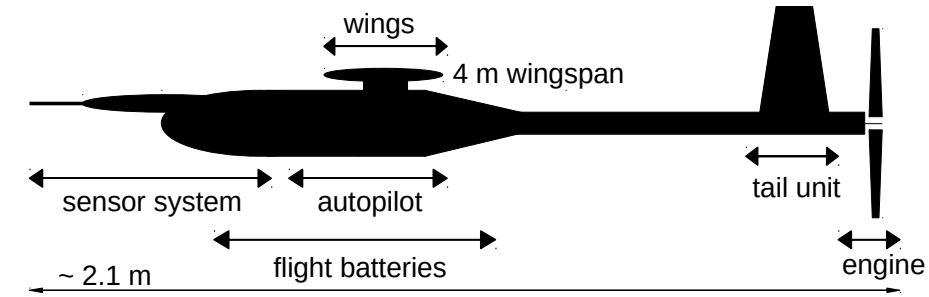

Figure 2.1: Multi-Purpose Airborne Sensor Carrier (MASC-3) sketch (**top**) and pictures of the airframe with the sensor system (**middle**) and five-hole probe (**bottom**).

Chapter 3

Results

This chapter will present the most important results, that were published in the peer-reviewed publications. The full first author articles are attached in Appendix A.

3.1 Comparison of Wind Speed and Direction Estimation Algorithms

Several approaches have been developed to estimate the wind vector without using multi-hole flow probes. This part of the thesis compares commonly used wind speed and direction estimation algorithms with the direct 3D wind vector measurement using multi-hole probes. This is relevant for the research that was conducted for the ISOBAR project, since one of the goals was to develop a strategy to combine different UAS platforms to densely sample SBL. Further analysis regarding the capabilities, uncertainties and applicability of simplified wind speed and direction estimation algorithms was required to judge which role each UAS can play. Combining the data of several measurement systems to increase the temporal or spatial resolution of the measurements and to gain further insight into certain phenomena also requires a wide-ranging understanding of the capabilities and limita-

Table 3.1: Flight sections with pattern and brief atmospheric condition.

Location	Flight Path	Condition
Boulder (BAO)	circular	weakly convective
Schnittlingen (SNT)	horizontal racetracks	sheared flow
Helgoland (HEL)	ascending racetracks	strong wind
Pforzheim (PFR)	lying eight, long straights	convective

tions of the presented algorithms. The comparison was done using the data of a fully equipped sensor system and by applying several algorithms to the same data set. To cover as many aspects as possible, a wide range of meteorological conditions and common flight patterns were considered in this comparison. The selection consists of four flight experiments with wind speeds between 2 and 15 m s^{-1}, as well as various flight patterns, including horizontal straight and level segments (legs), circles, lying eights, and ascending racetracks for height profiles. The data from the MHPA was compared to the PTA, which only requires a pitot-static tube and a standard INS measuring the Euler angles and position of the UAS. Modern autopilot system are mostly already equipped with a pitot-static tube, making the implementation of the algorithm relatively simple. Even less complex is the NFSA, which only requires GNSS to estimate wind speed and wind direction. These algorithms require temporal averaging. Two averaging periods of four and one minute ($M = 240$ s and $M = 60$ s) were applied in order to analyze the influence and show the limitations of each algorithm.

The comparison consists of four flight experiments with different flight paths and meteorological conditions. Table 3.1 gives an overview of the flight experiments.

The set of graphs in the Figures 3.1 - 3.2 show scatterplots of the horizontal wind speed. Figure 3.1 shows the results for an averaging window of $M = 240$ s. This timescale comprises at least two full racetracks for all experiments. Therefore, this timescale of 4 min was the choice for the com-

parison and is on the high end of reasonable averaging windows, pledging a robust performance. In comparison, a 1 min averaging time is analyzed, where approximately one racetrack in HEL and two circles at the BAO are inside the averaging window. This is a typical value for averaging in meteorology, where, on the one hand, full racetracks are included and, on the other hand, the performance resulting from data only having fractions of racetracks is addressed. Figure 3.2 shows these results for an averaging window of $M = 60$ s.

For quantifying the differences between the algorithms and averaging windows, histograms of the deviation from the MHPA are plotted in the Figures 3.3 - 3.4. The difference in the horizontal wind speed between the MHPA and the NFSA or the PTA is used. The normalized distribution is presented and the probability density function, together with the fitted normal distribution, is plotted for every experiment and algorithm. The mean μ of the fitted normal distribution can be interpreted as the bias between the algorithms, and the standard deviation σ can be taken as the precision Rautenberg et al. (2018). Each plot contains the results for both averaging periods, $M = 240$ s and $M = 60$ s, enabling a quantified comparison for each experiment between the averaging windows as well as between the algorithms.

For a window of 4 min, both simplifications work well, especially with the pitot-static tube measurement. When reducing the averaging period to 1 min and thereby increasing the temporal resolution, it becomes evident that only circular flight patterns with full racetracks inside the averaging window are applicable for the no-flow-sensor algorithm and that the additional flow information from the pitot-static tube improves precision significantly.

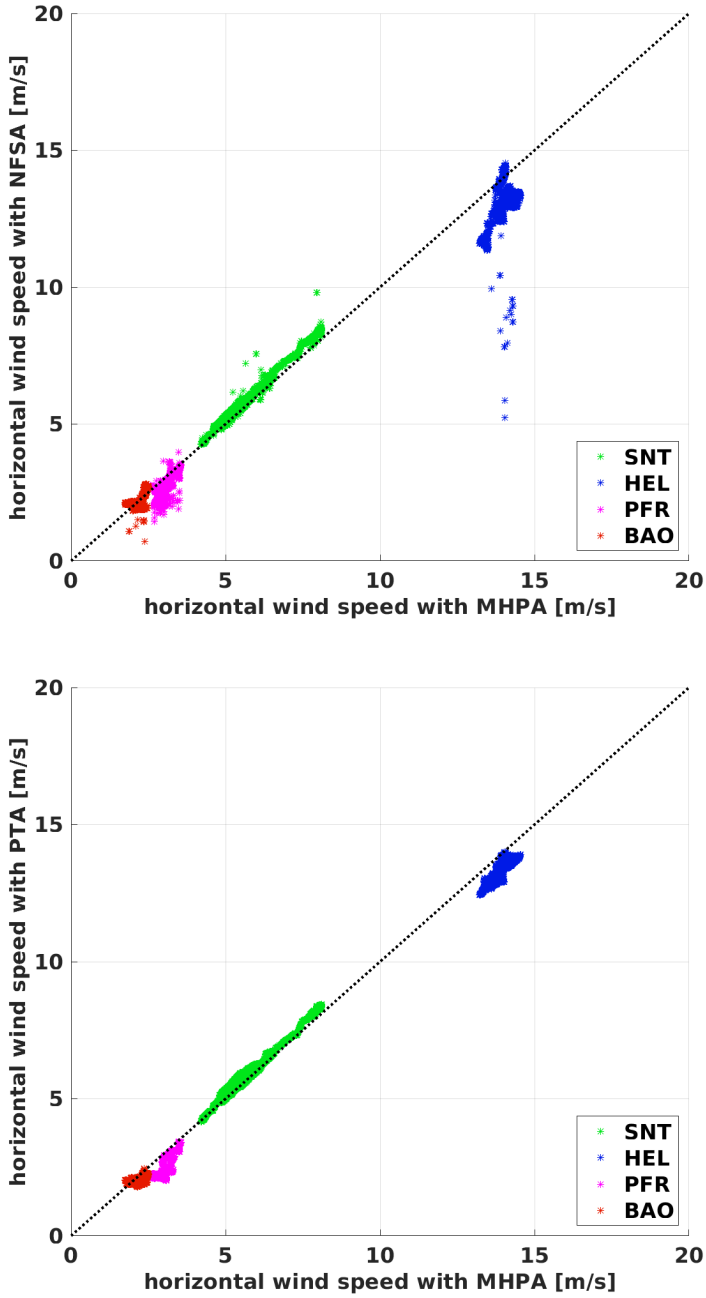

Figure 3.1: Comparison of the **horizontal wind speed** on a **window of 4 minutes** ($M = 240$ s) for the flights at the Boulder Atmospheric Observatory (BAO), Schnittlingen (SNT), Helgoland (HEL), and Pforzheim (PFR). The black dashed line shows the bisecting line where the multi-hole-probe algorithm (MHPA) equals the no-flow-sensor algorithm (NFSA) (**top**) and respectively the pitot tube algorithm (PTA) (**bottom**).

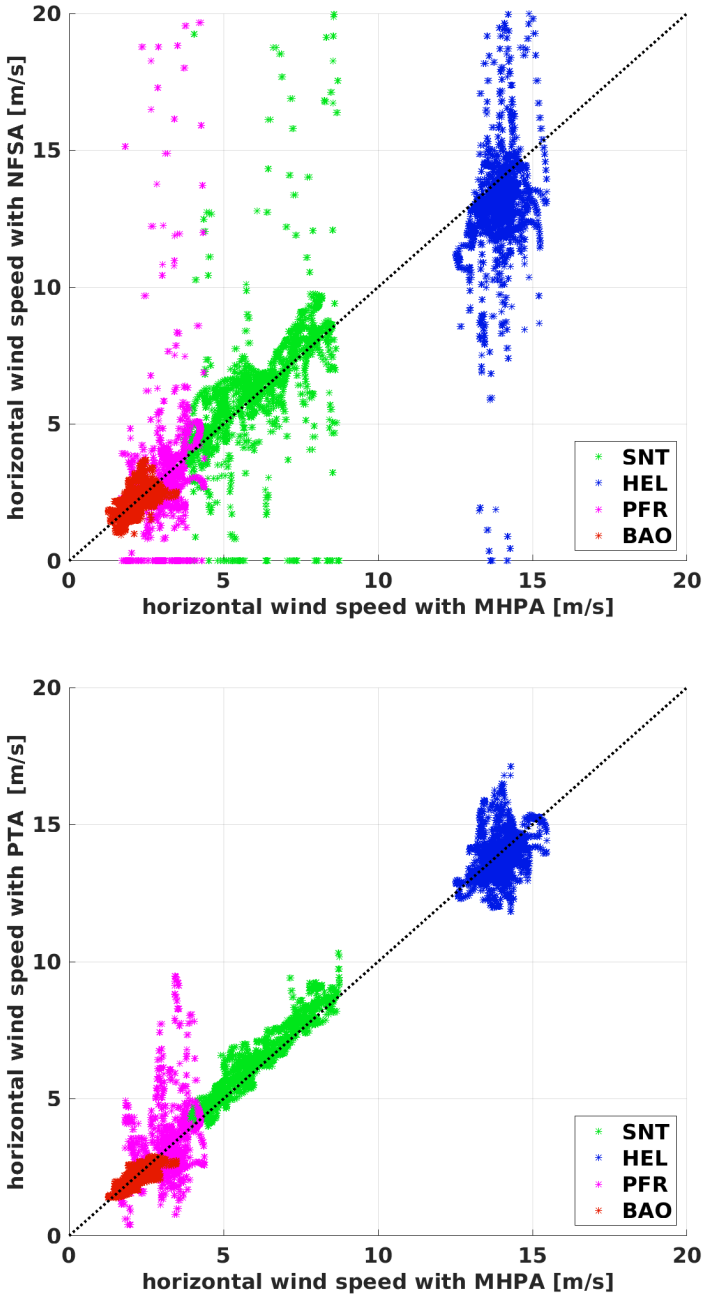

Figure 3.2: Comparison of the **horizontal wind speed** on a **window of 1 minute** ($M = 60$ s) for the flights at the Boulder Atmospheric Observatory (BAO), Schnittlingen (SNT), Helgoland (HEL), and Pforzheim (PFR). The black dashed line shows the bisecting line where the multi-hole-probe algorithm (MHPA) equals the no-flow-sensor algorithm (NFSA) (**top**) and respectively the pitot tube algorithm (PTA) (**bottom**).

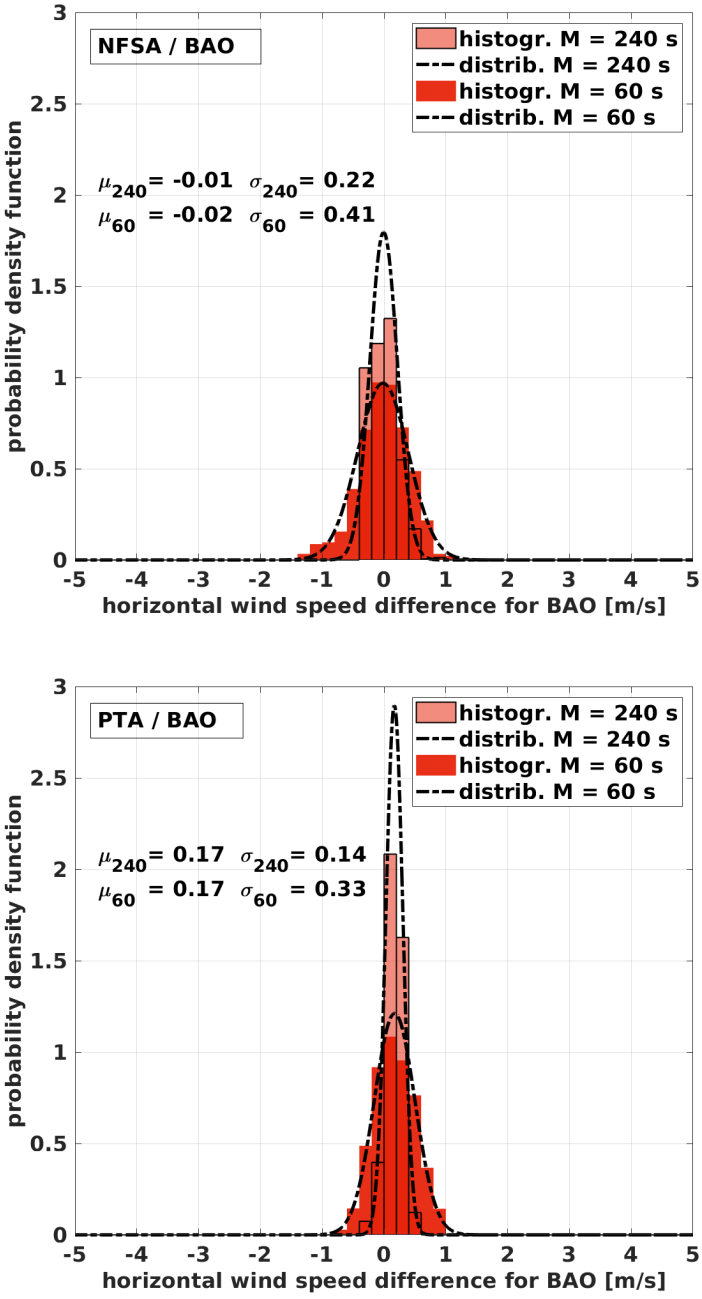

Figure 3.3: Normalized distribution and probability density function with the fitted normal distribution for the flight at the Boulder Atmospheric Observatory (**BAO**). The plots show the deviation between the MHPA and the **NFSA** (**top**) and the MHPA and the **PTA** (**bottom**) for $M = 240$ s and for $M = 60$ s.

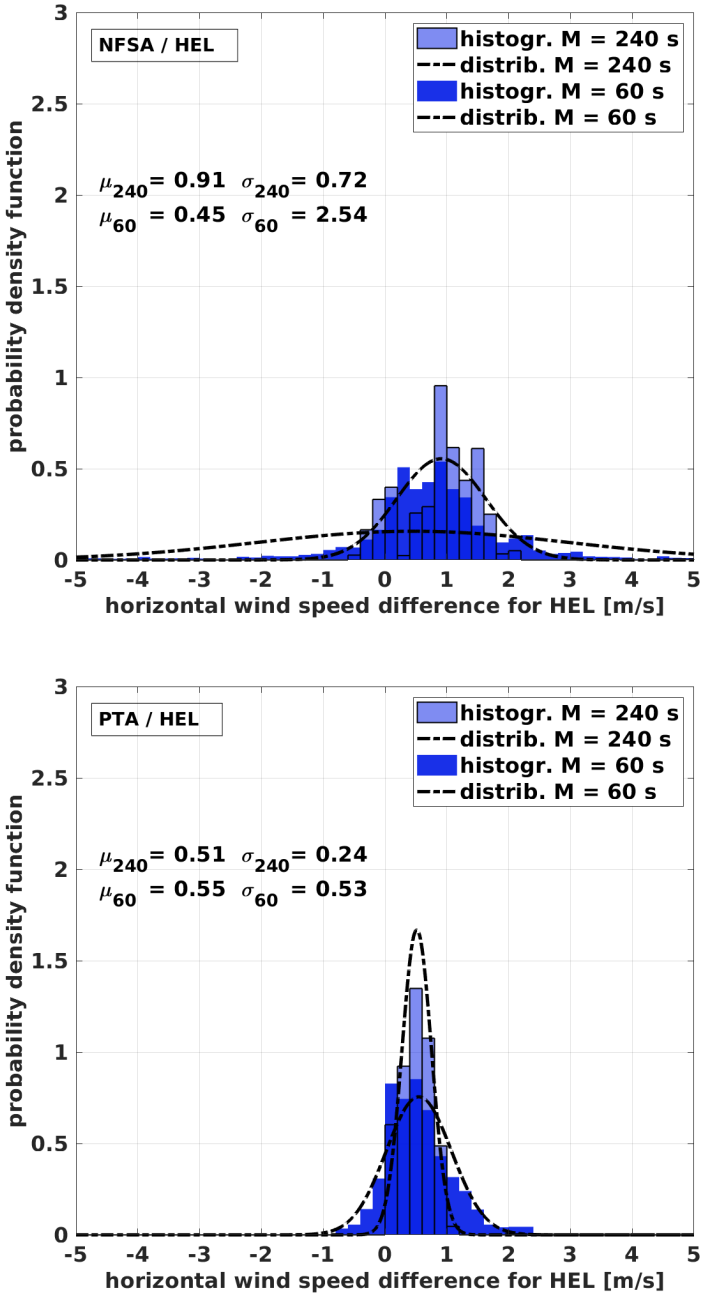

Figure 3.4: Normalized distribution and probability density function with the fitted normal distribution for the flight in Helgoland (**HEL**). The plots show the deviation between the MHPA and the **NFSA** (**top**) and the MHPA and the **PTA** (**bottom**) for $M = 240$ s and for $M = 60$ s.

The following itemization of the results for the long averaging period of $M = 240$ s, provides an overview of the findings:

- The NFSA is capable of estimating the wind speed, and not only for a circular flight pattern, if at least two full racetracks are inside the averaging window. Limitations arise for non-horizontal flight paths and high turbulence.
- The wind direction estimation is subject to large uncertainties with the NFSA.
- The PTA shows a very good agreement with the MHPA and is capable of measuring the horizontal wind speed and direction in all conditions with good accuracy.
- Fast ascent or descent of the UAS or strong vertical wind components leads to an underestimation of the horizontal wind speed when using the PTA.

For the short averaging period of $M = 60$ s, the following was found:

- The NFSA performs better when more than two racetracks are inside the averaging window, as well as for circular flight pattern. This reveals the very limited resolution.
- The PTA still performs well when only fractions of a racetrack are included in the algorithm. Limits arise when exclusively straight flight sections remain inside the averaging window.
- The PTA is capable of estimating reliably the mean wind speed and direction with a reasonable resolution.

A summary of the intercomparison between the two estimation algorithms for mean wind speed and direction is:

- The PTA is more accurate than the NFSA throughout all comparisons, even for the circular flight pattern.
- The PTA needs an additional sensor to estimate the true airspeed, but it achieves significantly higher accuracy and temporal resolution.

The simplicity of the NFSA is attractive for very small platforms, and the sUAS can be designed to be cheap, efficient, and robust enough to withstand miscellaneous environmental conditions. The PTA depends on the dynamic pressure measurement, which adds complexity to the sUAV. However, the enhancement of the wind speed and direction estimation is significant. Small, lightweight, cheap and easy to deploy UAS like for example SUMO (Small Unmanned Meteorological Observer, (Reuder et al., 2009)) play an important role for joint efforts like for example the ISOBAR measurement campaigns. The MHPA is the most sophisticated method and needs a set of differential pressure sensors in combination with extensive calibration, but the temporal resolution to measure at turbulent scales and the ability to measure the vertical wind component can only be achieved using the MHPA.

3.2 Advanced Calibration Method for the MHPA

When applying MASC for research in the atmospheric boundary layer and in the vicinity of wind turbines, the turbulent 3D wind vector is measured with a five-hole probe and an INS. Since non-zero vertical wind and varying horizontal wind causes variations in the airspeed of the UAS, and since it is desirable to sample with a flexible cruising airspeed to match a broad range of operational requirements, the influence of airspeed variations on mean values and turbulence statistics was investigated. Furthermore, a transect through the wake of a wind turbine and a tip vortex was analyzed, showing the instantaneous influence of the intense variations of the cruising airspeed

and the need for an evaluation of obtruding uncertainties. The accuracy of the wind vector measurement is crucial, and the propagation of errors has many influencing factors, originating in the attitude and ground speed measurement of the aircraft, the flow angles and flow magnitude (true airspeed vector) measurement with the multi-hole probe, and also in the measurement of the thermodynamic state of the air. Extensive studies for various systems and subsystems of the wind vector measurement with manned research aircraft (Metzger et al., 2011; Corsmeier et al., 2001; Williams and Marcotte, 2000; Khelif et al., 1999; Brown et al., 1983; Lenschow, 1986), including in-flight calibration procedures and uncertainty analysis (Hartmann et al., 2018; Drüe and Heinemann, 2013), and with UAS (e.g., for the M^2AV Van den Kroonenberg et al. (2008)) were performed. So far, for UAS, advanced calibration or verification maneuvers during flight were not addressed in terms of calibration and uncertainty analysis of the 3D wind vector measurement. The influence of airspeed variations on turbulence statistics of the wind vector measurement was not addressed for manned research aircraft, nor for UAS, yet. Although a dependency on the Reynolds number of the calculation of flow angles and magnitude (true airspeed vector) from the calibration is known Lee and Jun (2005); Dominy and Hodson (1993), it is common practice to choose one airspeed for the measurement and for the calibration in the wind tunnel and to assume that changes in the airspeed are negligible. Solely the study of Hartmann et al. (2018) mentions a linear proportionality for the conversion of pressure readings to flow angles in a certain range of Reynolds numbers for measurements with the Rosemount R858 five-hole probe. Since a lighter aircraft measures in a broader range of cruising airspeed than a heavier aircraft, when flying through the same atmospheric conditions, the uncertainty for UAS may be significantly higher than for manned research aircraft.

A variation in airspeed is primarily a change in the Reynolds number with the probe's tip diameter as reference length. Three calibrations of the five-

hole probe at three different airspeeds or Reynolds numbers are applied to the data of three flight experiments. The calibration polynomials of the five-hole probe were recorded at airspeeds of $v_{c1} = 15$m s^{-1} , $v_{c2} = 22.5$m s^{-1} and $v_{c3} = 28$m s^{-1}, yielding, with the apparent ambient pressure, temperature and humidity in the wind-tunnel facility, Reynolds numbers at the probe's tip of $\mathrm{Re}_{v1} = 3695$, $\mathrm{Re}_{v2} = 5538$ and $\mathrm{Re}_{v3} = 7031$. Mean values and statistical moments of second order, calculated from horizontal straight level flights are compared between flights in a stably stratified polar boundary layer and flights over complex terrain in high turbulence. Additionally, three calibrations were applied to the high resolution time series of the wind vector components and their primary quantities.

One flight from the ISOBAR campaign with low atmospheric turbulence is shown in the Figures 3.5–3.7 and compared to the COMPLEX flight in the Figures 3.8–3.10 with high turbulence in complex terrain. The COMPLEX flight was conducted in complex terrain near Schnittlingen on the Swabian Alp in the South of Germany. This flight was also used by the study of Wildmann et al. (2017), who investigated the flow field in the vicinity of the apparent test field for wind energy. Every data point consists of one headwind leg. To evaluate the persistent condition of these two flights, the set of plots in the Figures 3.5–3.10 consist in the subplot on the left-hand side, of height profiles of the quantities that are calculated with the polynomial at v_{c2}. The deviations are given in the subplot on the right-hand side, where the red (v_{c1}) and blue (v_{c3}) bars display the absolute deviations of the quantity to the value, calculated with the polynomial at v_{c2}. The deviations reveal their influence on the calculation of mean values. Generally, the influence on wind speed and direction, averaged over the whole leg, can be rated as very small according to Figure 3.5.

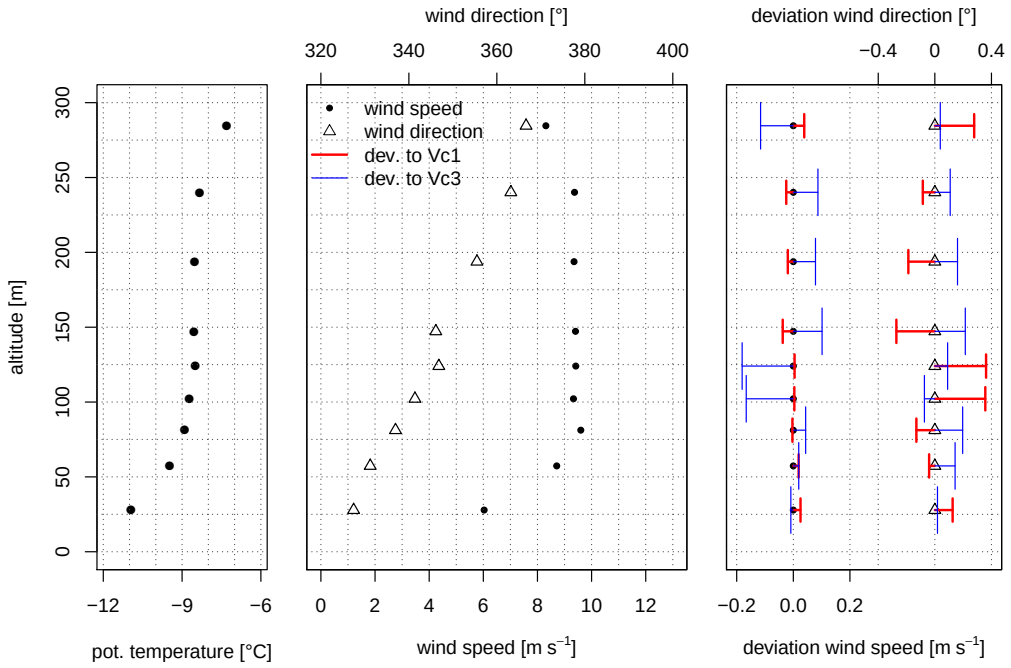

Figure 3.5: Height profiles of the ISOBAR flight with the altitude AMSL of the potential temperature (**left**), horizontal windspeed v_h and wind direction ϕ, calculated with the calibration polynomial at v_{c2} (**middle**). Deviations (**right**), when applying the calibration polynomials at v_{c1} and v_{c3}.

The profiles of TKE and the Var(w) in Figure 3.6 show a uniform distribution for the SBL, where turbulence is suppressed. With the persisting wind direction, the air mass had a fetch of at least 50 kilometers over the frozen Bothnian Bay, which is homogeneous terrain that cools the air above it. The surface layer forms due to friction, and TKE and Var(w) increase towards the ground. Another source of turbulence is the top of the surface inversion, where the geostrophic wind causes shear between the layers. This is also reflected in the measurements, since the TKE on 125 and 150 m AMSL is increased and the Var(w) too, although little. Here, the deviations when applying the calibration at v_{c1} and v_{c3} do have a clear trend. Higher turbulence towards the ground causes higher deviations, but a constant relative deviation does not exist. The relative deviations vary randomly between almost 0% and up to 20%.

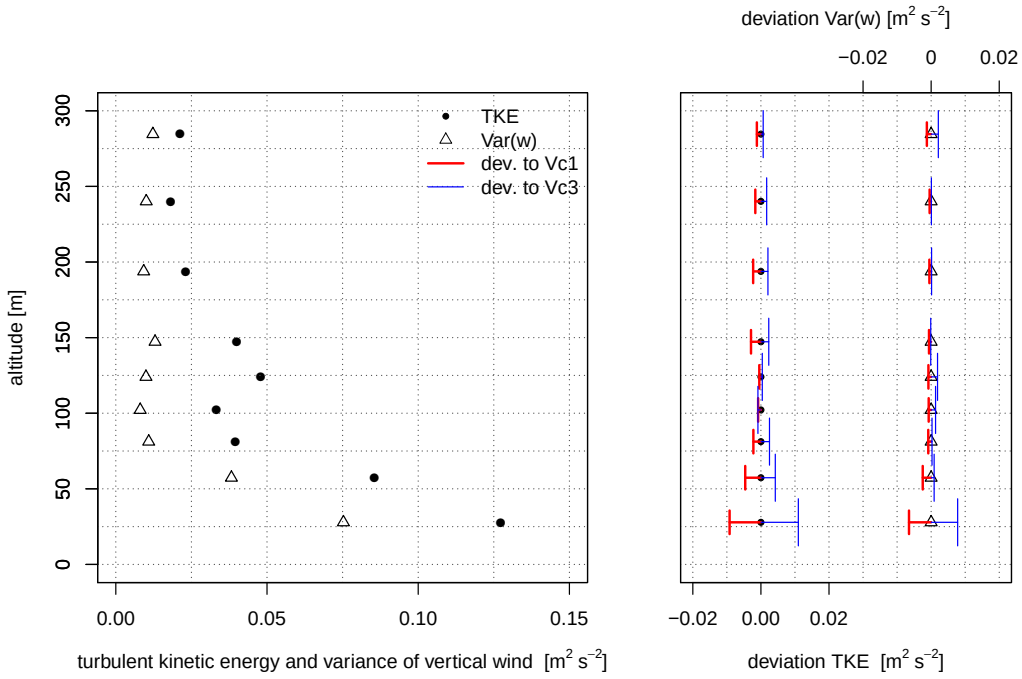

Figure 3.6: Height profiles of the ISOBAR flight with the altitude AMSL of the turbulent kinetic energy TKE and the variance of the vertical wind component Var(w), calculated with the calibration polynomial at v_{c2} (**left**). Deviations (**right**), when applying the calibration polynomials at v_{c1} and v_{c3}.

The covariances Cov(w, u) and Cov(w, v) in Figure 3.7 are used to estimate the turbulent momentum flux and are also directly influenced by the calibration of the five-hole probe. The spatial resolution in the surface layer is unfortunately too small to be able to give sufficient insight into the momentum flux, but it is remarkable that MASC can measure consistently small values close to zero without outliers. The deviations of the covariances are generally high and especially for the two height levels above the ground. The peak value for Cov(w, u) on the lowest flight level has relative deviations of 30% and 35% and for the covariance Cov(w, v) on 54 m AMSL, the relative deviation is almost 100%.

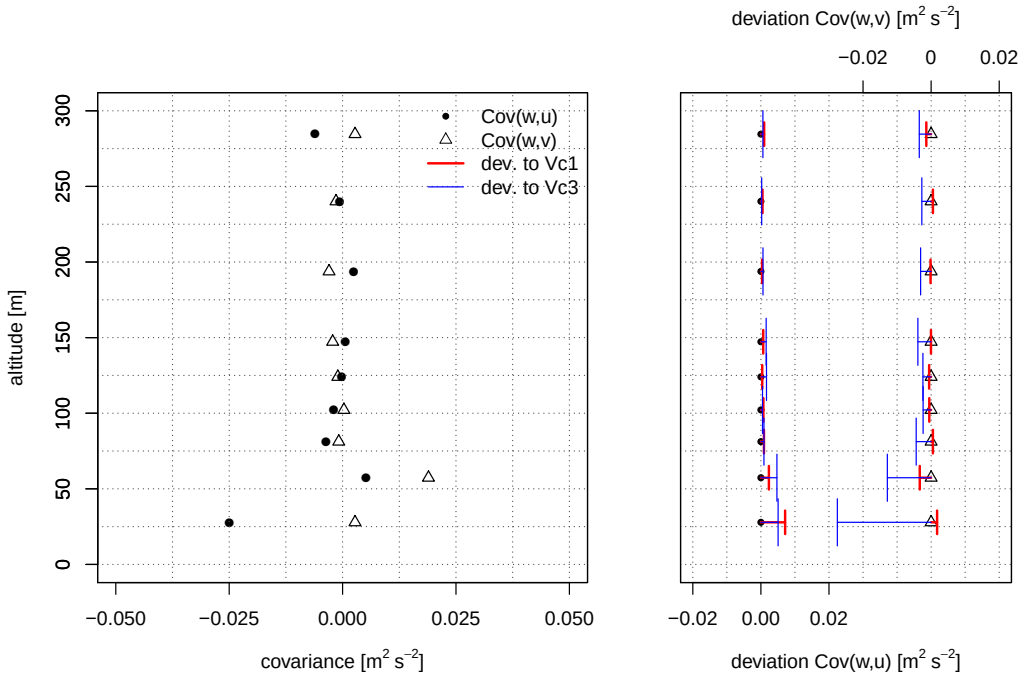

Figure 3.7: Height profiles of the ISOBAR flight with the altitude AMSL of the covariances Cov(w,u) and Cov(w,v), calculated with the calibration polynomial at v_{c2} (**left**). Deviations (**right**), when applying the calibration polynomials at v_{c1} and v_{c3}.

The potential temperature profile in Figure 3.8 indicates a convective ABL with a step of 0.4 °C between the forth and fifths height level. While the wind speed profile is relatively uniform, the profile of wind direction has also high gradients between 870 m and 915 m AMSL. Intensive shear, and the separation between two regimes persists. Despite strong turbulence, the deviations for mean values are, with a maximum of 0.1 m s^{-1} and 0.2°, small and in the same order of magnitude as for the ISOBAR flight.

TKE and Var(w) is, with more than 3 m^2 s^{-2} , higher than for the ISOBAR flight by a factor of 30. The two turbulence regimes above and below 915 m AMSL are clearly visible in Figure 3.9, since below the values spread around ≈ 2.2 m^2 s^{-2} and above around ≈ 0.8 m^2 s^{-2} . The deviations are higher, if the persistent TKE is higher, but the relative deviations are, with a maximum of 4.2%, very small compared to the ISOBAR flight. The devia-

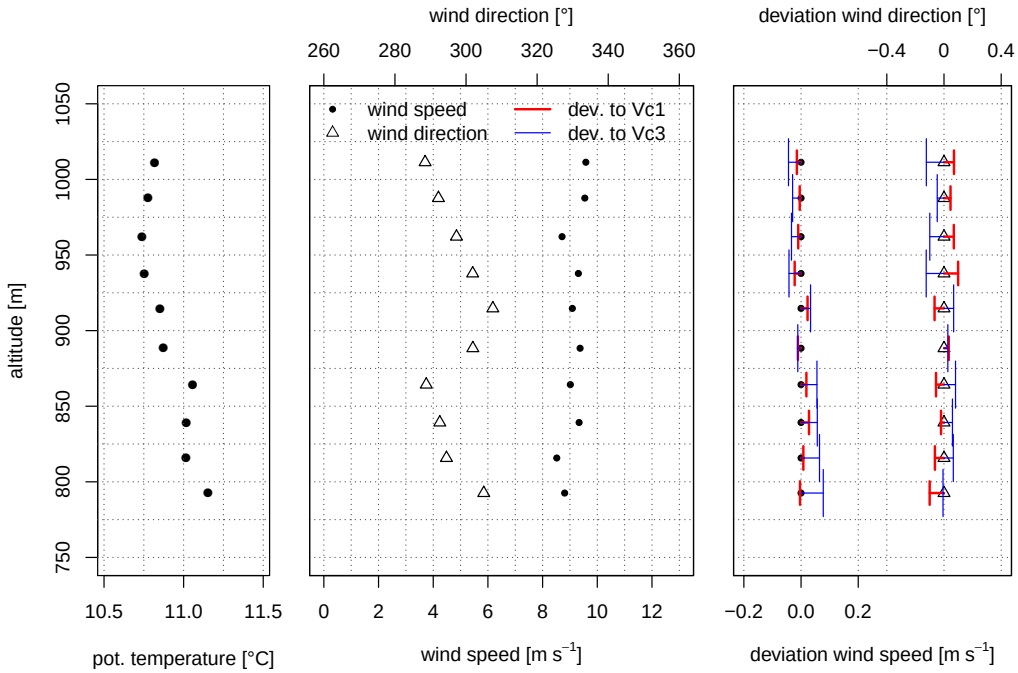

Figure 3.8: Height profiles of the COMPLEX flight with the altitude AMSL of the potential temperature (**left**), horizontal windspeed v_h and wind direction ϕ, calculated with the calibration polynomial at v_{c2} (**middle**). Deviations (**right**), when applying the calibration polynomials at v_{c1} and v_{c3}.

tions when using the calibration at v_{c3} and at v_{c1} give randomly higher and smaller values for the TKE, whereas the deviations for the variance Var(w) are uniformly distributed with higher values for the polynomial at v_{c3} and lower values for the polynomial at v_{c1}.

The covariances Cov(w,u) and Cov(w,v) in Figure 3.10 are, with up to -0.75 m^2 s^{-2} , by a factor of 30 higher than for the ISOBAR flight. Above 925 m AMSL, in the upper persistent layer, the stresses are closer to zero. In dissociation to the turbulent kinetic energy and the variance of the vertical wind component, the covariances depend strongly on the calibration of the five-hole probe. With relative deviations of more than 100% it is delicate, in terms of airspeed variations, to measure reliably covariances in high turbulence. It is interesting to see that the deviations for TKE and Var(w) do not scale with the magnitude of the value, since the ISOBAR flight in low

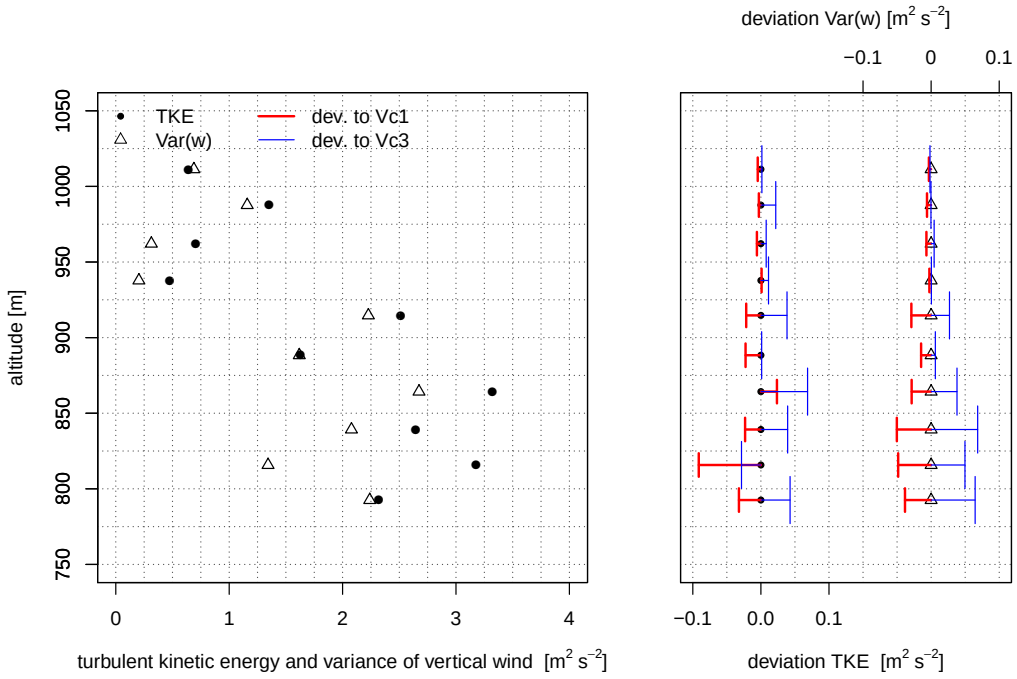

Figure 3.9: Height profiles of the COMPLEX flight with the altitude AMSL of the turbulent kinetic energy TKE and the variance of the vertical wind component Var(w), calculated with the calibration polynomial at v_{c2} (**left**). Deviations (**right**), when applying the calibration polynomials at v_{c1} and v_{c3}.

turbulence shows deviations of up to 20% and the COMPLEX flight in very high turbulence, only a maximum of 4%. The deviations of the covariances, on the other hand, do scale with the actual value and are, by a factor of ten, higher than for the ISOBAR flight. It is concluded that airspeed variations cause disproportionately high deviations for these statistical moments of second order, since the covariances are calculated from the turbulent part of two quantities, that are directly influenced by the calibration of the five-hole probe.

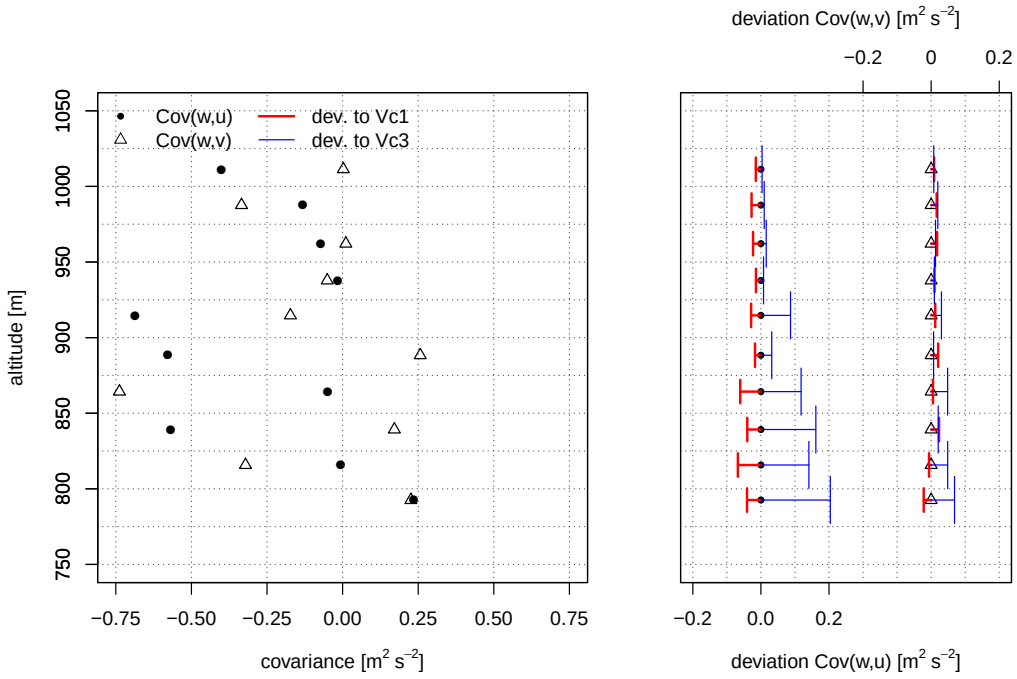

Figure 3.10: Height profiles of the COMPLEX flight with the altitude AMSL of the covariances Cov(w,u) and Cov(w,v), calculated with the calibration polynomial at v_{c2} (**left**). Deviations (**right**), when applying the calibration polynomials at v_{c1} and v_{c3}.

The third flight experiment (referred to as WAKE) is one transect through the wake of a wind turbine near Wilhemshaven in the North of Germany. To analyze the influence of airspeed variations, a transect on hub-height with a distance of one rotor diameter (1D) was chosen. The hub-height of the Enercon E-112 prototype WEC is 125 m AGL and the rotor diameter is 100 m . Figure 3.11 shows the flight path of MASC with the horizontal windspeed v_h in the color code for a transect from west to east. The wind direction and speed was about 25° and 9 m s^{-1} for the leg on hub-height and in front of the WEC. The windspeed deficit is clearly visible in Figure 3.11 and the tip vortices can be already identified. Moreover, Figure 3.11 shows the schematic orientation of detaching tip vortices of a turbine blade, when considering the cross-section of a horizontal plane on hub-height. Here, it can be assumed that the cross-section of the vortex lies untilted (flat) in a

horizontal plane through the center of the rotor. The measurement for this example is located 1D behind the WEC. Assuming that there is no deflection of the wake and the helix of vortices in any direction, the orientation of the vortex at 1D behind the WEC would be the same. The arrows indicate the position of the vortices that were encountered or passed with the flight leg. Assuming incompressible and divergence free flow, a vortex can be described by potential theory, where the velocity field is a simple function of the radius r of the vortex and the circulation Γ, which is the strength of the vortex. This is the basis for simple formulations to describe e.g., aircraft wake vortices Ahmad and Proctor (2014); Mauz et al. (2019). If a tip vortex were traversed through the center, the tangential velocity would increase to its maximum at the core radius $r = r_c$, and decrease to zero, when passing the center at $r = 0$, followed by another increase in the opposing direction to its second maximum at $r = r_c$ again. During the approach and after the vortex, outside r_c, the tangential velocity increases and decreases until the mean flow dominates. This simplification is the basis argumentation for the analysis and interpretation in this study.

The exact mechanism of the influence of airspeed variation and the role of the calibration polynomials of the five-hole probe for the individual deviation is given in the article in Appendix A. To summarize the influence it can be stated, that the deviations are moderate, when deriving qualitative features of the flow. For vortex models, the size of the core radius and the magnitude of the circulation Γ are of major interest, e.g., to validate numerical models or to study the decaying processes of vortices. Here, the deviation of almost 1 m s^{-1} for the wind vector component v between the calibration polynomials is relevant and considering the changes in airspeed would decrease the uncertainty significantly. To pick out an important feature of the influence of airspeed variations during the measurements and to introduce the following recommendation to improve the wind vector measurements, Figure 3.12 is given. It depicts the transect through the first tip vortex and the deviations

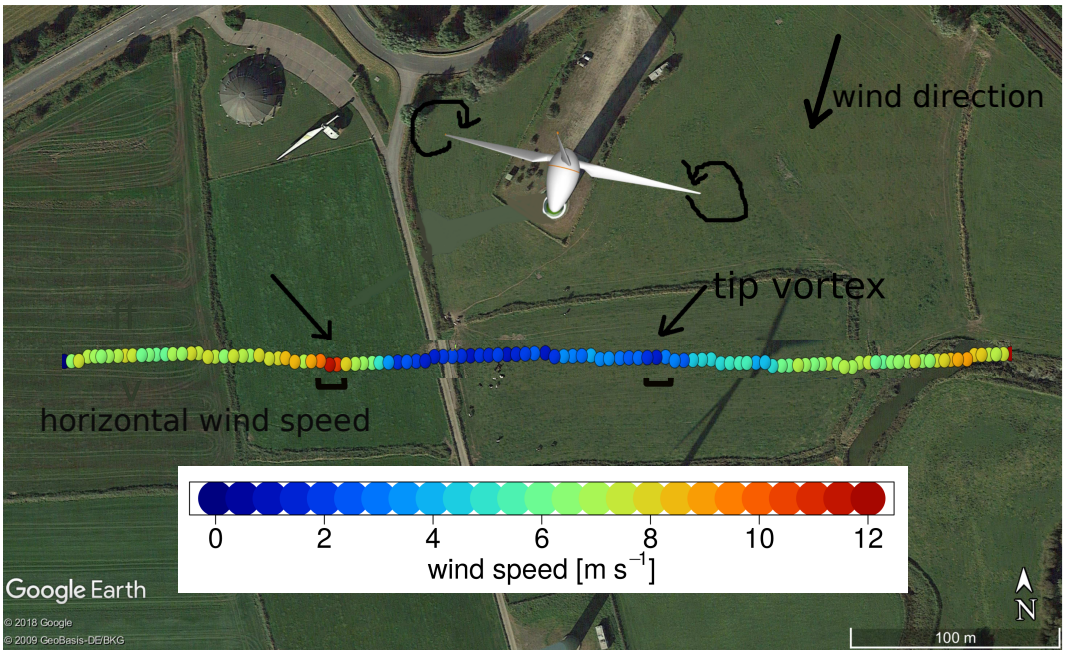

Figure 3.11: Top view with one leg in the wake of the Enercon E-112 prototype wind turbine with the horizontal windspeed (v_h) in the color code. The light direction was from west to east. The schematic turning direction of detaching tip vortices in a horizontal plane through the rotor center is sketched. The positions of the tip vortices of the measurement are indicated with arrows. The depicted wind turbine is an appended schematic model, indicating the azimuth-angle of the nacelle during the measurement.

when applying the different calibration polynomials of the five-hole probe. The sensitivity of the calibration of the dynamic pressure coefficient k_q is the main contributor here. During high angles of side-slip β, while crossing the tip vortex, the true airspeed measurement is more than 1 m s^{-1} apart between the curves with the polynomials at v_{c1} and v_{c3}. The calibration polynomials, where the significant difference for k_q between the calibration speeds are obvious (Appendix A), explain the deviations of the true airspeed in Figure 3.12. Besides the general offsets between the three time series during the transect of the tip vortex, also the shapes of the curves differ. The sensitivity of the calibration of the dynamic pressure coefficient k_q was found to be the main contributor to the uncertainties. In the following, a method of

interpolating the polynomials is suggested and an independent flow probe for the true airspeed measurement is recommended in order to minimize the influence of this uncertainty.

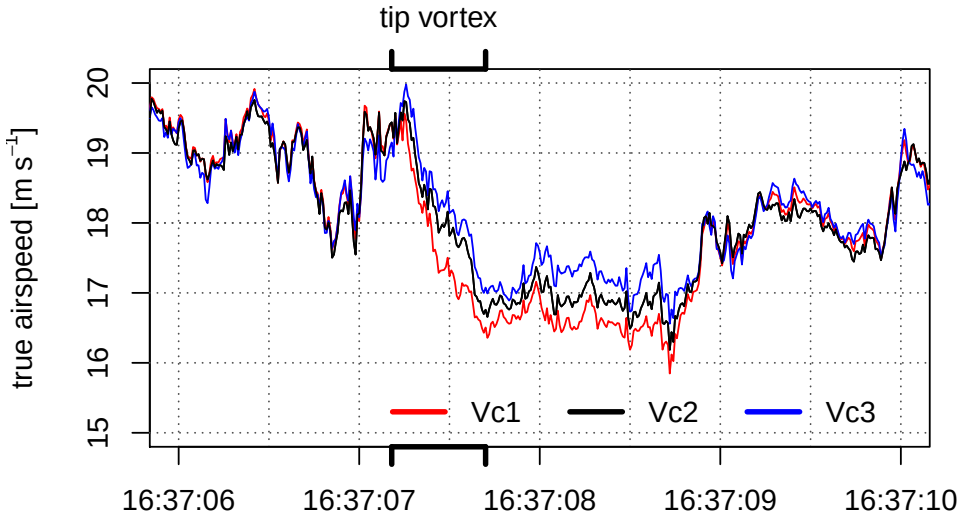

Figure 3.12: Fraction of the time series of the true airspeed $|\vec{u}_a|$. The data is plotted for the three calibrations at v_{c1}, v_{c2} and v_{c3}. The position of the tip vortex is indicated.

Inspired by the study of Hartmann et al. (2018), which mentions a linear proportionality for the conversion of pressure readings to flow angles in a certain range of Reynolds numbers, the following procedure to improve the accuracy while gaining flexibility and keeping the calibration effort small is suggested. The characteristic polynomials of the calibration of the five-hole probe ($\vec{k}\ \vec{c'}_x$) can be linearly interpolated with the Reynolds number between the three calibrations at v_{c1}, v_{c2} and v_{c3}. To demonstrate this, an interpolation between the polynomials at v_{c1} and v_{c3} onto the Reynolds number of $\mathrm{Re}_{v2} = 5538$ was made:

$$\vec{k}\ \vec{c'}_{x,\ ipol} = \vec{k}\ \vec{c'}_{x,\ v1} + \vec{k}\ \vec{c'}_{x,\ v3} - \vec{k}\ \vec{c'}_{x,\ v1} \left(\frac{\mathrm{Re}_{v2} - \mathrm{Re}_{v1}}{\mathrm{Re}_{v3} - \mathrm{Re}_{v1}} \right). \tag{3.1}$$

The deviation between the originally measured and interpolated polynomial can be analyzed directly from the wind-tunnel data. The polynomials calculated with the data of the calibration can be used to recalculate α and β

from the pressure readings. This verification reveals a significant improvement and is explained in detail in the article in Appendix A.

Mean values are robust against airspeed variations, but the turbulent kinetic energy, variances and especially covariances, and the integral length scale are strongly influenced. For turbulence statistics, flux calculations, and quantitative analysis of turbine wake characteristics, an independent measurement of the true airspeed with a pitot tube and the interpolation of calibration polynomials at different Reynolds numbers of the probe's tip onto the Reynolds number during the measurement, reduces the uncertainty significantly. The range of airspeeds, respectively Reynolds numbers, with three polynomials between $v_{c1} = 15$ m s^{-1} and $v_{c3} = 28$ m s^{-1} is large and must be decreased or improved upon, by measuring e.g., 5 polynomials. For quantitative studies of turbulence and single features of the wind field of interest, the uncertainty, coming from the wind vector measurement with five-hole probes, can be decreased by interpolation of the polynomials for the angle of attack α and the side-slip β and by using a pitot tube to measure the true airspeed independently.

3.3 MASC-3 and the Application in Polar Stable Boundary Layers

The airframe and the autopilot system as well as the embedded sensor system of MASC-3, were completely reworked compared to the previous version of MASC. The sketch in Figure 2.1 provides an overview of the new setup. The core of the data acquisition unit is a Raspberry Pi 3, allowing the use of various interfaces to sensor applications, telemetry modules and on-board data processing algorithms. The new central module for sampling analogue sensors is called CEBO-LC and provides further channels as well as significantly higher sampling rates compared to the old system. After each flight experiment, the stored data on the SD-Card of the Raspberry Pi

3 can be, for example, downloaded via Ethernet. Since the CEBO-LC, the INS Ellipse2-N and the Arduino that insures a uniform sampling of further sensors, have separated log files, the data has to be merged in the post-processing. The accuracy of the 32 Bit counter of the CEBO-LC and the INS, which also includes a 32 Bit counter as well as GNSS-time, ensures the accuracy of the synchronization, making the timestamps of the Raspberry Pi itself almost obsolete. A first quality control with several plots of the measured quantities along the flight legs are printed out after reading the logs and setting the calibration data. Additionally, the power spectra and structure functions of the main quantities are plotted for a quality control just after the measurements. Furthermore, vertical profiles of wind speed, wind direction and turbulence quantities are provided, containing the data of each flight leg. These quick looks are essential to get a brief overview of the meteorological conditions. An adaption of the flight patterns for consecutive flights can be considered, or a sensor malfunction can be identified. The set of plots is at hand, minutes after landing the UAS. The software concept and the first analysis on sight is the foundation for a detailed post-processing of all measured data but also a key element for successful field campaigns.

Two flight experiments were dedicated to closely comparing the MASC-3 measurements with meteorological tower measurements and were conducted in the evening of the 10 February 2018 during the ISOBAR campaign. The main aim is to validate the turbulent 3D wind vector measurement with MASC-3 and it's new features. To do so, mean values, statistical moments of second order and integral length scales can be compared and a spectral analysis can be performed. A comparison to established measurement systems and theory leads towards validation. With the data of the ISOBAR campaign, a close comparison with the measurements of a meteorological tower lead towards validation and secondly the data of the tower and the phased array 3D wind Sodar were plotted together with profiles of MASC-3 in a SBL.

The methods for the comparison were based on a comparative duration of the time series for the stationary and the moving measurement systems, which correspond to the individual fetch, or amount of air that is passed, of both systems. The comparisons by means of time series analysis for mean values of wind speed and direction, variances, turbulent kinetic energy, covariances and integral length scales of the 3D wind vector measurement were conducted. Differences concerning the fact that MASC-3 samples a quasi-spatial snapshot along a straight and horizontal flight leg with its cruising airspeed and that the stationary tower samples the advected air flow, can be considered by comparing the quantities of interest for time series that have the same temporal fetch. The temporal fetch is represented by the approximated time interval for the individual measurement system during which the same volume of air was sampled. To account for that, the considered duration of the time series Δt for the comparisons inherit the same temporal fetch calculated by

$$\Delta t_{\text{tower}} = \Delta t_{\text{UAS}} \frac{v_{\text{UAS}}}{v_{\text{tower}}} = \Delta t_{\text{UAS}} \frac{|\overline{\vec{u}_a}|}{\overline{v_h}}, \tag{3.2}$$

using the mean true airspeed $|\overline{\vec{u}_a}|$ of the UAS divided by the mean horizontal wind speed $\overline{v_h}$, measured by the UAS. This factorization for defining the duration of the compared time series complies with the full duration of the MASC-3 flight leg and the corresponding duration of the time series of the tower measurement Δt_{tower} is calculated with Equation (3.2).

The wavenumber spectra and the structure functions for the horizontal wind v_h in Figure 3.13 give insight in the resolution of both measurement systems. The inertial subrange of turbulence in an isotropic flow is characterized by the $k^{-5/3}$ slope in the power spectrum and by the $r^{2/3}$ slope in the structure function, indicating the ability and quality of the measurement system to resolve the spectrum of turbulent fluctuations in the atmospheric boundary layer Rautenberg et al. (2019b). Generally, the discretization of the structure function is sparse towards small lags and the influence of sensor noise is better visible in the power spectrum. Vice versa, the power

spectrum is sparsely discretised for small wave numbers and to study the production subrange and the onset of the inertial subrange, the structure function is beneficial. The power spectrum of v_h of the tower measurement is located slightly higher than the spectrum of the MASC-3 data, since the variances of the vertical wind Var_{v_h} of the tower measurement are also slightly higher. The structure functions of both time series for v_h agree well in the inertial subrange but in the production subrange the curve of the tower data lies above the curve of MASC-3, which can also be explained by the difference in the variance measurements of both systems of $\approx$ 0.05 m^2 s^{-2} . If the variance, as an indicator of turbulence, is higher, the spectra is located higher and the production subrange is elevated. Although only $\approx$2 m altitude offset persist between the sonic anemometer and the average flight level of MASC-3, this can explain the differences, since the structure of the surface layer changes strongly with height. The ability to resolve the smallest structures can be closely compared when looking at the power spectra and towards growing wavenumbers. For v_h and for both measurement systems, a flattening of the spectra into the horizontal, indicating sensor noise, can be observed starting from $k \approx 4$ m^{-1} for the tower and from $k \approx 10$ m^{-1} for MASC-3. The structure functions indicate, that the onset of the inertial subrange of v_h starts at lags of $\approx$ 20 m for MASC-3 and the tower. The structure function of v_h of the MASC-3 data become steeper towards the lowest lags, also indicating the onset of sensor noise. The structure function of the tower data do not indicate the onset of sensor noise as clear as the power spectra do. With sensor noise starting from $k \approx 4$ m^{-1} for the tower and from $k \approx 10$ m^{-1} for MASC-3 it can be stated that, MASC-3 has, with 30 Hz, a significantly higher temporal resolution as the sonic anemometer with 6 Hz.

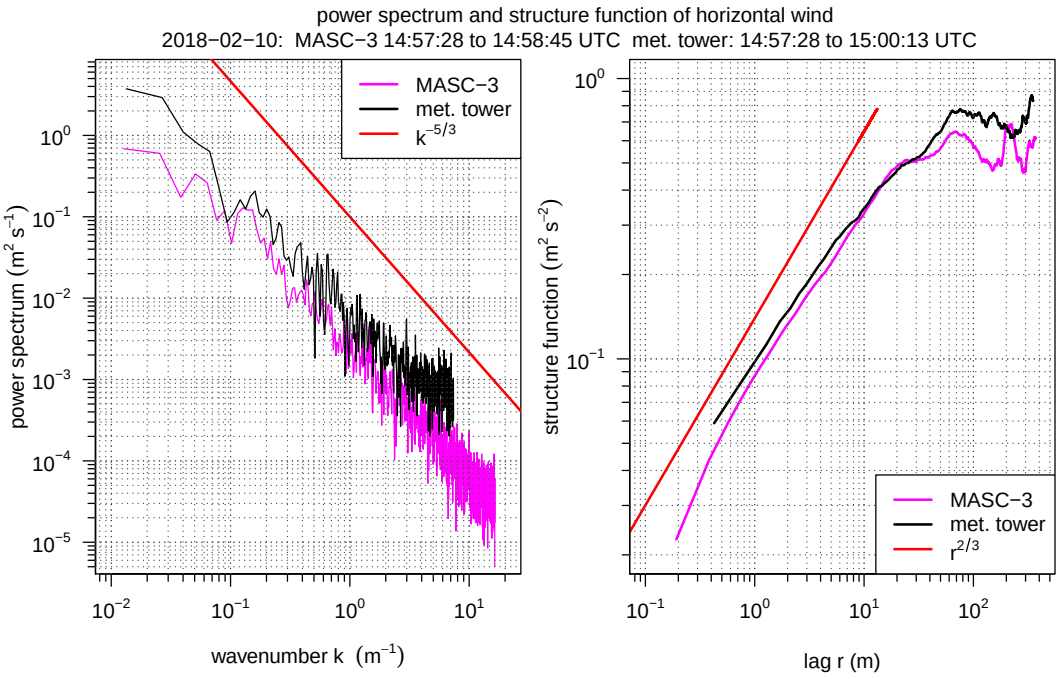

Figure 3.13: Wavenumber spectra (**left**) and structure functions (**right**) for the horizontal wind v_h. The data of the tower at the 10.3m level inherits a time series of $\Delta t_{\text{tower}} = 165$ s , corresponding to the fetch of the MASC-3 flight leg with a duration of $\Delta t_{\text{UAS}} = 77$ s . Flight #10 and the first leg at 11.7 m AGL is given.

The analysis of a fast evolving SBL during the second flight, where the height profiles performed with MASC-3 are supplemented with the tower and Sodar measurements on the ground, illuminates the vast potential of turbulence measurements with MASC-3 in SBL. The comparison includes the temporally and spatially closest tower measurement periods into the height profiles of the Figures 3.14 - 3.15. Figures 3.14 is also supplemented with the Sodar measurements and indicates the timestamps of the data of the three measurement systems. The Figures 3.14–3.15 inherit the tower measurements with the equivalent timestamps of the MASC-3 legs that are closest to the tower. MASC-3 ascended, descended and ascended for a second time during this flight (Flight #11). Two racetracks were conducted at every

height level, resulting in two consecutive headwind legs at each height level. During the first ascent, the lowest flight level was approximately 14 m AGL and after descending and before ascending the second time, the lowest flight level was 25 m AGL. The combined profiles measured by the MASC-3 (triangles), the tower (circles), and Sodar (lines) are presented.

Figure 3.14 shows the averages of potential temperature, wind speed and wind direction. Potential temperature increases with height, that is, 1.2 K in the lower 50 m, indicating the presence of a weak surface-based inversion. The first two profiles, ascent #1 and descent #1, indicate that a stable stratification persists up to 140 m; whereas the third profile, ascent #2, indicates that the atmosphere has cooled and approaches neutral stratification above 50 m. Furthermore, in the lower 50 m all flight patterns show a decrease in wind speed with height of about 3 m s^{-1} together with a change in wind direction of about 40°. The first two MASC profiles agree well with the corresponding Sodar profiles of wind speed and direction at 19:45 UTC and 20:15 UTC, whereas ascent #2 reveals for the wind speed features of both the Sodar profiles taken at 20:45 UTC and 20:55 UTC. During ascent #2, a strong instationarity related to a decrease in wind speed persisted.

During the whole flight, a stable boundary layer was present, but surface observations reveal that turbulence conditions were not stationary. Around 18:30 UTC clouds enter the area. Long-wave incoming radiation increases from 220 W m^{-2} to 280 W m^{-2} around 19:00 UTC, and recovers to its original values just after 20:00 UTC. At the same time, the sensible heat flux at 2 m height increases from -25 W m^{-2} at 18:00 UTC to 0 W m^{-2} at 19:00 UTC, and decreases to -20 W m^{-2} at 20:00 UTC. At 10 m height, the sensible heat flux also increased to 0 W m^{-2} at 18:00 UTC; but during the cloud free periods, the magnitude of the flux in 10 m height was about 5 W m^{-2} smaller than at 2 m height. Furthermore, stability at 2 m height was constant around 0.05 and, whereas at 10 m height values decreased

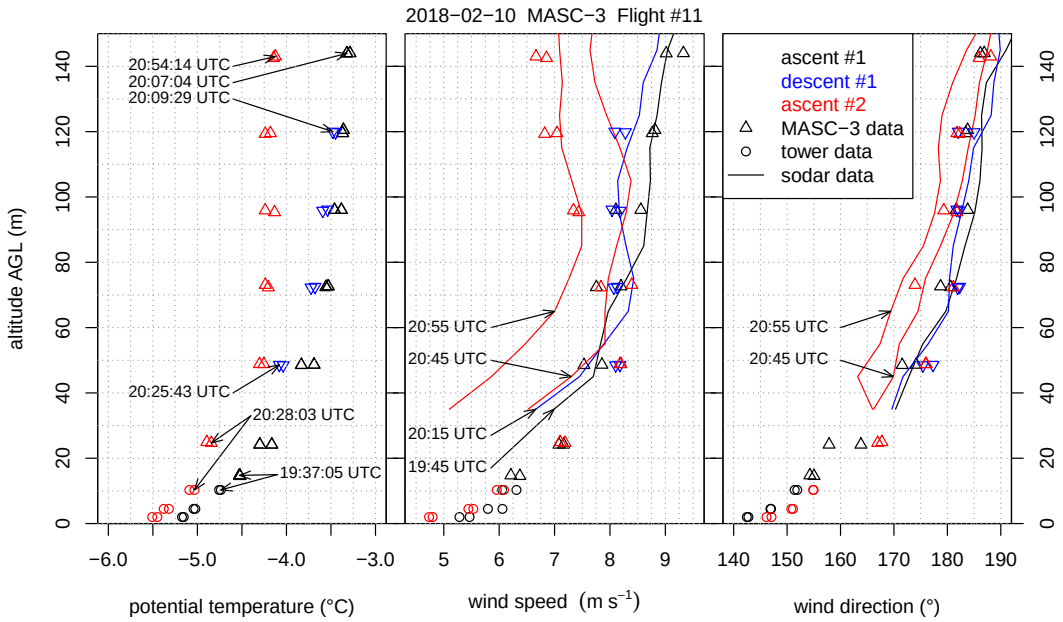

Figure 3.14: MASC-3 Flight #11 alongside the corresponding tower data and Sodar data as height profile for the potential temperature θ (**left**), the horizontal wind speed v_h (**middle**) and the wind direction ϕ (**right**). The time series of the tower data points have a duration of $\Delta t_{\text{tower}} = 170$ s, corresponding to the fetch of the MASC-3 flight legs at the lowest levels with an average duration of $\Delta t_{\text{UAS}} = 55$ s. The timestamps of the first measurement points of each profile and the timestamps of the Sodar profiles are given.

from 0.4 at 18:00 UTC to 0.05 at 19:00 UTC, recovering to 0.4 at 20:00 UTC. Finally, the friction velocity, u_*, steadily decreased from 0.25 m s^{-1} to 0.16 m s^{-1} during this time period.

To get more insight in the atmospheric structure, the MASC-3 measurements allow to consider second-order moments. Figure 3.15 presents the turbulent kinetic energy (TKE) and the covariance of horizontal and vertical winds $\text{Cov}_{wu_{\text{rot}}}$. Note that also these variables represent time averages for the tower data of $\Delta t_{\text{tower}} = 170$ s . This is a rather short averaging interval for second-order moments but it contains 90% of the relevant information as shown by the ogives Foken et al. (2006). Furthermore, profile scaling

functions of $\mathrm{Cov}_{wu_{\mathrm{rot}}}$ by Reference Nieuwstadt (1984) are plotted . The main assumptions for this model are a stationary boundary layer with constant Richardson and Richardson flux numbers Nieuwstadt (1984).

The profiles of TKE and $\mathrm{Cov}_{wu_{\mathrm{rot}}}$ as shown in Figure 3.15 show, that the last profile of TKE decreases in the lower 60 m AGL, whereas in the first profile TKE increases. The $\mathrm{Cov}_{wu_{\mathrm{rot}}}$, which is aligned in the mean wind and thus represents u_*, seems to follow the scaling profile of Nieuwstadt in all cases. Nevertheless, the first profile shows a greater spread between the two flight legs and suggests a maximum of $\mathrm{Cov}_{wu_{\mathrm{rot}}}$ at about 70 m AGL.

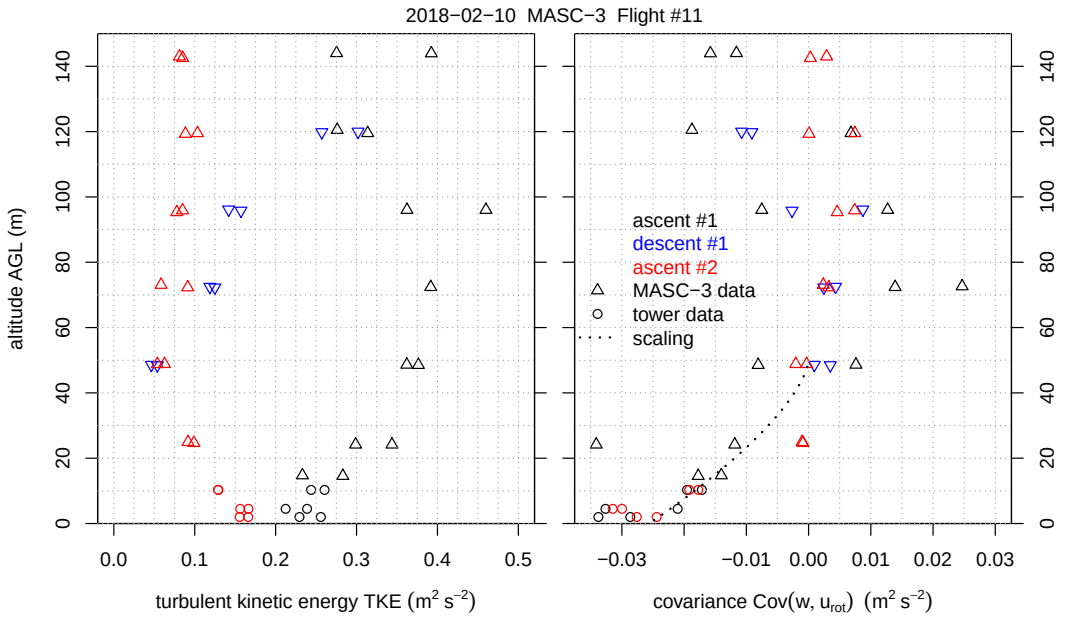

Figure 3.15: MASC-3 Flight #11 alongside the corresponding tower data as height profile for the TKE (**left**) and the covariance $\mathrm{Cov}_{wu_{\mathrm{rot}}}$ (**right**) of the vertical wind w and the transformed vector component u_h which is aligned with the mean wind direction. The time series of the tower data points have a duration of $\Delta t_{\mathrm{tower}} = 170$ s, corresponding to the fetch of the MASC-3 flight legs at the lowest levels with an average duration of $\Delta t_{\mathrm{UAS}} = 55$ s. The $\mathrm{Cov}_{wu_{\mathrm{rot}}}$ profile (right) inherits the scaling function.

These data show that during the cloudy atmospheric conditions the boundary layer is not in balance with the surface, that is, conditions are non-stationary. Ascent #1 took place in the period when the clouds were leaving the area. The radiative cooling starts to enhance the magnitude from the surface fluxes, but at greater heights turbulence is still more active due to the previously existent neutral conditions. One may argue that this profile suggests the existence of a so-called upside-down boundary layer, that is, a boundary-layer containing an elevated shear layer. However, since conditions are non-stationary, this relates rather to an elevated shear layer with the onset of radiative cooling at the surface than to an upside down boundary layer with an elevated source of turbulence cf. Reference Mahrt (1999); Banta et al. (2006). The boundary layer classification, may be considered a weakly stable boundary layer in the transition regime, that is, no constant flux layer and stability >0.1 Grachev et al. (2005).

It can be concluded that the MASC-3 measurements agree well with measurements of the meteorological tower and the Sodar and the combination of these measurement systems captures the interactive nature of the stable boundary layer well. The relatively long sampling time for a full ABL profile, consisting of several straight and vertically stacked legs, may however cause misleading interpretations when sampled under conditions with strong instationarity. For such cases, additional boundary layer remote sensing systems such as Sodar are highly valuable.

Chapter 4

Discussion and Outlook

This thesis described the development and applications of MASC and in particular the capabilities, limitations and uncertainties of wind and turbulence measurements in the ABL. Commonly used methods for wind vector estimation such as the NFSA and the more sophisticated PTA were compared with the direct measurement using the MHPA with UAS. By choosing a variety of flight patterns which are used for meteorological sampling and substantially different weather conditions, the comparison covers a broad band of scenarios. The NFSA is generally not limited to circular patterns, but it performs best when having a continuous and rather constant change in the heading of the aircraft. In these cases, the temporal resolution can be increased, and an averaging window which comprises two full racetracks still generates good results, but the increased temporal resolution comes with lower precision. It was shown that strong turbulence decreases the accuracy. Autopilot systems well tuned to perform regular circles at constant airspeed are crucial for the NFSA. The method is limited in cases with long straights. Using one more piece of information, namely, the vector component of the true airspeed in the flight direction, the wind speed and direction estimation can be strongly enhanced. The PTA allows for generally better results than the NFSA and, in particular, provides additional benefit during flight patterns

with long straight legs. Furthermore, the temporal resolution is much better without the need for a full racetrack inside the averaging window, although at least some change in the heading is still needed. In conclusion, both estimation algorithms achieve good results when applied within their limitations. The simplicity of the NFSA is attractive for very small platforms, and the UAS can be designed to be cheap, efficient, and robust enough to withstand miscellaneous environmental conditions. The PTA depends on the dynamic pressure measurement, which adds complexity to the UAS. However, the enhancement of the wind speed and direction estimation is significant.

The MHPA is the most sophisticated method and of the presented algorithms, the temporal resolution to measure at turbulent scales and the ability to measure the vertical wind component can only be achieved using the MHPA. Further development was needed for the MHPA during strong and sudden changes of the cruising airspeed of the UAS. During transects through the wake of wind turbines and in very strong turbulence, the domain of calibration was exceeded and uncertainties persisted. Also the small turbulent fluxes of a SBL required a close analysis of the uncertainties of the MHPA. Variations of the true airspeed cannot be avoided, since non-zero vertical wind and varying horizontal wind causes the UAS to accelerate and decelerate. A proportionality with the momentum of the UAS, the aerodynamic drag, and the flight-mechanical properties persists. The commands of the autopilot balance the reaction of the UAS, causing variations of the true airspeed. Moreover, the setting of the cruising speed cannot be made precisely prior to the flight, since the density of the air is not considered by the airspeed measurement of the autopilot. Additionally, flexibility for the cruising speed of flight experiments is desired, to sample denser by flying with lower airspeed, or respond to high windspeeds or extreme turbulence, by increasing the airspeed. Three calibration polynomials were applied to three flights in different atmospheric conditions in order to investigate the influence on the calculation of mean values and turbulence statistics of hori-

zontal flight legs and the influence on the high-resolution wind measurement during single events with large changes of the airspeed. The ISOBAR flight in a stably SBL with low turbulence was presented and compared to the COMPLEX flight in high turbulence over complex terrain. The mean values of wind speed and direction, calculated over one flight leg, are robust against changes of the true airspeed, widely independent of the intensity of turbulence, and generally small. The turbulent kinetic energy and the variances of the vertical wind component show relatively small deviations when applying the different polynomials, but the covariances and the integral length scales are sensitive. Airspeed variations of the UAS during measurements, and differences of the Reynolds number of the probe's tip between the calibration and the measurement, influence the results of the turbulence measurements randomly and it is not feasible to quantify the uncertainty, neither in general, nor for the individual statistical moments. Moreover, the uncertainties for flux calculations are high for turbulent conditions and for SBL, where small fluxes distinguish important characteristics. The analysis of the WAKE flight showed the mechanism of the influence of the calibration of the probe, revealing that the calibration of the dynamic pressure coefficient and the subsequent calculation of the true airspeed contributes strongly to the uncertainty. The deviations for a transect through the wake of a wind turbine and through a tip vortex were analyzed and if the size, orientation, and strength of a tip vortex is evaluated quantitatively, deviations must be expected, if the airspeed of the measurement varies strongly and does not match the airspeed of the calibration. To decrease uncertainties, to keep the calibration effort proportionate, and to gain flexibility for missions in terms of cruising airspeed, the interpolation of polynomials for the angle of attack and the side-slip in combination with an independent true airspeed measurement with a pitot tube is recommended. Further flexibility for operations was gained, since the recommended improvements allow for a broader range of the cruising airspeed during the measurements.

The recent mark of the Multi-Purpose Airborne Sensor Carrier MASC-3 improved the turbulent 3D wind vector measurement and gained endurance, since the flight mechanical performance of the wing design with a high lift/drag ratio and the streamlined design is less susceptible to turbulence. The influence on the location of the sensors was minimized by locating the engine behind the tail unit. The fuselage and the installed sensor hat, as well as the modular software architecture of the data acquisition system, allow for different payloads and a variety of applications that can be supplemented to the turbulent 3D wind vector measurement. The autopilot system and the durable airframe can be deployed in polar conditions and provides manifold maneuverability including a multitude of flight patterns for different missions, as well as automatic landing. The precision and repeatability of the Pixhawk 2.1 autopilot ensures the quality of turbulence measurements in the atmospheric boundary layer. The telemetry of the autopilot and the sensor system, as well as the post-processing software MADA, provide insight of the prevailing conditions on sight and enable interactive and adjusted measurement campaigns. Two flight experiments in a SBL and a close comparison with a meteorological measurement tower, equipped with sonic anemometers, depicted the capabilities of MASC-3. The close comparison with the data of the measurement tower showed, that variances, covariances, turbulent kinetic energy and the integral length scale can be reliably estimated and agree well. With MASC-3 and its sensor system, the turbulent structure of the ABL can be sampled faster and with higher resolution than standard sonic anemometers mounted on a measurement tower. Considering the individual fetch of a stationary measurement system and a moving UAS, the systems can be plotted together with continuous profiling systems, such as Sodar to depict fast evolving SBL. Due to the ability to transect the ABL, shorter averaging intervals for second-order moments are applicable when compared to stationary measurement systems, especially if the mean flow is weak and the advection over the stationary sensors is small. The tem-

poral evolution and transition phases between turbulence regimes can be captured with higher resolution and thus, MASC-3 is a valuable addition to meteorological towers and Sodar measurements when investigating the interactive nature of the stable boundary layer. The combination of several UAS at the same, supported by ground based and remote sensing techniques, requires detailed planning, close coordination and reliable equipment. In order to gain a dense picture of a meteorological phenomena of interest, the combination of different UAS is very promising, but challenging. Concepts and strategies, including forecasts of the expected situation and specific storyboards of the observational period should be further developed and analyzed in the future.

The MASC-3 system is capable of measuring detached tip vortices in the wake of a WEC. However the calibration range of the five-hole probe was too narrow for the occurring side flow and the strong pressure gradients during the flight through some vortices. In the future, the calibration of the five-hole probe should be expanded to larger angles, allowing a lower cruising airspeed of the UAS and therefore lower pressures at the pressure transducers and a better spatial resolution of the data. Wake meandering, and the evolution of the wake and the vortices with respect to meteorological conditions should be researched in the future. Among other possible scenarios, such spacious flow fields like the wake of a WEC, take a long time to be sampled with one single UAS and the meteorological conditions may change during that time. Multiple UAS, flying in a coordinated manner would increase the temporal and spatial resolution drastically. In order to be able to do so in the future, further automation for operating MASC-3, strategies for formation flights and advanced post-processing is needed. A flexible cruising airspeed and the functionality of the Pixhawk 2.1 autopilot system to perform a coordinated way point navigation are already at hand and important features for formation measurement flights of multiple MASC-3.

The design of the five-hole probe of MASC-3, with a tip diameter of 4 mm, a cone angle of 60°and forward facing holes follows the following compromise: smaller cone angles or “sharper” tips are more sensitive and the pressure coefficients of the probe react more strongly, if the angle of the inflow tilts. In other words, a small change in the angle of the airflow results in a higher change in the pressure readings, if the probe’s tip is sharp rather than bluff. The downside of sharp probe tips are smaller maximum angles that can be measured and a higher dependency on the Reynolds number. Considering turbulence measurements with a fully exploited frequency response of the tubing and the pressure transducers, the tip diameter should be kept significantly smaller than the smallest eddy that can be resolved. These design criteria provide the potential to customize the utilized flow probe to the requirements of the measurements. Furthermore, 3D printed probes could reduce costs and allow specific adaptions to the requirements of the measurement system. In combination with a virtual calibration using numerical flow simulations (Hall and Povey, 2017), the costs could be reduced further.

Since a misalignment between the multi-hole probe’s orientation and the aircraft cannot be avoided, an in-flight calibration must be applied. Still, only the simplest approach is common practice to do so. Namely, the assumption of a constant wind for two consecutive horizontal straights in opposing direction and the assumption of zero vertical wind. Calibration maneuvers during flight such as the “acceleration–deceleration maneuver”, the “yaw maneuver”, and the “box maneuver”, or using filtered fractions of the measurement data for the calibration of the vertical wind component, have not been performed with UAS, yet. The study of Hartmann et al. (2018) highlights the little attention that is paid to assess the calibration accuracy, when assuming constant wind during the maneuver. The practical guide by Drüe and Heinemann (2013) for wind calibration of a research aircraft, used for turbulent flux measurements, could be adapted to UAS, since the capabilities of modern flight guidance systems allow for a wide range of maneuvers. Such

flight maneuvers can also be a first analysis of the influence of the INS. Accompanied by that is the lack of an uncertainty analysis of the influence of the INS and it's extended Kalman filter on the turbulence measurements with multi-hole probes. The attitude and vehicle velocity estimations are directly inherited in the 3D wind vector calculations and a deeper understanding of the resolution is a future urging task.

Bibliography

Ahmad NN, Proctor F (2014) Review of idealized aircraft wake vortex models. In: 52nd Aerospace Sciences Meeting, National Harbor, MD, USA, p 0927

Bange J (2009) Airborne measurement of turbulent energy exchange between the earth surface and the atmosphere. Sierke Verlag, Göttingen, Germany, 174 pp

Banta RM, Pichugina YL, Brewer WA (2006) Turbulent velocity-variance profiles in the stable boundary layer generated by a nocturnal low-level jet. Journal of the atmospheric sciences 63(11):2700–2719

Brown EN, Friehe CA, Lenschow DH (1983) The use of pressure fluctuations on the nose of an aircraft for measuring air motion. J Climate Appl Meteor 22:171–180

Cormier M, Caboni M, Lutz T, Boorsma K, Krämer E (2018) Numerical analysis of unsteady aerodynamics of floating offshore wind turbines. Journal of Physics: Conference Series 1037:072,048

Corsmeier U, Hankers R, Wieser A (2001) Airborne turbulence measurements in the lower troposphere onboard the research aircraft Dornier 128-6, D-IBUF. Meteorol Z, N F 4:315–329

Dominy R, Hodson H (1993) An investigation of factors influencing the calibration of five-hole probes for three-dimensional flow measurements. Journal of Turbomachinery 115(3):513–519

Drüe C, Heinemann G (2013) A review and practical guide to in-flight calibration for aircraft turbulence sensors. Journal of Atmospheric and Oceanic Technology 30(12):2820–2837

Emeis S (2018) Wind energy meteorology: atmospheric physics for wind power generation. Springer

Fernando HJS, Weil JC (2010) Whither the stable boundary layer? Bulletin of the American Meteorological Society 91(11):1475–1484

Foken T, Wimmer F, Mauder M, Thomas C, Liebethal C (2006) Some aspects of the energy balance closure problem. Atmospheric Chemistry and Physics 6(12):4395–4402

Grachev AA, Fairall CW, Persson POG, Andreas EL, Guest PS (2005) Stable boundary-layer scaling regimes: The SHEBA data. Boundary-Layer Meteorology 116(2):201–235

Hall BF, Povey T (2017) The oxford probe: an open access five-hole probe for aerodynamic measurements. Measurement Science and Technology 28(3):035,004

Hartmann J, Gehrmann M, Kohnert K, Metzger S, Sachs T (2018) New calibration procedures for airborne turbulence measurements and accuracy of the methane fluxes during the AirMeth campaigns. Atmospheric Measurement Techniques 11(7):4567–4581

Khelif D, Burns S, Friehe C (1999) Improved wind measurements on research aircraft. Journal of atmospheric and oceanic technology 16(7):860–875

Kral ST, Reuder J, Vihma T, Suomi I, O'Connor E, Kouznetsov R, Wrenger B, Rautenberg A, Urbancic G, Jonassen MO, Båserud L, Maronga B, Mayer S, Lorenz T, Holtslag AAM, Steeneveld GJ, Seidl A, Müller M, Lindenberg C, Langohr C, Voss H, Bange J, Hundhausen M, Hilsheimer P,

Schygulla M (2018) Innovative strategies for observations in the arctic atmospheric boundary layer (ISOBAR)—the Hailuoto 2017 campaign. Atmosphere 9(7)

Van den Kroonenberg A, Martin T, Buschmann M, Bange J, Vörsmann P (2008) Measuring the wind vector using the autonomous mini aerial vehicle M2AV. Journal of Atmospheric and Oceanic Technology 25(11):1969–1982

Lee SW, Jun SB (2005) Reynolds number effects on the non-nulling calibration of a cone-type five-hole probe for turbomachinery applications. journal of Mechanical Science and Technology 19(8):1632–1648

Lenschow D (1970) Airplane measurements of planetary boundary layer structure. Journal of Applied Meteorology 9(6):874–884

Lenschow DH (1986) Probing the atmospheric boundary layer, vol 270. American Meteorological Society Boston, MA

Mahrt L (1999) Stratified atmospheric boundary layers. Boundary-Layer Meteorology 90(3):375–396

Mauz M, Rautenberg A, Platis A, Cormier M, Bange J (2019) First identification and quantification of detached-tip vortices behind a wind energy converter using fixed-wing unmanned aircraft system. Wind Energy Science 4(3):451–463

Metzger S, Junkermann W, Butterbach-Bahl K, Schmid H, Foken T (2011) Corrigendum to" measuring the 3-D wind vector with a weight-shift microlight aircraft" published in atmos. meas. tech., 4, 1421–1444, 2011. Atmospheric Measurement Techniques 4(7):1515–1539

Nieuwstadt FT (1984) The turbulent structure of the stable, nocturnal boundary layer. Journal of the Atmospheric Sciences 41(14):2202–2216

Platis A, Siedersleben SK, Bange J, Lampert A, Bärfuss K, Hankers R, Cañadillas B, Foreman R, Schulz-Stellenfleth J, Djath B, et al. (2018) First in situ evidence of wakes in the far field behind offshore wind farms. Scientific reports 8(1):2163

Rautenberg A, Graf MS, Wildmann N, Platis A, Bange J (2018) Reviewing wind measurement approaches for fixed-wing unmanned aircraft. Atmosphere 9(11)

Rautenberg A, Allgeier J, Jung S, Bange J (2019a) Calibration procedure and accuracy of wind and turbulence measurements with five-hole probes on fixed-wing unmanned aircraft in the atmospheric boundary layer and wind turbine wakes. Atmosphere 10(3)

Rautenberg A, Schön M, zum Berge K, Mauz M, Manz P, Platis A, van Kesteren B, Suomi I, Kral ST, Bange J (2019b) The multi-purpose airborne sensor carrier MASC-3 for wind and turbulence measurements in the atmospheric boundary layer. Sensors 19(10)

Reuder J, Brisset P, Jonassen M, Müller M, Mayer S (2009) The small unmanned meteorological observer sumo: A new tool for atmospheric boundary layer research. Meteorologische Zeitschrift 18(2):141–147

Sanderse B, Van der Pijl S, Koren B (2011) Review of computational fluid dynamics for wind turbine wake aerodynamics. Wind energy 14(7):799–819

Stull RB (2012) An introduction to boundary layer meteorology, vol 13. Springer Science & Business Media

Sullivan PP, Weil JC, Patton EG, Jonker HJJ, Mironov DV (2016) Turbulent winds and temperature fronts in large-eddy simulations of the stable atmospheric boundary layer. Journal of the Atmospheric Sciences 73(4):1815–1840

Wildmann N, Mauz M, Bange J (2013) Two fast temperature sensors for probing of the atmospheric boundary layer using small remotely piloted aircraft (rpa). Atmospheric Measurement Techniques 6(8):2101–2113

Wildmann N, Bernard S, Bange J (2017) Measuring the local wind field at an escarpment using small remotely-piloted aircraft. Renewable Energy 103:613–619

Williams A, Marcotte D (2000) Wind measurements on a maneuvering twin-engine turboprop aircraft accounting for flow distortion. Journal of Atmospheric and Oceanic Technology 17(6):795–810

Appendix A

Peer-reviewed first-author publications

A.1 Reviewing Wind Measurement Approaches for Fixed-Wing Unmanned Aircraft - Publication I

atmosphere

MDPI

Article

Reviewing Wind Measurement Approaches for Fixed-Wing Unmanned Aircraft

Alexander Rautenberg [1,*], Martin S. Graf [1], Norman Wildmann [2], Andreas Platis [1] and Jens Bange [1]

[1] Center for Applied Geoscience, Eberhard-Karls-Universität Tübingen, Hölderlinstr. 12, 72074 Tübingen, Germany; martingraf@mail.de (M.S.G.); andreas.platis@uni-tuebingen.de (A.P.); jens.bange@uni-tuebingen.de (J.B.)

[2] Deutsches Zentrum für Luft- und Raumfahrt e.V., Münchener Str. 20, 82234 Wessling, Germany; norman.wildmann@dlr.de

* Correspondence: alexander.rautenberg@uni-tuebingen.de; Tel.: +49-7071-29-74339

Received: 30 August 2018; Accepted: 24 October 2018; Published: 28 October 2018

Abstract: One of the biggest challenges in probing the atmospheric boundary layer with small unmanned aerial vehicles is the turbulent 3D wind vector measurement. Several approaches have been developed to estimate the wind vector without using multi-hole flow probes. This study compares commonly used wind speed and direction estimation algorithms with the direct 3D wind vector measurement using multi-hole probes. This was done using the data of a fully equipped system and by applying several algorithms to the same data set. To cover as many aspects as possible, a wide range of meteorological conditions and common flight patterns were considered in this comparison. The results from the five-hole probe measurements were compared to the pitot tube algorithm, which only requires a pitot-static tube and a standard inertial navigation system measuring aircraft attitude (Euler angles), while the position is measured with global navigation satellite systems. Even less complex is the so-called no-flow-sensor algorithm, which only requires a global navigation satellite system to estimate wind speed and wind direction. These algorithms require temporal averaging. Two averaging periods were applied in order to see the influence and show the limitations of each algorithm. For a window of 4 min, both simplifications work well, especially with the pitot-static tube measurement. When reducing the averaging period to 1 min and thereby increasing the temporal resolution, it becomes evident that only circular flight patterns with full racetracks inside the averaging window are applicable for the no-flow-sensor algorithm and that the additional flow information from the pitot-static tube improves precision significantly.

Keywords: wind speed and direction estimation algorithms; flow probes; airspeed measurement; small unmanned aircraft systems (sUAS); unmanned aerial vehicles (UAV); remotely piloted aircraft systems (RPAS)

1. Introduction

Atmospheric boundary layer (ABL) studies are increasingly complemented by in situ measurements using small unmanned aircraft systems (sUAS) [1–8]. Atmospheric sampling using sUAS dates back to 1961 [9] and has since been applied to atmospheric physics and chemistry [10–13], boundary-layer meteorology [14–25], and, more recently, also to wind-energy meteorology [26–28]. The capabilities of sUAS for meteorological sampling range from mean values for wind, thermodynamics, species concentration, etc., to highly resolved turbulence measurements, and from an accurate and diverse but larger sensor payload, down to small aircraft that can be operated from almost anywhere, with minimal logistical overhead. Elston et al. [29] provide details on the airframe parameters, estimation algorithms,

sensors, and calibration methods, examining previous and current efforts for meteorological sampling with sUAS.

Usually, at least mean values, and often highly resolved measurements of an in situ wind vector, are crucial for the investigation or necessary for a deeper understanding of the turbulent atmosphere and turbulent atmospheric transport. The common method for measuring the 3D wind vector from research aircraft is a multi-hole probe in combination with the measured attitude, position, and velocity of the aircraft. In the following, this method is referred to as the multi-hole-probe algorithm (MHPA). The attitude is measured with an inertial measurement unit (IMU), position, and velocity of the aircraft using a global navigation satellite system (GNSS). The combination of both systems, usually supplemented by an extended Kalman filter (EKF), is called an inertial navigation system (INS). The wind vector is defined in the Earth coordinate system and equals the vector difference between the inertial velocity of the aircraft and the true airspeed of the aircraft. The MHPA is used in manned aircraft, as published by Lenschow [30], among others, and was adapted for sUAS by researchers, such as Van den Kroonenberg et al. [31], with the Mini Aerial Vehicle (M^2AV) and by Wildmann et al. [32] using the Multi-purpose Airborne Sensor Carrier (MASC). The achievable high resolution and accuracy of this method demand a precise and fast INS, as well as pressure measurement with multi-hole probes. The study by de Jong et al. [33] introduced an algorithm (PTA, pitot tube algorithm) that does not require a multi-hole probe but only a pitot-static tube for dynamic pressure measurement, which makes it less complex and less expensive. Many common autopilot systems already use pitot-static tubes for airspeed measurement and are, without further instrumentation, capable of estimating the wind speed and direction. The study by Niedzielski et al. [34] also used this kind of approach with a consumer-grade sUAS. Unfortunately, there are no details on the algorithm documented. Even without a flow sensor aboard, the wind speed can be estimated using the 'no-flow-sensor' algorithm (NFSA), as published by Mayer et al. [35]. With the sUAS SUMO (Small Unmanned Meteorological Observer, [36]), extensive measurements (e.g., [37]) were performed using this method. The NFSA uses only ground speed and flight path azimuth information from GNSS and is the least complex and least expensive method in this comparison. Bonin et al. [38] introduced variants of the NFSA and compared them with SODAR measurements, among others. Shuqing et al. [39] introduced the sUAS RPMSS (robotic plane meteorological sounding system) and uses a close variation of the NFSA to estimate the wind speed in their work.

This study provides an overview and review of the three methods and highlights the capabilities and limitations of these types of wind estimation methods that use sUAS. All introduced methods can be applied with the fully equipped sensor system which was used in this investigation. It includes a five-hole probe [40] and the INS IG500-N from SBG-Systems. The PTA can be examined using the INS data and only the tip hole of the five-hole probe for true airspeed measurement, and the NFSA can be investigated using only the GNSS data. Data sets from several measurement campaigns provide a variety of conditions for this comparison. The main factors of influence are the atmospheric conditions and the choice of flight paths. A representative selection with wind speeds between 2 and 15 m s^{-1}, as well as various flight patterns, including horizontal straight and level segments (legs), circles, lying eights, and ascending racetracks for height profiles, were analyzed. Section 2 describes the measurement technology and the wind algorithms. Section 3 gives an overview of the experiments, Section 4 shows the results and discusses them, and Section 5 is the conclusion.

2. Methods and Measurement Techniques

For atmospheric research, boundary-layer meteorology, and wind-energy studies, the environment-physics group at the Centre for Applied Geo-Science (ZAG), University of Tübingen, Germany, designed and built the research unmanned aerial vehicle (UAV) MASC (Figure 1). The MASC [32] is an electrically propulsed single engine (pusher) aircraft with a 3.5 m wing span. The total weight of the aircraft is 6 kg, including a 1 kg scientific payload. This sUAS is operated at an airspeed of 22 m s^{-1}, as a trade-off between high spatial resolution of the measured data and gathering a snapshot

of the atmosphere in a short time frame. The MASC operates fully automatically (except for landing and take-off). Height, flight path, and all other parameters of flight guidance are controlled by the autopilot system ROCS (Research Onboard Computer System) developed at the Institute of Flight Mechanics and Control (IFR) at the University of Stuttgart. The overall endurance of the MASC is 60 min or 80 km.

Figure 1. Research unmanned aerial vehicle (UAV) Multi-purpose Airborne Sensor Carrier (MASC) during take-off with a bungee.

The scientific payload (Figure 2) for this investigation consists of several subsystems for measuring the 3D wind vector, air temperature, and water vapor. This includes a fast thermometer (fine wires, see [41]), a capacitive humidity sensor [32], a five-hole flow probe [31,40], and an INS. All sensors sample at 100 Hz and measure atmospheric turbulence. Considering the individual sensor inertia, a resolution of about 30 Hz (i.e., sub-meter resolution at 22 m s^{-1} airspeed, except for humidity, which is 3 Hz) is achieved. Thus, small turbulent fluctuations are resolved and the Nyquist theorem is fulfilled. The sensors and the data stream are controlled by the onboard measurement computer AMOC and stored at a 100 Hz rate. In order to watch the measurements online during flight, a data abstract is broadcasted to the ground station (standard laptop computer) at 1 Hz. The ground station also communicates with the autopilot. Changes in the flight plan are possible when the MASC is within a 5 km reach. Typical flight patterns with the MASC (these are common flight strategies for any research aircraft) are horizontal straight and level flights (so-called legs) both at constant height or stacked at various flight levels. These flight legs are used to calculate turbulence statistics, turbulent fluxes (e.g., [12,17]), spectra, and mean values, but they also measure the influence of surface heterogeneity and orography (complex terrain, e.g., [28]) on the lower atmosphere. The horizontal flights are usually supported by slanting flights that give data on the vertical profile of various atmospheric quantities, including the thermal stability (e.g., [42]). A combination of both (named the saw-tooth profile) returns both horizontal and vertical structures of the flow. For the sake of completeness, the star pattern or lying eights are commonly used to calibrate the MHPA method.

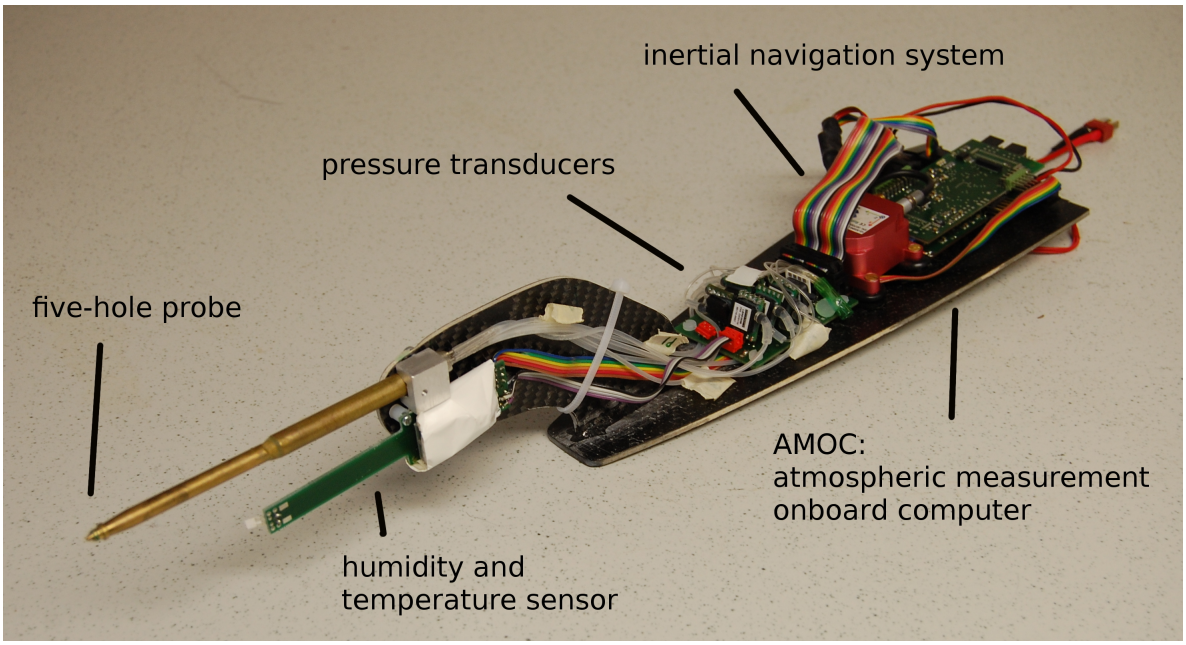

Figure 2. MASC measurement system with five-hole probe, capacitive humidity sensor and temperature sensor, pressure transducers, inertial navigation system (INS), and the measurement computer AMOC.

The standard sensor system developed for the MASC is self-sufficient and can be mounted on other airframes. To cover circular flight patterns, which are often used by flying wings like SUMO, or the return glider radiosonde (RGR, see [5]), data from a measurement campaign at the Boulder Atmospheric Observatory (BAO) were included: A commercially available flying wing (Skywalker X8) with a span of 2.1 m and a take-off weight of about 3.5 kg was equipped with the MASC sensor system and flown at the BAO. Figure 3 shows the Skywalker X8 flying wing with the sensor nose as used with the MASC. This sUAS is equipped with a Black Swift Technologies LLC (Boulder, CO , USA) autopilot system which maintains the airspeed, using a pitot-static tube, at 22 m s^{-1}.

Figure 3. Research UAV Skywalker X8 with the MASC measurement system.

2.1. Coordinate Systems

For the meteorological wind estimation, three Cartesian coordinate systems according to Boiffier [43] were used in the following, as shown in Figure 4. The first one is the Earth coordinate system or geodetic coordinate system with the index g. For example, the wind vector $\vec{w}_g$ in the geodetic coordinate system is defined by the vector components w_x being positive northward, w_y being positive eastward, and w_z positive when facing downward. Furthermore, the body-fixed coordinate system of the aircraft with the index b was used. The origin is at the center of gravity of the aircraft; x faces forward, y faces starboard, and z faces downward. Besides that, the aerodynamic coordinate system, with the index a oriented by the aerodynamic velocity of the aircraft, was used. The aerodynamic coordinate system has the same origin as the body-fixed coordinate system and, with the angle of attack α (positive for air flow from below) and side slip β (positive for flow from starboard), the aerodynamic coordinate system can be transformed into the aircraft coordinate system using the transformation $\mathbf{T}_{ba}$. Often, the wind vector $\vec{w}_m$ in meteorological coordinates (index m) instead of geodetic coordinates is used. The difference is a change in sign for the vertical component and a swapped first and second vector component. The meteorological wind vector $\vec{w}_m$ can be calculated using the transformation $\mathbf{T}_{mg}$ with

$$\vec{w}_m = \mathbf{T}_{mg}\vec{w}_g = \begin{pmatrix} 0 & 1 & 0 \\ 1 & 0 & 0 \\ 0 & 0 & -1 \end{pmatrix} \begin{pmatrix} w_x \\ w_y \\ w_z \end{pmatrix} \tag{1}$$

However, in this study, only the wind vector $\vec{w}_g$ in the geodetic coordinate system was used.

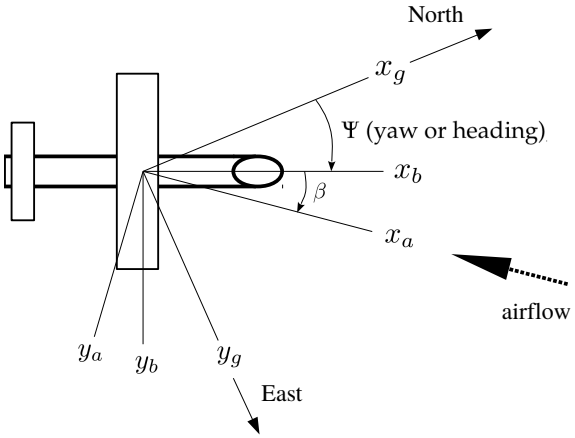

Figure 4. Top view of the wind measurement with the indices a, b, and g representing, respectively, the aerodynamic, body, and geodetic coordinate systems. Ψ is the yaw angle or true heading of the sUAV and β is the side slip angle between the aerodynamic and body-fixed coordinate system.

2.2. Wind Vector Estimation

The wind vector $\vec{w}$ is the orientation and magnitude of the airflow. A nonstationary observer (e.g., an sUAS) sees the relative velocity $\vec{u}$ only, and from a fixed point of view (e.g., the Earth coordinate system), the observer is moving with a resulting velocity $\vec{v}$ that is the sum of $\vec{u}$ and $\vec{w}$. This fundamental relation is the basis of all wind measurement techniques with fixed-wing aircraft. The wind vector $\vec{w}_g$ in the geodetic coordinate system is the difference between $\vec{v}_g$ and $\vec{u}_g$. The velocity vector $\vec{v}_g$ of the sUAS is generally estimated with GNSS data and can be measured at a good accuracy with consumer-grade GNSS receivers, whereas the true airspeed vector $\vec{u}_g$ relative to the sUAS represents a more challenging parameter to obtain for any wind measurement technique of a fixed-wing sUAS, as

well as the attitude (Eulerian angles) of the aircraft. The wind vector $\vec{w}_g$ has to be calculated (according to, e.g., Bange [44]) using

$$\vec{w}_g = \vec{v}_g + \mathbf{T}_{gb}\left(\vec{u}_b + \vec{\Omega}_b \times \vec{L}\right) \quad (2)$$

with the true airspeed vector $\vec{u}_b$ in the body-fixed coordinate system of the aircraft, and the transformation matrix $\mathbf{T}_{gb}$ in the geodetic coordinate system. The vector of angular body rates $\vec{\Omega}_b$ and its lever arm $\vec{L}$ describe the effect due to the spatial separation between INS and the multi-hole probe and can be (according to [45]) neglected since the lever arm $\vec{L}$ is only a few centimeters in our sUAS. Two fundamental approaches to measuring the true airspeed vector are possible. Either the true airspeed vector $\vec{u}_a$ of the sUAS in the aerodynamic coordinate system can be measured and transformed into geodetic coordinates, or the true airspeed vector $\vec{u}_g$ in the geodetic coordinate system is derived from the changes in $\vec{v}_g$ under the assumption of constant wind speed and direction. The first approach can be seen as the direct measurement, given that the relative wind vector and the position and attitude of the aircraft need to be measured. If these quantities are measured quickly and precisely, small wind vector fluctuations are resolved in time and space and turbulent fluxes, among other factors, can be calculated. If one of the quantities for the direct measurement is missing, assumptions have to be made to compensate for that, and averaging along the flight path is necessary. Summarizing, the MHPA method is the direct approach to solving Equation (2), with expected uncertainties that can be calculated through the propagation of sensor uncertainties [31], while both the PTA and NFSA methods estimate the wind vector, which is also averaging over a certain period. Averaged data do not allow for turbulent flux calculations, in general. Furthermore, the tuning of the autopilot and the aerodynamic design of the aircraft can influence the wind measurement, but this cannot be analyzed in the scope of this study.

2.2.1. Multi-Hole-Probe Wind Algorithm (MHPA)

Through measurements of a multi-hole probe, the true airspeed, side slip angle, and angle of attack are retrieved, which can be used to rotate the airspeed vector to the body-fixed coordinate system and, with the transformation $\mathbf{T}_{ba}$, it can be written as

$$\vec{w}_g = \vec{v}_g + \mathbf{T}_{gb}\mathbf{T}_{ba}\vec{u}_a \quad (3)$$

The true airspeed vector $\vec{u}_a$ in the aerodynamic coordinate system cannot be measured directly and requires intensive calibration of the multi-hole probes in the wind tunnel. The norm $|\vec{u}_a|$ is calculated with the total air temperature T_{tot}, which is assumed to be adiabatically stagnated on the probe's tip, and the static pressure p, as well as the dynamic pressure increment q. These quantities are the outcome of normalized pressure differences between the pressure holes on the multi-hole probe and the wind tunnel calibration.

$$|\vec{u}_a|^2 = 2c_p T_{\text{tot}}\left[1 - \left(\frac{p}{p+q}\right)^{\kappa}\right] \quad (4)$$

The Poisson number is defined by $\kappa = R\ {c_p}^{-1}$, with $R = 287$ J kg^{-1} K^{-1} being the gas constant for dry air and $c_p = 1004$ J kg^{-1} K^{-1} the specific heat of dry air. In our study, this was done for a five-hole probe according to Bange [44]. The true airspeed vector $\vec{u}_a$ must be transformed from the aerodynamic coordinate system into the body-fixed coordinate system using $\mathbf{T}_{ba}$ with the angle of attack α (positive for air flow from below) and side slip β (positive for flow from starboard). Since α and β are determined by the calibration procedure in the wind tunnel, there is a small difference between the body-fixed coordinate system of the sUAS and the experimental coordinate system in the wind tunnel due to the calibration procedure. According to Bange [44], this can be neglected for small angles. The true airspeed vector in the body-fixed coordinate system is:

$$\vec{u}_b = -\frac{|\vec{u}_a|}{\sqrt{1+\tan^2\alpha+\tan^2\beta}}\begin{pmatrix}1\\ \tan\beta\\ \tan\alpha\end{pmatrix}, \tag{5}$$

With $\mathbf{T}_{gb}$, which consists of three sequential turnings, the coordinate system is transformed from body-fixed into geodetic (index g) coordinates. $\mathbf{T}_1(\Phi)$ defines rolling about x_b, $\mathbf{T}_2(\Theta)$ defines pitching about y_b, and $\mathbf{T}_3(\Psi)$ defines yawing about z_b. Then,

$$\begin{aligned}\mathbf{T}_{gb} &= \mathbf{T}_1(\Phi)\mathbf{T}_2(\Theta)\mathbf{T}_3(\Psi)\\ &= \begin{pmatrix}1 & 0 & 0\\ 0 & \cos\Phi & -\sin\Phi\\ 0 & \sin\Phi & \cos\Phi\end{pmatrix}\begin{pmatrix}\cos\Theta & 0 & \sin\Theta\\ 0 & 1 & 0\\ -\sin\Theta & 0 & \cos\Theta\end{pmatrix}\begin{pmatrix}\cos\Psi & -\sin\Psi & 0\\ \sin\Psi & \cos\Psi & 0\\ 0 & 0 & 1\end{pmatrix}\end{aligned} \tag{6}$$

In accordance with methods previously described in [44], among other authors, and with the Euler angles measured by the INS, the wind vector $\vec{w}_g$ can be calculated. Together with $D = \sqrt{1+\tan^2\beta+\tan^2\alpha}$ and the Euler angles Φ (roll), Θ (pitch), and Ψ (yaw or heading), Equation (2) can be written with the wind vector in the geodetic coordinate system:

$$\begin{aligned}\vec{w}_g &= \vec{v}_g\\ &- \frac{|\vec{u}_a|}{D}\begin{pmatrix}\cos\Psi\cos\Theta+\tan\alpha(\sin\Phi\sin\Psi+\cos\Phi\cos\Psi\sin\Theta)+\tan\beta(\cos\Psi\sin\Phi\sin\Theta-\cos\Phi\sin\Psi)\\ \cos\Theta\sin\Psi+\tan\alpha(\cos\Phi\sin\Psi\sin\Theta-\cos\Psi\sin\Phi)+\tan\beta(\cos\Phi\cos\Psi+\sin\Phi\sin\Psi\sin\Theta)\\ -\sin\Theta+\cos\Phi\cos\Theta\tan\alpha+\cos\Theta\sin\Phi\tan\beta\end{pmatrix}\end{aligned} \tag{7}$$

Lenschow and Spyers-Duran [46] introduced a simplified version of Equation (7), using small-angle approximations for the measurement taken with manned aircraft during straight level flights. Calmer et al. [47] also applied this formulation to their vertical wind velocity measurements with sUAS. Since there is no benefit when applying these simplifications, other than a shorter formulation of the equation and a lower computational effort, the authors do not recommend using these simplifications for sUAS. For a manned aircraft, the inertia of mass is several orders of magnitude higher and, therefore, the movement of the aircraft in turbulence is less. Especially because there is no substantial benefit of such simplifications and because an investigation would need different methods from those in this study, simplifications were not considered.

2.2.2. The Pitot Tube Algorithm (PTA)

The PTA uses INS data and highly reduced flow information compared to the MHPA described in Section 2.2.1. A singular pitot-static tube in the nose of the aircraft is used. The PTA has a similar approach to that of the MHPA but needs temporal averaging to compensate for the missing information concerning the perpendicular vector components of the airspeed on the aircraft. Starting from Equation (2), the wind vector equals the vector difference between the ground speed of the sUAS and the true airspeed vector, whereas, when dissociated from the direct measurement, the airspeed of the sUAS can only be approximated with the pitot-static tube. The calculation of $\vec{u}_q$ is done in the simplest way by using the stagnation pressure and Bernoulli's principle for incompressible flows. For example, with a pitot-static tube, the first vector component of $u_{qx} = \sqrt{2dp_0/\rho}$ is calculated. The other components remain as unknowns in the algorithm of de Jong et al. [33].

$$\vec{u}_q = \begin{pmatrix}\sqrt{2dp_0/\rho}\\ u_{qy}\\ u_{qz}\end{pmatrix} \tag{8}$$

The pitot-static tube is mounted so it is aligned with x_b in the aircraft coordinate system (see also Figure 4). In opposition to the formulation in Section 2.2.1 for the MHPA and to highlight the differences, the nomenclature for the estimated true airspeed vector used for the PTA is $\vec{u}_q$. Only the lateral component of the true airspeed vector $\vec{u}_q$ is estimated, and misalignments between the aerodynamic and the aircraft coordinate systems cannot be considered. The estimated true airspeed vector $\vec{u}_q$ is assumed to be aligned with x_b and the transformation $\mathbf{T}_{ba}$ in Equation (3) is therefore neglected, and only the coordinate transformation $\mathbf{T}_{gb}$ from body-fixed to geodetic coordinates is performed.

$$\vec{w}_g = \vec{v}_g + \mathbf{T}_{gb}\vec{u}_q \tag{9}$$

Since the misalignment between the aerodynamic and the aircraft coordinate system cannot be considered, the true airspeed vector $\vec{u}_q$ in Equation (8) is referenced in body-fixed coordinates (see also Figure 4), with the origin at the center of gravity; x is along the fuselage and is positive when facing forward, y is positive when facing starboard, and z is positive when facing upward. Comparing Equation (8) for the PTA with Equation (5) for the MHPA, the differences in the true airspeed measurement are obvious. The PTA can give a precise estimate of the true airspeed only if $\alpha = \beta = 0$ and, therefore, the norm $|\vec{u}_q|$ is generally underestimated by the PTA. For this comparison, we simulated a pitot-static tube with our five-hole probe by using the pressure reading between the central hole of the five-hole probe and the static port just behind the probe tip. This represents a rather simple implementation of a standard pitot-static tube, which is reasonable for estimating the wind speed with the PTA and its expected precision. To calculate a solution using these measurements, the PTA needs reordering of the variables in Equations (8) and (9) and an averaging over a certain number of time steps. The measured quantities $\vec{v}_g$ and u_{qx} are separated from the unknowns, which are the wind vector $\vec{w}_g$ and the other vector components u_{qy} and u_{qz} of the true airspeed. The emerging system of equations becomes overdetermined when adjoining further measurements, defined by i, and the solution is calculated by solving, over one time step, a window of size M. To be able to separate the knowns and unknowns, Equation (9) is written in vector notation, using the vector components $\vec{v}_g = (v_x, v_y, v_z)$ and $\vec{w}_g = (w_x, w_y, w_z)$. The transformation matrix $\mathbf{T}_{gb}$ (see also Equation (6)) is split up into its elements by

$$\begin{aligned}\mathbf{T}_{gb} &= \begin{bmatrix} T_{1x} & T_{1y} & T_{1z} \\ T_{2x} & T_{2y} & T_{2z} \\ T_{3x} & T_{3y} & T_{3z} \end{bmatrix} \\ &= \begin{bmatrix} \cos\Theta\cos\Psi & \sin\Phi\sin\Theta\cos\Psi - \cos\Phi\sin\Psi & \cos\Phi\sin\Theta\cos\Psi + \sin\Phi\sin\Psi \\ \cos\Theta\sin\Psi & \sin\Phi\sin\Theta\sin\Psi + \cos\Phi\cos\Psi & \cos\Phi\sin\Theta\sin\Psi - \sin\Phi\cos\Psi \\ -\sin\Theta & \sin\Phi\cos\Theta & \cos\Phi\cos\Theta \end{bmatrix}\end{aligned} \tag{10}$$

and Equations (8) and (9) become

$$\begin{bmatrix} w_x \\ w_y \\ w_z \end{bmatrix} = \begin{bmatrix} v_x \\ v_y \\ v_z \end{bmatrix} + \begin{bmatrix} T_{1x}\,u_{qx} + T_{1y}\,u_{qy} + T_{1z}\,u_{qz} \\ T_{2x}\,u_{qx} + T_{2y}\,u_{qy} + T_{2z}\,u_{qz} \\ T_{3x}\,u_{qx} + T_{3y}\,u_{qy} + T_{3z}\,u_{qz} \end{bmatrix} \tag{11}$$

The equation is rewritten to separate the knowns from the unknowns,

$$\begin{aligned} v_x + T_{1x}\,u_{qx} &= w_x - T_{1y}\,u_{qy} - T_{1z}\,u_{qz} \\ v_y + T_{2x}\,u_{qx} &= w_y - T_{2y}\,u_{qy} - T_{2z}\,u_{qz} \\ v_z + T_{3x}\,u_{qx} &= w_z - T_{3y}\,u_{qy} - T_{3z}\,u_{qz} \end{aligned} \tag{12}$$

and the knowns can be aggregated in η_k. For every directional component $k \in \{x, y, z\}$, the three equations are:

$$\eta_k = v_k + T_{1k}\, u_{qx} = w_k - T_{2k}\, u_{qy} - T_{3k}\, u_{qz} \tag{13}$$

Assuming that $\vec{w}_g$ is temporally and spatially constant along the window of size M, the k Equation (13) can be combined with a linear independent system of equations. With every measurement point i, two new unknowns ($u_{qy}^{(i)}$ and $u_{qz}^{(i)}$) accrue to the system.

$$\begin{bmatrix} \eta_x^{(1)} \\ \eta_y^{(1)} \\ \eta_z^{(1)} \\ \eta_x^{(2)} \\ \eta_y^{(2)} \\ \eta_z^{(2)} \\ \vdots \\ \eta_x^{(N)} \\ \eta_y^{(N)} \\ \eta_z^{(N)} \end{bmatrix} = \begin{bmatrix} 1 & 0 & 0 & -T_{1y}^{(1)} & -T_{1z}^{(1)} & 0 & 0 & \cdots & 0 & 0 \\ 0 & 1 & 0 & -T_{2y}^{(1)} & -T_{2z}^{(1)} & 0 & 0 & \cdots & 0 & 0 \\ 0 & 0 & 1 & -T_{3y}^{(1)} & -T_{3z}^{(1)} & 0 & 0 & \cdots & 0 & 0 \\ 1 & 0 & 0 & 0 & 0 & -T_{1y}^{(2)} & -T_{1z}^{(2)} & \cdots & 0 & 0 \\ 0 & 1 & 0 & 0 & 0 & -T_{2y}^{(2)} & -T_{2z}^{(2)} & \cdots & 0 & 0 \\ 0 & 0 & 1 & 0 & 0 & -T_{3y}^{(2)} & -T_{3z}^{(2)} & \cdots & 0 & 0 \\ \vdots & \vdots & \vdots & \vdots & \vdots & \vdots & \vdots & \ddots & \vdots & \vdots \\ 1 & 0 & 0 & 0 & 0 & 0 & 0 & \cdots & -T_{1y}^{(M)} & -T_{1z}^{(M)} \\ 0 & 1 & 0 & 0 & 0 & 0 & 0 & \cdots & -T_{2y}^{(M)} & -T_{2z}^{(M)} \\ 0 & 0 & 1 & 0 & 0 & 0 & 0 & \cdots & -T_{3y}^{(M)} & -T_{3z}^{(M)} \end{bmatrix} \begin{bmatrix} w_x \\ w_y \\ w_z \\ u_{qy}^{(1)} \\ u_{qz}^{(1)} \\ u_{qy}^{(2)} \\ u_{qz}^{(2)} \\ \vdots \\ u_{qy}^{(M)} \\ u_{qz}^{(M)} \end{bmatrix} \tag{14}$$

The unknowns n and the number of equations m have the relation $n = 3 + \frac{2}{3}m$ and, therefore, starting from a window size of $M = 3$, the system of equations is solvable. In practice, the system of equations needs to be explicitly overdetermined to average over small-scale fluctuations in the wind field and obtain a solid mean wind. If the difference between v_g and u_g remains unchanged during the averaging period, the matrix is close to singular. For this reason, some variation in flight direction is essential for the algorithm. Equation (14) is solved numerically for w_x, w_y, and w_z with the least square method. The obtained wind vector $\vec{w}_g$ in the geodetic coordinate system is the best fit for the i measurements inside the averaging window M. It must be noted that the PTA cannot provide a vertical wind component w_z with reasonable uncertainty, at least for the presented flight pattern. Given that pitch angles θ are generally small in the presented flights, the vertical component of the airspeed measurements ($T_{3x}\, u_{qx}$ in Equation (12)) will be small, which leads to high uncertainties if errors are propagated through the PTA for the vertical wind component. Additionally, the long averaging periods that are necessary for the PTA will average over the most significant small-scale vertical motions.

2.2.3. The No-Flow-Sensor Algorithm (NFSA)

Imagining an aircraft flying horizontal circles in a constant wind field, it is evident that the ground speed is dependent on the angle between the wind direction and the flight path. Figure 5 shows the vector sum of the horizontal ground speed $\vec{v}_g^{(h)}$, the horizontal true airspeed $\vec{u}_g^{(h)}$, and the horizontal wind speed $\vec{w}_g^{(h)}$, which are used for the NFSA. The ground speed of the aircraft is minimal when flying directly against the wind and is maximal vice versa. It is presumed that the airspeed of the aircraft is constant; for the MASC and the Skywalker X8, this is assured by the autopilot systems. Applying a constant throttle and/or pitch rate to keep a constant airspeed makes the application of the NFSA even easier since the autopilot does not even require a pitot-static tube. This approach is followed with the SUMO, among other systems. Differences between these flight guidance approaches (constant throttle and/or pitch rate setting of the autopilot or an autopilot with pitot-static tube) to keep a constant

airspeed can be neglected for this comparison since they are insignificant when averaging over the window M.

Starting from Equation (2), according to Mayer et al. [35], the mean norm of the horizontal true airspeed $\vec{u}_g^{(h)}$ inside the window M is related to the difference in the horizontal ground speed $\vec{v}_g^{(h)}$ and the horizontal wind speed $\vec{w}_g^{(h)}$, using the geodetic coordinate system as a reference.

$$|\overline{\vec{u}_g^{(h)}}| = \frac{1}{M}\sum_i^M |\vec{v}_{gi}^{(h)} - \vec{w}_g^{(h)}| \tag{15}$$

where M is the number of measurement points in the averaging window, and the method presumes that the aircraft is flying at constant airspeed and assumes that the wind speed is constant. Therefore, the components on each side of Equation (15) must level each other out for every measurement i. To deal with fluctuations in the wind field and to solve for the horizontal wind speed, Equation (15) is reordered and the variance σ^2 of the measurements in the window M is introduced:

$$\sigma^2 = \frac{1}{M}\sum_i^M \left(|\vec{v}_{gi}^{(h)} - \vec{w}_g^{(h)}| - |\overline{\vec{u}_g^{(h)}}| \right)^2 \tag{16}$$

To calculate the horizontal wind speed from Equation (16), the smallest possible value for the variance is approximated numerically using the downhill-simplex method according to McKinnon [48]. More details can be found in Mayer et al. [35].

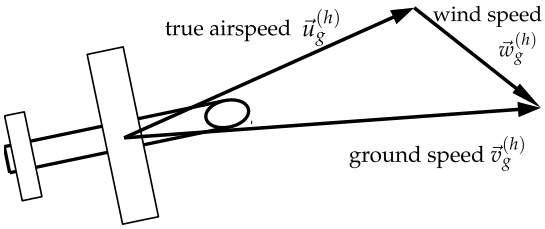

Figure 5. Vector sum of the no-flow-sensor algorithm (NFSA) with the horizontal ground speed $\vec{v}_g^{(h)}$, the horizontal true airspeed $\vec{u}_g^{(h)}$, and the horizontal wind speed $\vec{w}_g^{(h)}$.

3. Experiments

The wind field and turbulence of the atmospheric boundary layer and the choice of flight paths are the main factors to argue the potential differences between these wind estimation algorithms. A representative pick from four measurement campaigns with wind speeds between 2 and 15 m s^{-1}, as well as various flight patterns, including horizontal straight flight legs, circles, lying eights, and ascending racetracks for height profiles, were selected. A brief description of the prevailing atmospheric conditions is also gathered in Table 1.

Table 1. Flight sections with location, date, and duration in local time, pattern, and brief atmospheric condition.

Location	Date	From	Until	Flight Path	Condition
Boulder (BAO)	8 August 2014	3:12 p.m.	3:35 p.m.	circular	weakly convective
Schnittlingen (SNT)	7 May 2015	11:23 a.m.	11:51 a.m.	horizontal racetracks	sheared flow
Helgoland (HEL)	10 October 2014	9:20 a.m.	9:51 a.m.	ascending racetracks	strong wind
Pforzheim (PFR)	11 July 2013	9:50 a.m.	10:08 a.m.	lying eight, long straights	convective

To compare the performance of the three methods MHPA, PTA, and NFSA and to highlight limitations, two averaging periods M were chosen in this study and applied to all experiments. The long averaging period is $M = 240$ s and acts in accordance with the experiment in Pforzheim (PFR), where the longest racetracks were performed. $M = 240$ s comprised two racetracks in PFR. The short averaging period is $M = 60$ s and comprises two circles for the shortest racetracks at the BAO.

3.1. Boulder Atmospheric Observatory (BAO)

The Boulder Atmospheric Observatory (BAO) was a test facility of the National Oceanic and Atmospheric Administration (NOAA) in the USA. It was located in the state of Colorado at around 1580 m above sea level. The flight took place on 8 August in 2014 and the presented data fraction was measured between 3:12 and 3:35 p.m. local time. The wind was ≈2 m s^{-1} from the east. This data was measured with the Skywalker X8 flying wing (see also Section 2) performing fixed-radius circles (Figure 6) at a constant height of 100 m above ground level (AGL) and with an airspeed of 22 m s^{-1}. A full circle takes about half a minute. This is a typical pattern [35] when using the NFSA for wind speed and direction estimation. To ensure a sufficient quantity of data, a period of 43 consecutive circles was chosen.

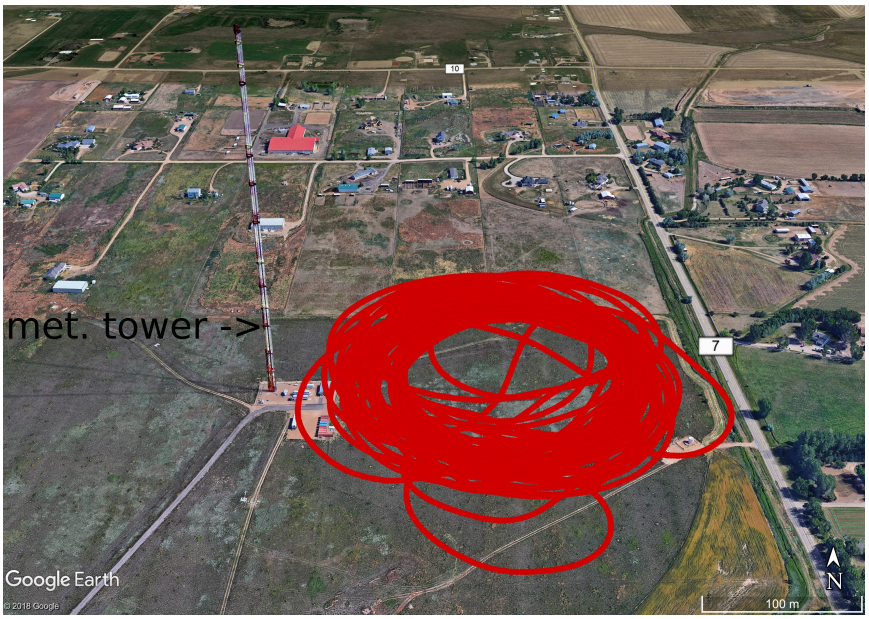

Figure 6. Flight path in red at the Boulder Atmospheric Observatory (BAO) on 8 August 2014 with the meteorological tower in the northwest. During the measurement, low wind speeds from eastern directions with weak convection prevailed.

For this flight, data from a meteorological tower with a resolution of 1 min, located northeast of the circular flight path, was available for comparison. The tower is visible in Figure 6, and the data measured by the aircraft and the tower is shown in Table 2.

The comparison of the mean wind speed and direction, as well as the standard deviation measured by the tower (Table 2), agree well with the 1 min averages of the tower data. During the last period, the mean wind speed measured by the tower is lower and the standard deviation is higher than the measurement of the Skywalker X8 with the MHPA. The convective situation with thermal blooms may have caused this. The wind speed was constant and low during the whole period of investigation, and the wind direction turned from ≈90° to ≈ 60° during the first 450 s.

Table 2. Horizontal wind speed and wind direction at Boulder Atmospheric Observatory meteorological tower. Data at 100 m above ground level (AGL) in comparison with the multi-hole-probe algorithm (MHPA) for the flight on 8 August 2014 between 3:12:06 p.m. and 3:34:36 p.m. local time. Additionally, the data is divided into three intervals of 450 s each.

	3:12:06 p.m. Until 3:34:36 p.m.	First 450 s	Second 450 s	Last 450 s
Tower BAO	2.02 ± 0.26 m s^{-1} $68 \pm 21°$	2.18 ± 0.31 m s^{-1} $93 \pm 8°$	2.01 ± 0.16 *m s*$^{-1}$ $57 \pm 11°$	1.87 ± 0.19 *m s*$^{-1}$ $52 \pm 7°$
MHPA BAO	2.25 ± 0.24 m s^{-1} $68 \pm 17°$	2.39 ± 0.06 m s^{-1} $89 \pm 10°$	2.16 ± 0.14 m s^{-1} $57 \pm 5°$	2.20 ± 0.34 *m s*$^{-1}$ $59 \pm 8°$

3.2. Schnittlingen (SNT)

The Schnittlingen (SNT) test site is located in southern Germany on the border of the Swabian Alp. The flight was performed just over the crest, which rises from the valley at about 500 m above mean sea level (AMSL) up to the plateau at 650 m. With westerly wind, the flow was hitting the crest perpendicularly, forming up-drafts and strongly sheared flow in the vicinity. Many flights and other measurement systems, such as LiDAR, have been used to investigate the site. Results from intensive measurements on several days were published by Wildmann et al. [28], and a comparison between sUAV measurements and a numerical simulation of the area was reported by Knaus et al. [49]. For this comparison, a flight on 7 May 2015 was chosen, with overcast and neutral stratification showing the typical phenomena described in these publications. With wind on the ground from the west-northwest direction and an average wind speed of about 6 m s^{-1}, up-drafts over the crest and sheared flow were pronounced. As shown in Figure 7, rectangular so-called racetracks with long legs forth and back over the crest in vertical steps of 25 m were performed. One racetrack comprises two legs including turns or one full round. For every height, two rectangles were flown between 75 and 200 m AGL, summing up to 12 racetracks for the selected data fraction.

Figure 7. Flight path (so-called racetracks) in red in Schnittlingen (SNT) on 7 May 2015, with the meteorological tower east of the flight path. During the measurement, moderate westerly winds prevailed. The crest forms partial up-drafts and strongly sheared flow.

A meteorological tower located in the east of the rectangular flight path is available for comparison (Figure 7 and Table 3).

Table 3. Horizontal wind speed and wind direction at Schnittlingen meteorological tower. Data at 98 m AGL in comparison with the MHPA for the flight on 7 May 2015 between 11:23:16 p.m. and 11:50:46 p.m. local time. Additionally, the data is divided into three intervals of 550 s each.

	11:23:16 a.m. Until 11:50:46 a.m.	**First 550 s**	**Second 550 s**	**Last 550 s**
Tower SNT	6.02 ± 1.50 m s^{-1} $283 \pm 14°$	5.28 ± 1.08 m s^{-1} $282 \pm 16°$	5.47 ± 1.21 m s^{-1} $285 \pm 13°$	7.30 ± 1.29 m s^{-1} $283 \pm 12°$
MHPA SNT	6.05 ± 1.28 m s^{-1} $286 \pm 6°$	5.04 ± 0.87 m s^{-1} $286 \pm 7°$	5.51 ± 0.47 m s^{-1} $290 \pm 5°$	7.59 ± 0.48 m s^{-1} $281 \pm 2°$

In this complex terrain, the comparison between the meteorological tower and the flight data is not straightforward since surface heterogeneities influence the wind field strongly and the spatial separation between the measurement systems can cause large deviations for the mean flow and the statistics. Nevertheless, the mean values agree very well (Table 3), while the standard deviation in the tower data appears to be larger up to a factor of almost 3 compared to the aircraft data. The higher standard deviation of the tower measurement is caused by the downstream location. As shown by Wildmann et al. [28], the wind field attenuates in this area after the deviation caused by the crest about 1000 m upstream. This causes increased fluctuations and nonstationary behavior. Due to the spatial separation, the data in Table 3 cannot be used for a close comparison, but it shows the development of the wind speed at the site during the experiment. The first period of 550 s represents the four racetracks of the MASC at 75 m and 100 m AGL. During the almost half-hour-long flight, the wind speed varies between approximately 5 m s^{-1} and 7 m s^{-1}, making the selection interesting when looking at the performance of different wind measurement algorithms.

3.3. Pforzheim (PFR)

The main reason for this flight was the research of turbulent fluxes in the lower ABL. The test site is located in south Germany close to Pforzheim and near the Rhine rift. The area is flat and extensively used for agriculture. With light winds from the northeast and clear sky conditions, lying eights with long, crossing straights at 150 m AGL (Figure 8) were flown on 11 July in 2013 to investigate the turbulent fluxes above heterogeneous terrain with various agricultural land use. The latent and sensible heat fluxes were significantly large between 9:50:09 a.m. and 10:08:29 a.m. local time, indicating strong convective conditions. The data consists of nine racetracks of about 120 s each.

Figure 8. Flight path in red near Pforzheim (PFR) on 11 July 2013. During the measurement, low wind speed from northeast directions and pronounced convection prevailed.

3.4. Helgoland (HEL)

The selected flight from the Helgoland campaign was conducted on 10 October in 2014, during strong wind conditions from the southeast. Helgoland is Germany's only island in the North Sea with offshore conditions. The undisturbed marine boundary layer with a fetch of several hundred kilometers was measured upstream from the take-off site on the west shore. The data used in this study was gathered during an ascending maneuver from 100 m to 550 m in vertical steps of 50 m. The take-off and landing site, as well as the flight path, are shown in Figure 9. During the long north-south legs, the MASC was climbing 50 m, and the short east-west passages were flown at a constant height. This flight strategy produces data on the vertical profile of various atmospheric quantities. The flight took place between 9:20 a.m. and 9:51 a.m. local time.

Figure 9. Flight path in red on Helgoland (HEL) on 10 October 2014. The figure shows the flight path on the west coast of Helgoland. The undisturbed marine boundary layer with strong winds from the southeast was measured.

4. Results

The set of graphs in the Figures 10–13 show scatterplots of the horizontal wind speed and wind direction. Sections 2.2.2 and 2.2.3 state the importance of the averaging window for the applied simplification of the wind measurement with the NFSA and the PTA. Figures 10 and 11 show the results for an averaging window of $M = 240$ s. This timescale comprises at least two full racetracks for all experiments (see Section 3.3). Therefore, this timescale of 4 min is the choice for the comparison and is on the high end of reasonable averaging windows, pledging a robust performance. Longer periods would weaken the studies' distinctions and not add further comprehension. In comparison, a 1 min averaging time is analyzed, where approximately one racetrack in HEL and two circles at the BAO are inside the averaging window. This is a typical value for averaging in meteorology, where, on the one hand, full racetracks are included and, on the other hand, the performance resulting from data only having fractions of racetracks is addressed. Figures 12 and 13 show these results for an averaging window of $M = 60$ s. Preliminary studies showed that significantly shorter periods become unusable for this study since the deviations of the NFSA and the PTA from the MHPA become very large. For quantifying the differences between the algorithms and averaging windows, histograms of the deviation from the MHPA are plotted in Figures 14–17. The difference in the horizontal wind speed between the MHPA and the NFSA or the PTA is used. The normalized distribution is presented and the probability density function, together with the fitted normal distribution, is plotted for every experiment and algorithm. The mean μ of the fitted normal distribution can be interpreted as the bias between the algorithms, and the standard deviation σ can be taken as the precision. Each plot contains the results for both averaging periods, $M = 240$ s and $M = 60$ s, enabling a quantified comparison for each experiment (BAO in Figure 14, SNT in Figure 15, HEL in Figure 16, and PFR in Figure 17) between the averaging windows as well as between the algorithms. It must be noted that the results are also influenced by the tuning of the autopilot and by the aerodynamic design of the sUAS. However, that cannot be analyzed in this study. Furthermore, the airframe and the autopilot for the experiment at the BAO (Skywalker X8 with a Black Swift Technologies LLC autopilot system) and for the other experiments (MASC with the ROCS autopilot) differ and, therefore, the quantified intercomparison

between these experiments is influenced by this difference. On the other hand, all experiments were conducted with the same sensor system, and the analysis of the performance of the algorithms when flying different flight patterns is not affected.

4.1. Long Averaging Periods for Robust Performance ($M = 240$ s)

The long period with at least two full racetracks inside the averaging window in Figures 10 and 11 generally shows a good agreement between the different algorithms. Nevertheless, significant differences between the NFSA and the PTA are found. Limitations arise for the NFSA in Figure 10 where large differences for the high wind speeds in HEL occur. The main reason for these is the rapid and inconsistent changes in the heading of the aircraft during the sharp turns caused by the high wind speed and turbulence. This also becomes apparent when looking at Figure 16 where the standard deviation of the fitted normal distribution is the highest for the long averaging period by a factor of 2 ($\sigma = 0.72$). Larger differences in the wind speed and especially for the wind direction can also be observed during the very long straights performed in PFR. This is explainable by drifts in the calculated wind speed, which occur because the change rates of the heading during the long straights are too low and the fact that only two racetracks are included. Figure 17 underlines that. The wind direction estimation is generally rather unfavorable with the NFSA. Although long straights lower the confidence, the NFSA is capable of estimating the wind speed and, with reservations, the direction for flight patterns other than circles. The histograms indicate which flight patterns are beneficial when using the NFSA. For two main reasons, the circles at the BAO, but also the horizontal racetracks in SNT, perform best with $M = 240$ s. Considerably more than two racetracks comprise the averaging window, and the flight was oriented horizontally. Especially for the experiment in HEL, which has the least favorable conditions for the NFSA, the neglected vertical vector components in Equation (16) become significant. For the HEL experiment, when applying the long averaging period, the NFSA is not capable of estimating the wind speed and direction reliably. On the other hand, for all other experiments, the NFSA yields acceptable results with at least two full racetracks inside the averaging window.

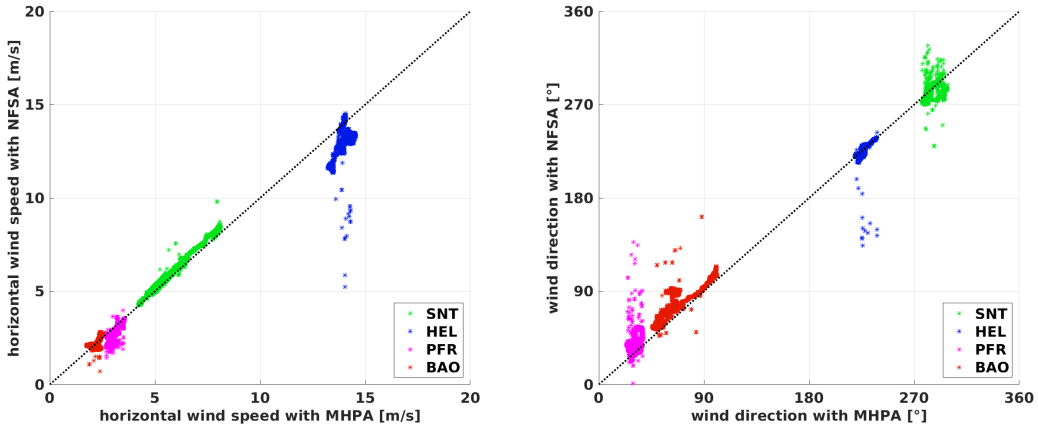

Figure 10. Comparison of the **horizontal wind speed** (**left**) and the **wind direction** (**right**) on a **window of 4 min** for the flights at the Boulder Atmospheric Observatory (BAO), Schnittlingen (SNT), Helgoland (HEL), and Pforzheim (PFR). The black dashed line shows the bisecting line where the multi-hole-probe algorithm (MHPA) equals the no-flow-sensor algorithm (NFSA). The data is calculated on a window with $M = 240$ s. The results from the **MHPA** are plotted against the results from the **NFSA**.

The PTA in Figure 11 shows a very good agreement in its ability to measure the horizontal wind speed precisely in all conditions and for all flight patterns. Taking a closer look at the high wind speeds

measured in HEL, the PTA reveals its limitations when used during ascents. The vertical component of the airspeed during ascension results in an underestimation of the horizontal wind speed that is caused directly by the formulation. The same phenomenon is observable during the convective conditions in PFR. The histograms in Figure 16 with a mean of $\mu = 0.51$ in HEL and in Figure 17 with a mean of $\mu = 0.56$ for the flight in PFR support this and show the limitations for cases with nonzero vertical wind (e.g., flights during convective conditions) or the constant ascent or descent of the sUAS. The effect can be also seen in the NFSA results. For example, this is explainable for the PTA with Equation (8) and the NFSA with Equation (15), where the vertical wind causes an underestimation of the airspeed $\vec{u_q}$ of the PTA, or of the horizontal airspeed $\vec{u}_g^{(h)}$ of the NFSA. This error propagates through the algorithms and causes an underestimation of the horizontal wind speed. The wind direction estimation with the PTA is robust and reliable in a range of $\approx \pm 10°$, and the wind speed estimation is very good for the long averaging period, with some differences for the strong prevailing vertical motion of either the wind field or the sUAS. Generally, the histograms in Figures 14–17 show that the PTA is more precise than the NFSA throughout all the comparisons. Even for the circular flight pattern at the BAO, the PTA performs significantly better since the standard deviation is lower.

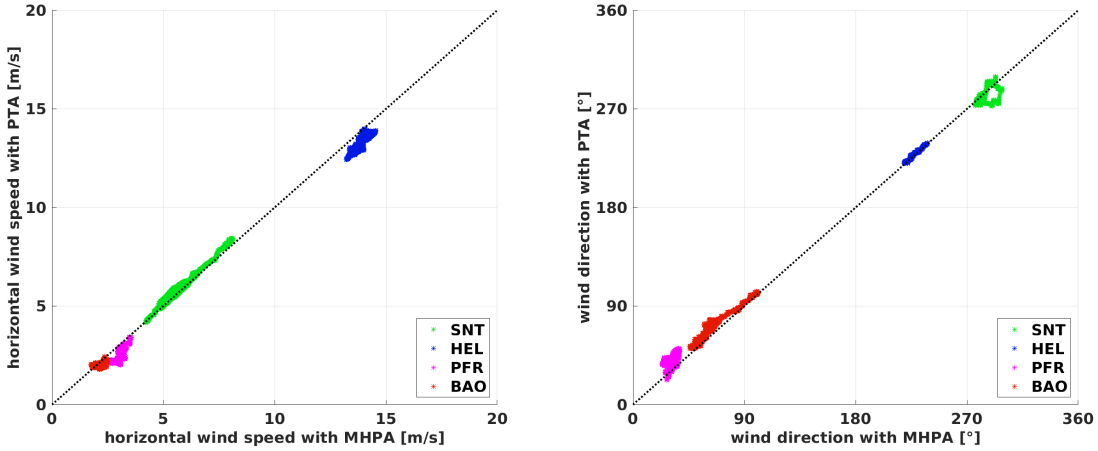

Figure 11. Comparison of the **horizontal wind speed** (**left**) and the **wind direction** (**right**) on a **window of 4 min** for the flights at the Boulder Atmospheric Observatory (BAO), Schnittlingen (SNT), Helgoland (HEL), and Pforzheim (PFR). The black dashed line shows the bisecting line where the multi-hole-probe algorithm (MHPA) equals the pitot tube algorithm (PTA). The data is calculated on a window with $M = 240$ **s**. The results from the **MHPA** are plotted against the results from the **PTA**.

4.2. Short Averaging Periods for Enhanced Temporal Resolution ($M = 60$ s)

Since 4 min is quite a long averaging time, a 1 min window is presented in Figures 12 and 13 to argue which limitations arise when increasing the temporal resolution. A flight time of 1 min corresponds to only about one leg (half a racetrack) in PFR and in SNT, almost one racetrack in HEL, and two circles or full racetracks at the BAO. To begin with the NFSA in Figure 12, it is evident that the results are quite bad since the scatter is high for a significant portion of the values and for all maneuvers which are not circular. For the BAO flight, the scatter is also significantly higher than for the big averaging window, especially for the wind direction. The standard deviation of the fitted normal distribution in Figure 14 increases from $\sigma = 0.22$ to $\sigma = 0.41$. This significant decrease in precision appears although there are still two full circles in the averaging window. An explanation is that changes in wind speed and direction at scales smaller than a circle are inadequately represented by the algorithm. These small structures in the wind field cause the aircraft to bear away, leading to a false emphasis on the calculation of mean values when averaging too short a period. In other words, if strong and sudden turbulence causes the autopilot to steer the sUAS with a rather strong movement,

this section of the flight path is not representative for the mean flow. This is also critical when taking into account that the boundary layer during the experiment at the BAO was relatively calm, and it suggests that the two circles inside the averaging window could perform even worse under more turbulent conditions. The window M can be decreased from 240 s in some conditions but only when having several full racetracks in the averaging window. For the data at the BAO with $M = 60$ s, the result varies within a range of $\approx$2 m s^{-1} around the MHPA. For the generally low wind speeds during this measurement, this is already a quite large difference, leading to the conclusion that two full circles are not enough for reliable results.

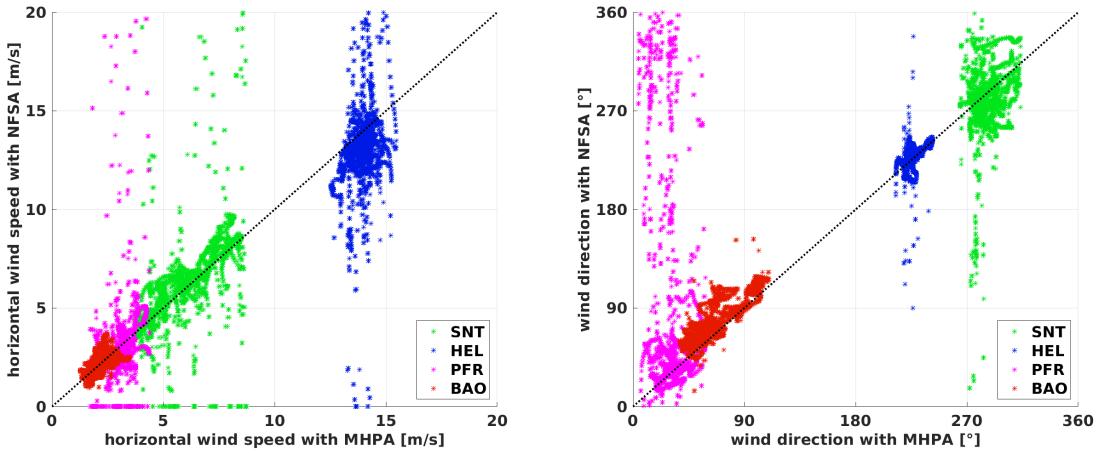

Figure 12. Comparison of the **horizontal wind speed** (**left**) and the **wind direction** (**right**) on a **window of 1 min** for the flights at the Boulder Atmospheric Observatory (BAO), Schnittlingen (SNT), Helgoland (HEL), and Pforzheim (PFR). The black dashed line shows the bisecting line where the multi-hole-probe algorithm (MHPA) equals the no-flow-sensor algorithm (NFSA). The data is calculated on a window with $M = 60$ s. The results from the **MHPA** are plotted against the results from the **NFSA**.

The PTA in Figure 13 shows good agreement, although the scatter of the MHPA data is greater compared to the long averaging period. The standard deviations σ of the histograms in Figures 14–16 for the BAO, SNT, and HEL experiment increase from $M = 240$ s to $M = 60$ s by a factor of 2–4, and the deviation stays within a range of $\approx$2 m s^{-1} and $\approx$20°. Challenges become visible for the long straights in PFR. The convection is not the biggest contribution to the increased scatter anymore; instead, the fact that the flow information cannot compensate for excessively low change rates in the heading along the averaging window leads to the differences. The solution of the overdetermined matrix in Equation (14) cannot compensate for the occurrence of small-scale fluctuations if the ground speed and heading become almost constant inside the averaging window M. The results for the SNT flight over complex terrain are, on the other hand, remarkably good for these harsh conditions. Here, the benefit of the algorithm compared to the NFSA is shown for situations when there is less than a full racetrack inside the averaging window and, therefore, a quite high temporal resolution. The mean of the fitted normal distribution in Figure 16 for the HEL flight is $\mu = 0.55$, which is in the same range as that for the long averaging period. Except for the underestimation of the wind speed described in Section 4.1, the PTA performs well in this strong and turbulent wind field. Even in high wind speeds, turbulence, shear, and strong up-drafts, the PTA is capable of giving a good estimation of wind speed and direction with reasonable resolution. In comparison to the NFSA, the PTA has considerable benefits when using the additional flow information. The limitations are the resolution of the small scales and turbulent features, which only the MHPA can resolve.

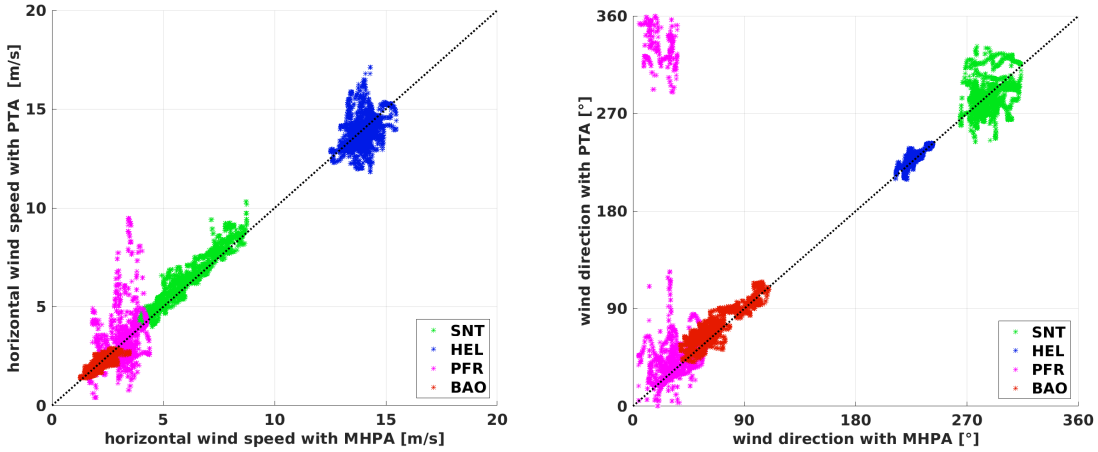

Figure 13. Comparison of the **horizontal wind speed** (**left**) and the **wind direction** (**right**) on a **window of 1 min** for the flights at the Boulder Atmospheric Observatory (BAO), Schnittlingen (SNT), Helgoland (HEL), and Pforzheim (PFR). The black dashed line shows the bisecting line where the multi-hole-probe algorithm (MHPA) equals the pitot tube algorithm (PTA). The data is calculated on a window with $M = 60$ s. The results from the **MHPA** are plotted against the results from the **PTA**.

4.3. Intercomparison of the Algorithms and Quantification of the Results

The histograms in Figures 14–17 show the quantified differences between the algorithms and highlight the advantages of the PTA over the NFSA, as well as the influence of the averaging period on the performance of both algorithms. The intercomparison of the histograms of the four flight experiments also reveals the limitations. The NFSA must comprise at least two full racetracks, and the PTA can cope with fractions of one racetrack as long as there are not exclusively straight flight paths available. The wind speed estimation is better for all experiments and for all averaging periods with the PTA than with the NFSA, as expected. However, the capabilities of the NFSA are surprisingly good not only for circular flight pattern, as long as the averaging window is long enough. For example, this can be seen when looking at the normal distribution with $M = 240$ s for the SNT experiment, which is good for both algorithms. The mean of $\mu = -0.21$ for the NFSA is only slightly worse than the $\mu = -0.16$ for the PTA, with the standard deviations being the same. On the other hand, it is also evident that the temporal resolution of the NFSA is very limited, since the results are not usable for $M = 60$ s in SNT and in general, except for the circular flight at the BAO.

Summarizing the results for the long averaging period of $M = 240$ s, the following was found:

- The NFSA is capable of estimating the wind speed, and not only for a circular flight pattern, if at least two full racetracks are inside the averaging window. Limitations arise for non-horizontal flight paths and high turbulence.
- The wind direction estimation is subject to large uncertainties with the NFSA.
- The PTA shows a very good agreement with the MHPA and is capable of measuring the horizontal wind speed and direction in all conditions with good accuracy.
- Fast ascent or descent of the sUAS or strong vertical wind components leads to an underestimation of the horizontal wind speed when using the PTA.

For the short averaging period of $M = 60$ s, the following was found:

- The NFSA performs better when more than two racetracks are inside the averaging window, as well as for circular flight pattern. This reveals the very limited resolution.
- The PTA still performs well when only fractions of a racetrack are included in the algorithm. Limits arise when exclusively straight flight sections remain inside the averaging window.

- The PTA is capable of estimating reliably the mean wind speed and direction with a reasonable resolution.

A summary of the intercomparison between the two estimation algorithms for mean wind speed and direction is:

- The PTA is more accurate than the NFSA throughout all comparisons, even for the circular flight pattern.
- The PTA needs an additional sensor to estimate the true airspeed, but it achieves significantly higher accuracy and temporal resolution.

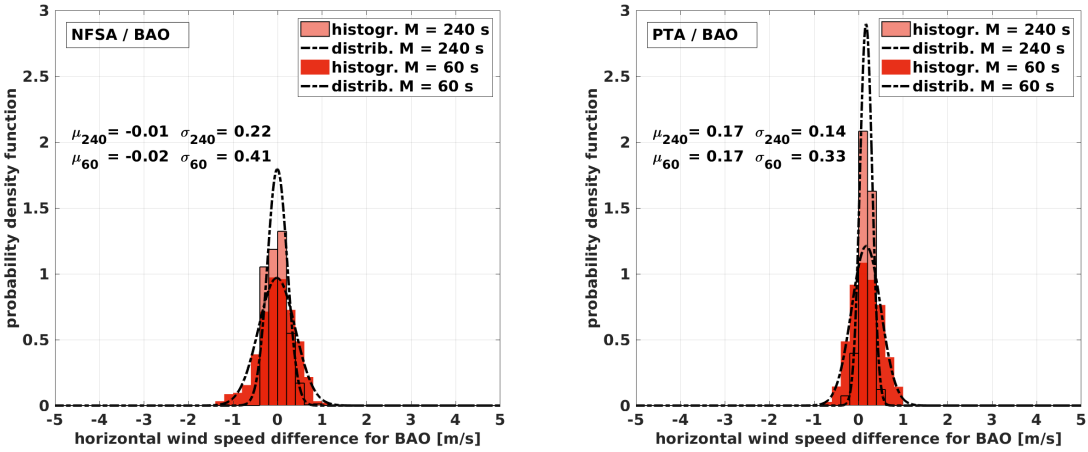

Figure 14. Normalized distribution and probability density function with the fitted normal distribution for the flight at the Boulder Atmospheric Observatory (**BAO**). The plots show the deviation between the MHPA and the **NFSA** (**left**) and the MHPA and the **PTA** (**right**) for $M = 240$ s and for $M = 60$ s.

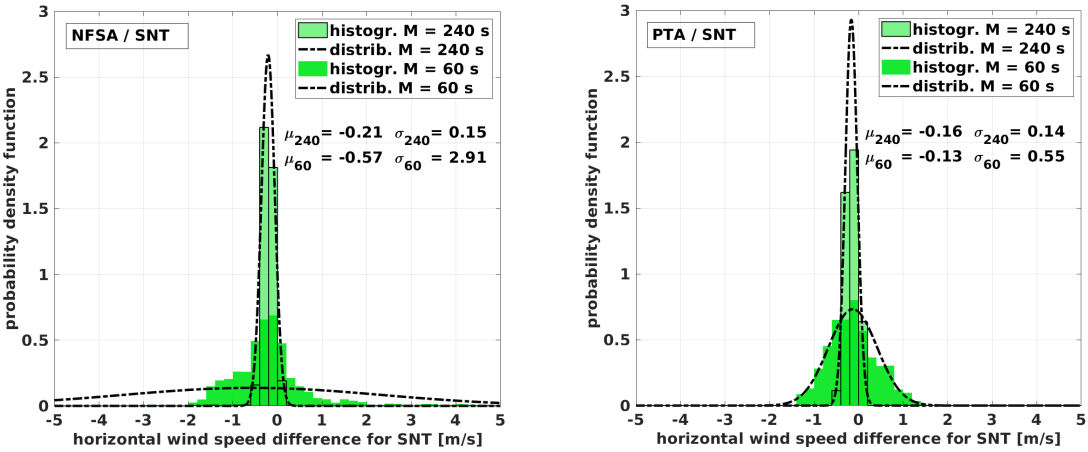

Figure 15. Normalized distribution and probability density function with the fitted normal distribution for the flight over complex terrain near Schnittlingen (**SNT**). The plots show the deviation between the MHPA and the **NFSA** (**left**) and the MHPA and the **PTA** (**right**) for $M = 240$ s and for $M = 60$ s.

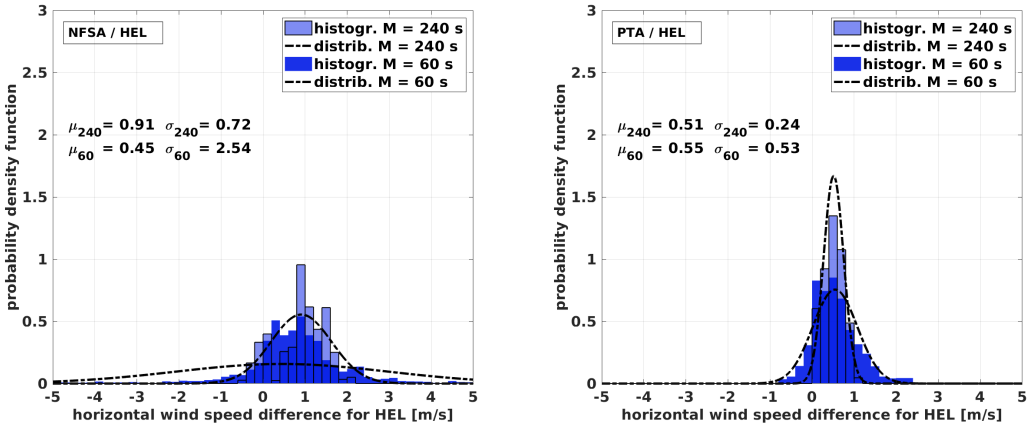

Figure 16. Normalized distribution and probability density function with the fitted normal distribution for the flight in Helgoland (**HEL**). The plots show the deviation between the MHPA and the **NFSA** (**left**) and the MHPA and the **PTA** (**right**) for $M = 240$ s and for $M = 60$ s.

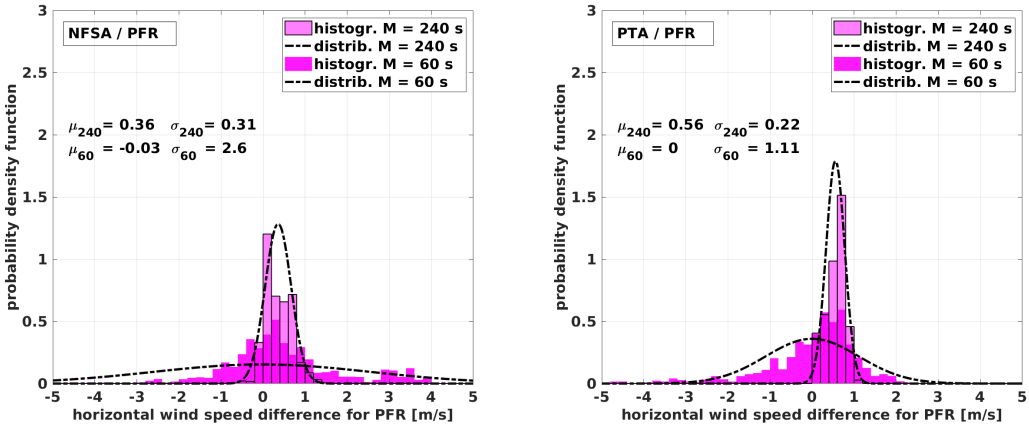

Figure 17. Normalized distribution and probability density function with the fitted normal distribution for the flight near Pforzheim (**PFR**). The plots show the deviation between the MHPA and the **NFSA** (**left**) and the MHPA and the **PTA** (**right**) for $M = 240$ s and for $M = 60$ s.

5. Conclusions

This study shows the capabilities and limitations of the commonly used methods for wind vector estimation. The no-flow-sensor algorithm and the more sophisticated pitot tube algorithm are compared with the direct measurement using the multi-hole-probe algorithm on a small UAV. The sensor system used in this work is capable of applying all three methods by neglecting parameters during post-processing. By choosing a variety of flight patterns which are used for meteorological sampling and substantially different weather conditions, the comparison covers a broad band of scenarios. The NFSA is generally not limited to circular patterns, but it performs best when having a continuous and rather constant change in the heading of the aircraft. In these cases, the temporal resolution can be increased, and an averaging window which comprises two full racetracks still generates good results, but the increased temporal resolution comes with lower precision. It is shown that strong turbulence decreases the accuracy. Autopilot systems well tuned to perform regular circles at constant airspeed are crucial for the NFSA. The method is limited in cases with long straights. Using one more piece of information, namely, the vector component of the true airspeed in the flight direction, the wind speed and direction estimation can be strongly enhanced. The PTA allows for generally better results than the NFSA and, in particular, provides additional benefit during flight patterns with

long straight legs. Furthermore, the temporal resolution is much better without the need for a full racetrack inside the averaging window, although at least some change in the heading is still needed. Another influencing factor is a nonzero vertical vector component, as seen during ascents in Helgoland and in convective conditions in Pforzheim. The horizontal wind speed is slightly underestimated for these conditions. In conclusion, both estimation algorithms achieve good results when applied within their limitations. The simplicity of the NFSA is attractive for very small platforms, and the sUAS can be designed to be cheap, efficient, and robust enough to withstand miscellaneous environmental conditions. The PTA depends on the dynamic pressure measurement, which adds complexity to the sUAV. However, the enhancement of the wind speed and direction estimation is significant. The MHPA is the most sophisticated method and needs a set of differential pressure sensors in combination with extensive calibration. It is deduced that, of the presented algorithms, the temporal resolution to measure at turbulent scales and the ability to measure the vertical wind component can only be achieved using the MHPA.

Author Contributions: A.R. performed the analysis, created the figures, and wrote the paper. M.S.G. provided the computational implementation of the code and made contributions to the figures and the text. N.W. carried out the measurements and provided advice on the text and interpretation of the results. A.P. provided advice on the text. J.B. provided guidance and advice on all aspects of the study and contributed to the text.

Acknowledgments: The authors wish to acknowledge the helpful comments of the reviewers. Data from Schnittlingen was sampled for the project 'KonTest' (grant number 0325665), which was funded by the Federal Ministry for Economic Affairs and Energy based on a decision of the German Bundestag. The data for the Helgoland experiment was sampled for the project 'OWEA Loads' (grant number 0325577), which was funded by the Federal Ministry for Environment, Nature Conservation and Nuclear Safety, and conducted in cooperation with the Research at alpha ventus (RAVE) research initiative. We want to thank the Boulder Atmospheric Observatory for providing the tower data and helping with the experiment. We acknowledge Jack Elston for organizing and inviting us to join the "Multi-sUAS Evaluation of Techniques for Measurement of Atmospheric Properties (MET MAP)" campaign (grant number 1551786), which was funded by the United States National Science Foundation. We further acknowledge open access publishing funding by Deutsche Forschungsgemeinschaft (DFG) and the University of Tübingen.

Conflicts of Interest: The authors declare no conflict of interest. The founding sponsors had no role in the design of the study; in the collection, analyses, or interpretation of data; in the writing of the manuscript, and in the decision to publish the results.

References

1. Holland, G.; Webster, P.; Curry, J.; Tyrell, G.; Gauntlett, D.; Brett, G.; Becker, J.; Hoag, R.; Vaglienti, W. The Aerosonde robotic aircraft: A new paradigm for environmental observations. *Bull. Am. Meteorol. Soc.* **2001**, *82*, 889–901. [CrossRef]
2. Chilson, P.B.; Bonin, T.A.; Zielke, B.S.; Kirkwood, S. The Small Multi-Function Autonomous Research and Teaching Sonde (Smartsonde): Relating In-Situ Measurements of Atmospheric Parameters to Radar Returns. In Proceedings of the 20th Symposium on European Rocket and Balloon Programmes and Related Research, Hyères, France, 22–26 May 2011; Volume 700, pp. 387–394.
3. Reuder, J.; Jonassen, M.O. First results of turbulence measurements in a wind park with the Small Unmanned Meteorological Observer SUMO. *Energy Procedia* **2012**, *24*, 176–185. [CrossRef]
4. Altstädter, B.; Platis, A.; Wehner, B.; Scholtz, A.; Wildmann, N.; Hermann, M.; Käthner, R.; Baars, H.; Bange, J.; Lampert, A. ALADINA—An unmanned research aircraft for observing vertical and horizontal distributions of ultrafine particles within the atmospheric boundary layer. *Atmos. Meas. Tech.* **2015**, *8*, 1627–1639. [CrossRef]
5. Kräuchi, A.; Philipona, R. Return glider radiosonde for in situ upper-air research measurements. *Atmos. Meas. Tech.* **2016**, *9*, 2535–2544. [CrossRef]
6. Witte, B.M.; Singler, R.F.; Bailey, S.C. Development of an Unmanned Aerial Vehicle for the Measurement of Turbulence in the Atmospheric Boundary Layer. *Atmosphere* **2017**, *8*, 195. [CrossRef]
7. Kral, S.T.; Reuder, J.; Vihma, T.; Suomi, I.; O'Connor, E.; Kouznetsov, R.; Wrenger, B.; Rautenberg, A.; Urbancic, G.; Jonassen, M.O.; et al. Innovative Strategies for Observations in the Arctic Atmospheric Boundary Layer (ISOBAR)—The Hailuoto 2017 Campaign. *Atmosphere* **2018**, *9*, 268. [CrossRef]

8. Jacob, J.D.; Chilson, P.B.; Houston, A.L.; Smith, S.W. Considerations for Atmospheric Measurements with Small Unmanned Aircraft Systems. *Atmosphere* **2018**, *9*, 252. [CrossRef]
9. Hill, M.; Konrad, T.; Meyer, J.; Rowland, J. A small, radio-controlled aircraft as a platform for meteorological sensors. *APL Tech. Dig.* **1970**, *10*, 11–19.
10. Caltabiano, D.; Muscato, G.; Orlando, A.; Federico, C.; Giudice, G.; Guerrieri, S. Architecture of a UAV for volcanic gas sampling. In Proceedings of the 10th IEEE Conference on Emerging Technologies and Factory Automation (ETFA 2005), Catania, Italy, 19–22 September 2005; Volume 1, p. 6.
11. Diaz, J.A.; Pieri, D.; Wright, K.; Sorensen, P.; Kline-Shoder, R.; Arkin, C.R.; Fladeland, M.; Bland, G.; Buongiorno, M.F.; Ramirez, C.; et al. Unmanned aerial mass spectrometer systems for in-situ volcanic plume analysis. *J. Am. Soc. Mass Spectrom.* **2015**, *26*, 292–304. [CrossRef] [PubMed]
12. Platis, A.; Altstädter, B.; Wehner, B.; Wildmann, N.; Lampert, A.; Hermann, M.; Birmili, W.; Bange, J. An Observational Case Study on the Influence of Atmospheric Boundary-Layer Dynamics on New Particle Formation. *Bound.-Layer Meteorol.* **2016**, *158*, 67–92. [CrossRef]
13. Schuyler, T.J.; Guzman, M.I. Unmanned Aerial Systems for Monitoring Trace Tropospheric Gases. *Atmosphere* **2017**, *8*, 206. [CrossRef]
14. Hobbs, S.; Dyer, D.; Courault, D.; Olioso, A.; Lagouarde, J.P.; Kerr, Y.; Mcaneney, J.; Bonnefond, J. Surface layer profiles of air temperature and humidity measured from unmanned aircraft. *Agron. Sustain. Dev.* **2002**, *22*, 635–640. [CrossRef]
15. Van den Kroonenberg, A.; Bange, J. Turbulent flux calculation in the polar stable boundary layer: Multiresolution flux decomposition and wavelet analysis. *J. Geophys. Res. (Atmos.)* **2007**, *112*. [CrossRef]
16. Thomas, R.; Lehmann, K.; Nguyen, H.; Jackson, D.; Wolfe, D.; Ramanathan, V. Measurement of turbulent water vapor fluxes using a lightweight unmanned aerial vehicle system. *Atmos. Meas. Tech.* **2012**, *5*, 243–257. [CrossRef]
17. Van den Kroonenberg, A.; Martin, S.; Beyrich, F.; Bange, J. Spatially-averaged temperature structure parameter over a heterogeneous surface measured by an unmanned aerial vehicle. *Bound.-Layer Meteorol.* **2012**, *142*, 55–77. [CrossRef]
18. Beyrich, F.; Bange, J.; Hartogensis, O.K.; Raasch, S.; Braam, M.; van Dinther, D.; Gräf, D.; van Kesteren, B.; Van den Kroonenberg, A.C.; Maronga, B.; et al. Towards a validation of scintillometer measurements: The LITFASS-2009 experiment. *Bound.-Layer Meteorol.* **2012**, *144*, 83–112. [CrossRef]
19. Jonassen, M.O.; Ólafsson, H.; Ágústsson, H.; Rögnvaldsson, Ó.; Reuder, J. Improving high-resolution numerical weather simulations by assimilating data from an unmanned aerial system. *Mon. Weather Rev.* **2012**, *140*, 3734–3756. [CrossRef]
20. Reuder, J.; Ablinger, M.; Agústsson, H.; Brisset, P.; Brynjólfsson, S.; Garhammer, M.; Jóhannesson, T.; Jonassen, M.O.; Kühnel, R.; Lämmlein, S.; et al. FLOHOF 2007: An overview of the mesoscale meteorological field campaign at Hofsjökull, Central Iceland. *Meteorol. Atmos. Phys.* **2012**, *116*, 1–13. [CrossRef]
21. Bonin, T.; Chilson, P.; Zielke, B.; Fedorovich, E. Observations of the early evening boundary-layer transition using a small unmanned aerial system. *Bound.-Layer Meteorol.* **2013**, *146*, 119–132. [CrossRef]
22. Martin, S.; Beyrich, F.; Bange, J. Observing Entrainment Processes Using a Small Unmanned Aerial Vehicle: A Feasibility Study. *Bound.-Layer Meteorol.* **2014**, *150*, 449–467. [CrossRef]
23. Wildmann, N.; Rau, G.A.; Bange, J. Observations of the Early Morning Boundary-Layer Transition with Small Remotely-Piloted Aircraft. *Bound.-Layer Meteorol.* **2015**, *157*, 345–373. [CrossRef]
24. Wainwright, C.E.; Bonin, T.A.; Chilson, P.B.; Gibbs, J.A.; Fedorovich, E.; Palmer, R.D. Methods for evaluating the temperature structure-function parameter using unmanned aerial systems and large-eddy simulation. *Bound.-Layer Meteorol.* **2015**, *155*, 189–208. [CrossRef]
25. Bonin, T.A.; Goines, D.C.; Scott, A.K.; Wainwright, C.E.; Gibbs, J.A.; Chilson, P.B. Measurements of the temperature structure-function parameters with a small unmanned aerial system compared with a sodar. *Bound.-Layer Meteorol.* **2015**, *155*, 417–434. [CrossRef]
26. Båserud, L.; Flügge, M.; Bhandari, A.; Reuder, J. Characterization of the SUMO turbulence measurement system for wind turbine wake assessment. *Energy Procedia* **2014**, *53*, 173–183. [CrossRef]
27. Subramanian, B.; Chokani, N.; Abhari, R.S. Drone-based experimental investigation of three-dimensional flow structure of a multi-megawatt wind turbine in complex terrain. *J. Sol. Energy Eng.* **2015**, *137*, 051007. [CrossRef]
28. Wildmann, N.; Bernard, S.; Bange, J. Measuring the local wind field at an escarpment using small remotely-piloted aircraft. *Renew. Energy* **2017**, *103*, 613–619. [CrossRef]

29. Elston, J.; Argrow, B.; Stachura, M.; Weibel, D.; Lawrence, D.; Pope, D. Overview of Small Fixed-Wing Unmanned Aircraft for Meteorological Sampling. *J. Atmos. Ocean. Technol.* **2015**, *32*, 97–115. [CrossRef]
30. Lenschow, D.H. *Probing the Atmospheric Boundary Layer*; American Meteorological Society: Boston, MA, USA, 1986; Volume 270.
31. Van den Kroonenberg, A.; Martin, T.; Buschmann, M.; Bange, J.; Vörsmann, P. Measuring the wind vector using the autonomous mini aerial vehicle M2AV. *J. Atmos. Ocean. Technol.* **2008**, *25*, 1969–1982. [CrossRef]
32. Wildmann, N.; Hofsäß, M.; Weimer, F.; Joos, A.; Bange, J. MASC—A small Remotely Piloted Aircraft (RPA) for wind energy research. *Adv. Sci. Res.* **2014**, *11*, 55–61. [CrossRef]
33. de Jong, R.; Chor, T.; Dias, N. Medição da velocidade do vento a bordo de um Veículo Aéreo Não Tripulado. *Ciênc. Nat.* **2011**, *33*, 71–74.
34. Niedzielski, T.; Skjøth, C.; Werner, M.; Spallek, W.; Witek, M.; Sawiński, T.; Drzeniecka-Osiadacz, A.; Korzystka-Muskała, M.; Muskała, P.; Modzel, P.; et al. Are estimates of wind characteristics based on measurements with Pitot tubes and GNSS receivers mounted on consumer-grade unmanned aerial vehicles applicable in meteorological studies? *Environ. Monit. Assess.* **2017**, *189*, 431. [CrossRef] [PubMed]
35. Mayer, S.; Hattenberger, G.; Brisset, P.; Jonassen, M.; Reuder, J. A 'no-flow-sensor' wind estimation algorithm for unmanned aerial systems. *Int. J. Micro Air Veh.* **2012**, *4*, 15–30. [CrossRef]
36. Reuder, J.; Brisset, P.; Jonassen, M.; Müller, M.; Mayer, S. The Small Unmanned Meteorological Observer SUMO: A new tool for atmospheric boundary layer research. *Meteorol. Z.* **2009**, *18*, 141–147. [CrossRef]
37. Mayer, S.; Jonassen, M.O.; Sandvik, A.; Reuder, J. Profiling the Arctic stable boundary layer in Advent valley, Svalbard: measurements and simulations. *Bound.-Layer Meteorol.* **2012**, *143*, 507–526. [CrossRef]
38. Bonin, T.; Chilson, P.; Zielke, B.; Klein, P.; Leeman, J. Comparison and application of wind retrieval algorithms for small unmanned aerial systems. *Geosci. Instrum. Methods Data Syst.* **2013**, *2*, 177–187. [CrossRef]
39. Shuqing, M.; Hongbin, C.; Gai, W.; Yi, P.; Qiang, L. A miniature robotic plane meteorological sounding system. *Adv. Atmos. Sci.* **2004**, *21*, 890–896. [CrossRef]
40. Wildmann, N.; Ravi, S.; Bange, J. Towards higher accuracy and better frequency response with standard multi-hole probes in turbulence measurement with remotely piloted aircraft (RPA). *Atmos. Meas. Tech.* **2014**, *7*, 1027–1041. [CrossRef]
41. Wildmann, N.; Mauz, M.; Bange, J. Two fast temperature sensors for probing of the atmospheric boundary layer using small remotely piloted aircraft (RPA). *Atmos. Meas. Tech.* **2013**, *6*, 2101–2113. [CrossRef]
42. Martin, S.; Bange, J.; Beyrich, F. Meteorological Profiling the Lower Troposphere Using the Research UAV 'M^{2}AV Carolo'. *Atmos. Meas. Tech.* **2011**, *4*, 705–716. [CrossRef]
43. Boiffier, J.L. *The Dynamics of Flight*; Wiley: Chichester, UK, 1998; p. 353.
44. Bange, J. *Airborne Measurement of Turbulent Energy Exchange between the Earth Surface and the Atmosphere*; Sierke Verlag: Göttingen, Germany, 2009; 174p, ISBN 978-3-86844-221-2.
45. Lenschow, D. Airplane measurements of planetary boundary layer structure. *J. Appl. Meteorol.* **1970**, *9*, 874–884. [CrossRef]
46. Lenschow, D.; Spyers-Duran, P. *Measurement Techniques: Air Motion Sensing*; National Center for Atmospheric Research, Bulletin: Boulder, CO, USA, 1989.
47. Calmer, R.; Roberts, G.C.; Preissler, J.; Sanchez, K.J.; Derrien, S.; O'Dowd, C. Vertical wind velocity measurements using a five-hole probe with remotely piloted aircraft to study aerosol–cloud interactions. *Atmos. Meas. Tech.* **2018**, *11*, 2583–2599. [CrossRef]
48. McKinnon, K.I. Convergence of the Nelder–Mead Simplex Method to a Nonstationary Point. *SIAM J. Optim.* **1998**, *9*, 148–158. [CrossRef]
49. Knaus, H.; Rautenberg, A.; Bange, J. Model comparison of two different non-hydrostatic formulations for the Navier-Stokes equations simulating wind flow in complex terrain. *J. Wind Eng. Ind. Aerodyn.* **2017**, *169*, 290–307. [CrossRef]

A.2 Calibration Procedure and Accuracy of Wind and Turbulence Measurements with Five-Hole Probes on Fixed-Wing Unmanned Aircraft in the Atmospheric Boundary Layer and Wind Turbine Wakes - Publication II

atmosphere

MDPI

Article

Calibration Procedure and Accuracy of Wind and Turbulence Measurements with Five-Hole Probes on Fixed-Wing Unmanned Aircraft in the Atmospheric Boundary Layer and Wind Turbine Wakes

Alexander Rautenberg *, Jonas Allgeier, Saskia Jung and Jens Bange

Center for Applied Geoscience, Eberhard-Karls-Universität Tübingen, Hölderlinstr. 12, 72074 Tübingen, Germany; jonas.allgeier@uni-tuebingen.de (J.A.); saskia.jung@student.uni-tuebingen.de (S.J.); jens.bange@uni-tuebingen.de (J.B.)

* Correspondence: alexander.rautenberg@uni-tuebingen.de; Tel.: +49-7071-29-74339

Received: 6 February 2019; Accepted: 1 March 2019; Published: 7 March 2019

Abstract: For research in the atmospheric boundary layer and in the vicinity of wind turbines, the turbulent 3D wind vector can be measured from fixed-wing unmanned aerial systems (UAS) with a five-hole probe and an inertial navigation system. Since non-zero vertical wind and varying horizontal wind causes variations in the airspeed of the UAS, and since it is desirable to sample with a flexible cruising airspeed to match a broad range of operational requirements, the influence of airspeed variations on mean values and turbulence statistics is investigated. Three calibrations of the five-hole probe at three different airspeeds are applied to the data of three flight experiments. Mean values and statistical moments of second order, calculated from horizontal straight level flights are compared between flights in a stably stratified polar boundary layer and flights over complex terrain in high turbulence. Mean values are robust against airspeed variations, but the turbulent kinetic energy, variances and especially covariances, and the integral length scale are strongly influenced. Furthermore, a transect through the wake of a wind turbine and a tip vortex is analyzed, showing the instantaneous influence of the intense variations of the airspeed on the measurement of the turbulent 3D wind vector. For turbulence statistics, flux calculations, and quantitative analysis of turbine wake characteristics, an independent measurement of the true airspeed with a pitot tube and the interpolation of calibration polynomials at different Reynolds numbers of the probe's tip onto the Reynolds number during the measurement, reducing the uncertainty significantly.

Keywords: calibration of multi-hole probes; airspeed variations; turbulence measurements; 3D wind vector measurement; wind turbine wake; tip vortex; flow probes; unmanned aerial systems (UAS); unmanned aerial vehicles (UAV)

1. Introduction

For environmental science in the atmospheric boundary layer (ABL), airborne measurements supplement the limited coverage of ground-based measurements or tethered balloons. Manned research aircraft have intensively investigated a wide range of processes and phenomena [1–3] and unmanned aerial systems (UAS) adopted the measurement techniques of quantities such as temperature, humidity, and the wind vector [4–7], but are not limited to these, as shown by Bärfuss et al. [8] for aerosol and radiation measurements, or by Schuyler and Guzman [9] for gas concentrations. The 3D wind vector using multi-hole probes is calculated by the summation of the ground speed vector of the vehicle and the true airspeed vector. By calibration, the pressure readings of the individual holes of multi-hole probes are used to estimate the airspeed vector. With the

attitude, position, and velocity of the vehicle, measured by an inertial navigation system (INS), multiple coordinate transformations finally yield the wind vector. This method is widely used in manned aircraft [1,10] and on fixed-wing UAS [4–7]. The accuracy of the wind vector measurement is crucial, and the propagation of errors have many influencing factors, originating in the attitude and ground speed measurement of the aircraft, the flow angles and flow magnitude (true airspeed vector) measurement with the multi-hole probe, and also in the measurement of the thermodynamic state of the air. Extensive studies for various systems and subsystems of the wind vector measurement with manned research aircraft [11–16], including in-flight calibration procedures and uncertainty analysis [10,17], and with UAS (e.g., for the M^2AV [7]) were performed.

So far, for UAS, calibration maneuvers during flight and the influence of airspeed variations on the wind vector measurement were not addressed in terms of calibration and uncertainty analysis for the 3D wind vector measurement with multi-hole probes. Since a misalignment between the multi-hole probe's orientation and the aircraft cannot be avoided, an in-flight calibration must be applied [16]. Calibration maneuvers during flight such as the "acceleration–deceleration maneuver", the "yaw maneuver", and the "box maneuver" [18–21] for single-engine manned aircraft, or by Hartmann et al. [10], who uses filtered fractions of the measurement data for the calibration of the vertical wind component, have not been performed with UAS, yet. The study of Van den Kroonenberg et al. [7] uses the assumption of a constant wind for two consecutive horizontal straights in opposing direction and the assumption of zero vertical wind to calibrate the wind measurement. The study of Hartmann et al. [10] highlights the little attention that is paid to assess the calibration accuracy, when assuming constant wind during the maneuver. The practical guide by Drüe and Heinemann [17] for wind calibration of a research aircraft, used for turbulent flux measurements, could be adapted to UAS, since the capabilities of modern flight guidance systems allow for a wide range of maneuvers.

Also, for manned aircraft, there is limited work done to account for the influence of airspeed variations on the wind vector measurement, especially when considering the influence on turbulence measurements. Due to non-zero vertical wind velocity on turbulent scales, or other motions like e.g., thermals or up- and down-drafts due to orography, the aircraft reacts to acceleration or deceleration relative to the air. To fulfil the requirements of constant altitude, constant flight direction, and constant airspeed, the auto pilot system of the UAS controls the angle of attack and the throttle. Furthermore, changes in the horizontal windspeed accelerate and decelerate the UAS due to its drag. The reactions of the UAS to changes in the wind field correlate, and are proportional to the momentum and the aerodynamic drag of the UAS. Moreover, the individual flight-mechanical behavior influences the reaction of the UAS. Obviously, a manned aircraft with a mass of several tons, as well as an aircraft with low drag, reacts less to changes in the wind field than a lightweight UAS with aerodynamic properties that are susceptible to interaction with the turbulence. The study of Metzger et al. [11] also raises the question of whether lower mass of the vehicle increases the error due to the motion of the aircraft. However, they did not consider that a lighter aircraft measures in a broader range of airspeed than a heavier aircraft, when flying through the same atmospheric conditions. A variation in airspeed is primarily a change in the Reynolds number with the probe's tip diameter as reference length. Secondly also the Mach number changes, but since the influence is very small [22] and the Mach number remains below 0.2, compressibility can be generally neglected for this study.

Although a dependency on the Reynolds number of the calculation of flow angles and magnitude (true airspeed vector) from the calibration is known [22,23], it is common practice to choose one airspeed for the measurement and for the calibration in the wind tunnel and to assume that changes in the airspeed are negligible. Compared to manned research aircraft, this investigation for UAS becomes even more important when taking into account that UAS are intended to be used e.g., in complex terrain with immense up-drafts and shear [24] or in the wake of wind turbines [6], where the transects through the wake cause a sudden change in airspeed.

Numerical models play an important role for wind energy [25–27], connecting the gap between wind-tunnel experiments, field measurements with e.g., UAS [6] and simplified empirical models [28]. Even the most expensive numerical simulations imply high uncertainties, since it is challenging to combine precise blade aerodynamics on the small scales with atmospheric dynamics on the larger scales. Especially smaller structures in the wake of wind turbines are poorly resolved in numerical models and not well understood. To be able to compare the data of UAS measurements of the wake of wind turbines with numerical simulations and to validate the models, the uncertainties and errors of the wind measurement are of major importance.

When resolving the complex wake aerodynamics of wind turbines [29], it is desirable for the UAS to sample with the maximum spatial resolution and therefore with the lowest airspeed possible, while ensuring accuracy. Another important motivation for this study is the question of whether the cruising airspeed of the Multi-Purpose Airborne Sensor Carrier (MASC) can be freely chosen for the wind measurement or if further calibration in the wind tunnel is required to gain this flexibility. For atmospheric research, boundary-layer meteorology, and wind-energy studies, the environment-physics group at the Center for Applied Geoscience (ZAG), University of Tübingen, Germany, designed and built MASC [4,6]. The airspeed of MASC can be set between 15 and 30 m s^{-1}, depending on the payload and the targeted flight time or battery load, making it versatile for different scenarios. In low windspeeds the airspeed can be set low to sample with a high spatial resolution or, if a certain feature in complex terrain or in the vicinity of wind turbines is under investigation. In high windspeeds of >15 m s^{-1} MASC can still be operated safely but the airspeed must be set to $\geq$25 m s^{-1}. Another scenario where high airspeeds are beneficial is if the flight distance of the measurement will be maximized, or, vice versa, if the flight time will be maximized. Furthermore, the autopilot keeps a constant descent and ascent rate for vertical profiling. These maneuvers also require a certain flexibility for the cruising airspeed of the wind measurement, since the true airspeed is not set directly. Finally, the true airspeed cannot be set precisely prior to the flight, since the autopilot cannot account for the density of the air and a deviation always persists. For manned aircraft, different Reynolds numbers were studied in the wind tunnel for the Rosemount R858 probe [10,30], where a linear proportionality was found for the conversion of pressure readings to flow angles in a certain range of Reynolds numbers. Whether this is possible for the desired range of airspeeds with MASC and its probe, and what the uncertainties and accuracy are, is one of the scopes of this study.

Furthermore, this study investigates the influence of the calibration of the probe, namely the conversion of the pressure readings to flow angles and magnitude, on turbulence measurements. In the literature a similar question was posed by Martin and Bange [31] and Braam et al. [32] who highlighted two important issues. Firstly, airspeed variations cause an uneven sampling of turbulent structures due to the acceleration and deceleration of the UAS, resulting from non-zero vertical wind and gusts. During up-drafts the sampling is denser due to increased airspeed, and vice versa. Secondly, when compared to other measurement systems such as a scintillometer or other ground-based measurements, path-weighting functions must be considered to account for differences between the spatial and the temporal resolution of the measurement of a quantity. The uncertainties of the wind vector measurement and its calibration actually precede those investigated by Martin and Bange [31] and Braam et al. [32]. The influence of the calibration of the probe on turbulence measurements is difficult to investigate in the wind tunnel, and impossible for natural atmospheric turbulence. Since the turbulence in the ABL cannot be measured repeatedly, the way to address these issues is to apply different calibrations from the wind tunnel on the same data of several flight experiments. Flying with different airspeed-settings in a swarm, or similar approaches, would not be comparable. By applying a calibration that does not match the airspeed of the UAS and comparing it with one that does, the uncertainty can be approximated. Furthermore, flight experiments with large changes in the true airspeed of the UAS can be analyzed. By choosing a flight with very low turbulence in a polar, and stably stratified boundary layer (SBL) from measurements during the ISOBAR campaign [33], and a very turbulent flight from the measurements in complex terrain by [24],

deviations can be analyzed and localized. A single event with large changes in airspeed, namely a transect through the wake of a wind turbine, gives insight in the impact of severe turbulence, the accuracy of the wind measurement and the importance of considering changes of the Reynolds number on the probe's tip.

With the following procedure, this study analyzes the influence of airspeed variations on the wind and turbulence measurement with five-hole probes on UAS in the ABL and in the wake of wind turbines. Three calibrations of the same sensor system are determined in the wind tunnel, plus one additional measurement in the same conditions, to ensure the reproducibility of the procedure. Firstly, the five-hole probe "Pressures-to-Airflow-Vector" conversion and the 3D wind vector measurement is described. Secondly the influence of airspeed variations on mean values and statistical moments of second order are analyzed. Two flight experiments in low and high turbulence were chosen and the horizontal straight level flight segments (legs) on multiple heights are shown to study the different regimes of the ABL. One flight with low turbulence in homogeneous terrain in an SBL in the north of Finland, and one in complex terrain with high turbulence, intensive up- and down-drafts, and sheared flow over a crest in the South of Germany were selected. The influence of the three calibrations at three airspeeds is depicted for mean values and turbulence statistics. The three calibrations in the wind tunnel are applied to the data set and the deviations from each other are displayed. A third flight was chosen and a single event, namely the transect through the wake of a wind turbine, was analyzed to see the instantaneous effect of airspeed variations and the influence of the calibration of the five-hole probe. Subsequently, possible proceedings to improve the accuracy of the measurements are presented. The polynomials of the calibration can be interpolated and an independent measurement of the true airspeed with a pitot tube reduces the uncertainty, especially in high turbulence.

2. Materials and Methods

The following section briefly describes the method of calculating the 3D wind vector from the pressure readings of the five-hole probe and the data of the INS. Subsequently, the design and tubing setup of the five-hole probe and the procedure of the calibration in the wind tunnel is presented. Furthermore, the UAS MASC is introduced and its flight strategy to derive mean values and turbulence statistics is explained. The circumstances of the three chosen flight experiments to argue the influence of the calibration of the five-hole probe on the accuracy of the wind and turbulence measurements are presented subsequently.

2.1. Wind Vector Measurement with Multi-hole Probes

Following Boiffier [34], and displayed in Figure 1, we use the Earth coordinate system, or geodetic coordinate system (index g). Furthermore, the body-fixed coordinate system of the aircraft (index b) is used. The origin is in the center of gravity of the aircraft; x faces forward, y faces starboard, and z faces downward when flying horizontally with zero angle of attack. Besides, the aerodynamic coordinate system (index a), oriented by the direction of the flow relative to the aircraft, is used. The aerodynamic coordinate system has the same origin than the body-fixed coordinate system and, with the angle of attack α (positive for air flow from below) and side-slip angle β (positive for flow from starboard), the aerodynamic coordinate system can be transformed into the aircraft coordinate system using the transformation $\mathbf{T}_{ba}$. The aerodynamic coordinate system and the body-fixed coordinate system have the same origin, but a misalignment between the multi-hole probe's orientation and the aircraft cannot be avoided and [20,34,35] causes a small difference between the measured flow angles $\tilde{\alpha}$, $\tilde{\beta}$ (in the wind tunnel or during the flight experiment) and the actual angle of attack α and side-slip β. It can be shown that $\tilde{\alpha} \equiv \alpha$ and that $\tilde{\beta} \approx \beta$ for small angles of attack [35]. Therefore, this is neglected in this study. The coordinate systems and angles are shown in Figure 1. The wind vector $\vec{w}_g$ is calculated [35] using

$$\vec{w}_g = \vec{v}_g + \mathbf{T}_{gb}\left(\vec{u}_b + \vec{\Omega}_b \times \vec{L}\right) \quad (1)$$

with the true airspeed vector $\vec{u}_b$ in the body-fixed coordinate system of the aircraft, and the transformation matrix $\mathbf{T}_{gb}$ into the geodetic coordinate system. The velocity vector $\vec{v}_g$ of the UAS, as well as the Euler angles Φ (roll), Θ (pitch), and Ψ (yaw or heading) are used to determine $\mathbf{T}_{gb}$ and are estimated with an INS, consisting of a GNSS receiver, an Inertial Measurement Unit (IMU) and an Extended Kalman Filter (EKF). The vector of angular body rates $\vec{\Omega}_b$ and its lever arm $\vec{L}$ describe the transformation due to the spatial separation between INS and the multi-hole probe and can be (according to Lenschow [36]) neglected since the lever arm $\vec{L}$ is only a few centimeters in our UAS. With the true airspeed vector $\vec{u}_a$ in the aerodynamic coordinate system, the transformation $\mathbf{T}_{ba}$ into body-fixed coordinates and the rotation into geodetic coordinates $\mathbf{T}_{gb}$, Equation (1) can be written as

$$\vec{w}_g = \vec{v}_g + \mathbf{T}_{gb}\mathbf{T}_{ba}\vec{u}_a \tag{2}$$

The true airspeed vector $\vec{u}_a$ in the aerodynamic coordinate system requires intensive calibration of the multi-hole probe. The norm $|\vec{u}_a|$ is calculated with the total air temperature T_{tot}, which is assumed to be adiabatically stagnated on the probe's tip, and the static pressure p, as well as the dynamic pressure increment q.

$$|\vec{u}_a|^2 = 2c_p T_{\text{tot}} \left[1 - \left(\frac{p}{p+q}\right)^{\kappa}\right] \tag{3}$$

The quantities p and q are calculated with normalized pressure differences between the pressure holes on the multi-hole probe and the wind-tunnel calibration. The Poisson number is defined by $\kappa = R\ {c_p}^{-1}$, with $R = 287\ \text{J kg}^{-1}\ \text{K}^{-1}$ being the gas constant for dry air and $c_p = 1004\ \text{J kg}^{-1}\ \text{K}^{-1}$ the specific heat of dry air. The true airspeed vector $\vec{u}_a$ must be transformed from the aerodynamic coordinate system into the body-fixed coordinate system using $\mathbf{T}_{ba}$

$$\vec{u}_b = -\frac{|\vec{u}_a|}{\sqrt{1+\tan^2\alpha+\tan^2\beta}} \begin{pmatrix} 1 \\ \tan\beta \\ \tan\alpha \end{pmatrix} \tag{4}$$

using α and β.

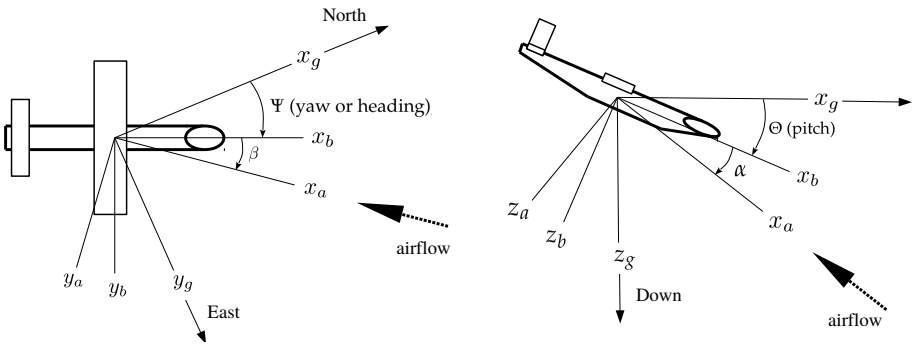

Figure 1. Top view (**left**) and side view (**right**) of the coordinate systems with the indices a, b, and g representing, the aerodynamic, body, and geodetic coordinate systems. Ψ is the yaw angle or true heading and Θ is the pitch angle of the UAV. The side-slip angle β and the angle of attack α are located between the aerodynamic and body-fixed coordinate system.

With $\mathbf{T}_{gb}$, which consists of three sequential turnings (rolling, pitching and yawing), the coordinate system (see also Figure 1) is transformed from body-fixed into geodetic (index g) coordinates. $\mathbf{T}_1(\Phi)$ defines rolling about x_b, $\mathbf{T}_2(\Theta)$ defines pitching about y_b, and $\mathbf{T}_3(\Psi)$ defines yawing about z_b.

$$\begin{aligned}\mathbf{T}_{gb} &= \mathbf{T}_1(\Phi)\mathbf{T}_2(\Theta)\mathbf{T}_3(\Psi) \\ &= \begin{pmatrix} 1 & 0 & 0 \\ 0 & \cos\Phi & -\sin\Phi \\ 0 & \sin\Phi & \cos\Phi \end{pmatrix} \begin{pmatrix} \cos\Theta & 0 & \sin\Theta \\ 0 & 1 & 0 \\ -\sin\Theta & 0 & \cos\Theta \end{pmatrix} \begin{pmatrix} \cos\Psi & -\sin\Psi & 0 \\ \sin\Psi & \cos\Psi & 0 \\ 0 & 0 & 1 \end{pmatrix}\end{aligned} \tag{5}$$

Finally, the wind vector $\vec{w}_g$ can be calculated with Equation (2) and transformed into meteorological coordinates (index m) using the transformation $\mathbf{T}_{mg}$:

$$\vec{w}_m = \mathbf{T}_{mg}\vec{w}_g = \begin{pmatrix} 0 & 1 & 0 \\ 1 & 0 & 0 \\ 0 & 0 & -1 \end{pmatrix} \begin{pmatrix} w_x \\ w_y \\ w_z \end{pmatrix} \tag{6}$$

The vector components of the wind vector in meteorological coordinates $\vec{w}_m = (u, v, w)$ are u being positive eastward, v being positive northward, and w positive when facing upwards. The presented data in this study is given in the meteorological coordinate system.

2.2. Five-Hole Probe "Pressures-to-Airflow-Vector"

Generally, there are two fundamental approaches to convert the pressure readings to flow angles, stagnation, and dynamic pressure. Firstly, the pressure field around spherical heads can be described by an analytical model derived with potential theory for fluid dynamics, e.g., as with the BAT probe used by Black et al. [37] or the flow probe used by Metzger et al. [11]. Only spheres or elliptic shapes can be reliably described with this frictionless and incompressible formulation of the flow field with a curl free vector field. Cone tips, on the other hand, are generally fully calibrated in the wind tunnel and the cone angle allows for an adjustment of the angle-sensitivity of the measurement. An overview of relevant geometries and aerodynamic probe design, can be found e.g., in the study of Hall and Povey [38]. MASC uses a five-hole probe (Figure 2) with a tip diameter of 4 mm, a cone angle of $\phi = 60°$, forward facing holes and is calibrated from $-20°$ to $20°$. The probe, manufactured by the Institute of Fluid Mechanics at the Technische Universität Braunschweig, Germany, follows the following compromise: smaller cone angles or "sharper" tips are more sensitive and the pressure coefficients of the probe react more strongly, if the angle of the inflow tilts. In other words, a small change in the angle of the airflow results in a higher change in the pressure readings, if the probe's tip is sharp rather than bluff. The downside of sharp probe tips are smaller maximum angles that can be measured and a higher dependency on the Reynolds number. The sensitivity of spheres can be compared with cone angles $\phi > 60°$ and can be used for flow angles of up to $40°$ and more. The precision around $\pm 5°$ flow angle, where the measurement with UAS and manned aircraft is most important, is worse. Considering turbulence measurements with a fully exploited frequency response of the tubing and the pressure transducers, a tip diameter of 4 mmwas chosen, since the tip diameter should be kept significantly smaller than the smallest eddy that can be resolved [39]. To find a relationship between the measured pressure differences dP_i and the airflow angles α and β, as well as the dynamic pressure q and static pressure p at any airflow angle within the calibration range, wind-tunnel calibrations were conducted. Previous efforts to measure the 3D wind vector with a similar five-hole probe were made e.g., by [7] with the Mini Aerial Vehicle (M^2AV). The study by Wildmann et al. [6], who were using the MASC, improved the frequency response and accuracy of the probe by using a different tubing between the pressure holes of the five-hole probe and the pressure transducers, and by applying dimensionless calibration coefficients according to Treaster and Yocum [40]. The same setup as by Wildmann et al. [6] is also used in this study and the description of the holes, the dimensions, the schematic tubing and a picture of the probe's tip are given in Figure 2.

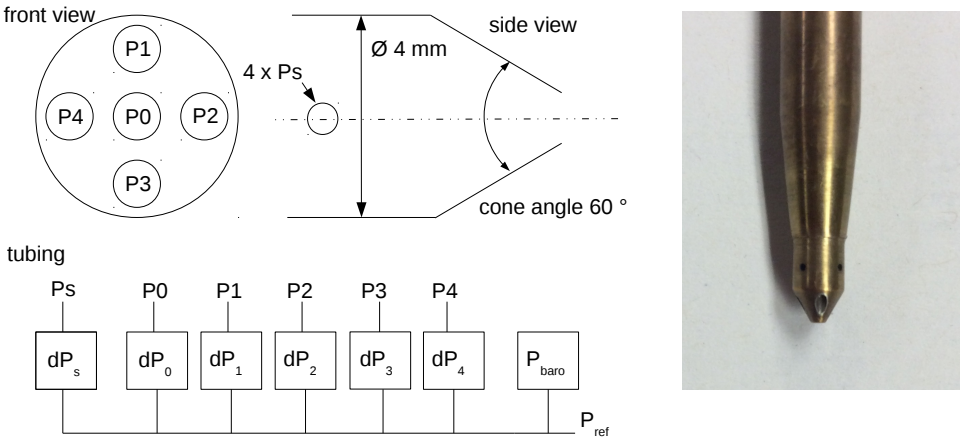

Figure 2. Five-hole probe pressure holes convention, dimensions and tubing schematic (**left**). Picture of the probe tip, used in this study (**right**).

To find a relationship between the measured pressure differences dP_i and the airflow angles α, β, as well as q and p, a polynomial fit is applied and dimensionless coefficients [6,40] are defined:

$$\begin{aligned} \Delta P &= \frac{(dP_1 + dP_2 + dP_3 + dP_4)}{4} \\ q_c &= \frac{1}{2}\,\rho\, v_c^2 \\ k_\alpha &= \frac{dP_1 - dP_3}{dP_0 - \Delta P} \\ k_\beta &= \frac{dP_2 - dP_4}{dP_0 - \Delta P} \\ k_q &= \frac{dP_0 - q_c}{dP_0 - \Delta P} \\ k_p &= \frac{P_s + \Delta P - \Delta p_c}{dP_0 - \Delta P} \end{aligned} \tag{7}$$

In the wind tunnel a dynamic pressure q_c is set for the calibration and the static pressure p_c is recorded. The dimensionless coefficients k_α and k_β are the variables of the polynomial functions for α, β, k_p and k_q, whereas k_p and k_q are correction values for the measurement of q and p with regards to the airflow angle at the probe. The probe, when used as pitot-static tube, would not be independent of the flow angles, since the aerodynamic design of the probe's tip is unsuitable for that. The aim of the calibration is to find the functions $f_x(k_\alpha k_\beta)$ to calculate α, β, k_p and k_q from the pressure readings of a flight experiment:

$$\begin{aligned} \alpha &= f_\alpha(k_\alpha, k_\beta) \\ \beta &= f_\beta(k_\alpha, k_\beta) \\ k_q &= f_q(k_\alpha, k_\beta) \\ k_p &= f_p(k_\alpha, k_\beta) \end{aligned} \tag{8}$$

For all the four functions f_x, a polynomial fit is selected with a specific set of parameters $\vec{c}_x$ for each function. The functions $f_x(k_\alpha, k_\beta)$ can be determined from the scalar product of the two vectors $\vec{k}(k_\alpha, k_\beta)$ and $\vec{c}_x$

$$f_x(k_\alpha, k_\beta) = \vec{k}(k_\alpha, k_\beta)\,\vec{c}_x = \left(k_\alpha^0\,k_\beta^0,\quad k_\alpha^0\,k_\beta^1,\quad \cdots,\quad k_\alpha^0\,k_\beta^m,\quad k_\alpha^1\,k_\beta^0,\quad \cdots,\quad k_\alpha^m\,k_\beta^m\right)\begin{pmatrix} c_{x,0,0} \\ c_{x,0,1} \\ \vdots \\ c_{x,0,m} \\ c_{x,1,0} \\ \vdots \\ c_{x,m,m} \end{pmatrix}, \tag{9}$$

whereas $\vec{c}_x$ is a constant parameter vector with, in this case, the parameters for $m = 9$ and a polynomial of 9th order. The goal of the calibration procedure is to determine the four parameter vectors $\vec{c}_\alpha$, $\vec{c}_\beta$, $\vec{c}_q$ and $\vec{c}_p$. They are estimated from the calibration data, consisting of the quantities α, β, k_α, k_β, k_q and k_p. Both α and β are changed from $-20°$ to $20°$, in steps of $2°$, resulting in 21×21 data points. This leads to an overestimated system of equations that is solved with a least squares method for the unknown parameter vectors $\vec{c'}_x$. The solution $\vec{c'}_x$ is the best fit of the least squares method and is used to estimate velocity and flow angles in arbitrary flows by converting the instantaneous pressure measurements at each hole of the probe to instantaneous $\Delta P, k_\alpha, k_\beta$ according to Equation (7). Subsequently, α, β, k_q and k_p are calculated with

$$\begin{aligned} \alpha &= \vec{k}\ \vec{c'}_\alpha \\ \beta &= \vec{k}\ \vec{c'}_\beta \\ k_q &= \vec{k}\ \vec{c'}_q \\ k_p &= \vec{k}\ \vec{c'}_p \end{aligned} \tag{10}$$

and finally, the static pressure p and the dynamic pressure q are calculated by using Equation (7) and solving for p and q:

$$\begin{aligned} p &= P_s + \Delta P - k_p \cdot (dP_0 - \Delta P) \\ q &= dP_0 - k_q \cdot (dP_0 - \Delta P) \end{aligned} \tag{11}$$

2.3. Wind-Tunnel Measurements

Since the reference side, or low-pressure side, of the differential pressure transducers for the calibration is well out of the turbulent self-similar round jet [41], there is no difference between the ambient pressure in the facility and the static pressure inside the flow field of the open jet during the calibration. The static pressure difference during the calibration is therefore $\Delta p_c = 0$. The airspeed v_c is constant throughout the calibration and continuously monitored with an independent measuring system. The ambient pressure p_{baro}, the airspeed v_c, as well as temperature and relative humidity are recorded continuously. The probe head blockage was 0.02% of the nozzle exit area, which has a diameter of 0.2 m and the calibration is therefore not influenced according to Dominy and Hodson [22]. The calibration apparatus ensures that the probe's tip is always in the same position for all angle combinations during the calibration. This middle section of the open jet stream was analyzed prior to the calibrations. The turbulence intensity, calculated with a 10 min time series of the central hole dP_0 at $\alpha = \beta = 0°$, for $v_c = 22.5$ m s^{-1}, yields 0.04%.

2.4. MASC and the Methods for Deriving Mean Values and Turbulence Statistics

The environment-physics group at the Center for Applied Geoscience (ZAG), University of Tübingen, Germany, designed and built the research UAS MASC (see Figure 3). Together with the ground control station for the autopilot and the sensor system, MASC is classified as UAS. MASC [6] is an electrically propelled single-engine (pusher) aircraft of 4 m wing span and weighs about 6 kg, including 1 kg scientific payload. Height, flight path and all other parameters of flight guidance are

controlled by the autopilot system PixHawk 2.1. The scientific payload consists of several subsystems to measure the 3D wind vector, air temperature and water vapor, including a fast thermometer (fine wires, see [42]), a five-hole flow probe [7,39] and an INS called Ellipse2-N by SBG-systems.

Figure 3. MASC with enlightening (**top**). Picture of the probe tip (**bottom**).

All sensors are sampled at 100 Hz and measure atmospheric turbulence. Considering the individual sensor inertia, a final resolution of about 30 Hz is achieved and thus, small turbulent fluctuations are resolved, while the Nyquist theorem is fulfilled. Typical flight patterns with MASC (these are common flight strategies for any research aircraft) are horizontal straight and level flights (so-called legs) both at constant height or stacked at various flight levels. These flight legs are used to calculate turbulence statistics and turbulent fluxes (e.g., [43,44]), spectra, mean values but also the influence of surface heterogeneity and orography on the lower atmosphere. Two consecutive straight legs including the turns (a full round) are referred to as racetrack. The probe (five-hole probe, see Figures 2 and 3) in use with MASC operates normally at 22.5 m s^{-1} and the Reynolds number in an International Standard Atmosphere (ISA) is Re = 6.04 $\times 10^3$, calculated with

$$\mathrm{Re} = \frac{|\vec{u}_a|\rho d}{\mu}, \tag{12}$$

using the norm of the true airspeed vector $|\vec{u}_a|$, the density ρ and the dynamic viscosity μ of the air and the characteristic length d, being the tip diameter of the probe. The desired margin for the probe in the setup with MASC, ranges from 15 m s^{-1} until 30 m s^{-1} cruising speed, under polar condition with -20 °C until 40 °C, and from sea level pressure of 1013 hPa until high altitude flights and low ambient pressure. The desired range can be from Re $\approx 10.41 \times 10^3$ at 30 m s^{-1} true airspeed, -20 °C and sea level pressure and Reynolds numbers as low as Re $\approx 2.50 \times 10^3$ on a hot summer day in high altitudes and low airspeed. In this context, it is important to consider the behavior of the PixHawk

2.1 flight controller, which controls the indicated airspeed during the measurement. The indicated airspeed (IAS) is measured with a pressure transducer and the influence of the density of the air is not considered. As a rule of thumb, the true airspeed equals the IAS under ISA conditions, and with increasing altitude, round about every 300 m, the true airspeed is 2% higher than IAS. The actual true airspeed is calculated in the post-processing and may vary significantly if the altitude changes during the experiment. The Reynolds number cascade measured in the study of Dominy and Hodson [22] ranges from $4 \times 10^3 < \mathrm{Re} < 500 \times 10^3$ and identifies formally the effects of flow separation from the body of the probe or from the leading edge. Especially for the lower Reynolds numbers towards $\mathrm{Re} = 4 \times 10^3$, flow separation becomes sensitive and it has been demonstrated that artificial turbulence in the wind-tunnel influences the measurement generally for $\mathrm{Re} < 20 \times 10^3$.

Three flights were chosen for this study. The first flight experiment (in the following referred to as ISOBAR) was conducted during the ISOBAR campaign, which was described by Kral et al. [33], presenting the numerous measurement systems of the campaign. The second flight (in the following referred to as COMPLEX) was conducted in complex terrain near Schnittlingen on the Swabian Alp in the South of Germany. This flight was also used by the study of Wildmann et al. [24], who investigated the flow field in the vicinity of the apparent test field for wind energy. The third flight experiment (in the following referred to as WAKE) is one transect through the wake of a wind turbine near Wilhemshaven in the North of Germany. The flights ISOBAR and COMPLEX were chosen to analyze the influence of airspeed variations on mean and turbulence quantities. The basis for all these quantities is the straight level flights (legs), where the turns are cut off. The mean values for temperature, windspeed, and direction are directly calculated from the time series of each flight leg. To analyze the influence on the turbulence measurement, the turbulent kinetic energy TKE, the variance of the vertical wind component $\mathrm{Var}(w)$, the covariance of the vertical and horizontal wind components $\mathrm{Cov}(w,u)$ and $\mathrm{Cov}(w,v)$ and the integral length scale of the vertical $L(w)$ and horizontal wind $L(v_h)$ are calculated, since these are dependent on the calibration of the probe and the most important quantities for ABL studies. The third flight WAKE was chosen, because large changes in airspeed occur during the transect through the wake of the wind turbine, and to show the instantaneous effect of the calibration of the five-hole probe on features in the wind field. The high-resolution data is plotted as a time series to analyze the deviations and uncertainties if the airspeed of the measurement does not fit the airspeed of the calibration. Along with the windspeed and direction, also the calculated angle of attack α and side-slip angle β are analyzed together with data from the INS, showing the motion of the UAS during the transect through the wake of the wind turbine.

The horizontal windspeed v_h is calculated with the wind vector components u and v by

$$v_h = \sqrt{u^2 + v^2}. \tag{13}$$

The variance of a variable X is calculated, using Reynolds decomposition where the fluctuations X' are separated from the mean $\overline{X}$, with

$$\mathrm{Var}(X) = \frac{1}{N-1}\sum_{i=1}^{N}(X_i - \overline{X})^2 = \overline{X'}^2, \tag{14}$$

where N is the number of data points and $\overline{X}$ denotes the average of the variable within the data window or, in this case, within the individual flight leg. The covariance $\mathrm{Cov}(X,Y)$ of two variables is calculated respectively by

$$\mathrm{Cov}(X,Y) = \frac{1}{N-1}\sum_{i=1}^{N}(X_i - \overline{X})(Y_i - \overline{Y}). \tag{15}$$

The turbulent kinetic energy TKE is calculated with the velocity fluctuations (variances) $\mathrm{Var}(u)$, $\mathrm{Var}(v)$ and $\mathrm{Var}(w)$ of the wind vector components

$$\mathrm{TKE} = \frac{1}{2}\left(\mathrm{Var}(u) + \mathrm{Var}(v) + \mathrm{Var}(w)\right) \tag{16}$$

and equals the turbulent normal stress. The integral length scale L [35,45–47] is calculated by multiplying the integral time scale I with the mean true airspeed of the flight leg. The integral time scale $I(v_h)$ of, for instance, the horizontal windspeed v_h is defined by

$$I(v_h) = \int_0^{\tau_1} \delta\tau \, \frac{\overline{v_h}'(t+\tau)\,\overline{v_h}'(t)}{\overline{v_h}'^2} \tag{17}$$

and multiplied by the mean true airspeed $|\overline{\vec{u}_a}|$

$$L(v_h) = I(v_h)\,|\overline{\vec{u}_a}| \tag{18}$$

to get the integral length scale $L(v_h)$. The integral time scale I is the autocorrelation function of the variable and calculated by integration from zero lag to the first crossing with zero at τ_1 [47]. The integral length scale of the vertical wind vector component $L(w)$ is calculated respectively, with $I(w)$ multiplied by $|\overline{\vec{u}_a}|$. The integral length scale can be interpreted as the typical size of the largest, or most energy-transporting eddy.

3. Results and Discussion

Firstly, this study investigates the magnitude of deviations of mean values and turbulence quantities, when measuring with a calibration that does not exactly match the airspeed during the experiment. To some extent this is not avoidable, since turbulence and non-stationary flow causes the UAS to accelerate and decelerate due to its momentum, drag, and the flight-mechanical properties. To evaluate that, the deviations when calculating mean values and the deviations when calculating turbulent quantities must be considered. It is impossible to setup an experimental study in the wind tunnel, since atmospheric turbulence cannot be artificially produced in a representative way. Qualitative studies in the wind tunnel, where the turbulence intensity increased consecutively, showed that the flow separation on the probe's tip is influenced, especially for $\mathrm{Re} < 20 \times 10^3$ [22].

The second main issue of this study is the desired flexibility for the cruising airspeed of the autopilot and a procedure to compensate for deviations between the airspeed of the calibration and the flight experiment.

3.1. Polynomials at Different Reynolds Numbers

To investigate the deviations when calculating mean values from calibrations at different airspeeds, the data from the wind tunnel is already giving insight. In Figure 4, the results of three calibrations in the wind tunnel are presented. The polynomials were recorded at airspeeds of $v_{c1} = 15$ m s^{-1}, $v_{c2} = 22.5$ m s^{-1} and $v_{c3} = 28$ m s^{-1}, yielding, with the apparent ambient pressure, temperature and humidity in the wind-tunnel facility, Reynolds numbers at the probe's tip of $\mathrm{Re}_{v1} = 3695$, $\mathrm{Re}_{v2} = 5538$ and $\mathrm{Re}_{v3} = 7031$. The high speed v_{c3} is the maximum for the used sensor system, because the maximum differential pressure of the front hole is 500 Pa. The low airspeed of $v_{c1} = 15$ m s^{-1} was chosen to mark the lowest expected airspeed of the measurement, since the cruising airspeed of MASC can be set as low as $\approx$18 m s^{-1} and during turbulence the airspeed can reduce further. The plots show the 21×21 dimensionless coefficients k_α, k_β plotted for α and β in steps of 2° from −20° to 20°. The comparison in Figure 4 already reveals how important a consideration in this margin of Reynolds numbers is. Especially for angles $\geq \pm 10°$ the differences are obvious. Since the calibration map for $\mathrm{Re}_{v1} = 3695$ is uniform and almost linear throughout the whole span from −20° to 20°, the sensitivity throughout the whole domain is nearly constant, yielding that this airspeed is better for the measurement, than higher airspeeds. The polynomials of $\mathrm{Re}_{v2} = 5538$ and $\mathrm{Re}_{v3} = 7031$ become skewed and therefore less sensitive for higher α and β. This means that a change in α and β of e.g.,

2° corresponds to a smaller change in the pressure readings. The map of k_α and k_β is best in terms of precision, if it spans a wide grid and if it is uniform throughout the domain of definition.

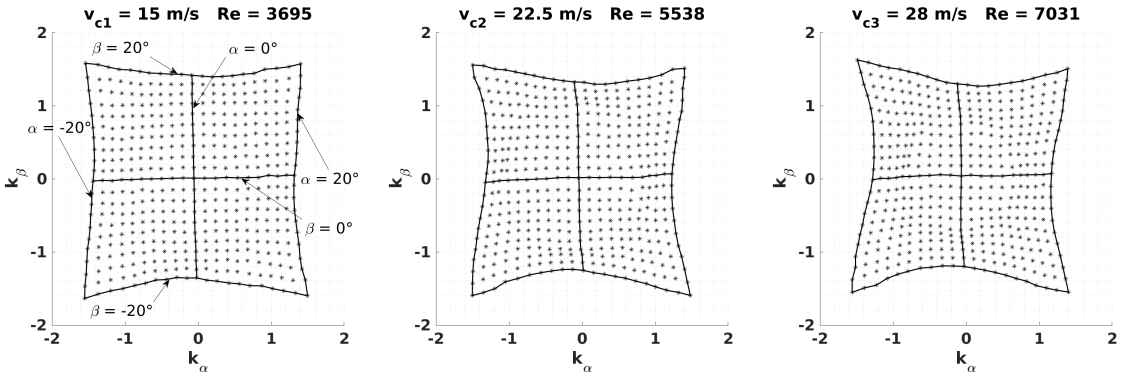

Figure 4. Calibration maps of k_β over k_α for $-20° \leq \alpha \leq 20°$ and $-20° \leq \beta \leq 20°$. The lines with constant α and β are only labelled in the map of $v_{c1} = 15$ m s^{-1}, but account for all calibration maps.

Figure 5 shows an evaluation of the coefficients k_q and k_p. As an example, the coefficients are plotted over β, ranging from $-20°$ to $20°$. Three constant angles of attack $\alpha = -10°$, $\alpha = 0°$ and $\alpha = 20°$ are chosen to show the behavior of k_q and k_p for the three calibrations.

The following behavior of k_q at v_{c1}, v_{c2} and v_{c3} is stated:

- The dynamic pressure coefficients k_q for v_{c2} and v_{c3} are close together, but k_q for v_{c1} lies below and has a larger offset.

For $\alpha = 0°$ the dynamic pressure coefficients k_q for v_{c2} and v_{c3} are close together, but for v_{c1} at $\alpha = 0°$ and $\alpha = -10°$, the difference is significant. For $\alpha = 0°$ all three curves generally vary little over the considered range of β and for all three calibration speeds. The magnitude of k_q at v_{c1} varies the least over range of β compared to v_{c2} and v_{c3} at $\alpha = 0°$ and $\alpha = -10°$. The varying generally increases for $\alpha = -10°$ and again for $\alpha = 20°$, revealing the necessity of the calibration of the dynamic measurement. It is remarkable how strong the changes of k_q for v_{c2} and v_{c3} are between $\alpha = -10°/\alpha = 0°$ and the biggest angle $\alpha = 20°$, because the level of k_q drops significantly for v_{c2} and v_{c3} and the curve of v_{c3} even lies below v_{c2} for $\alpha = 20°$. The curves of k_q for $\alpha = 20°$, drop to significantly to smaller values for v_{c2} and v_{c3}, because the structure of the flow separation on the probe's tip behaves differently between v_{c2} / v_{c3} and v_{c1}. This is also visible for k_p.

- A characteristic local minimum persists around $\beta = 0°$ for $\alpha = 0°$ and for all three curves of k_q. This feature varies for the individual parameters.

For $\alpha = 0°$, a characteristic drop of k_q between $-10° \leq \beta \leq 10°$, where a local minimum persists at $\beta = 0°$, is also showing a dependency on the calibration speed. This feature is pronounced for v_{c1}, significantly weaker for v_{c2} and not apparent for v_{c3}. For $\alpha = -10°$, $\alpha = 0°$ and $\alpha = 20°$, the curves of k_q show a similar behavior for the range of β when inter-compared, although the local minimum at $\beta = 0°$ does not exist for $\alpha = -10°$ and $\alpha = 20°$.

- It is concluded that the polynomials of k_q and k_p for v_{c1} is the most robust for tilted flow, since the curves for v_{c2} and v_{c3} have a stronger gradient between $\alpha/\beta \leq -10°$ and $\alpha/\beta \geq 10°$.

The curves of the static pressure coefficients k_p, when compared between the three angles of attack α, change their characteristics in a similar way for all three calibration speeds, except for $\alpha = -10°$ and v_{c1}. Here, the flow separation on the probe's tip behaves differently. For $\alpha = 20°$, the curves of k_p for v_{c1} and v_{c2} have a local minimum at $\beta = 0°$, but v_{c3} does not. Generally, the static pressure measurement is the most sensitive compared to k_q and the measurement of α and β themselves in tilted flow [6] and when looking at Figure 5 it becomes clear that the dependency on the Reynolds number

is also very high. Generally, the static pressure is an elaborated task, since many influencing factors disturb the measurements [48] and only trailing cones can reliably measure the undisturbed static pressure from an aircraft. Therefore, further evaluation considering the true static pressure estimation is not made in this study.

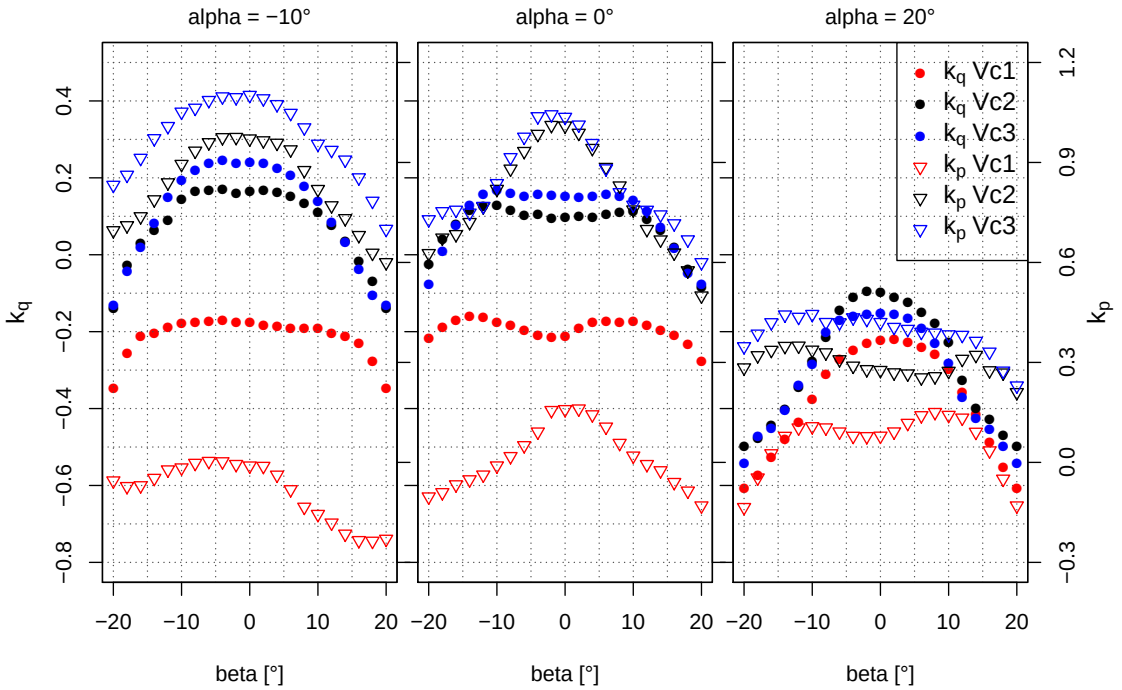

Figure 5. Dynamic pressure calibration coefficients k_q and static pressure calibration coefficients k_p, plotted over $-20° \leq \beta \leq 20°$ for the three calibration speeds $v_{c1} = 15$ m s^{-1}, $v_{c2} = 22.5$ m s^{-1} and $v_{c3} = 28$ m s^{-1}. Three examples of the calibration at $\alpha = -10°$, $\alpha = 0°$ and $\alpha = 20°$ are shown. The axis of k_q is for all subplots on the left side, and k_p is on the right side. The axis-labelling of the middle plot is left out.

The best calibration polynomials can be calculated from the calibration at v_{c1}, since k_q and k_p in Figure 5, and also k_α and k_β in Figure 4, are the most uniform throughout the domain of definition. The enhanced skewness of k_β over k_α in Figure 4, for v_{c2} and v_{c3}, leads to more skewed polynomials for k_q and k_p. It is concluded that the calibration reacts strongly to changes of the Reynolds number for both k_q and k_p, as well as for k_α and k_β. Section 3.4 discusses the application of the interpolation between polynomials to increase the precision, and the use of an independent pitot-static tube is suggested. Doing so, the determination of the true airspeed and the static pressure with the five-hole probe becomes obsolete, since a pitot-static tube can measure theses quantities more reliable in tilted flow and for varying Reynolds numbers and with almost no calibration effort.

3.2. In-Flight Calibration of the Wind Measurement

The aerodynamic coordinate system and the body-fixed coordinate system have the same origin, but a misalignment between the multi-hole probe's orientation and the aircraft cannot be avoided, and a correction must be applied. Therefore, three offset corrections for Φ (roll), Θ (pitch), and Ψ (yaw or heading) must be determined. A forth correction factor f_{tas} for the norm of the true airspeed vector $|\vec{u}_a|$ must be determined to account for the calibration in the wind tunnel, which never matches exactly the conditions during the measurements, since the calibration of the whole UAS including the engine etc. is not feasible and especially because the reference side of the pressure transducers have the ambient pressure of the wind-tunnel facility as reference during the calibration, and because in-flight,

the pressure inside the fuselage is the reference for the pressure transducers. The procedure to calculate the correction factors was explained in detail by Van den Kroonenberg et al. [7]. The assumption for the in-flight calibration are a constant mean horizontal wind, a mean vertical wind near zero and low turbulence or turbulent transport. This allows a comparison of the wind components for two consecutive straights in opposite directions (star pattern), or identical legs in reverse direction. This procedure yields the correction offset $\Delta\Psi$ for the yaw angle, $\Delta\Theta$ for the pitch angle and the correction factor f_{tas} for the norm of the true airspeed $|\vec{u}_a|$. The offset $\Delta\Phi$ for the roll angle is set to zero and can be, according to Van den Kroonenberg et al. [7], neglected, since the influence on the wind components is very small. The offsets $\Delta\Psi$ and $\Delta\Theta$ are applied to the transformation $\mathbf{T}_{gb}$ in Equation (5) and the factor f_{tas} is multiplied with the norm of the true airspeed vector $|\vec{u}_a|$ in Equation (4). To ensure comparability between the three calibrations, the correction offsets and factors are determined in the exact same way. Meeting the assumptions of constant wind and zero vertical wind is always a delicate task. For the flights ISOBAR and COMPLEX, the three pairs of consecutive legs on the highest flight level were chosen to calculate the correction offsets and factors. The average of those was calculated and applied to the whole flight. The results for the three calibration polynomials are written in Table 1. The WAKE flight uses fractions of two consecutive racetracks on 125 m AGL that were not disturbed by the wake of the turbine. These fractions of the legs represent the free stream, passing the wind turbine. The averages of two pairs were taken and the results are also written in Table 1.

Table 1. Correction offsets $\Delta\Psi$ (yaw angle), $\Delta\Theta$ (pitch angle) and correction factor f_{tas} (multiplied with the norm of the true airspeed $|\vec{u}_a|$). Three sets of correction factors for the flight experiments, and for the three calibration speeds at v_{c1}, v_{c2} and v_{c3} are listed.

v_c [m s^{-1}]	ISOBAR	COMPLEX	WAKE	
15	−1.64	−3.12	2.85	
22.5	−1.59	−3.18	3.00	$\Delta\Psi$ (yaw) [°]
28	−1.11	−3.06	3.66	
15	1.88	−1.56	−0.92	
22.5	2.01	−1.46	−0.71	$\Delta\Theta$ (pitch) [°]
28	1.91	−1.68	−0.99	
15	0.92	0.96	0.87	
22.5	1.08	1.13	1.00	f_{tas} [-]
28	1.09	1.15	1.01	

Table 1 shows that the offsets $\Delta\Psi$ and $\Delta\Theta$ are in the same range for all applied calibrations and vary ≈1–6° between the flights. This is mainly due to the previously described misalignment of the probe and the UAS. The correction factors f_{tas} for the true airspeed vary systematically for the three calibrations, since the values smaller than 1 were calculated for the calibration speeds v_{c1} for all experiments, causing a reduction of the true airspeed. The values of f_{tas} for v_{c2} are slightly bigger, or equal to 1, and the values for v_{c3} are again higher. This is expected, since k_q in Figure 5 is significantly lower for v_{c1} and the actual true airspeed of the measurement was set to 22.5 m s^{-1} for the autopilot. The results for the correction factors f_{tas} for v_{c2} and v_{c3} follow the same logic, but differ less significant, since the curves for k_q in Figure 5 are also closer together. The level of the three correction factors f_{tas} when inter-compared between the experiments also differs, which is mainly caused by the thermodynamic differences, or differences in the density of the air, and by the airspeed setting of the autopilot, which is also affected by that, and generally not precisely calibrated. The actually measured true airspeeds during the individual flight experiments, as well as an overview of the persisting meteorological conditions, are written in the Tables 2–4.

Two things are very important to be noted here. All correction factors do influence each other to some extent and are not independent, but since they are all derived in the exact same way, the comparison in terms of deviations between the calibrations is not affected by that. On the

other hand, it cannot be stated that there were no general offsets caused by the correction factors. This remains as an uncertainty and is subject to the overall conclusion and recommendations for future measurements.

3.3. Flight Experiments: Influence of Different Calibration Speeds on Mean Values, Turbulence Statistics and Single Flow Features

Three different polynomials are applied to data of three flights in different atmospheric conditions to be able to argue the influence of airspeed variations of the UAS during the measurements. Firstly, the ISOBAR flight with low atmospheric turbulence is shown in the Figures 6–9 and compared to the COMPLEX flight in the Figures 10–13 with high turbulence in complex terrain. Every data point consists of one headwind leg. To evaluate the persistent condition of these two flights, the set of plots in the Figures 6–13 consist in the subplot on the left-hand side, of height profiles of the quantities that are calculated with the polynomial at v_{c2}. The deviations are given in the subplot on the right-hand side, where the red (v_{c1}) and blue (v_{c3}) bars display the absolute deviations of the quantity to the value, calculated with the polynomial at v_{c2}.

To show the influence of a big and sudden change in airspeed, when passing through tip vortices and the windspeed deficit of the wind turbine, the WAKE flight is analyzed in the Figures 14–17. The time series of the whole transect for several quantities of the measurement system is given in Figure 15, and a zoom into the first passage in the vicinity of a tip vortex, is given in the Figures 16 and 17.

3.3.1. Low Turbulence in Stably Stratified Nocturnal Polar Boundary Layer (ISOBAR)

The ISOBAR flight was conducted in the north of the Bothnian Bay in Finland on the 21 February 2017 between 05:01 and 05:48 UTC, which is 07:01 a.m. local time. The intensive measurement campaign was described by Kral et al. [33]. MASC was operated in the dark and started on the lowest flight level of 25 m AMSL and ascended afterwards in steps of 25 m to 150 m AMSL, followed by steps of 50 m. The lower surface layer is sampled denser to capture the ground-based inversion. The orientation of the racetracks and the flight direction of the legs, contained in the set of plots, was about 350° to be oriented against the mean wind direction. The data only consist of the headwind legs, since the fetch, when flying headwind, differs significantly from the tailwind legs. The length of the legs is about 1200 m. An overview of the conditions during the ISOBAR flight is given in Table 2. The stably stratified surface layer was about 75 to 100 m thick, as indicated by the profiles of potential temperature, windspeed and direction in Figure 6. The windspeed was ≈6 m s^{-1} on the lowest level and ≈9.5 m s^{-1} above the ground-based inversion quite high and the wind direction turned from ≈325° to ≈365° on 275 m AMSL. The profile of the wind direction indicates another slightly different regime above 125 m AMSL and again, visible in the profile of potential temperature and windspeed, a layer above 250 m AMSL.

The deviations when using the calibrations at v_{c1} and v_{c3}, which do not fit the actual airspeed of the measurement, reveal their influence on the calculation of mean values. Generally, the influence on windspeed and direction, averaged over the whole leg, can be rated as small. The maximum deviation is 0.2 m s^{-1} and 0.4°. Supported by the investigations of other flights during this campaign, no trend or significant correlation with other parameters was found for the absolute deviations of the mean values. Furthermore, also relative deviations do not show any trend or correlation for the deviations of the mean values. The actual averaged true airspeed, calculated with the polynomial at $v_{c2} = 22.5$ m s^{-1} for the ISOBAR flight was, averaged over all flight levels, $|\overline{\vec{u}_a}| = 24.46$ m s^{-1}. The highest standard deviation was measured on the lowest level with $|\overline{\vec{u}_a}| = 24.18 \pm 0.31$ m s^{-1}. The highest true airspeed of the whole ISOBAR flight was $|\vec{u}_a| = 25.53$ m s^{-1} and the lowest true airspeed was $|\vec{u}_a| = 22.98$ m s^{-1}. Although the autopilot was set to 22.5 m s^{-1}, the post-processing revealed a higher true airspeed.

Table 2. Overview of the conditions during the ISOBAR flight.

barometric pressure ground	989 hPa
temperature ground	−14.3 °C
air density ground	1.33 kg m^{-3}
windspeed	≈6–9.5 m s^{-1}
wind direction	≈325–5°
averaged true airspeed of the whole flight	$\|\overline{\vec{u}_a}\| = 24.46$ m s^{-1}
highest true airspeed of the whole flight	$\|\vec{u}_a\| = 25.53$ m s^{-1}
lowest true airspeed of the whole flight	$\|\vec{u}_a\| = 22.98$ m s^{-1}
leg with highest standard deviation of the true airspeed	$\|\overline{\vec{u}_a}\| = 24.18 \pm 0.31$ m s^{-1}

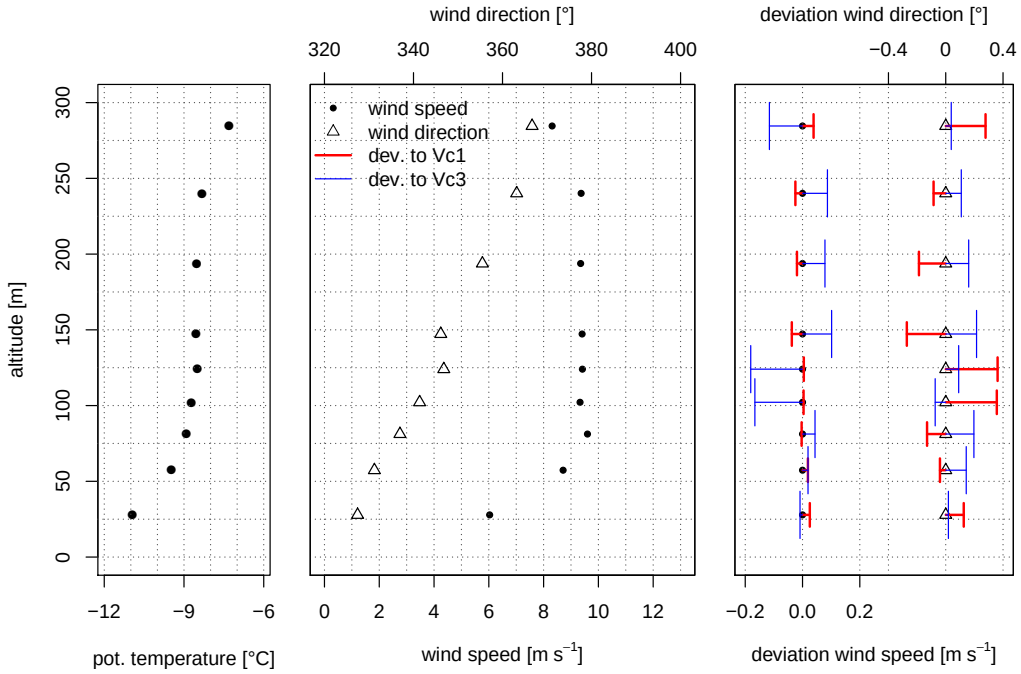

Figure 6. Height profiles of the ISOBAR flight with the altitude AMSL of the potential temperature (**left**), horizontal windspeed v_h and wind direction ϕ, calculated with the calibration polynomial at v_{c2} (**middle**). Deviations (**right**), when applying the calibration polynomials at v_{c1} and v_{c3}.

The profiles of TKE and the Var(w) in Figure 7 show a uniform distribution for the SBL, where turbulence is suppressed. With the persisting wind direction, the air mass had a fetch of at least 50 km over the frozen Bothnian Bay, which is homogeneous terrain that cools the air above it. The surface layer forms due to friction, and TKE and Var(w) increase towards the ground. Another source of turbulence is the top of the surface inversion, where the geostrophic wind causes shear between the layers. This is also reflected in the measurements, since the TKE on 125 and 150 m AMSL is increased and the Var(w) too, although little. Here, the deviations when applying the calibration at v_{c1} and v_{c3} do have a clear trend. Higher turbulence towards the ground causes higher deviations, but a constant relative deviation does not exist. The relative deviations vary randomly between almost 0% and up to 20%.

The covariances Cov(w, u) and Cov(w, v) in Figure 8 are used to estimate the turbulent momentum flux and are also directly influenced by the calibration of the five-hole probe. The values between 75 and 250 m AMSL are close to zero, indicating that there was no significant vertical flux of momentum. On the highest flight level, the temperature and windspeed profiles indicate a change of the wind field, which is also visible in the profile of covariances. In the surface layer, a negative momentum flux towards the surface is expected. The lowest leg on ≈25 m AMSL gives a negative flux, but the next flight level has a slightly positive flux and is already influenced by the shear above the surface-based

inversion [49]. Certainly, one would have to transform the coordinate system into the main wind direction for further analysis. The resolution in the surface layer is unfortunately too small to be able to give sufficient insight into the momentum flux, but it is remarkable that MASC can measure consistently small values close to zero without outliers. The deviations of the covariances are generally high and especially for the two height levels above the ground. The peak value for Cov(w, u) on the lowest flight level has relative deviations of 30% and 35% and for the covariance Cov(w, v) on 54 m AMSL, the relative deviation is almost 100%. This time, the deviations, when using the calibration at v_{c3}, do result in a higher deviation, than using the calibration at v_{c1}. This is not the case for the other parameters. There was no reason found for that and the amount of data is not sufficient to draw further conclusions.

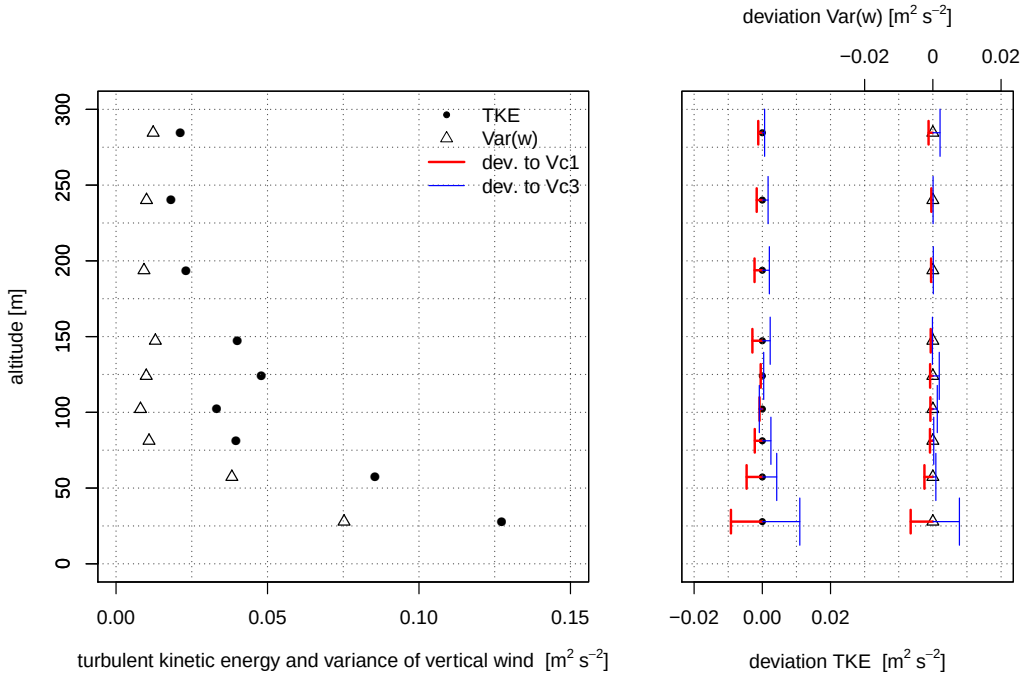

Figure 7. Height profiles of the ISOBAR flight with the altitude AMSL of the turbulent kinetic energy TKE and the variance of the vertical wind component Var(w), calculated with the calibration polynomial at v_{c2} (**left**). Deviations (**right**), when applying the calibration polynomials at v_{c1} and v_{c3}.

The integral length scale L is an important criterion to judge, whether the time series and the fetch of the measurement was long enough to measure turbulence representatively, and to estimate turbulent fluxes [50]. Besides, the statistical error can be calculated according to Mann and Lenschow [51]. The L was calculated for the vertical and the horizontal wind in Figure 9. The profile of $L(v_h)$ reflects the previously described structure of the ABL, according to the turbulence regimes in the different layers. The turbulence regime in the surface layer has a strong gradient but is poorly resolved. The layer above, driven by shear, inherits the biggest structures for the horizontal wind components, and in the third turbulence regime towards the highest flight levels, $L(v_h)$ increases again. Here, also $L(w)$ increases. With a length of the legs of about 1200 m and a maximum L of 75 m, the biggest eddies of the flow are sampled at least 15 times. The $L(w)$, in general, is small, since the ABL is stably and neutrally stratified. On the one hand, the deviations of $L(v_h)$ are slightly higher if the actual values are high. However, no trend for the absolute or relative deviation, either towards the calibration at v_{c1} nor the calibration at v_{c3} can be identified. Although the turbulent kinetic energy and the variance of the vertical wind on the lowest level is increased, the deviations of the L on the lowest level are not. This is another indication that airspeed variations must be considered and that the calibration of the probe is of major importance for the turbulence statistics, since the random nature of turbulence does not allow for simplifications, causing high uncertainties. Unavoidable airspeed fluctuations

during the measurement do influence the turbulence measurements, and significant offsets between the airspeed of the measurement and the airspeed of the calibration must be considered. The influence for turbulence statistics is significantly higher than for mean values.

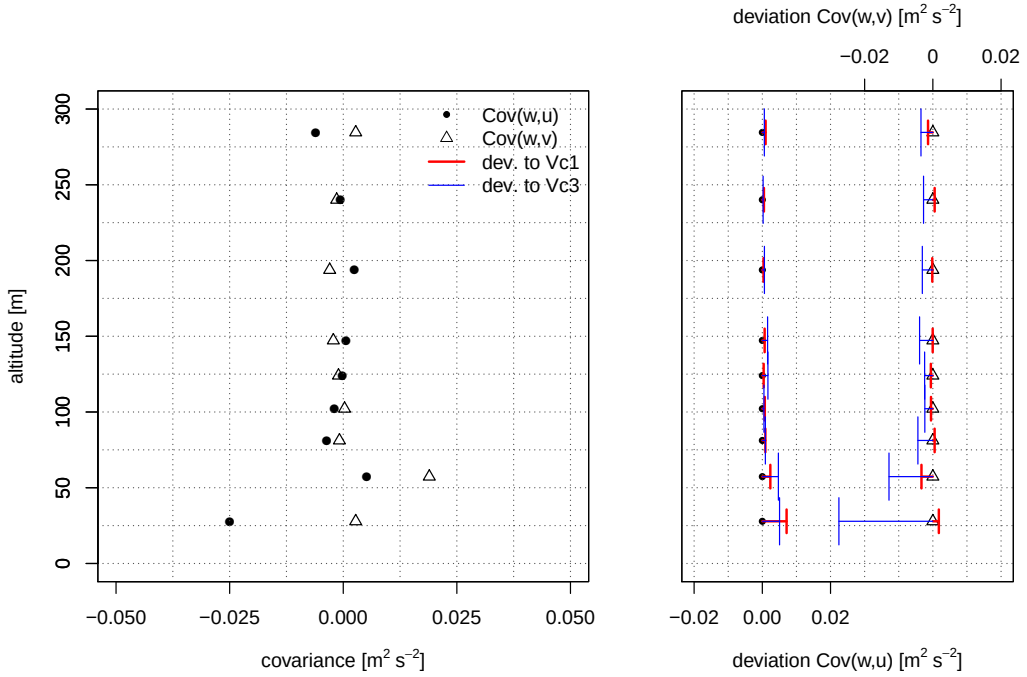

Figure 8. Height profiles of the ISOBAR flight with the altitude AMSL of the covariances Cov(w, u) and Cov(w, v), calculated with the calibration polynomial at v_{c2} (**left**). Deviations (**right**), when applying the calibration polynomials at v_{c1} and v_{c3}.

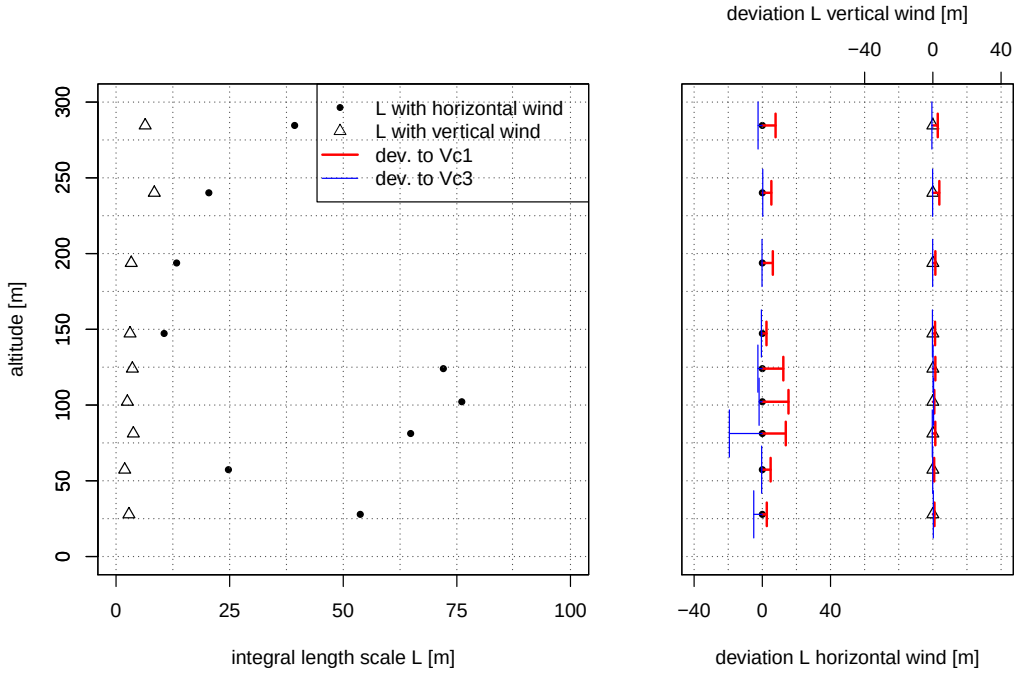

Figure 9. Height profiles of the ISOBAR flight with the altitude AMSL of the integral length scale of the horizontal windspeed $L(v_h)$ and the vertical windspeed $L(w)$, calculated with the calibration polynomial at v_{c2} (**left**). Deviations (**right**), when applying the calibration polynomials at v_{c1} and v_{c3}.

3.3.2. High Turbulence in Complex Terrain (COMPLEX)

The mission of the COMPLEX flight was the investigation of a test site for wind energy in complex terrain. The test site is located on the Swabian Alb, in the South of Germany, near Geislingen an der Steige. The plateau, where the potential site for wind turbines is located, is about 200 m elevated from the valley and in the vicinity of a crest (or escarpment) that is located westerly. The study of Wildmann et al. [24] investigates the flow field using MASC and the studies of Knaus et al. [52] and Schulz et al. [53] compare MASC measurements with numerical simulations, LiDAR and meteorological tower measurements. The COMPLEX flight in this study was conducted in the afternoon of the 27 March 2015 between 13:02 and 13:46 UTC in convective conditions with cumulus overclouding, westerly wind directions and 8 to 9 m s^{-1} mean windspeed. The ISOBAR flight in Figure 6 and the COMPLEX flight in Figure 10 were chosen, because the windspeed has about the same magnitude, making this comparison significant when analyzing the substantially different turbulence regimes of these flights. This flight is one of the 18 flights of the study by Wildmann et al. [24] and was also used in the comparisons [52,53]. The wind field in these conditions is strongly influenced by the crest, which is overflown forth and back with an orientation of the flight path of ≈285° for the headwind legs. The lowest flight level is 75 m above the take-off position on the plateau of the Swabian Alp, which corresponds to about 790 m AMSL. After the lowest level, MASC ascended in steps of 25 m to 1015 m. The length of the legs is about 1000 m. In dissociation of the study of Wildmann et al. [24], investigating the wind field, in this manuscript, the mean values and turbulence statistics are calculated from the whole leg. To study the wind field, Wildmann et al. [24] split up the legs into certain windows, but for the analysis of deviations due to airspeed variations, the total length of the time series is used for the calculations. The length of each leg was about 1000 m and, to foreclose argumentation concerning the turbulence statistics, with an L of up to 200 m, the turbulent flux of momentum cannot be calculated representatively with a single leg. In this wind field, essentially influenced by the crest, it is more explicit to interpret the covariances as the off-diagonal components of the Reynolds stress tensor and the variances of the wind components as the diagonal components [41]. Standard ABL profiles cannot be expected. Previous studies showed Wildmann et al. [24], Knaus et al. [52] that normalization and averaging with several flights in similar conditions, yields representative local features of the wind field, by averaging out transient flow features and convection. Nevertheless, to argue the deviations when applying different calibrations of the five-hole probe, the turbulent conditions are insightful and in comparison with the rather calm conditions of the ISOBAR flight, the influence of airspeed variations becomes distinct.

An overview of the conditions during the COMPLEX flight is given in Table 3. The potential temperature profile in Figure 10 indicates a convective ABL with a step of 0.4 °C between the forth and fifths height level. While the windspeed profile is relatively uniform, the profile of wind direction has also high gradients between 870 m and 915 m AMSL. Intensive shear, and the separation between two regimes persists. The lower layer is strongly influenced by upstream features of the orography and the crest itself. Despite strong turbulence, the deviations for mean values are, with a maximum of 0.1 m s^{-1} and 0.2°, small and in the same order of magnitude as for the ISOBAR flight. The actual averaged true airspeed, calculated with the polynomial at $v_{c2} = 22.5$ m s^{-1} for the COMPLEX flight was, averaged over all flight levels, $|\overline{\vec{u}_a}| = 24.13$ m s^{-1}. The highest standard deviation was measured on 915 m AMSL with $|\overline{\vec{u}_a}| = 24.21 \pm 1.14$ m s^{-1}. The highest true airspeed of the whole COMPLEX flight was $|\vec{u}_a| = 28.59$ m s^{-1} and the lowest true airspeed was $|\vec{u}_a| = 20.14$ m s^{-1}. The variations of the true airspeed are significantly higher than for the ISOBAR flight.

The turbulent kinetic energy TKE and the variance of the vertical wind component Var(w) is, with more than 3 m^2 s^{-2} , higher than for the ISOBAR flight by a factor of 30. The two turbulence regimes above and below 915 m AMSL are clearly visible in Figure 11, since below the values spread around ≈2.2 m^2 s^{-2} and above around ≈0.8 m^2 s^{-2} . The deviations are higher, if the persistent TKE is higher, but the relative deviations are, with a maximum of 4.2%, very small compared to the ISOBAR flight. The deviations when using the calibration at v_{c3} and at v_{c1} give randomly higher and smaller values

for the TKE, whereas the deviations for the variance Var(w) are uniformly distributed with higher values for the polynomial at v_{c3} and lower values for the polynomial at v_{c1}. The covariances Cov(w, u) and Cov(w, v) in Figure 12 are, with up to -0.75 m^2 s^{-2} , by a factor of 30 higher than for the ISOBAR flight. At a first glance, one would expect an upward transport of momentum due to the upwind, caused by the crest. This is true, if fractions, or windows of the legs that represent specifically the footprint of the crest are analyzed. Since only less than a third of the legs inherit an up-draft, and the downstream part of the wind field re-attenuates to the plateau, the mean direction of the momentum in the lower five flight levels is oriented downwards. Above 925 m AMSL, in the upper persistent layer, the stresses are closer to zero. In dissociation to the turbulent kinetic energy and the variance of the vertical wind component, the covariances depend strongly on the calibration of the five-hole probe. With relative deviations of more than 100% it is delicate, in terms of airspeed variations, to measure reliably covariances in high turbulence. It is interesting to see that the deviations for TKE and Var(w) do not scale with the magnitude of the value, since the ISOBAR flight in low turbulence shows deviations of up to 20% and the COMPLEX flight in very high turbulence, only a maximum of 4%. The deviations of the covariances, on the other hand, do scale with the actual value and are, by a factor of ten, higher than for the ISOBAR flight. It is concluded that airspeed variations cause disproportionately high deviations for these statistical moments of second order, since the covariances are calculated from the turbulent part of two quantities.

Table 3. Overview of the conditions during the COMPLEX flight.

barometric pressure ground	938 hPa
temperature ground	8.2 °C
air density ground	1.16 kg m^{-3}
windspeed	≈9 m s^{-1}
wind direction	≈285–305°
averaged true airspeed of the whole flight	$\lvert\overline{\vec{u}_a}\rvert = 24.13$ m s^{-1}
highest true airspeed of the whole flight	$\lvert\vec{u}_a\rvert = 28.59$ m s^{-1}
lowest true airspeed of the whole flight	$\lvert\vec{u}_a\rvert = 20.14$ m s^{-1}
leg with highest standard deviation of the true airspeed	$\lvert\overline{\vec{u}_a}\rvert = 24.21 \pm 1.14$ m s^{-1}

The plot of L in Figure 13 inherits also the two layers below and above 925 m AMS, with very small values for $L(w)$ on the two lowest levels, where also the deviations of those are very small. The reason is that close to the ground, the scales of the vertical wind are small and cannot grow due to the surface underneath. The $L(v_h)$ is, with ≈100 m, quite constant in the lower layer and varies more in the higher layer. This is inversely correlated with the TKE and the Var(w) which is also the case for the ISOBAR flight in the highest two legs. While the influence of the surface decreases, patterns of the geostrophic wind become dominant, shifting the spectrum of the turbulent features towards bigger structures. The influence of the calibration polynomials at v_{c3} and v_{c1} in the right-hand subplot of Figure 13 are asymmetric. The calibration at v_{c1} deviates more than the calibration at v_{c3}, both for $L(v_h)$ and $L(w)$, whereas the opposite behavior occurs for the covariances. The ISOBAR flight does not show this behavior. There was no explanation found for that and it is concluded that airspeed variations must be considered, especially for the calculation of covariances and integral length scales.

To some extent, the absolute deviations of all turbulence quantities show a trend, since high values cause higher deviations and vice versa. For the ISOBAR flight this is also indicated, but less obvious. The trend for the absolute deviations is overlain by the random nature of turbulence and relative deviations do neither have a trend, nor do absolute and relative deviations correlate with each other. Therefore, airspeed variations, or variations of the Reynolds number on the probe's tip during the measurement, clearly randomly influence the result. The airspeed of the calibration of the probe is of major importance, especially for statistical moments of second order and particularly for covariances and integral length scales of wind vector components.

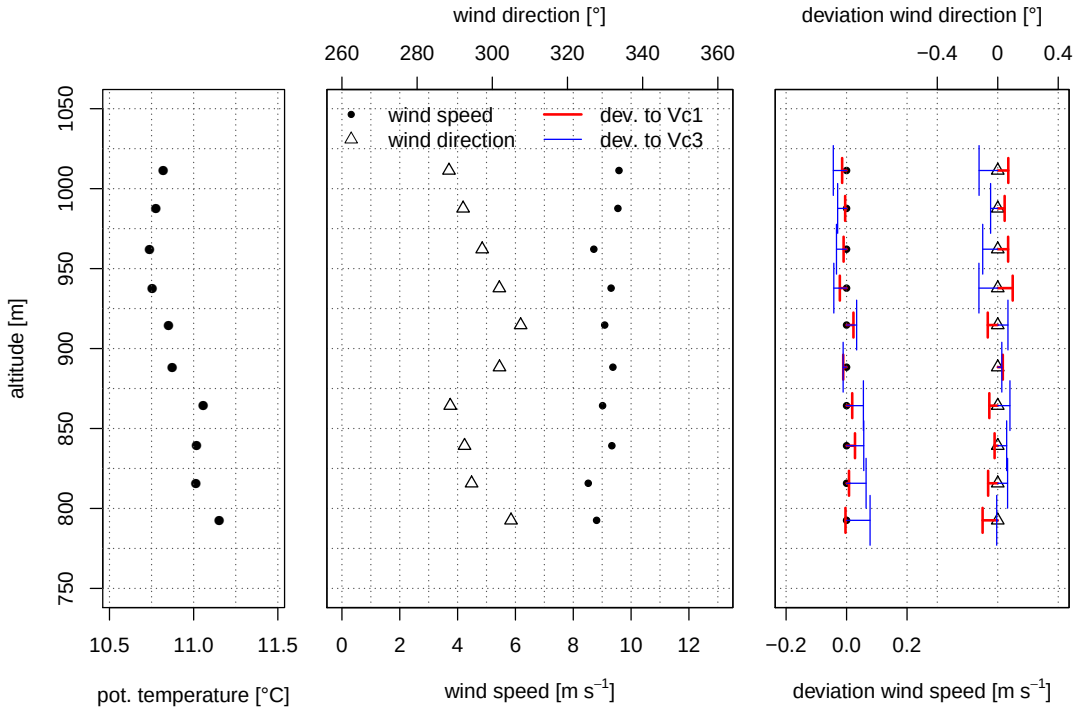

Figure 10. Height profiles of the COMPLEX flight with the altitude AMSL of the potential temperature (**left**), horizontal windspeed v_h and wind direction ϕ, calculated with the calibration polynomial at v_{c2} (**middle**). Deviations (**right**), when applying the calibration polynomials at v_{c1} and v_{c3}.

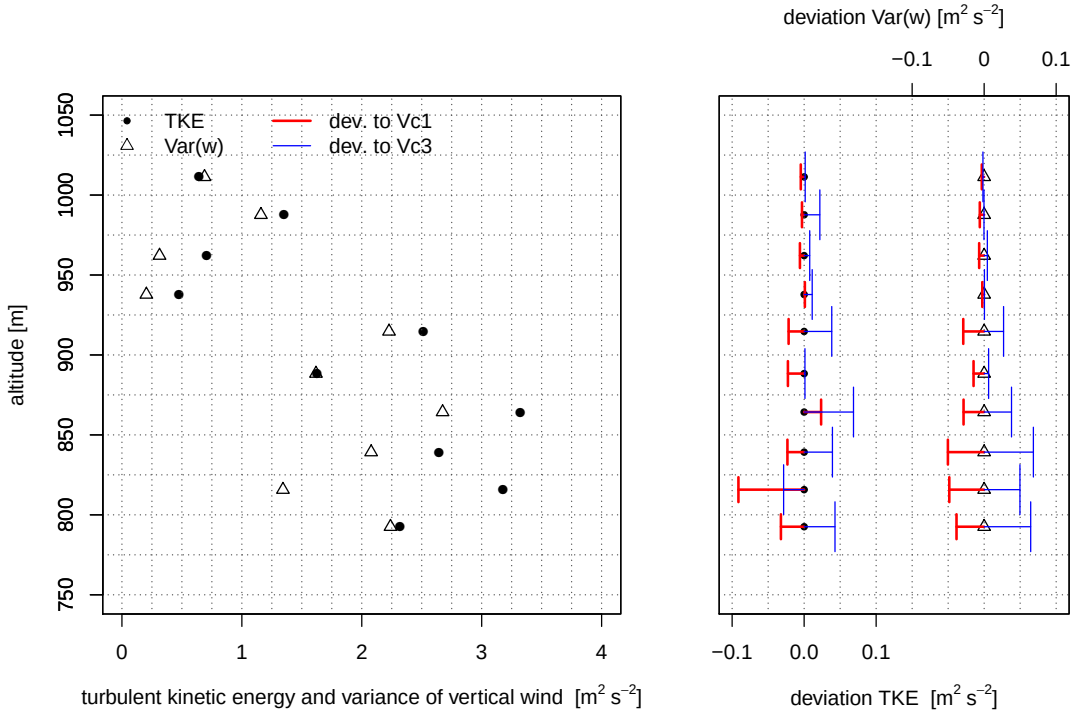

Figure 11. Height profiles of the COMPLEX flight with the altitude AMSL of the turbulent kinetic energy TKE and the variance of the vertical wind component Var(w), calculated with the calibration polynomial at v_{c2} (**left**). Deviations (**right**), when applying the calibration polynomials at v_{c1} and v_{c3}.

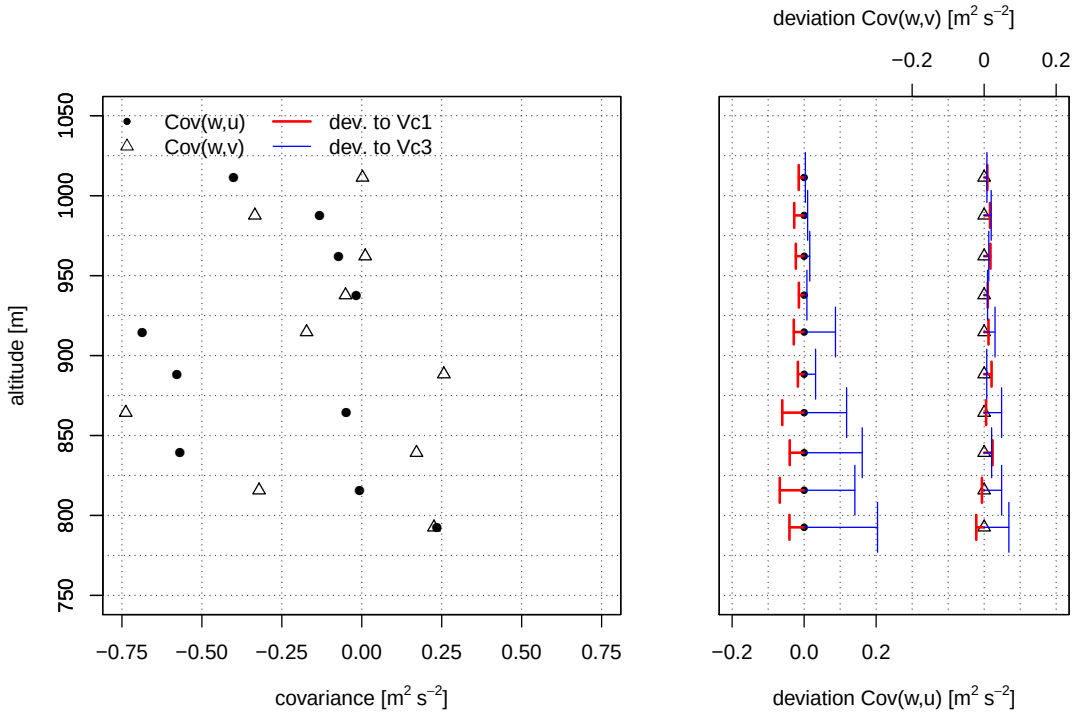

Figure 12. Height profiles of the COMPLEX flight with the altitude AMSL of the covariances Cov(w, u) and Cov(w, v), calculated with the calibration polynomial at v_{c2} (**left**). Deviations (**right**), when applying the calibration polynomials at v_{c1} and v_{c3}.

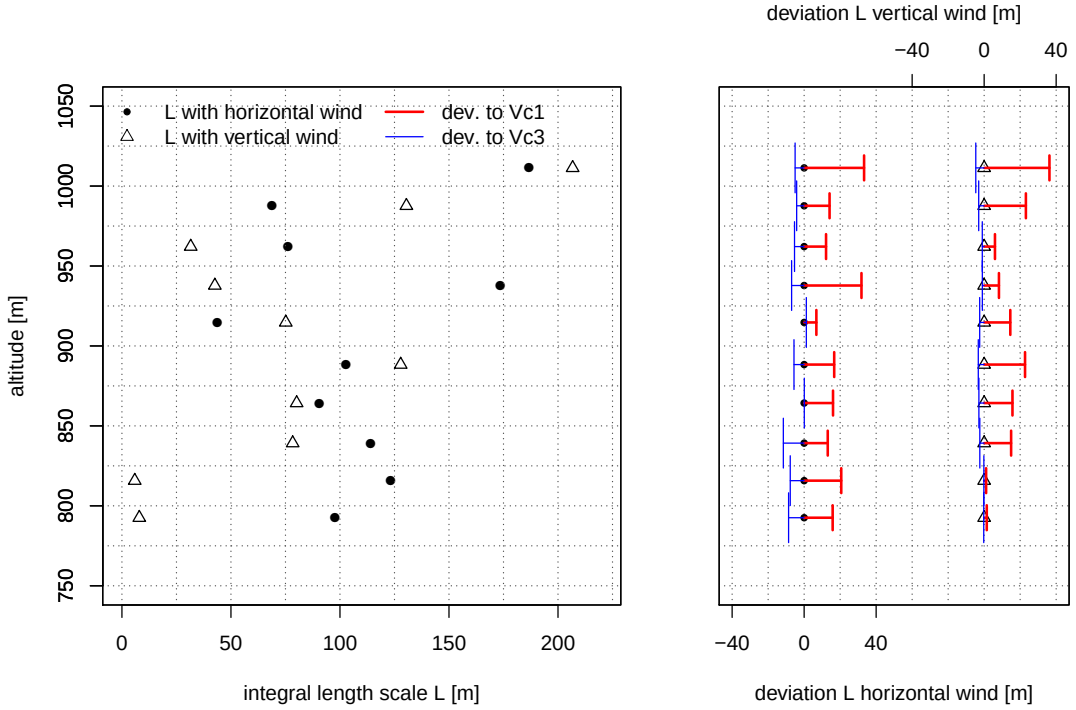

Figure 13. Height profiles of the COMPLEX flight with the altitude AMSL of the integral length scale of the horizontal windspeed $L(v_h)$ and the vertical windspeed $L(w)$, calculated with the calibration polynomial at v_{c2} (**left**). Deviations (**right**), when applying the calibration polynomials at v_{c1} and v_{c3}.

3.3.3. Transect of the Wake of a Wind Turbine (WAKE)

The third flight was performed to study the wind field around wind-energy converters (WEC). In the North of Germany, near Wilhelmshaven, the flow in the vicinity of an Enercon E-112 prototype turbine in the Jade Wind Park, close to the shore line of the German Ocean, was investigated. The helical hose of detaching tip vortices, growing and decaying gradually downstream the WEC, are of great interest, since numerical models show high uncertainties. However, field measurements of small-scale features of the wake and especially the tip vortex helix do not exist and MASC provides unique possibilities to sample in situ measurements of the small scales. A big uncertainty in models is the evolution of the tip vortex helix and decay-rates of the vortices in different atmospheric conditions. To be able to study these processes and validate numerical models, the uncertainties of the wind measurement must be analyzed precisely, since a transect through a tip vortex causes very high gradients of the wind vector components, involving sudden changes in airspeed and attitude of the UAS. The strategy to encounter the tip vortex is shown in Figure 14, where the wake is crossed perpendicular to the mean flow from west to east. Dependent on the position relative to the WEC, the expected size, strength, and orientation of the tip vortices differ and coming along with, the chances to fly through or pass by a vortex.

To analyze the influence of airspeed variations, a transect on hub-height with a distance of one rotor diameter (1D) was chosen. The hub-height of the Enercon E-112 prototype WEC is 125 m AGL and the rotor diameter is 100 m. Figure 14 shows the flight path of MASC with the horizontal windspeed v_h in the color code for a transect from west to east. The data is downscaled to 5 Hz. The displayed WEC is only a schematic model and does not have exact dimensions. The yaw angle of the WEC during the measurement is indicated by the 3D model. The wind direction and speed was about 25° and 9 m s^{-1} for the leg on hub-height and in front of the WEC. The windspeed deficit is clearly visible in Figure 14 and the tip vortices can be identified.

Moreover, Figure 14 shows the schematic orientation of detaching tip vortices of a turbine blade, when considering the cross-section of a horizontal plane on hub-height. Here, it can be assumed that the cross-section of the vortex lies untilted (flat) in a horizontal plane through the center of the rotor. The measurement for this example is located 1D behind the WEC. Assuming that there is no deflection of the wake and the helix of vortices in any direction, the orientation of the vortex at 1D behind the WEC would be the same. The arrows indicate the position of the vortices that were encountered or passed with the flight leg. Assuming incompressible and divergence free flow, a vortex can be described by potential theory, where the velocity field is a simple function of the radius r of the vortex and the circulation Γ, which is the strength of the vortex. This is the basis for simple formulations to describe e.g., aircraft wake vortices [54]. If a tip vortex were traversed through the center, the tangential velocity would increase to its maximum at the core radius $r = r_c$, and decrease to zero, when passing the center at $r = 0$, followed by another increase in the opposing direction to its second maximum at $r = r_c$ again. During the approach and after the vortex, outside r_c, the tangential velocity increases and decreases until the mean flow dominates. This simplification is the basis argumentation for the analysis at which position the vortex was encountered in this study. Further definitions and criteria for vortices are given by Jeong and Hussain [55].

An overview of the conditions during the WAKE flight is given in Table 4. The wind vector components u, v and w, along with the horizontal windspeed and wind direction, the flow angles onto the FHP α and β, the true airspeed $|\vec{u}_a|$, the heading Ψ and the ground speed in east-west direction $v_{g,\,ew}$ are plotted as a time series in Figure 15. The time series is the same data as in the Google Earth pictures in Figure 14 and shows the windspeed deficit of the wake. The true airspeed and all data in Figure 15 is calculated with the polynomial of $v_{c2} = 22.5$ m s^{-1}, which is off the actual airspeed, set for the autopilot. The averaged true airspeed and the standard deviation, calculated with the polynomial at $v_{c2} = 22.5$ m s^{-1} for the WAKE flight leg, was $|\overline{\vec{u}_a}| = 18.23 \pm 0.76$ m s^{-1}. The highest true airspeed of the WAKE flight leg was $|\vec{u}_a| = 20.45$ m s^{-1} and the lowest was $|\vec{u}_a| = 16.13$ m s^{-1}. The autopilot was set to 19 m s^{-1} to be able to sample with a higher resolution in the wake of the WEC.

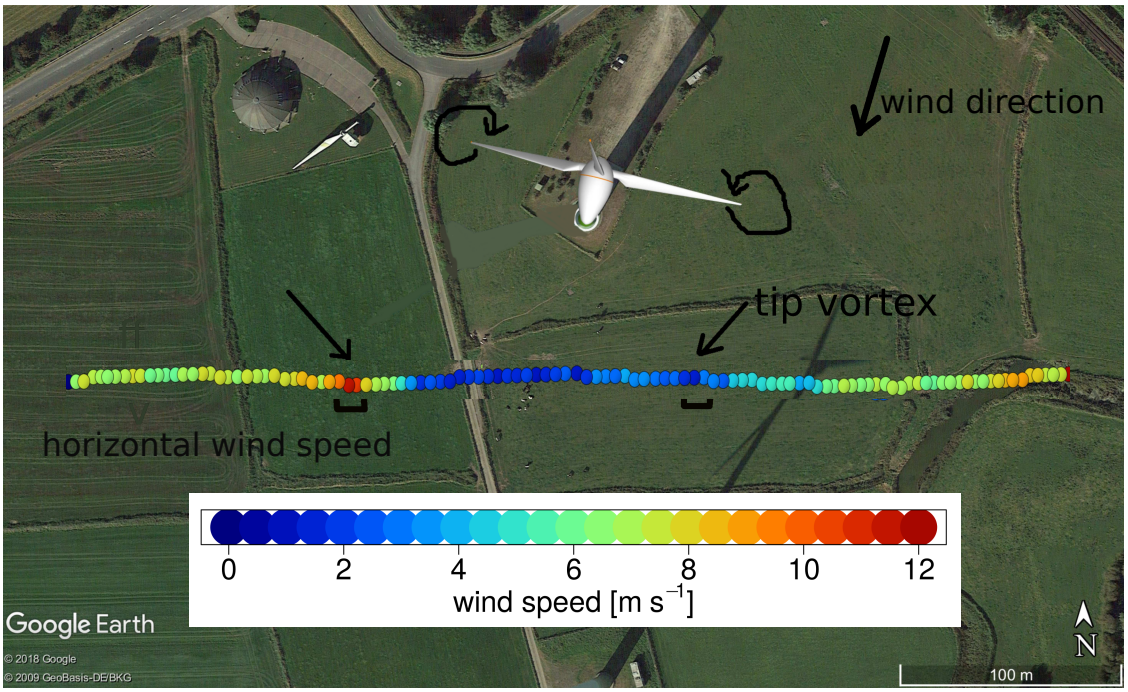

Figure 14. Top view with one leg in the wake of the Enercon E-112 prototype wind turbine with the horizontal windspeed (v_h) in the color code. The light direction was from west to east. The schematic turning direction of detaching tip vortices in a horizontal plane through the rotor center is sketched. The positions of the tip vortices of the measurement are indicated with arrows. The depicted wind turbine is an appended schematic model, indicating the azimuth-angle of the nacelle during the measurement.

Table 4. Overview of the conditions during the WAKE flight.

barometric pressure ground	1014 hPa
temperature ground	27 °C
air density ground	1.17 kg m^{-3}
windspeed	≈9 m s^{-1}
wind direction	≈25°
averaged true airspeed of the flight leg	$\|\overline{\vec{u}_a}\| = 18.23 \pm 0.76$ m s^{-1}
highest true airspeed of the flight leg	$\|\vec{u}_a\| = 20.45$ m s^{-1}
lowest true airspeed of the flight leg	$\|\vec{u}_a\| = 16.13$ m s^{-1}

Prior to the drop in the windspeed deficit of the WEC, v_h in Figure 15 has a peak, indicating the encounter of a tip vortex. For the prevailing wind direction and with the previously described assumptions, the wind vector component v is almost oriented with the mean flow and u is perpendicular to it. The vector component v becoming more negative and u jumping from ≈−3 m s^{-1} back to zero indicates that the vortex center is located south of the flight path. Figure 16 zooms into this event and reveals that the core radius was encountered, since the magnitude of v_h and v have a significant drop which is surrounded by two peaks. After the first vortex, the wind deficit of the WEC is crossed where turbulent conditions persist. The wind direction turns strongly in the middle part of the wind deficit and has the highest peak at the end of the wake, where another vortex was passed. This event looks different, but again, the vortex is located south of the flight path. The core radius was not reached this time. Generally, the vertical wind w is close to zero for the transect and for the first encounter of the vortex, but has a negative peak, when passing the second vortex. Therefore, the location of the vortex core is south and above the flight path, but the assumption that the cross-section of the vortex at hub-height is flat, might be not correct for this incident. Further analysis and a statistical approach with more data is needed.

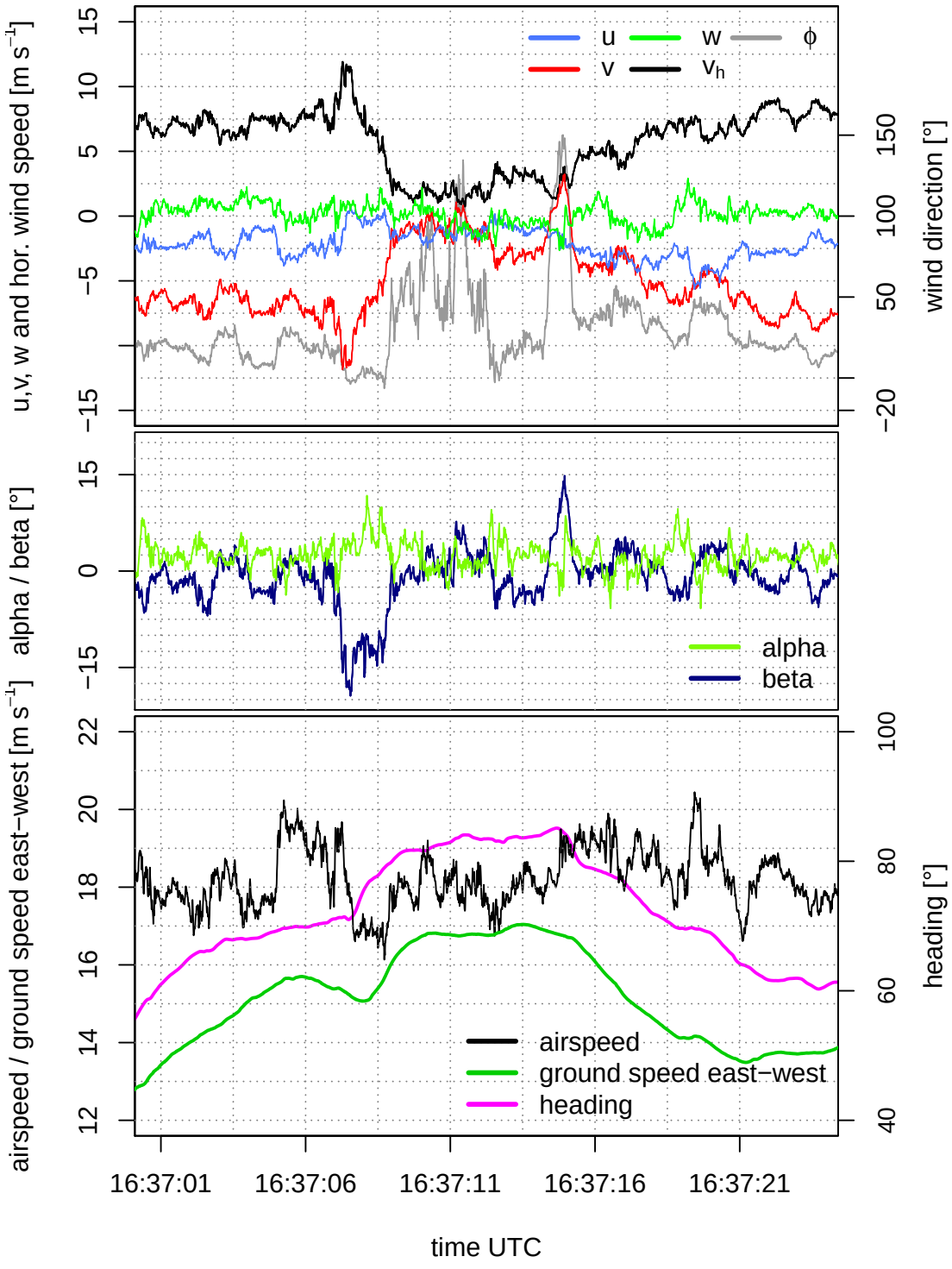

Figure 15. Time series of the wind vector components u, v and w, along with the horizontal windspeed v_h and wind direction ϕ (**top**), the flow angles onto the five-hole probe α and β (**middle**), the true airspeed $|\vec{u}_a|$, the heading Ψ and the ground speed in east-west direction $v_{g,\,ew}$ (**bottom**).

The middle subplot in Figure 15 shows the flow angles α and β in the aerodynamic coordinate system. The side-slip angle β and the angle of attack α reflect the situation and illustrate the importance of the calibration, since the flow angle onto the five-hole probe is strongly tilted during the transect of the wake and the calibration maps in Figure 4 show that especially for high α and β, the deviations are significant.

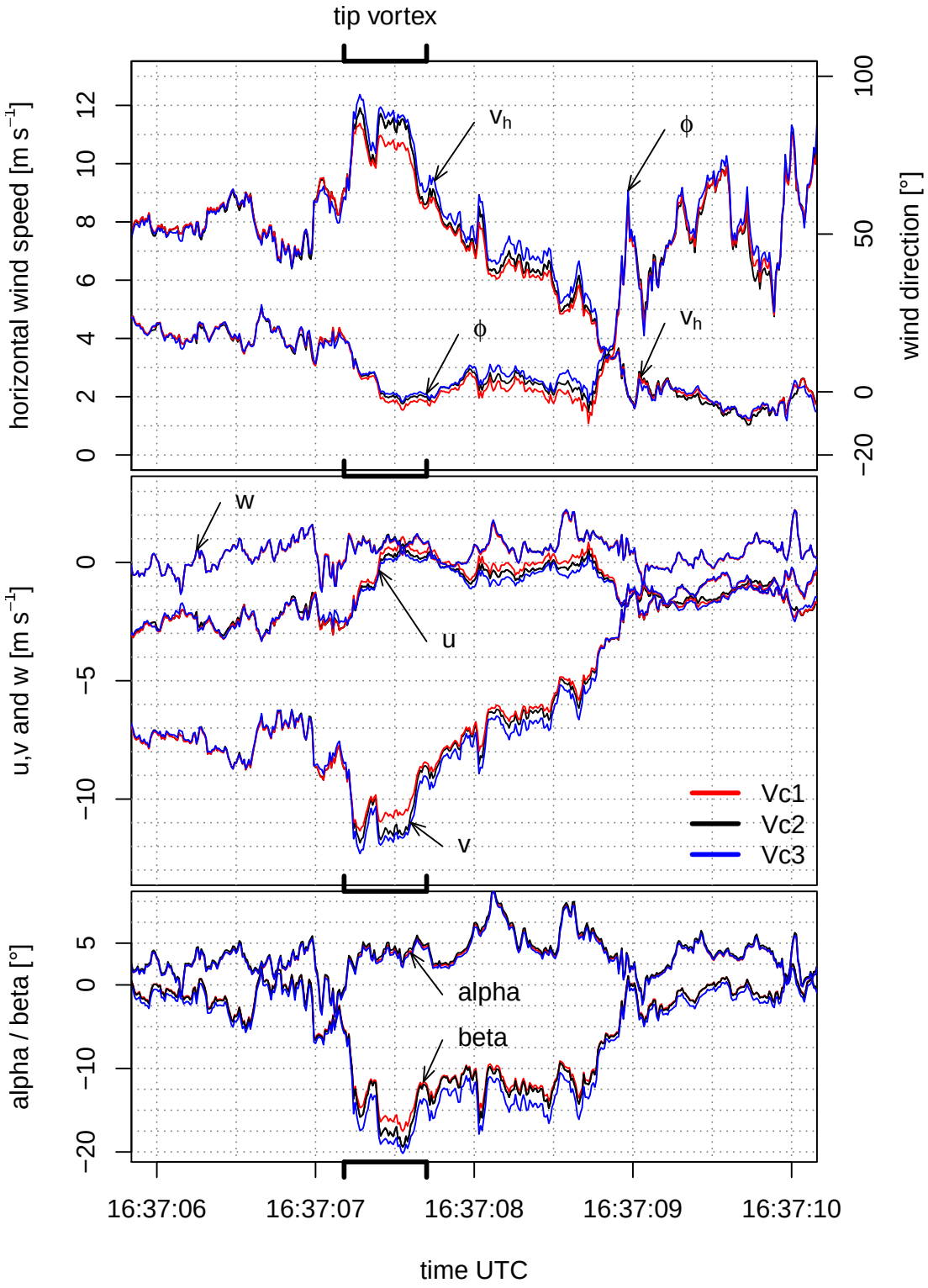

Figure 16. Fraction of the time series of the horizontal windspeed v_h and wind direction ϕ (**top**), the wind vector components u, v and w (**middle**) and the flow angles onto the five-hole probe α and β (**bottom**). All data is plotted for the three calibrations at v_{c1}, v_{c2} and v_{c3}. The position of the tip vortex is indicated.

The third subplot in Figure 15 gives insight in the motion of the UAS. Prior to entering the wake, turbulence causes MASC to accelerate, followed by a sudden drop when entering the wake. The autopilot increases the throttle and the airspeed increases again. This is also visible in the ground

speed $v_{g,\,ew}$ of the UAS. The heading during 9 m s^{-1} cross wind is between $\Psi = 60^\circ$ and 70°, although the flight path is oriented along 90°. When MASC enters the wake, the nose turns into the flight direction due to the windspeed deficit and after exiting the wake, the heading is gradually 60° again. The ground speed implies the acceleration and deceleration due to the change between the mean flow and the wake of the WEC and inherits the reaction of the autopilot. Since the autopilot's throttle reacts much more slowly compared to the changes in the wind field, an overshooting is noticeable. The intense motion of the UAS illustrates the importance of considering airspeed variations, since the attitude, airspeed, and ground speed are highly transient.

In Figure 16 a zoom into the transect through the first tip vortex is displayed and the location of the tip vortex is indicated. The deviations between the three time series in Figure 16, where the three polynomials are applied to the data and plotted together, are generally small where α and β are close to zero, and significant for higher absolute values of α and β. The curves of v_h lie up to 1 m s^{-1} apart from each other and during the passage through the vortex, v_{c1} has the highest offset and after the vortex, v_{c3} deviates more. For the vector components, v has the highest offset of up to 1 m s^{-1}, mostly caused by the deviations in β while u deviates not more than 0.4 m s^{-1}. The vertical wind w shows almost no deviation, since the magnitude is with a maximum of $\pm$2 m s^{-1}, small, and the mainly inherited quantity α with a maximum of 8°, moderate.

The horizontal windspeed v_h and the wind vector component v, show the expected behavior when crossing the core radius r_c of the vortex. The deviations are moderate, when deriving qualitative features of the flow. For vortex models, the size of the core radius and the magnitude of the circulation Γ are of major interest, e.g., to validate numerical models or to study the decaying processes of vortices. Here, the deviation of almost 1 m s^{-1} for the wind vector component v between the calibration at v_{c1} and v_{c3} is significant and considering the changes in airspeed would decrease the uncertainty significantly. The actual airspeed variations are smaller than the difference in airspeed between the applied polynomials, and therefore the real deviation is smaller than 1 m s^{-1} for the wind vector component v for this transect, but other transects exhibited larger flow angles and bigger changes in airspeed, also violating the domain of definition for α and β from -20° to 20°. To cope with that, the airspeed setting of the autopilot can be increased to fly faster through the wake, and the domain of the calibration can be extended. This illustrates again that a flexible airspeed setting is needed, and that airspeed variations must be considered to decrease the uncertainty of the measurement.

Figure 17 reveals, how sensitive the calibration of the dynamic pressure coefficient k_q is. During high angles of β, while crossing the tip vortex, the true airspeed measurement is more than 1 m s^{-1} apart between the curves with the polynomials at v_{c1} and v_{c3}. The calibration polynomials in Figure 5, where the significant difference for k_q between the calibration speeds are obvious, explain the deviations of the true airspeed. Besides the general offsets between the three time series during the transect of the tip vortex, also the shapes of the curves differ. Also, the time series of the wind vector components in Figure 16 exhibit slightly different shapes when compared to each other, since the true airspeed is inherited in them, causing a contribution to the deviations. Further analysis is conducted in the following chapter, where a method of interpolating the polynomials is suggested and an independent flow probe for the true airspeed measurement is recommended.

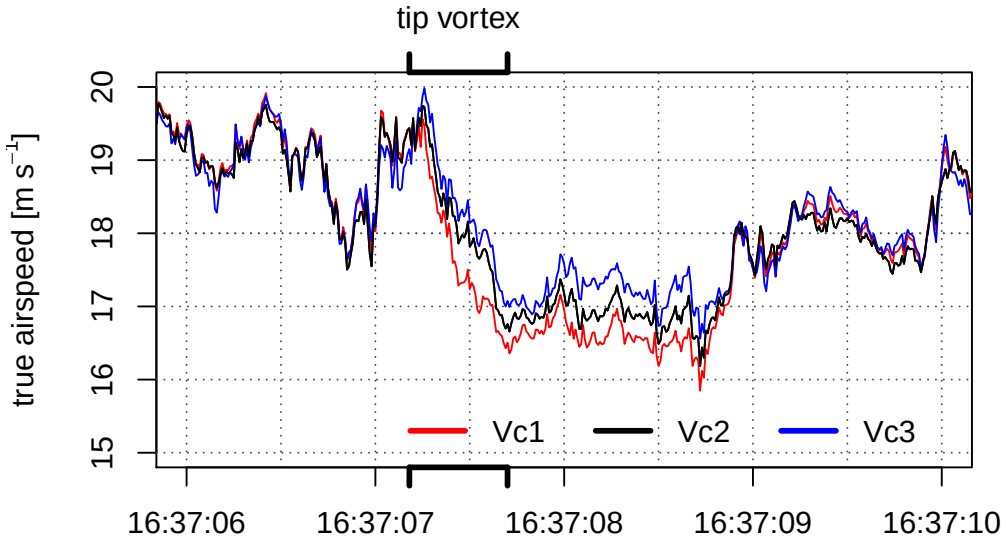

Figure 17. Fraction of the time series of the true airspeed $|\vec{u}_a|$. The data is plotted for the three calibrations at v_{c1}, v_{c2} and v_{c3}. The position of the tip vortex is indicated.

3.4. Interpolation of Polynomials and Independent True Airspeed Measurement for Improved Accuracy

Inspired by the study of Hartmann et al. [10], which mentions a linear proportionality for the conversion of pressure readings to flow angles in a certain range of Reynolds numbers for measurements with the Rosemount R858 FHP, the following procedure to improve the accuracy while gaining flexibility and keeping the calibration effort small is suggested. The polynomials $\vec{k}\,\vec{c'}_x$ from Equation (10) can be linearly interpolated with the Reynolds number between the three calibrations at v_{c1}, v_{c2} and v_{c3}. To demonstrate this, an interpolation between the polynomials at v_{c1} and v_{c3} onto the Reynolds number of $\mathrm{Re}_{v2} = 5538$ was made:

$$\vec{k}\,\vec{c'}_{x,\,ipol} = \vec{k}\,\vec{c'}_{x,\,v1} + \vec{k}\,\vec{c'}_{x,\,v3} - \vec{k}\,\vec{c'}_{x,\,v1}\left(\frac{\mathrm{Re}_{v2} - \mathrm{Re}_{v1}}{\mathrm{Re}_{v3} - \mathrm{Re}_{v1}}\right). \tag{19}$$

The deviation between $\vec{k}\,\vec{c'}_{x,\,ipol}$ and $\vec{k}\,\vec{c'}_{x,\,v2}$ can be analyzed directly from the wind-tunnel data. The polynomials, which are the best fit of the least squares method, calculated with the data of the calibration and Equation (9), can be used to recalculate α and β from the pressure readings. Figure 18 shows the error when recalculating the angles α and β with the correct polynomial, the interpolated polynomial, the polynomial at v_{c3} and the polynomial at v_{c1}. The largest error is plotted in red and the root mean squared error from all recalculated data points of the calibrations is plotted in black. The fitted polynomial itself produces already an error, which is, with the largest error of 0.5° for β and a root mean squared error of 0.1°, small. The interpolated polynomial has a slightly larger error than the directly calculated polynomial at v_{c2}, but the improvement, when compared to the error when using the polynomials at the wrong airspeed, is high. The highest error for the interpolated polynomial is 1° and if the polynomial at v_{c3} would be used, the highest error is more than 6°. The root mean squared error for the interpolated polynomial is, with 0.4°, higher than 0.1° for the actual polynomial of the calibration. For the polynomial at v_{c3}, the root mean squared error for β is 0.9°. Especially the maximum error can be reduced significantly with an interpolation between polynomials, but the root mean squared error is increased, indicating that the span of 13 m s^{-1} between $v_{c1} = 15$ m s^{-1} and $v_{c3} = 28$ m s^{-1} is too large for a reliable application of this procedure. For future applications, the span should be decreased, or the amount of calibrations increased.

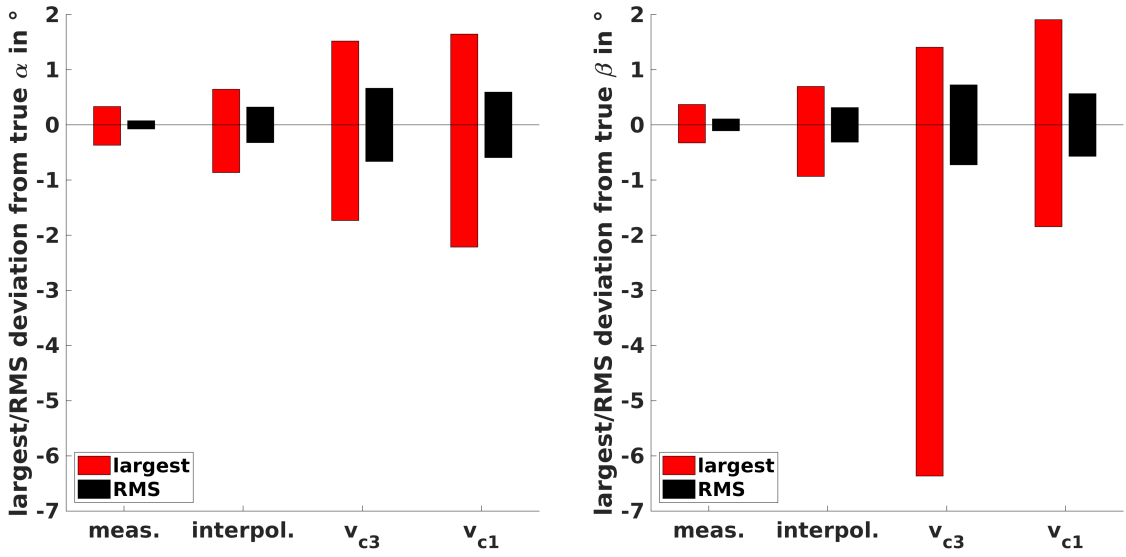

Figure 18. Deviations (largest deviation and root mean squared deviation) of the recalculation of α (**left**) and β (**right**) with the polynomial of the actual calibration at v_{c2} (meas.), the interpolated polynomial (interpol.) and the polynomials at v_{c3} and v_{c1}.

4. Outlook and Conclusions

The polynomials for α and β can be interpolated and the expected error, respectively the uncertainty, becomes smaller if the true airspeed of the flight experiment did not agree with the airspeed of the calibration. In practice this means that to perform an interpolation onto the Reynolds number, some sort of iteration is needed. Assuming, one calculates the mean true airspeed of one leg with an initial polynomial, calibrated at the nearest Reynolds number, requires at least one iteration step. After interpolating the polynomials with the initially estimated Reynolds number, the wind vector and the correction factors must be calculated again. Iterating only once, could be done in the future, if conditions similar to the ISOBAR flight, with moderate turbulence persist. The variation of the airspeed is relatively small and an offset of the mean true airspeed, calculated in the post-processing, could be accounted for, by interpolating the nearest two polynomials of the wind-tunnel calibration onto the actually persisting true airspeed of the flight leg. A single iteration allows for the correction of the desired, and not precisely set airspeed of the autopilot, which does not account for the density of the air. Furthermore, this procedure allows for the desired flexibility of the set airspeed and the mission can be adapted according to the prevailing conditions. Considering the COMPLEX flight, where the highest and lowest true airspeed was $|\vec{u}_a| = 28.59$ m s^{-1} and 20.14 m s^{-1} and the standard deviation measured on 915 m AMSL was $|\overline{\vec{u}_a}| = 24.21 \pm 1.14$ m s^{-1}, iterating once with the mean value of the whole leg can be reviewed. Applying an iteration on windows of a certain size may be applicable and a hyperbolism of this would be an iteration for every time step. The authors do not recommend that, since the sensitive calibration polynomials of k_q would be the support of the interpolation.

If the support of the interpolation, namely the Reynolds number of the flow over the probe's tip, is independently measured, the results can be improved. Standard pitot-tubes can measure the dynamic pressure in tilted airflow independently. High angles of attack onto the pitot tube influencing the measurement of the dynamic pressure, could be even corrected with the flow angles, measured by the five-hole probe. The range of airspeeds, respectively Reynolds numbers, with three polynomials between $v_{c1} = 15$ m s^{-1} and $v_{c3} = 28$ m s^{-1} is large and must be decreased or improved upon, by measuring e.g., 5 polynomials. For quantitative studies of turbulence and single features of the wind field of interest, the uncertainty, coming from the wind vector measurement with FHP, can be decreased by interpolation of the polynomials for α and β and by using a pitot tube to measure the true

airspeed independently. Many sensor systems used for 3D wind vector measurements with multi-hole probes already use pitot-tubes for the autopilot system and an integration of the presented algorithm is a rather simple task. Furthermore, the correction factor f_{tas} can be set to 1, opening further possibilities for the in-flight calibration, since one quantity in the system of equations, yielding the correction offsets, becomes distinct.

Not only the calibration of the five-hole probe influences the wind vector measurement, but also the INS, which measures the attitude and the GNSS-velocities of the UAS. Although the data of the attitude and the Kalman-filtered GNSS-velocities is given at 100 Hz, it is unknown, whether the resolution of the measurement influences the results. Following that, it is possible that the INS behaves differently, when flying through different turbulence regimes and that a correlation with turbulence influences the measurement of the wind vector. After implementing the interpolation of the polynomials for α and β and an independent measurement of the dynamic pressure, the influence of the measurement of the attitude and GNSS-velocities of the UAS must be analyzed. The precision, uncertainties, and influencing factors of commonly used INS for wind vector measurements with multi-hole probes on UAS is widely unknown.

It is concluded that variations of the true airspeed cannot be avoided, since non-zero vertical wind and varying horizontal wind causes the UAS to accelerate and decelerate. A proportionality with the momentum of the UAS, the aerodynamic drag, and the flight-mechanical properties persists. The commands of the autopilot balance the reaction of the UAS, causing variations of the true airspeed. Moreover, the setting of the cruising speed cannot be made precisely prior to the flight, since the density of the air is not considered by the airspeed measurement of the autopilot. Additionally, flexibility for the cruising speed of flight experiments is desired, to sample denser by flying with lower airspeed, or respond to high windspeeds or extreme turbulence, by increasing the airspeed. Three calibration polynomials at $v_{c1} = 15$ m s^{-1}, $v_{c2} = 22.5$ m s^{-1} and $v_{c3} = 28$ m s^{-1} were applied to three flights in different atmospheric conditions in order to investigate the influence on the calculation of mean values and turbulence statistics of horizontal flight legs and the influence on the high-resolution wind measurement during single events with large changes of the airspeed. The ISOBAR flight in a stably SBL with low turbulence was presented and compared to the COMPLEX flight in high turbulence over complex terrain. The mean values of windspeed and direction, calculated over one flight leg, are robust against changes of the true airspeed, widely independent of the intensity of turbulence, and generally small. The turbulent kinetic energy and the variances of the vertical wind component show relatively small deviations when applying the different polynomials, but the covariances and the integral length scales are sensitive. Airspeed variations of the UAS during measurements, and differences of the Reynolds number of the probe's tip between the calibration and the measurement, influence the results of the turbulence measurements randomly and it is not feasible to quantify the uncertainty, neither in general, nor for the individual statistical moments. Moreover, the uncertainties for flux calculations are high for turbulent conditions and for stably SBLs, where small fluxes distinguish important characteristics. The analysis of the WAKE flight showed the mechanism of the influence of the calibration of the probe, revealing that the calibration of the dynamic pressure coefficient k_q and the subsequent calculation of the true airspeed contributes strongly to the uncertainty. The deviations for a transect through the wake of a wind turbine and through a tip vortex were analyzed and if the size, orientation, and strength of a tip vortex is evaluated quantitatively, deviations must be expected, if the airspeed of the measurement varies strongly and does not match the airspeed of the calibration.

To decrease uncertainties, to keep the calibration effort proportionate, and to gain flexibility for missions in terms of cruising airspeed, the interpolation of polynomials for the angle of attack α and the side-slip β in combination with an independent true airspeed measurement with a pitot tube is recommended.

Author Contributions: A.R. carried out the measurements, performed the analysis, created the figures, interpreted the results and wrote the paper. J.A. contributed to the analysis of the wind-tunnel data and the text. S.J. contributed to the analysis of the flight experiments and the text. J.B. provided guidance and advice on all aspects of the study and contributed to the text.

Funding: Data from the COMPLEX flight was sampled for the project 'KonTest' (grant number 0325665), which was funded by the Federal Ministry for Economic Affairs and Energy. The ISOBAR flight was integral part of the Hailuoto-I campaign of the ISOBAR project, funded by the Research Council of Norway (RCN) under the FRINATEK scheme (project number: 251042/F20). The WAKE flight was conducted for the project HeliOW (grant number 0324121), which was funded by the Federal Ministry for Economic Affairs and Energy.

Acknowledgments: The authors wish to acknowledge the advice on the text and interpretation, given by Bram van Kesteren and Andreas Platis. We want to thank all colleagues who were participating in the three measurement campaigns for their help, gathering the data. The authors wish to acknowledge the helpful comments of the reviewers.

Conflicts of Interest: The authors declare no conflict of interest. The founding sponsors had no role in the design of the study; in the collection, analyses, or interpretation of data; in the writing of the manuscript, and in the decision to publish the results.

References

1. Wolfe, G.M.; Kawa, S.R.; Hanisco, T.F.; Hannun, R.A.; Newman, P.A.; Swanson, A.; Bailey, S.; Barrick, J.; Thornhill, K.L.; Diskin, G.; et al. The NASA Carbon Airborne Flux Experiment (CARAFE): Instrumentation and methodology. *Atmos. Meas. Tech.* **2018**, *11*, 1757–1776. [CrossRef]
2. Bange, J.; Esposito, M.; Lenschow, D.H.; Brown, P.R.; Dreiling, V.; Giez, A.; Mahrt, L.; Malinowski, S.P.; Rodi, A.R.; Shaw, R.A.; et al. Measurement of aircraft state and thermodynamic and dynamic variables. In *Airborne Measurements for Environmental Research: Methods and Instruments*; Wiley-VCH Verlag GmbH & Co., KGaA: Weinheim, Germany, 2013; pp. 7–75, doi:10.1002/9783527653218.ch2.
3. Lenschow, D.H. Aircraft Measurements in the Boundary Layer. In *Probing the Atmospheric Boundary Layer*; Lenschow, D.H., Ed.; American Meteorological Society: Boston, MA, USA, 1986; pp. 39–53.
4. Rautenberg, A.; Graf, M.; Wildmann, N.; Platis, A.; Bange, J. Reviewing Wind Measurement Approaches for Fixed-Wing Unmanned Aircraft. *Atmosphere* **2018**, *9*, 422. [CrossRef]
5. Witte, B.M.; Singler, R.F.; Bailey, S.C. Development of an Unmanned Aerial Vehicle for the Measurement of Turbulence in the Atmospheric Boundary Layer. *Atmosphere* **2017**, *8*, 195. [CrossRef]
6. Wildmann, N.; Hofsäß, M.; Weimer, F.; Joos, A.; Bange, J. MASC—A small Remotely Piloted Aircraft (RPA) for wind energy research. *Adv. Sci. Res.* **2014**, *11*, 55–61, doi:10.5194/asr-11-55-2014. [CrossRef]
7. Van den Kroonenberg, A.; Martin, T.; Buschmann, M.; Bange, J.; Vörsmann, P. Measuring the wind vector using the autonomous mini aerial vehicle M2AV. *J. Atmos. Ocean. Technol.* **2008**, *25*, 1969–1982. [CrossRef]
8. Bärfuss, K.; Pätzold, F.; Altstädter, B.; Kathe, E.; Nowak, S.; Bretschneider, L.; Bestmann, U.; Lampert, A. New Setup of the UAS ALADINA for Measuring Boundary Layer Properties, Atmospheric Particles and Solar Radiation. *Atmosphere* **2018**, *9*, 28. [CrossRef]
9. Schuyler, T.J.; Guzman, M.I. Unmanned Aerial Systems for Monitoring Trace Tropospheric Gases. *Atmosphere* **2017**, *8*, 206. [CrossRef]
10. Hartmann, J.; Gehrmann, M.; Kohnert, K.; Metzger, S.; Sachs, T. New calibration procedures for airborne turbulence measurements and accuracy of the methane fluxes during the AirMeth campaigns. *Atmos. Meas. Tech.* **2018**, *11*, 4567–4581. [CrossRef]
11. Metzger, S.; Junkermann, W.; Butterbach-Bahl, K.; Schmid, H.; Foken, T. Corrigendum to "Measuring the 3-D wind vector with a weight-shift microlight aircraft" published in Atmos. Meas. Tech., 4, 1421–1444, 2011. *Atmos. Meas. Tech.* **2011**, *4*, 1515–1539. [CrossRef]
12. Corsmeier, U.; Hankers, R.; Wieser, A. Airborne Turbulence Measurements in the Lower Troposphere Onboard the Research Aircraft Dornier 128-6, D-IBUF. *Meteorol. Z.* **2001**, *4*, 315–329. [CrossRef]
13. Williams, A.; Marcotte, D. Wind measurements on a maneuvering twin-engine turboprop aircraft accounting for flow distortion. *J. Atmos. Ocean. Technol.* **2000**, *17*, 795–810. [CrossRef]
14. Khelif, D.; Burns, S.; Friehe, C. Improved wind measurements on research aircraft. *J. Atmos. Ocean. Technol.* **1999**, *16*, 860–875. [CrossRef]
15. Brown, E.N.; Friehe, C.A.; Lenschow, D.H. The Use of Pressure Fluctuations on the Nose of an Aircraft for Measuring Air Motion. *J. Clim. Appl. Meteorol.* **1983**, *22*, 171–180. [CrossRef]

16. Lenschow, D.H. *Probing the Atmospheric Boundary Layer*; American Meteorological Society: Boston, MA, USA, 1986; Volume 270.
17. Drüe, C.; Heinemann, G. A review and practical guide to in-flight calibration for aircraft turbulence sensors. *J. Atmos. Ocean. Technol.* **2013**, *30*, 2820–2837. [CrossRef]
18. Mallaun, C.; Giez, A.; Baumann, R. Calibration of 3-D wind measurements on a single-engine research aircraft. *Atmos. Meas. Tech.* **2015**, *8*, 3177–3196. [CrossRef]
19. Vellinga, O.S.; Dobosy, R.J.; Dumas, E.J.; Gioli, B.; Elbers, J.A.; Hutjes, R.W. Calibration and quality assurance of flux observations from a small research aircraft. *J. Atmos. Ocean. Technol.* **2013**, *30*, 161–181. [CrossRef]
20. Leise, J.; Masters, J.M. *Wind Measurement From Aircraft*; U.S. Department of Commerce, National Oceanic and Atmospheric Administration, Aircraft Operation Center: Charleston, SC, USA, 1993.
21. Bögel, W.; Baumann, R. Test and calibration of the DLR Falcon wind measuring system by maneuvers. *J. Atmos. Ocean. Technol.* **1991**, *8*, 5–18. [CrossRef]
22. Dominy, R.; Hodson, H. An investigation of factors influencing the calibration of five-hole probes for three-dimensional flow measurements. *J. Turbomach.* **1993**, *115*, 513–519. [CrossRef]
23. Lee, S.W.; Jun, S.B. Reynolds number effects on the non-nulling calibration of a cone-type five-hole probe for turbomachinery applications. *J. Mech. Sci. Technol.* **2005**, *19*, 1632–1648. [CrossRef]
24. Wildmann, N.; Bernard, S.; Bange, J. Measuring the local wind field at an escarpment using small remotely-piloted aircraft. *Renew. Energy* **2017**, *103*, 613–619. [CrossRef]
25. Cormier, M.; Caboni, M.; Lutz, T.; Boorsma, K.; Krämer, E. Numerical analysis of unsteady aerodynamics of floating offshore wind turbines. *J. Phys. Conf. Ser.* **2018**, *1037*, 072048. [CrossRef]
26. Sanderse, B.; Van der Pijl, S.; Koren, B. Review of computational fluid dynamics for wind turbine wake aerodynamics. *Wind Energy* **2011**, *14*, 799–819. [CrossRef]
27. Wu, Y.T.; Porté-Agel, F. Large-eddy simulation of wind-turbine wakes: Evaluation of turbine parametrisations. *Bound.-Layer Meteorol.* **2011**, *138*, 345–366. [CrossRef]
28. Bastankhah, M.; Porté-Agel, F. A new analytical model for wind-turbine wakes. *Renew. Energy* **2014**, *70*, 116–123. [CrossRef]
29. Vermeer, L.; Sørensen, J.N.; Crespo, A. Wind turbine wake aerodynamics. *Prog. Aerosp. Sci.* **2003**, *39*, 467–510. [CrossRef]
30. Rodi, A.R.; Leon, D. Correction of static pressure on a research aircraft in accelerated flight using differential pressure measurements. *Atmos. Meas. Tech.* **2012**, *5*, 2569–2579. [CrossRef]
31. Martin, S.; Bange, J. The Influence of Aircraft Speed Variations on Sensible Heat-Flux Measurements by Different Airborne Systems. *Bound.-Layer Meteorol.* **2014**, *150*, 153–166, doi:10.1007/s10546-013-9853-7. [CrossRef]
32. Braam, M.; Beyrich, F.; Bange, J.; Platis, A.; Martin, S.; Maronga, B.; Moene, A.F. On the Discrepancy in Simultaneous Observations of the Structure Parameter of Temperature Using Scintillometers and Unmanned Aircraft. *Bound.-Layer Meteorol.* **2016**, *158*, 257–283, doi:10.1007/s10546-015-0086-9. [CrossRef]
33. Kral, S.T.; Reuder, J.; Vihma, T.; Suomi, I.; O'Connor, E.; Kouznetsov, R.; Wrenger, B.; Rautenberg, A.; Urbancic, G.; Jonassen, M.O.; et al. Innovative Strategies for Observations in the Arctic Atmospheric Boundary Layer (ISOBAR)—The Hailuoto 2017 Campaign. *Atmosphere* **2018**, *9*, 268. [CrossRef]
34. Boiffier, J.L. *The Dynamics of Flight*; Wiley: Chichester, UK, 1998; p. 353.
35. Bange, J. *Airborne Measurement of Turbulent Energy Exchange Between the Earth Surface and the Atmosphere*; Sierke Verlag: Göttingen, Germany, 2009; 174p, ISBN 978-3-86844-221-2.
36. Lenschow, D. Airplane measurements of planetary boundary layer structure. *J. Appl. Meteorol.* **1970**, *9*, 874–884. [CrossRef]
37. Black, P.G.; D'Asaro, E.A.; Drennan, W.M.; French, J.R.; Niiler, P.P.; Sanford, T.B.; Terrill, E.J.; Walsh, E.J.; Zhang, J.A. Air–sea exchange in hurricanes: Synthesis of observations from the coupled boundary layer air–sea transfer experiment. *Bull. Am. Meteorol. Soc.* **2007**, *88*, 357–374. [CrossRef]
38. Hall, B.F.; Povey, T. The Oxford Probe: An open access five-hole probe for aerodynamic measurements. *Meas. Sci. Technol.* **2017**, *28*, 035004. [CrossRef]
39. Wildmann, N.; Ravi, S.; Bange, J. Towards higher accuracy and better frequency response with standard multi-hole probes in turbulence measurement with remotely piloted aircraft (RPA). *Atmos. Meas. Tech.* **2014**, *7*, 1027–1041, doi:10.5194/amt-7-1027-2014. [CrossRef]

40. Treaster, A.L.; Yocum, A.M. *The Calibration and Application of Five-Hole Probes*; Technical Report; Pennsylvania State Univ University Park Applied Research Lab: State College, PA, USA, 1978.
41. Pope, S.B. *Turbulent Flows*; Cambridge University Press: Cambridge, UK, 2001.
42. Wildmann, N.; Mauz, M.; Bange, J. Two fast temperature sensors for probing of the atmospheric boundary layer using small remotely piloted aircraft (RPA). *Atmos. Meas. Tech.* **2013**, *6*, 2101–2113, doi:10.5194/amt-6-2101-2013. [CrossRef]
43. Platis, A.; Altstädter, B.; Wehner, B.; Wildmann, N.; Lampert, A.; Hermann, M.; Birmili, W.; Bange, J. An Observational Case Study on the Influence of Atmospheric Boundary-Layer Dynamics on New Particle Formation. *Bound.-Layer Meteorol.* **2016**, *158*, 67–92. [CrossRef]
44. Van den Kroonenberg, A.; Martin, S.; Beyrich, F.; Bange, J. Spatially-averaged temperature structure parameter over a heterogeneous surface measured by an unmanned aerial vehicle. *Bound.-Layer Meteorol.* **2012**, *142*, 55–77. [CrossRef]
45. Rotta, J. *Turbulente Strömungen: Eine Einführung in Die Theorie und ihre Anwendung (Turbulent Flows: An Introduction to the Theory and Its Application)*; Teubner: Stuttgart, Germany, 1972.
46. Kaimal, J.C.; Finnigan, J.J. *Atmospheric Boundary Layer Flows: Their Structure And Measurement*; Oxford University Press: Oxford, UK, 1994.
47. Lenschow, D.H.; Stankov, B.B. Length Scales in the Convective Boundary Layer. *J. Atmos. Sci.* **1986**, *43*, 1198–1209. [CrossRef]
48. Brown, E.N. *Position Error Calibration of a Pressure Survey Aircraft Using a Trailing Cone*; Tech. Rep. NCAR/TN-313+STR; National Center for Atmospheric Research: Boulder, CO, USA, 1988. doi:10.5065/D6X34VF1.
49. Stull, R.B. *An Introduction to Boundary Layer Meteorology*; Springer Science & Business Media: New York, NY, USA, 2012; Volume 13.
50. Lenschow, D.H.; Mann, J.; Kristensen, L. How Long Is Long Enough When Measuring Fluxes and Other Turbulence Statistics. *J. Atmos. Ocean. Technol.* **1994**, *11*, 661–673. [CrossRef]
51. Mann, J.; Lenschow, D.H. Errors in airborne flux measurements. *J. Geophys. Res. Atmos.* **1994**, *99*, 14519–14526. [CrossRef]
52. Knaus, H.; Rautenberg, A.; Bange, J. Model comparison of two different non-hydrostatic formulations for the Navier-Stokes equations simulating wind flow in complex terrain. *J. Wind Eng. Ind. Aerodyn.* **2017**, *169*, 290–307. [CrossRef]
53. Schulz, C.; Hofsäß, M.; Anger, J.; Rautenberg, A.; Lutz, T.; Cheng, P.W.; Bange, J. Comparison of Different Measurement Techniques and a CFD Simulation in Complex Terrain. *J. Phys. Conf. Ser.* **2016**, *753*, 082017. [CrossRef]
54. Ahmad, N.N.; Proctor, F. Review of idealized aircraft wake vortex models. In Proceedings of the 52nd Aerospace Sciences Meeting, National Harbor, MD, USA, 13–17 January 2014; p. 0927.
55. Jeong, J.; Hussain, F. On the identification of a vortex. *J. Fluid Mech.* **1995**, *285*, 69–94. [CrossRef]

A.3 The Multi-Purpose Airborne Sensor Carrier MASC-3 for Wind and Turbulence Measurements in the Atmospheric Boundary Layer - Publication III

sensors

MDPI

Article

The Multi-Purpose Airborne Sensor Carrier MASC-3 for Wind and Turbulence Measurements in the Atmospheric Boundary Layer

Alexander Rautenberg [1,*], Martin Schön [1], Kjell zum Berge [1], Moritz Mauz [1], Patrick Manz [1], Andreas Platis [1], Bram van Kesteren [1], Irene Suomi [2], Stephan T. Kral [3] and Jens Bange [1]

1 Center for Applied Geoscience, Eberhard-Karls-Universität Tübingen, Hölderlinstr. 12, 72074 Tübingen, Germany; martin.schoen@uni-tuebingen.de (M.S.); kjell.zum-berge@uni-tuebingen.de (K.z.B.); moritz.mauz@uni-tuebingen.de (M.M.); manzp@gmx.de (P.M.); andreas.platis@uni-tuebingen.de (A.P.); bram.vankesteren@uni-tuebingen.de (B.v.K.); jens.bange@uni-tuebingen.de (J.B.)

2 Finnish Meteorological Institute, P.O. Box 503, 00101 Helsinki, Finland; irene.suomi@fmi.fi

3 Geophysical Institute and Bjerknes Centre for Climate Research, University of Bergen, Postbox 7803, 5020 Bergen, Norway; stephan.kral@uib.no

* Correspondence: alexander.rautenberg@uni-tuebingen.de; Tel.: +49-7071-29-74339

Received: 18 March 2019; Accepted: 13 May 2019; Published: 17 May 2019

Abstract: For atmospheric boundary-layer (ABL) studies, unmanned aircraft systems (UAS) can provide new information in addition to traditional in-situ measurements, or by ground- or satellite-based remote sensing techniques. The ability of fixed-wing UAS to transect the ABL in short time supplement ground-based measurements and the ability to extent the data horizontally and vertically allows manifold investigations. Thus, the measurements can provide many new possibilities for investigating the ABL. This study presents the new mark of the Multi-Purpose Airborne Sensor Carrier (MASC-3) for wind and turbulence measurements and describes the subsystems designed to improve the wind measurement, to gain endurance and to allow operations under an enlarged range of environmental conditions. The airframe, the capabilities of the autopilot Pixhawk 2.1, the sensor system and the data acquisition software, as well as the post-processing software, provide the basis for flight experiments and are described in detail. Two flights in a stable boundary-layer and a close comparison to a measurement tower and a Sodar system depict the accuracy of the wind speed and direction measurements, as well as the turbulence measurements. Mean values, variances, covariance, turbulent kinetic energy and the integral length scale agree well with measurements from a meteorological measurement tower. MASC-3 performs valuable measurements of stable boundary layers with high temporal resolution and supplements the measurements of meteorological towers and sodar systems.

Keywords: fixed-wing unmanned aircraft; turbulence measurement; 3D wind vector measurement; stable boundary layer; comparison with measurement tower; unmanned aircraft system (UAS); remotely piloted aircraft (RPA)

1. Introduction

For atmospheric boundary-layer (ABL) studies, unmanned aircraft systems (UAS) can provide new information in addition to traditional in-situ measurements or ground- and satellite-based remote sensing techniques. Recent developments of UAS and high-performance high-resolution in-situ sensors allow the observation of processes at different levels within the ABL, which so far can only be accomplished by tall meteorological towers or to some extent, although with limited spatial and temporal resolution, by ground based remote sensing systems. The ability of fixed-wing UAS to

sample data of the ABL along the flight path supplements ground based measurements and the ability to extend the data horizontally and vertically allows manifold investigations. Representative samples of the ABL can be gathered with a high temporal resolution, or area representative evaluations without the need for multiple measurement platforms. Turbulence along a straight horizontal flight path is not precisely a spatial snapshot, nor a temporally averaged snapshot, but a mixture of both, which can be labeled as quasi-spatial snapshot. The use of such data presumes the following assumptions, pros and cons. The most important compendium is Taylor's hypothesis of frozen turbulence [1,2] which must be questioned for low frequencies (or low wavenumber) of the spectrum of atmospheric turbulence [3]. Even the inertial subrange of the spectrum according to Reference [4] may not follow Taylor's hypothesis of frozen turbulence and if eddies of different sizes travel at different velocities, the turbulent wave number spectrum cannot be simply interpreted as the frequency spectrum [5,6]. With aircraft measurements, Taylor's hypothesis is rather valid, since a long distance is covered within a short time period [7,8]. The downside of transecting the turbulence regime is the shift of the spectrum towards higher frequencies and the need of sensors to be accordingly faster than those of stationary measurement systems. A moving platform in general may be technically more challenging than a stationary measurement system, since the wind vector must be transformed from a moving into an earth bound coordinate system. On the other hand, turbulence measurements along a straight horizontal flight path sampled with a fixed-wing UAS, compared to turbulence measured at a stationary point, enables a faster measurement of the quantity, since the same amount of data can be sampled in shorter time. The UAS moves with its airspeed through the ABL and the measurement at a fixed point samples the air which is advected with the mean flow. This correlation can be beneficial for example, for measurements of transition phases of the ABL, where the state of the ABL changes quickly. The need of statistical significance when calculating turbulence statistics [9] implements further challenges for UAS, because the flight distances along flight paths may be limited due to technical restrictions or legal issues. Generally, heterogeneity of the surface and inhomogeneous footprints of moving and stationary systems also implement difficulties and cause discrepancies for a direct comparison of the two systems. This study aims to validate the measurements of the new mark of the Multi-Purpose Airborne Sensor Carrier (MASC-3) by closely comparing them with measurements from a meteorological tower and subsequently being able to fuse both systems for investigations of stable boundary layers (SBL).

Like micro-meteorological stations, remotely piloted aircraft (RPA) can be equipped with fast and accurate sensors in order to measure atmospheric turbulence. The airframe of the vehicle is referred to as RPA and if the sensor systems and ground control systems are also referred to, the terminology is UAS. UAS can be equipped with similar measurement systems than manned aircraft but are limited by the size of the UAS. Since the beginning of the millennium, the rapid progress in micro-electronics and component miniaturization allowed for a fast development of airframes, autopilots and meteorological sensors for research in the ABL. One of the first low-cost attempts was the remotely-controlled, but not auto-piloted system, KALI, which performed more than 150 flights in Nepal and Bolivia to investigate thermally driven flows modified by orography [10,11]. The following years showed rapidly increasing activities by various research groups, making their sensors and instrumentation airborne within a reasonable budget. Most of those earlier systems are based on fixed-wing airframes as for example, M2AV [12], SUMO [13,14], Smartsonde [15,16], Manta [17], MASC [18], ALADINA [19,20], Pilatus [21] and BLUECAT5 [22]. UAS were used for research in the field of atmospheric physics and chemistry [23–26], boundary layer meteorology [17,27–38], and more recently also to wind-energy meteorology [39–41]. The capabilities of UAS for meteorological sampling are broad. The UAS designs range from a more accurate and diverse—but larger—sensor payload, down to small aircraft that can be operated with minimal logistical overhead. Since 2010, the use of rotary-wing multi-copter systems for atmospheric research has increased [38,42–44]. With their ability to hover and to slowly ascend and descend vertically, they are the preferred choice for many measurement tasks related to boundary- and surface-layer profiling, but are limited when measuring turbulence.

Measuring the wind speed and direction is a fundamental and elaborate requirement for understanding the processes of the ABL. The common method to measure the turbulent 3D wind vector from research aircraft is a multi-hole probe in combination with an inertial navigation system (INS). By calibration, the pressure readings are used to estimate the airspeed vector of the UAS and with the INS data, multiple coordinate transformations yield the 3D wind vector [45]. This technique originates from manned research aircraft [46] and was adopted by UAS [22,47]. Simplified algorithms to measure the temporally averaged horizontal wind speed and direction such as the "no-flow-sensor" or the "pitot-tube" algorithm, also exist and were compared to the direct 3D wind vector measurement using a five-hole probe by Reference [48].

UAS have the potential to provide new information about the SBL, when applied together with traditional in-situ measurement techniques. Parametrizations of the processes in numerical weather prediction and climate models, yet only apply for stationary and homogeneous surface conditions. The parametrization schemes, for example, the Monin–Obukhov similarity theory (MOST) are known for their shortcomings in characterizing the SBL [49]. Continuous turbulence as a quasi-stationary state may break down and become intermittent. Non-local features such as the stability at higher levels and gravity waves become important, the Coriolis effect and inertial oscillations influence the structure of the SBL and Low Level Jets (LLJ) can develop and generate turbulence by the vertical wind shear [50–54]. For weakly stable boundary layers, transition phases and very stable boundary layers [55] UAS can supplement the limited spatial or temporal coverage of ground-based measurements. On the other hand, SBL conditions also impose challenges for both stationary measurement systems and UAS, since weak turbulent fluxes are difficult to measure and require a high accuracy of the measurement system. Precise and fast measurements of the turbulent 3D wind vector from UAS in combination with meteorological towers and ground-based remote sensing techniques yield new possibilities [56].

The main aim of this study is to validate the turbulent 3D wind vector measurement with MASC-3. To do so, mean values, statistical moments of second order, integral length scales and a spectral analysis can be performed. A comparison to established measurement systems and theory leads towards validation. Firstly, a close comparison with the measurements of a meteorological tower are presented and secondly the data of the tower and the phased array 3D wind Sodar are plotted together with profiles of MASC-3 in a SBL. MASC-3 aims to improve the wind measurement, to gain endurance, to allow operations under an enlarged range of environmental conditions and to enable easy implementation of further sensors by the following measures. The influence on the 3D wind vector measuremnt by the flow field around the aircraft [57] is an important criterion and therefore the new airframe of MASC-3 features a pusher engine in the very back (behind the tail unit) of the UAS as well as a forward-spaced and streamlined sensor hat, where a five-hole probe is mounted (see Section 2.1). Also the flight guidance and the autopilot are of major importance for the 3D wind vector measurement, since the attitude of the UAS, as well as the vehicle velocity, are directly inherited in the calculations. A steady and precise flight of MASC-3 is implemented by the Pixhawk 2.1 "Cube" autopilot (see Section 2.2). The fuselage and the installed sensor hat allow for different payloads, making MASC-3 versatile for many scenarios. The standard payload is described in Section 2.3 and includes an inertial navigation system (INS) Ellipse2-N from sbg-systems [58], a five-hole probe manufactured by the Institute of Fluid Mechanics at the Technische Universität Braunschweig, Germany [59], a fine wire platinum resistance thermometer (FWPRT) developed by Reference [60] and further temperature, surface temperature and humidity sensors. The software architecture is described in Section 2.4 and runs on a Raspberry Pi 3, which allows an easy implementation of future sensors. The in-house developed post-processing software MADA (see Section 2.5) provides a standardized quality control of the gathered data within min after the flight experiment and enables comprehensive quick-looks of mean values and turbulence statistics of the flight experiment.

The measurements of this study were collected during an intensive measurement campaign—"Hailuoto-II"—of the project called Innovative Strategies for Observations in the Arctic

Atmospheric Boundary Layer (ISOBAR). The campaign took place over sea ice at the western shore of Hailuoto island in the northern Bothnian Bay on the coast of Finland in February 2018. The main motivation for the ISOBAR project is to develop and apply a new and innovative observation strategy for the stably stratified boundary layer that is based on meteorological UAS, ground-based in-situ and remote-sensing profiling systems [38]. Two flight experiments were dedicated to closely comparing the MASC-3 measurements with the meteorological tower measurements and were conducted in the evening of the 10 February 2018 over the completely frozen bay area of Hailuoto. The methods for the comparison are described in Section 3.2 and are based on a comparative duration of the time series for the stationary and the moving measurement systems, which correspond to the individual fetch of both systems. Section 4.1 compares the measurements by means of time series analysis for mean values of wind speed and direction, variances, turbulent kinetic energy, covariances and integral length scales of the 3D wind vector measurement. The analysis of a fast evolving SBL during the second flight is given in Section 4.2, where the height profiles performed with MASC-3 are supplemented with the tower and Sodar measurements on the ground, illuminating the vast potential of turbulence measurements with MASC-3 in SBL.

2. Multi-Purpose Airborne Sensor Carrier—MASC-3

A detailed description of the Multi-Purpose Airborne Sensor Carrier (MASC-3) is presented. The design criteria and capabilities of the airframe are given in Section 2.1, followed by a description of the autopilot system Pixhawk 2.1 "Cube" in Section 2.2. The airframe and the autopilot system, as well as the embedded sensor system of MASC-3, were completely reworked compared to the previous version of MASC. The sketch in Figure 1 provides an overview of the new setup. The core of the data acquisition unit is a Raspberry Pi 3, allowing the use of various interfaces to sensor applications, telemetry modules and on-board data processing algorithms. We describe the sensor system in Section 2.3, the data acquisition procedure in Section 2.4 and the post-processing procedure in Section 2.5.

2.1. Airframe Design

MASC-3 is a further development of the environment-physics group at the Center for Applied Geo-Science (ZAG), University of Tübingen, Germany and is based on the previous UAS, which was described, for example, in Reference [18,48]. The overall goals for the new design were increasing the accuracy of the wind measurement, gaining endurance, having more flexibility in implementing further sensors in future applications and allowing operations under an enlarged range of environmental conditions. Figure 1 shows the airframe with its sensor nose in the very front of the fuselage. The positioning was chosen in order to be as far away as possible from potential influences on the measurement. Figure 1 shows the sensor system with the five-hole probe, temperature and humidity sensors. Moreover, the engine is positioned in the back, behind the V-tail of the UAV. Due to the significantly increased distance between the measurement system in the nose and the engine position (see Figure 1), compared to the previous version of MASC, potential influences on the measurements are minimized.

The prop wash, vibrations and the magnetic field of the engine are further away from the sensor system. The power unit consists of a highly efficient electrical pusher setup with a gear unit in order to use a large diameter for the propellers, while keeping the engine speed low. The aerodynamic efficiency is high for cruising speeds around 20 ms^{-1}, since a propeller requires large diameters at rather slow drive rates, resulting, with Li-Ion battery packs, in a highly improved overall efficiency of the drive train, compared to the previous version of MASC. Besides, the point of application of the thrust vector has a much smaller lever arm onto the center of gravity compared to the previous MASC with a pusher engine above and behind the main wings, improving the stability of the flight during acceleration and deceleration of the engine. Due to non-zero vertical wind velocity and changes in

the horizontal wind speed on turbulent scales, or other motions, for example, thermals or up- and down-drafts due to orography, the aircraft reacts with acceleration or deceleration relative to the air.

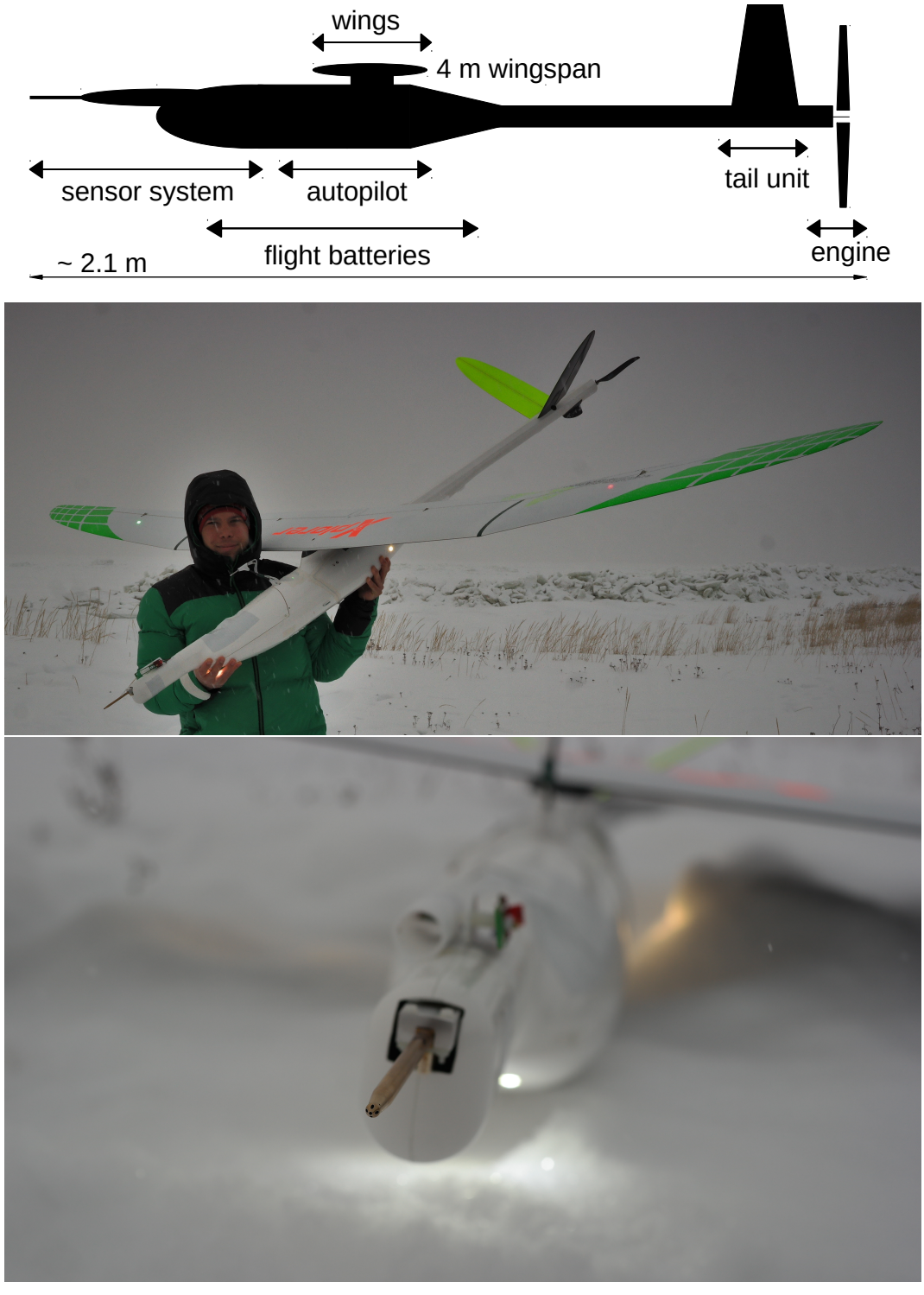

Figure 1. Multi-Purpose Airborne Sensor Carrier (MASC-3) sketch (**top**) and pictures of the airframe with the sensor system (**middle**) and five-hole probe (**bottom**).

To fulfill the requirements of constant altitude, constant flight direction and constant airspeed, the autopilot system of the UAS controls the angle of attack and the throttle. The reactions of the UAS on changes in the wind field, correlate and are proportional to the momentum and the aerodynamic

drag of the UAS. Also, the individual flight mechanical behaviour of the UAS and its ability to be susceptible to interaction with turbulence are important. Therefore, the aerodynamic drag must be low and the flight mechanical performance of the wing design with a high lift/drag ratio are very important issues for the precision of the wind and turbulence measurement with five-hole probes [45]. MASC-3 meets these requirements superior to the previous version, since the wings and tail are from an aircraft (XPLORER 3 by NAN Models) of international championships in F3J and F5J glider competitions. The wingspan is 4 m. The streamlined fuselage design offers space for versatile configurations and with the broad range of possible wing loads, the total weight can range from 3.5 kg with a standard measurement setup and small battery capacity, up to ≈8 kg. The maximum flight duration with 18 ms^{-1} cruising airspeed was proven to be 2 h and is estimated to be 3 h and more. The wings, tail and fuselage are manufactured with fibreglass and carbon fibre composite materials, providing high durability and a light weight construction. With the thermodynamic management of the electrical components, MASC-3 can operate under polar conditions as well as in hot environments. Take-off is performed with a bungee or a winch, if for example, cold temperatures below ≈−10 °C cause the rubber bungee to fail. Trained pilots can land MASC-3 on a strip of less than 10 × 4 m, since large air brakes allow fast descents and precise steering during the approach. High manoeuvrability and a broad range of cruising airspeeds between 14 ms^{-1} and more than 30 ms^{-1} allow sampling with high resolution as well as operations in high wind speeds and extreme turbulence.

A new feature of MASC-3 is that it can be equipped with position and strobe lights . Figure 1 shows the lights following the conventions of manned aircraft, allowing take off and landing during night time. As the lighting of MASC-3 fulfills the requirements of the SERA 923/2012 regulation, (see for more details Reference [61]) the aircraft can obtain special permission of the local civil flight authorities for UAS operations during night time and beyond visual line of sight (BVLOS).

Since reduced visibility is challenging for the pilot, the flight guidance with the autopilot system PixHawk 2.1 (see also Section 2.2) allows automatic mode just after release from the take-off rope and automatic approach for manual landing procedures or even entirely autonomous landing, as shown in Figure 2.

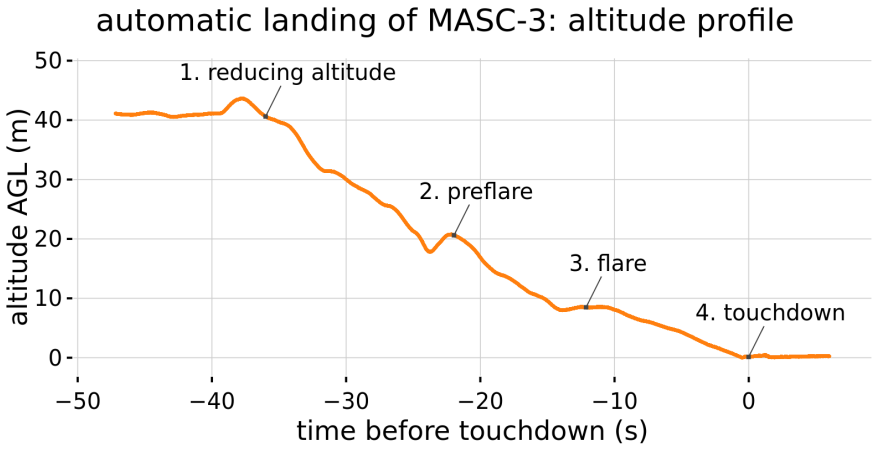

Figure 2. MASC-3 altitude profile during automatic landing procedure.

2.2. Flight Guidance, Autopilot System and Flight Patterns

When measuring wind and turbulence with a five-hole probe, the UAS needs to be able to repeat a flight pattern over the course of multiple flights to increase the statistical validity of the captured data and to allow for comparisons between different measurement flights. These requirements are met by the autopilot system. Common UAS autopilot systems use an INS (Inertial Navigation System) consisting of one or multiple triple-axis accelerometers, gyroscopes and magnetometers (IMU) for attitude and heading control as well as a GNSS (global navigation satellite system) reciever (GPS,

GLONASS, Beidou and/or Galileo) to measure ground speed and location. Some systems may also include a laser altimeter to measure altitude above ground or infrared receivers for communication with ground-based beacons for precision landing. The autopilot system of MASC-3 consists of a Pixhawk 2.1 "Cube" autopilot using a Here+ RTK GPS and magnetometer for position, velocity and heading and a mrobotics MS5525 digital airspeed sensor connected to a pitot-static tube for airspeed measurement. The heated IMU of the Cube allows MASC-3 to operate reliably in very low temperatures and the RTK GPS improves location accuracy over standard GNSS solutions. The Cube is running the open-source Ardupilot autopilot firmware and flight patterns can be programmed before take-off or wirelessly during the flight. Figure 3 shows the flight patterns used for MASC-3 and performed during the ISOBAR campaign Hailuoto-II. The "Rectangle" pattern is the most common one with MASC-3, performing long up- and downwind measurement legs. A rectangle (also called racetrack) is repeated several times at one altitude and one measurement flight normally consists of several racetracks at different altitudes. The up- and downwind portions of one racetrack are called measurement legs. The track marked as Flight #10/#11 shows the flight path of the upwind legs of a rectangle pattern that is used for the comparison in Section 4. The length of the flight legs is $\approx$1100 m and the northern edge (next to the measurement tower) is the starting point for the southward orientation of the flight legs. The locations of the meteorological tower and the Sodar are also marked in Figure 3 and are used to compared the data with the MASC-3 measurements. The "Circle" pattern is used for profiling with constant vertical ascent rate. With a large enough radius and consequently a low bank angle of the UAS, this pattern can be used for continuous profiles of wind speed, direction, temperature and other quantities. For complex terrain and inhomogeneous conditions, the "Kite" pattern is advantageous over the standard rectangle pattern due to its lack of lateral displacement of the up- and downwind leg. However, while flying Kite patterns, the UAV spends more time in turns, and subsequently, the time spent flying measurement legs per flight is lower than with the rectangle pattern.

The Ardupilot firmware running on the Cube features automatic landings. Figure 2 shows the automatic landing process of MASC-3, which was continuously performed for nocturnal operations during the Hailuoto-II campaign. While approaching the landing spot, MASC-3 engages its flaps and reduces its altitude to 20 m above ground level (AGL). It then executes a preflare by reducing throttle and increasing the pitch angle to reduce its airspeed to 16 ms^{-1}. After further descent to 8 m AGL it executes a flare with further reduction of airspeed to 12.5 ms^{-1}.

The remaining altitude is reduced until touchdown with 12.5 ms^{-1} airspeed. This implemented procedure assures reliable landings of MASC-3 and therefore increases the efficiency of a measurement campaign, especially during operations at night.

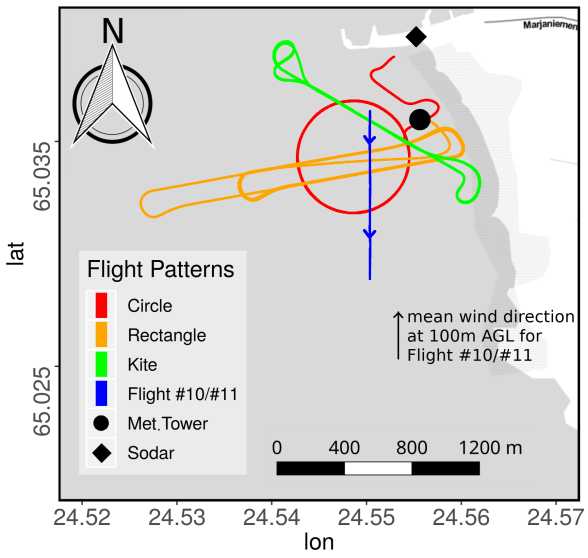

Figure 3. MASC-3 flight paths during the Hailuoto-II campaign. The island is indicated in white color and the grey area indicates water, which was completely frozen during the measurements allowing the installation of the indicated measurement tower. The sodar was installed on the island. The flight paths are plotted from the longitude and latitude readings of the inertial navigation system. The flight path section (leg) of Flight #10 and Flight #11 was used for the comparison between the tower, the Sodar and MASC-3. During Flight #10 and Flight #11 the mean wind direction at 100 m above ground level (AGL) is indicated. Map tiles by Stamen Design (http://stamen.com/) under CC BY 3.0 (http://creativecommons.org/licenses/by/3.0). Data by Open Street Map (http://openstreetmap.org/) under ODbL (http://www.openstreetmap.org/copyright).

2.3. Sensor System Setup

Attached to the Raspberry Pi 3, the standard setup of MASC-3 has a variety of meteorological sensors and power handling devices. The flow diagram in Figure 4 shows the schematic powering and the data flow of the sensor system. The whole system is powered by a single 3S lithium polymer battery with a nominal capacity of 2700 mAh, allowing up-times of ≈4 h. The inertial navigation system (INS) Ellipse2-N from sbg-systems is directly powered by the battery. Since sensors and other periphery are running with 5V, the voltage coming from the battery is stepped done by a Traco Power (2 Ampere maximum current) DC-DC converter, providing a low noise power source. A USB Hub and the Raspberry Pi are directly powered from the 5V DC source. The USB Hub powers the CEBO-LC analogue-digital converter which handles the analogue signals and an Arduino which controls the digital sensors. The USB connections are also the data interfaces, for the CEBO-LC and the Arduino. The INS Ellipse2-N is also connected via USB to the Raspberry Pi.

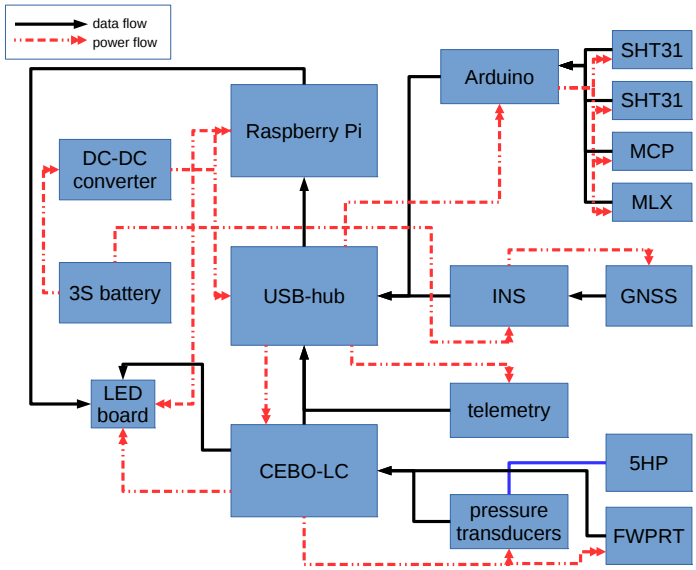

Figure 4. Data and power flow diagram of the MASC-3 sensor system.

The standard sensor system consists of the following sensors:

- Inertial navigation system (INS) Ellipse2-N from sbg-systems [58]; consisting of an inertial measurement unit, a GNSS receiver and an extended Kalman Filter, measuring attitude, position and velocity of MASC-3. With 3 Axis Gyroscopes, 3 Axis Accelerometers, 3 Axis Magnetometers, a pressure sensor and an external GNSS receiver, the INS has 0.1° roll and pitch accuracy, ≈0.5° heading accuracy, 0.1 ms^{-1} velocity accuracy and 2 m position accuracy. The accuracy is provided by the manufacturer and the test conditions for these specifications are proprietary and may not represent the performance during flight.
- Five-hole probe; manufactured by the Institute of Fluid Mechanics at the Technische Universität Braunschweig, Germany, measuring the flow angles and magnitude (airspeed vector) onto the probe at turbulent scales [59].
- Pressure transducers; 5× LDE-E 500, 1× LDE-E 250 for the static pressure port and a HCA0811ARG8 barometer. The differential pressure transducers are rated with an offset long term stability of ±0.05 Pa and a response time (τ63) of 5 ms.
- Fine wire platinum resistance thermometer (FWPRT); developed by Reference [60] with a 12.5 µm platinum wire, in order to measure the air temperature at turbulent scales.
- CEBO-LC from CESYS; providing an analogue-digital conversion of 14 single-ended or 7 differential analogue inputs with a measurement resolution of 16 bit. The accuracy is rated 0.005% Full Scale (typical) after Calibration and provides high-impedance operational amplifier inputs with a total sample-rate of 65 to 85 kSPS and a response-time (latency) of typically 0.9 ms and maximum 4 ms.
- SHT31 temperature and humidity sensor from Sensirion; fully calibrated, linearized, and temperature compensated digital output of temperature and relative humidity with a typical accuracy of ±2% RH and ±0.3 °C. The response time for humidity (τ63) is rated to be 8 s and the response time of the temperature (τ63) is 2 s.
- MLX90614 infrared object temperature sensor; facing downwards surface temperature measurement with a resolution of 0.02 °C and a measurement accuracy of 0.5 °C
- MCP9808 temperature sensor; additional temperature measurement for surveillance of the temperature of the electrical components of the sensor system.

The analogue signals of the turbulence measurements of the temperature and the 3D wind vector, acquired by the FWPRT and the five-hole probe together with the pressure transducers, are sampled with 500 Hz and converted by the CEBO-LC analogue-digital converter. The data stream is buffered by the CEBO-LC microcontroller, using a 32 Bit counter to ensure accurate temporal progression, and is logged by the Raspberry Pi 3. The digital sensors (SHT31, MLX, MCP) are controlled by an Arduino and logged with 10 Hz. The INS data has an update rate of 100 Hz (can be set to maximum 200 Hz) and is logged directly by the Raspberry Pi 3. Besides, a telemetry link to a laptop with a ground-station software allows the surveillance of an abstract of the data at 1 Hz.

Malfunctions of the sensors can be detected during flight and preliminary results can be plotted and, if needed, the flight strategy can be adapted. This telemetry link is provided by a small radio module (XBee) within the 2.4 Ghz band. The ground station software is also capable of calculating and displaying the potential temperature profile of the ABL on the fly, making it possible to sample more often in the layers of interest. The SHT31 sensor is mounted in two positions on the sensor system. One of them is mounted outside in a tube (see Figures 1 and 5), acting as radiation shield, in order to measure the ambient air temperature and humidity alike the FWPRT. The other one is mounted inside the sensor hat to measure the temperature and humidity close to the other hardware and to monitor the temperature inside, which might be crucial in very hot or very cold conditions. The MCP9808 temperature sensor is mounted close to the pressure transducers, which are further in the front of the sensor hat, in order to monitor changes of the temperature also there. Figure 5 shows the sensor hat that is mounted on the MASC-3.

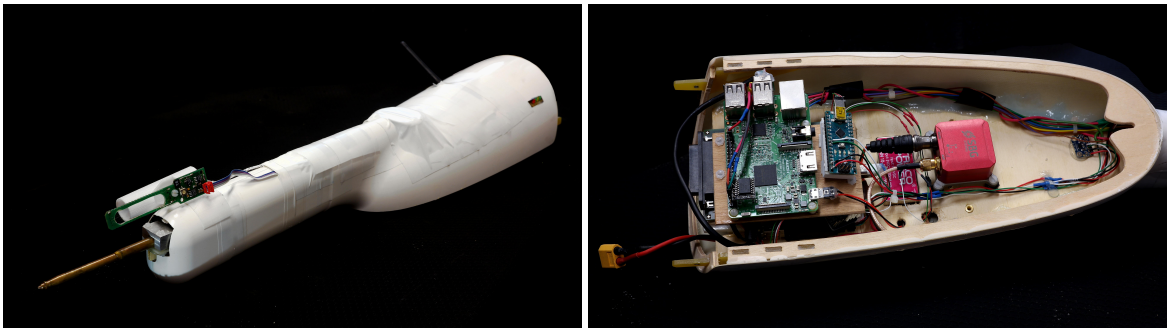

Figure 5. Sensor system hat (**left**) and mounted electronics inside the sensor hat (**right**).

2.4. Sensor System Software

The data acquisition on board the sensor hat of MASC-3 is managed by the open-source single-board computer Raspberry Pi 3. The software is designed to be a modular system that allows for switching between different sensor configurations as well as installing new sensors. A large pool of open source code examples and ready made application programming interfaces (API) allow fast implementation of new sensors. Figure 6 shows the schematic architecture of the software. The data acquisition of each individual sensor is managed by a self-contained process that connects to the sensor, logs the data on the SD card and transmits a reduced live data stream to the ground station. This design was chosen to allow for maximum freedom in choosing sensors without the restriction of being dependent on a specific programming language used by the available API of the sensor. The data acquisition software for a sensor can be written in any programming language supported by that sensors API, instead of having to create a new and potentially unreliable interface in a different programming language. The transmission of the live data stream from each sensor to the ground station software is handled by the Sensor Manager. This process is launched after the Raspberry Pi booted and starts the respective data acquisition program for each sensor in the current configuration. The live data stream from the sensor data acquisition processes is then captured and forwarded to the ground station via telemetry modules. The ground station software detects the incoming data streams and allows plotting them against each other. To ensure the modularity of the system, the logged data

is not synchronized on-board. Instead, all data is oversampled and has both, the timestamp or counter of the underlying sensor, as well as the timestamp of the system time of the operating system, which itself is updated and checked against an external hardware clock. The data is synchronized during post processing by cross-checking the timestamps and counters of each of the sensors. The Raspberry Pi 3 provides data of critical parameters of the Hardware and the operating system, including for example, CPU (central processing unit) working load, CPU temperature and so forth. Along with the remaining capacity on the SD-card, which helps the ground station observer to see whether the logging process runs properly, this data is also logged and partially transmitted to the ground station.

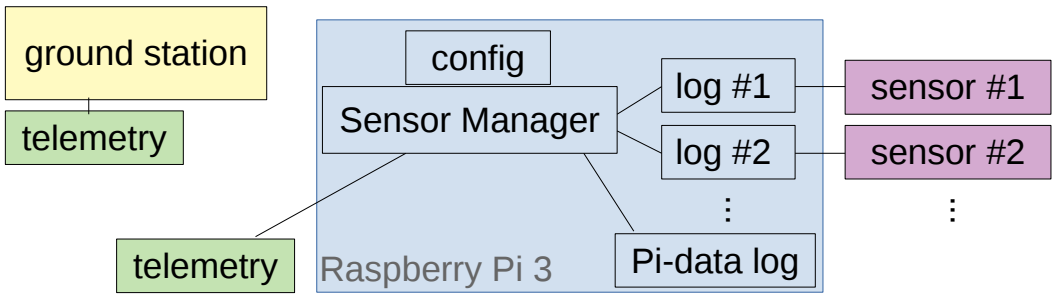

Figure 6. Schematic software setup of the sensor system on-board MASC-3.

2.5. Meteorological Airborne Data Analysis (MADA)

After each flight experiment, the stored data on the SD-Card of the Raspberry Pi 3 can be for example, downloaded via Ethernet. Since the CEBO-LC, the INS Ellipse2-N and the Arduino have separated log files, the data has to be merged. The first post-processing is done with the developed software MADA (Meteorological Airborne Data Analysis) which is a cumulative series of scripts based on the open source software R. The most important issue is the temporal synchronization of the data to one common time vector. The accuracy of the 32 Bit counter of the CEBO-LC and the INS, which also includes a 32 Bit counter as well as GNSS-time, ensures the accuracy of the synchronization, making the timestamps of the Raspberry Pi itself almost obsolete. Only the first and last timestamps of the Raspberry Pi inside the individual sensor log files are used to initially synchronise the logs. Subsequently the Pi time is used to double check the accurate temporal progression of the fused data. After synchronization, MADA provides scaling of the analogue sensors (e.g., FWPRT, pressure transducers, etc.) according to the calibration and data sheets. Then all data is sorted and meteorological data is calculated (e.g., air density etc.). After this pre-post-processing a first wind calculation is performed.

The 3D wind vector, using five-hole probes, is calculated by the summation of the ground speed vector of the UAS and the true airspeed vector of the UAS. The ground speed vector is directly given by the INS Ellipse2-N. By calibration, the pressure readings of the individual holes of the probe are used to estimate the true airspeed vector. To find a relationship between the measured pressure differences on the prope's pressure holes and the airflow angles, as well as the dynamic and static pressure at any airflow angle within the calibration range, wind-tunnel calibrations were conducted. In the wind tunnel, the airspeed is set for the calibration. With dimensionless coefficients, a set of polynomial functions for the airflow angles and the dynamic and static pressure are determined. These calibration polynomials are finally used to convert the pressure readings of the measurement to the true airspeed vector of the UAS [45]. With the attitude, position and velocity of the UAS, measured by the INS, multiple coordinate transformations finally yield the wind vector. This method is widely used with UAS [18,22,47] and was originally used with manned aircraft [62]. A detailed description of the method

is given in the study described in Reference [48], which also compares this direct method of the 3D wind vector measurement with simplified algorithms.

After the initial calculation of the 3D wind vector, a set of plots is printed out in order to get a first overview of the flight. Subsequently, suitable pairs of flight legs (straight, horizontal flight sections) for the wind correction [47] are identified by the software MADA. Since a misalignment between the five-hole probe's orientation and the UAS cannot be avoided, three offset corrections for the Euler Angles $\Delta\Phi$ (roll), $\Delta\Theta$ (pitch) and $\Delta\Psi$ (yaw or heading) must be determined. A fourth correction factor f_{tas} for the norm of the true airspeed vector accounts mostly for the calibration in the wind tunnel, which never matches exactly the conditions during the measurements. The assumptions for the in-flight calibration are a constant mean horizontal wind, a mean vertical wind near zero and low turbulence or turbulent transport. This allows a comparison of the wind components for two consecutive straights in opposite directions (star pattern), or identical legs in reverse direction. The correction offsets and factor for the presented flights in Section 4 were each determined with two pairs of legs in reverse direction on ≈100 m AGL. The procedure to calculate the correction factors was explained in detail in Reference [47] and analyzed with regard to the calibration of the five-hole probe and turbulence measurements in Reference [45]. If the meteorological conditions did not change substantially, the correction offsets and factor can be taken from previous flights, at least for a preliminary analysis in the field.

Afterwards, the meteorological data is processed again, including the corrections for the wind vector components. A first quality control with several plots of the measured quantities along the flight legs are printed out. Additionally, the power spectra and structure functions of the main quantities are plotted for a the quality control just after the measurements. Furthermore, vertical profiles of wind speed, wind direction and turbulence quantities are provided, containing the data of each flight leg. These quick looks are essential to get a brief overview of the meteorological conditions. An adaption of the flight patterns for consecutive flights can be considered, or a sensor malfunction can be identified. The set of plots is at hand, minutes after landing the UAV. The MADA software concept and the first analysis on sight is the foundation for a detailed post-processing of all measured data but also a key element for successful field campaigns. Uncertainty analysis of the wind vector measurement, such as the influence of the calibration procedures of the five-hole probe, airspeed variations of the UAS during the measurement, the influence of dynamic motion of the UAS and an estimation for the error propagation is given in References [45,47].

3. Methods and Data

An important difference, when comparing turbulence measurements with fixed-wing UAS along a straight, horizontal flight path (leg), with measurements of meteorological towers is, that the UAS transects the air with its cruising airspeed and the tower measures the air that is advected with the mean flow. Since MASC-3 is not dependant on the mean flow it is capable of gathering quasi-spatial snapshots with higher temporal resolution than the tower. The most important criteria to do so is a fast sensor, able to capture most of the energy inheriting fraction of the inertial sub-range of turbulence. The most important underlying assumption for a comparison is Taylor's hypothesis of frozen turbulence [1], which was found to be applicable to the smallest scales of turbulence at high frequencies or low wave numbers [2]. For the larger scales, especially for atmospheric flow under the influence of the diurnal cycle, coherent structures or the variability of the geostrophic wind, differences due to production and diffusion processes of turbulence persist if a quasi-spatial snapshot is sampled with an aircraft and compared to fixed-point measuremnt with a tower [3,63]. Coming along with that, the important question of how long is long enough for a horizontal flight leg [9] when calculating turbulence statistics, causes further complexity, making comparisons between the moving UAS and a stationary tower challenging.

3.1. Statistical Methods

The wind vector components can be compared separately and a differentiation between the horizontal components u (positive eastward) and v (positive northward) and the vertical wind component w (positive when facing upwards) is insightful. The horizontal wind speed v_h is calculated with the wind vector components u and v by

$$v_h = \sqrt{u^2 + v^2}. \tag{1}$$

Furthermore, the variances for the wind vector components must be compared for a validation. The variance of a variable X is

$$\mathrm{Var}_X = \sigma_X^2 = \frac{1}{N-1} \sum_{i=1}^{N} (X_i - \overline{X})^2, \tag{2}$$

where N is the number of data points and $\bar{X}$ denotes the mean of the variable within the data window which, in this case, is the length of individual flight leg. The covariance Cov_{XY} of two variables is

$$\mathrm{Cov}_{XY} = \frac{1}{N-1} \sum_{i=1}^{N} (X_i - \overline{X})(Y_i - \overline{Y}). \tag{3}$$

The turbulent kinetic energy TKE is

$$\mathrm{TKE} = \frac{1}{2} \left(\mathrm{Var}_u + \mathrm{Var}_v + \mathrm{Var}_w \right). \tag{4}$$

The integral time scale $I(X)$ of a quantity X is defined by

$$I(X) = \int_0^{\tau_1} \frac{\sigma_X(t+\tau)\, \sigma_X(t)}{\sigma_X^2} \, d\tau. \tag{5}$$

The integral time scale $I(X)$ is the autocorrelation function of the variable X and calculated by integration from zero lag to the first crossing with zero at τ_1 [64] and is multiplied by the mean true airspeed $\overline{|\vec{u}_a|}$, calculated for example, according to Reference [45],

$$L(X) = I(X)\, \overline{|\vec{u}_a|} \tag{6}$$

or, respectively for the measurement tower, by the mean horizontal wind speed $\overline{v_h}$ in order to get the integral length scale $L(X)$ [3,64–66].

The integral length scales of the horizontal wind speed $L(v_h)$ and the vertical wind $L(w)$ are considered in this study. The integral length scale can be interpreted as the typical size of the largest, or most energy-transporting eddy. To analyse the scale dependence of turbulence and to evaluate whether the inertial sub-range is suffiently resolved [4], spectra and structure functions of the horizontal v_h and vertical wind w are analysed and compared to the measurements of the tower. The frequency spectrum—or power spectrum $S_X(f)$—of a quantity X is calculated for a time series of length Δt with the time steps t and after applying a Hann window by

$$S_w(f) = \int_0^{\Delta t} \mathrm{Cov}_{XX}(t) e^{2\pi i f t} \, dt = \frac{1}{\Delta t} \, \tilde{X}^*(f) \, \tilde{X}(f) = \frac{1}{\Delta t} |\tilde{X}(f)|^2 \tag{7}$$

with the frequency f, imaginary unit i, covariance function from Equation (3) and the Fourier transformed frequency series $\tilde{X}(f)$ and its complex conjugate $\tilde{X}^*(f)$. For locally isotropic turbulence, the inertial subrange is characterized by the $-5/3$ slope in the spectrum. In order to compare the data

of a moving UAS with the data of a stationary measurement tower, the frequency spectra $S_X(f)$ are transformed into wavenumber spectra $S_X(k)$ by

$$k = \frac{2\pi f}{\overline{v}} \tag{8}$$

using for the transformation of the evaluated period the mean velocity $\overline{v} = \overline{v_h}$ of the horizontal wind speed of the measurement tower and the mean true airspeed $\overline{v} = \overline{|\vec{u}_a|}$ of the UAS measurements. The structure function $D_X(s)$ of a quantity X is calculated for a time series with N data points, the time steps t and the temporal shift or lag s by

$$D_X(s) = \frac{1}{N-n} \sum_{i=1}^{N-n} (X(t) - X(t+s))^2, \tag{9}$$

where n is the number of data points associated with the lag s. For locally isotropic turbulence, the inertial subrange is characterized by the a $2/3$ slope in the structure function.

To compare the structure function $D_X(s)$ of a time series between the moving UAS data and the stationary tower data, the temporal shift or lag s is transformed into a spacial lag r by

$$r = s\,\overline{v} \tag{10}$$

also using for the transformation of the evaluated period the mean velocity $\overline{v} = \overline{v_h}$ measured by the tower and $\overline{v} = \overline{|\vec{u}_a|}$ measured by the UAS. The structure function and the power spectra of the horizontal wind D_{v_h}, S_{v_h} and the vertical wind D_w, S_w are considered in this study.

Differences concerning the fact that MASC-3 samples a quasi-spatial snapshot along a straight and horizontal flight leg with its cruising airspeed and that the stationary tower samples the advected air flow can be considered by comparing the quantities of interest for time series that have the same temporal fetch. The temporal fetch is represented by the approximated time interval for the individual measurement system during which the same volume of air was sampled. To account for that, the considered duration of the time series Δt for the comparisons in Section 4 inherit the same temporal fetch calculated by

$$\Delta t_{\text{tower}} = \Delta t_{\text{UAS}} \frac{v_{\text{UAS}}}{v_{\text{tower}}} = \Delta t_{\text{UAS}} \frac{\overline{|\vec{u}_a|}}{\overline{v_h}}, \tag{11}$$

using the mean true airspeed $\overline{|\vec{u}_a|}$ of the UAS divided by the mean horizontal wind speed $\overline{v_h}$, measured by the UAS.

This factorization for defining the duration of the compared time series complies with the full duration of the MASC-3 flight leg and the corresponding duration of the time series of the tower measurement Δt_{tower} is calculated with Equation (11).

3.2. Meteorological Tower and Sodar Measurements for Comparison

During the Hailuoto-II measurement campaign at the eastern coast of the north Bothnian Bay, Finland, two flight experiments were dedicated to compare the MASC-3 measurements with the meteorological tower (see Figure 7) measurements. Both flights, Flight #10 and #11 (Figure 3), were conducted on the 10 February 2018 around 17:00 (EET) and 22:00 (EET) over the completely frozen bay area west of the island Hailuoto. Civil Twilight started at 17:25 (EET) and night started at 19:21 (EET) on the measurement day.

The meteorological conditions during the evening of the 10 February 2018 were characterized by a high pressure system over Siberia and a low pressure system just south of Iceland with a relatively weak pressure gradient at our observation site. The local conditions were mostly cloudy or partially cloudy with a cloud base height below 500 m before 17:00 UTC. Between 17:00–18:30 UTC the sky opened

up and became clear. Temperatures were quite moderate, slightly below freezing and decreasing throughout the evening and night. The wind direction was from south with a weak shift towards SSW and SW during the night. Relatively high wind speeds of up to 10 ms^{-1}, observed at the permanent weather station at 46 m above sea level declined and stabilized at 5–7 ms^{-1} after 22:00 UTC.

Figure 7. Meteorological measurement tower during the Hailuoto-II campaign. Viewing direction is north-north-east towards the harbour and the village Marjaniemi. The picture was taken by Kristine Flacké Haualand.

The MASC-3 measurements were synchronized with the mast measurements using the Equation (11), because the aim is to sample the same volume of air with both systems. Since both flights started nearby the mast (Figure 3), the first timestamp was chosen to be the same for both systems.

CSAT3 (Campbell Scientific, Inc., Shepshed, UK) sonic anemometers were deployed at three levels of the meteorological tower, at 2.0 m, 4.5 m and 10.3 m heights. These instruments provide measurements of the three wind velocity components and the sonic temperature at 20 Hz frequency. The data were first checked for unphysical values and spikes. The thresholds for unphysical values were ± 30 ms^{-1} for horizontal wind components, ± 10 ms^{-1} for the vertical wind component and ± 30 °C for the sonic temperature. Spikes were detected using the method described by Reference [7]. The value of the next point in the time series was predicted based on weighted average of the last value and the mean of the last 80 values (which corresponds to a time interval of 4 s with 20 Hz sampling frequency). The weight of the last value depends on the auto-covariance between the consecutive values in the window of 80 values. If the absolute difference between the predicted and the observed value exceeds a certain threshold times the standard deviation of the last 80 values, the observation is considered as a spike. The detection algorithm was applied with a moving window of 80 values and a spike detection threshold of 4.0 and 5.5 (and an increase in threshold by 0.1 and 0.5 after each iteration, to account for the decreased standard deviation after removal of spikes) for the wind components and the sonic temperature, respectively. Spike detection was first applied forward in time and then backwards. Only those spikes that were detected as spikes from both directions were finally considered as spikes. During the selected period, 14:30–22:00 UTC on 10 February 2018, only a few (from 0 to 4 out of 540,000) individual suspicious values were detected for each variable and measurement height. These individual spikes in the 20 Hz data were replaced by linear interpolation using neighboring good quality values. After the quality control, momentum flux convergence was evaluated by ogive test [67]. Ogive function is the cumulative integral of the co-spectrum starting from the highest frequencies. The convergence is achieved when the function reaches a certain level where

no more energy is gained by including larger scales. In ideal conditions, ogive function can be used to detect the location of the spectral gap between the turbulent scales and diurnal/synoptic scales. Results of the ogive method are shown in Figure 8 for the 3 different heights of the tower indicated by different colors.

The ogive functions are normalized by the value at the point closest to the frequency corresponding to 10 min period. At all levels, the ogive function reached the value 1.0, that is, the convergence, in less than 10 min. As expected, the convergence was reached faster closer to the surface than at higher levels of the tower. Further, at least 80% of the total flux was covered already within 60 s, which makes the data set suitable for comparison of turbulence measurements from the tower and MASC-3. Based on the results from the ogive test, we chose a fixed 10 min sample length for the tower measurements. For each 10-min sample, the wind components (originally in the inertial coordinate system) were rotated using 2D rotation method to align the wind components along the mean wind ($\overline{u_{rot}}$=$\overline{v_h}$) and perpendicular to it ($\overline{v_{rot}} = \overline{w_{rot}} = 0$). The turbulence statistics were then calculated using these rotated 10 min samples.

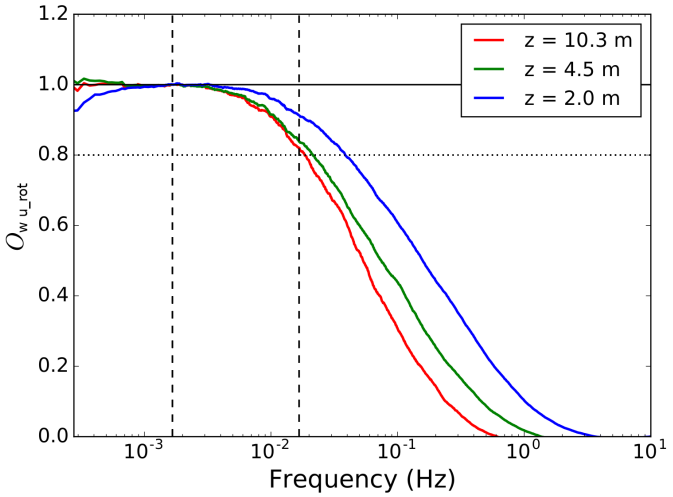

Figure 8. Results of the ogive test between vertical w and the horizontal u_{rot} wind components using all observations from the three tower heights during the period 10 February 2018 14:30–22:00 UTC. Ogives are normalized by the value at the point closest to the frequency corresponding to 10 min, indicated by the first vertical dashed line from left. The second vertical dashed line represents the frequency corresponding to 60 s.

With the prevailing wind direction for both Flights #10/#11 of $\phi \approx 150°$ at the height level of the comparison between the tower and MASC-3, the flow is advected over the south-western edge of the island Hailuoto (see Figure 3). For these conditions, the shore of Hailuoto was ≈1500 m away from the tower. The shore area is not forested but the structure of the surface comprises unevenness. Generally, the structure of the surface and its roughness was not totally homogeneous. Apart from the shore of Hailuoto and the harbor, the vicinity of the measurement site was covered with isolated ice features with heights of ≤0.5 m. Close to the shore area, some bigger ice ridges of up to 3 m persisted. The footprint for both systems, MASC-3 and the tower may therefore influence the comparison.

A MFAS Sodar system (Scintec AG) was installed at the Hailuoto-II field site on the shore line (see Figure 3) with a base height of approximately 5 m above the sea level. The acoustic Sodar antenna of the MFAS consists of 64 piezo-electric transducers, emitting and receiving sound pulses at 10 different frequencies in the range 1650 Hz–2750 Hz and an output power of 7.5 W . The MFAS can emit acoustic signals in 5 different directions, vertically and tilted in N, E, S and W direction. This enables for the computation of 3-dimensional wind profiles at a vertical resolution of 10 m, ranging from 30 m to 1000 m. However the maximum range of the system was typically below

600 m. The temporal resolution of the Sodar data is 10 min, due to measurement sequence chosen for Hailuto-II. The manufacturer stated the accuracy for the wind speed and direction to be ± 0.3 ms^{-1} and $\pm 1.5^{\circ}$, repsectively. For the comparison of the vertical profiles of the horizontal wind we chose one or two Sodar profiles, that matched the time periods of the MASC-3 ascents or descents. Only high quality Sodar data (i.e., high cumulative significance and significance density; temporal and spatial consistency) are taken into account for the analyses presented in Section 4.2.

4. Results

In this Section, we will first compare measurements from two horizontal low level flight legs of Flight #10 with measurements from the meteorological tower (Section 4.1). This will provide an overview of the quality of the MASC-3 data. Then, in Section 4.2, we will illustrate the potential of MASC-3 to complement meteorological mast and Sodar measurements by providing measurements from several heights of Flight #11. From these horizontal flights at multiple heights it is possible to derive profiles of mean atmospheric quantities that can be compared to the sodar measurements, as well as profiles of turbulence quantities.

4.1. Comparison of Measurements from MASC-3 and the Meteorological Tower

For Flight #10, with a mean sampling time for the two flight legs of $\Delta t_{\mathrm{UAS}} = 80$ s, the corresponding sampling time of the measurement tower is $\Delta t_{\mathrm{tower}} = 170$ s, since the true airspeed was $|\overline{\vec{u}_a}| = 19.7$ ms^{-1} and the mean horizontal wind speed $\overline{v_h} = 9.25$ ms^{-1} (Equation (11)). The first part in Section 4.1 analyses the power spectra (see Equation (7)) and the structure function (see Equation (9)) of the horizontal and vertical wind of one flight leg of MASC-3 and the corresponding data of the measurement tower in Figure 9. To allow comparability, the frequency spectra are transformed into a wavenumber spectra, using Equation (8) and the structure functions, computed over temporal lags, are transformed into spatial legs with Equation (10). To closely compare the two measurement systems, the time series of the measurement tower is plotted and the data of the two spatially closest flight legs of Flight #10 are included in the set of plots in the Figures 10–13. The time series inherited in the power spectra and the structure functions is the same than the first flight leg in the following set of figures.

The set of figures consist of the two neighboring sets of data points, which are the 10 min periods of the tower measurement on the three height levels (10.3 m, 4.5 m, 2 m AGL). Additionally, the data at 10.3 m AGL is plotted as moving average, variances covariance and TKE calculated on a moving window. The window size for the moving calculation of the quantities is $\Delta t_{\mathrm{tower}} = 170$ s, allowing a close comparison with the data points of the MASC-3 measurement. Further, the integral length scales of the horizontal $L(v_h)$ and vertical $L(w)$ wind are plotted A moving calculation of the integral length scale according to Equation (5) is not feasible, since the autocorrelation function must be manually checked for plausibility since it may fail and not converge to a τ_1 [64]. Therefore, a moving integral length scale is not feasible, but the actual comparison with MASC-3 and the additional calculations of L on time series of length $\Delta t_{\mathrm{tower}} = 170$ s are given to analyze the temporal variability during the comparison.

The wavenumber spectra and the structure functions for the horizontal wind v_h and the vertical wind component w in Figure 9 give insight in the resolution of both measurement systems. The inertial subrange of turbulence in an isotropic flow is characterized by the $k^{-5/3}$ slope in the power spectrum and by the $r^{2/3}$ slope in the structure function, indicating the ability and quality of the measurement system to resolve the spectrum of turbulent fluctuations in the atmospheric boundary layer. Generally, the discretization of the structure function is sparse towards small lags and the influence of sensor noise is better visible in the power spectrum. Vice versa, the power spectrum is sparsely discretised for small wave numbers and to study the production subrange and the onset of the inertial subrange, the structure function is beneficial.

The power spectrum of v_h of the tower measurement is located slightly higher than the spectrum of the MASC-3 data, since the variances of the vertical wind Var_{v_h} (visible in Figure 11) of the tower measurement are also slightly higher. The structure functions of both time series for v_h agree well in the inertial subrange but in the production subrange the curve of the tower data lies above the curve of MASC-3, which can also be explained by the difference in the variance measurements of both systems of $\approx 0.05\ \mathrm{m^2\ s^{-2}}$. If the variance, as an indicator of turbulence, is higher, the spectra is located higher and the production subrange is elevated. Although only ≈2 m altitude offset persist between the sonic anemometer and the average flight level of MASC-3, this can explain the differences, since the structure of the surface layer changes strongly with height (indicated e.g., by the 10 min averages at the three tower levels in the set of plots in the Figures 10 and 11). The power spectra and the production subrange in the structure functions lie close together for the vertical wind component w, since the variances of the vertical wind Var_w are almost identical. Also the gradient $\Delta \mathrm{Var}_w / \Delta z$ is smaller than $\Delta \mathrm{Var}_{v_h} / \Delta z$, when looking at the ten minute averages of the tower measurements (see Figure 11).

The ability to resolve the smallest structures can be closely compared when looking at the power spectra and towards growing wavenumbers. For v_h and w and for both measurement systems, a flattening of the spectra into the horizontal, indicating sensor noise, can be observed starting from $k \approx 4\ \mathrm{m^{-1}}$ for the tower and from $k \approx 10\ \mathrm{m^{-1}}$ for MASC-3. Both measurement systems seem to resolve the fluctuations of w slightly further. The structure functions indicate, that the onset of the inertial subrange of v_h starts at lags of ≈20 m for MASC-3 and the tower. Discrepancies can be seen in the structure functions of w, where the $r^{2/3}$ slope is reached only at smaller lags for MASC-3 ($r \approx 20$ m) than for the tower ($r \approx 10$ m). The inertial subrange for the vertical wind component close to the ground is shifted towards smaller structures due to the stability of the boundary layer. The length scales of the vertical wind are smaller than for the horizontal wind, which is also reflected in Figure 13. Following that, the inter-comparison of the structure functions for the MASC-3 data between v_h and w does reflect this. For the tower data, this feature is less pronounced. The structure functions of v_h and w of the MASC-3 data become steeper towards the lowest lags, also indicating the onset of sensor noise. The structure functions of the tower data do not indicate the onset of sensor noise as clear as the power spectra do. With sensor noise starting from $k \approx 4\ \mathrm{m^{-1}}$ for the tower and from $k \approx 10\ \mathrm{m^{-1}}$ for MASC-3 and by using Equation (8) it can be stated that, MASC-3 has, with 30 Hz, a significantly higher temporal resolution as the sonic anemometer with 6 Hz.

Figure 10 shows the horizontal wind v_h and the wind direction ϕ during the period when MASC-3 performed the flight legs of Flight #10 at the lowest level. The graph consists of the 10 min averages for the tower measurement at the height levels 10.3 m, 4.5 m and 2 m AGL, as well as of the moving average and the moving standard deviation at 10.3 m of v_h and ϕ. The wind speed, calculated from the MASC-3 flight legs, is higher than the curve of the moving average of the tower but the error bars are overlapping. One reason is the strong gradient of the horizontal wind speed, as indicated by the 10 min averages of the tower measurement. The height offset of the flight path and the highest level of the tower is only 1–2 m and the offset of v_h is 0.75–1 $\mathrm{ms^{-1}}$. Although considering the gradient of the 10 min averages of the tower, a slight discrepancy of the wind speed with MASC-3 persists. The longitudinal offset of ≈100 m between the flight path and the tower and the slightly different footprint of the flow may explain this remaining small offsets. The wind direction ϕ agrees with the moving average of the tower for the first leg and differs by only 2° for the second leg. For both legs, the values of MASC-3 are within the error band of the tower measurement. Figure 10 shows, that the wind direction and speed was quite stationary during the period of comparison. The average flight level of MASC-3 with 11.7 ± 0.2 m AGL for the first leg and 11.4 ± 0.3 m AGL for the second leg indicate that the flight level is held precisely by the autopilot. Especially in SBL with large vertical gradients, this is important for the accuracy of the measurements with MASC-3.

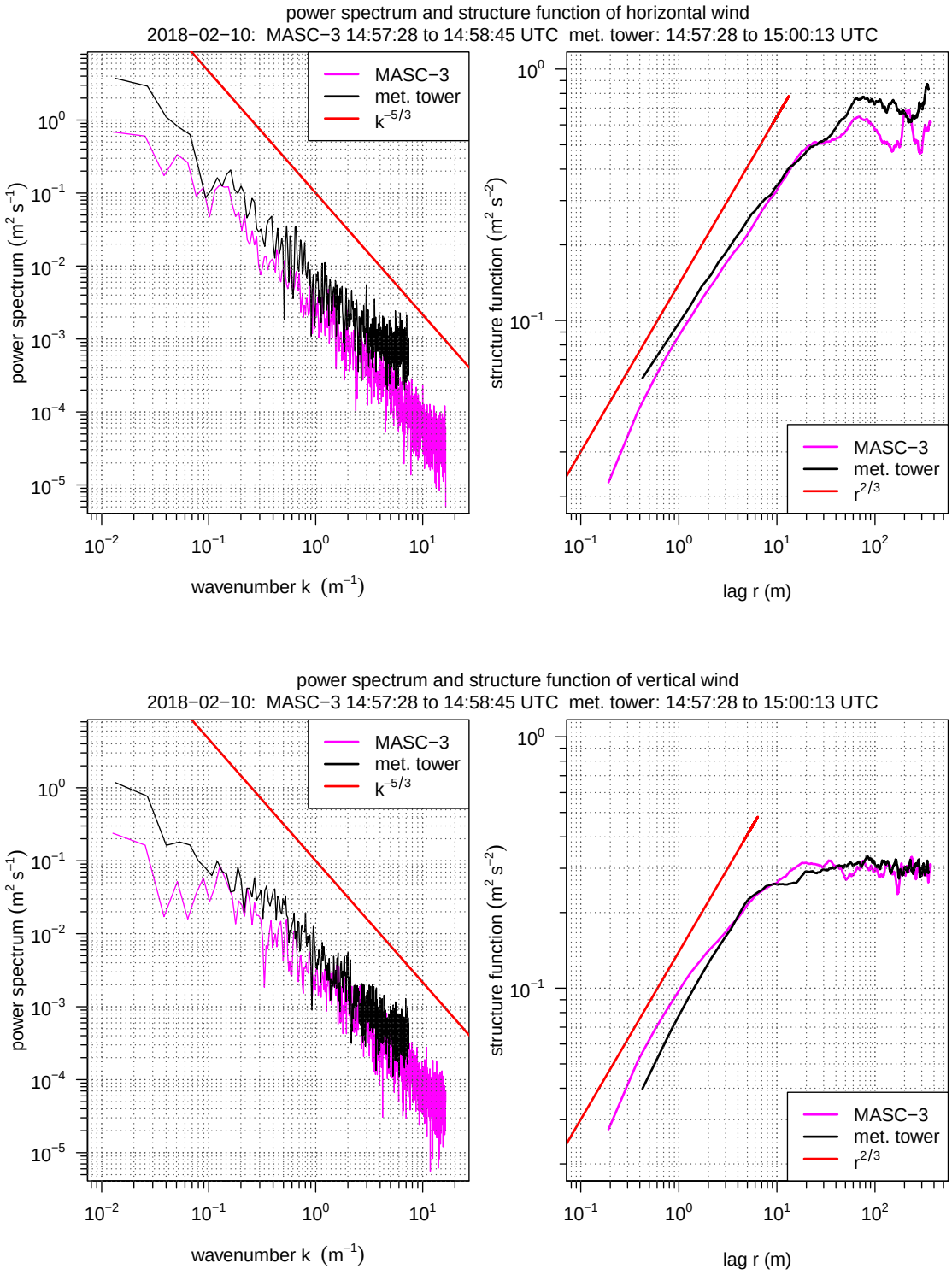

Figure 9. Wavenumber spectra (**left**) and structure functions (**right**) for the horizontal wind v_h (**top**) and the vertical wind vector component w (**bottom**). The data of the tower at the 10.3 m level inherits a time series of $\Delta t_{\text{tower}} = 165$ s, corresponding to the fetch of the MASC-3 flight leg with a duration of $\Delta t_{\text{UAS}} = 77$ s. Flight #10 and the first leg at 11.7 m AGL is given.

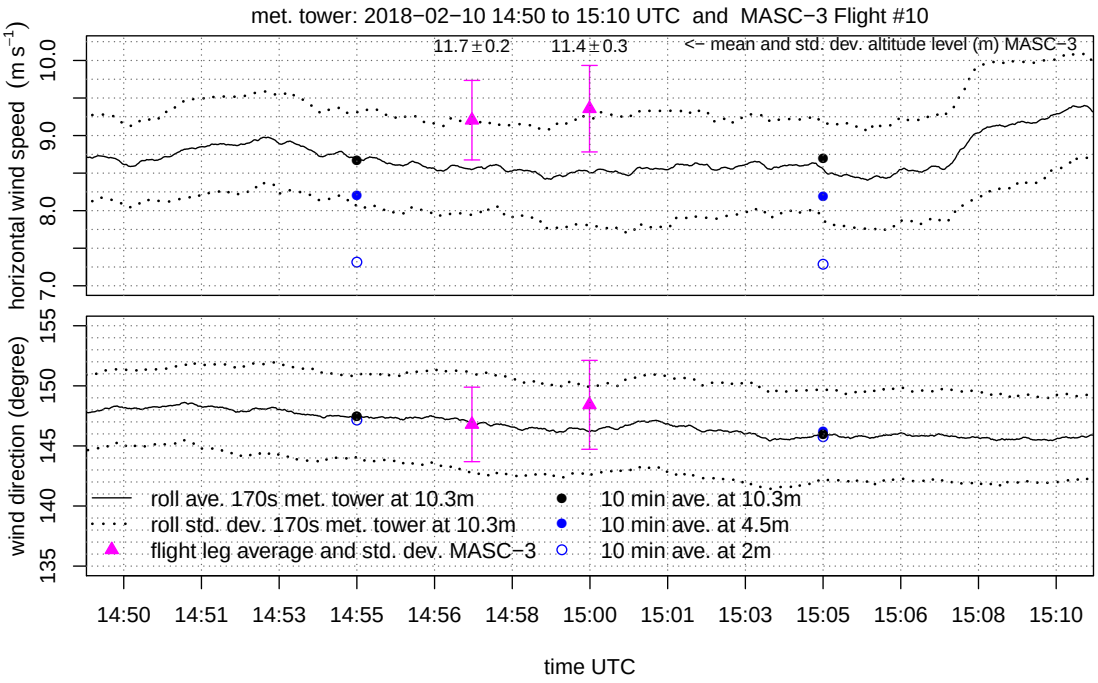

Figure 10. Time series of the tower with the corresponding leg averages and standard deviation of MASC-3 at the lowest flight levels for the horizontal wind v_h (**top**) and the wind direction ϕ (**bottom**). The mean altitude and standard deviation of the individual flight leg is given for the MASC-3 data points. The data of the tower at 10.3 m is plotted as rolling (moving) average with standard deviation and a window length of $\Delta t_{\text{tower}} = 170$ s corresponding to the fetch of the MASC-3 flight legs with an average duration of $\Delta t_{\text{UAS}} = 80$ s. Furthermore the neighboring ten minute averages of the tower at all height levels are given.

The variances of the horizontal wind speed Var_{v_h} and the vertical wind vector component Var_w are given in Figure 11. The first flight leg of MASC-3 shows, with ≈0.05 m^2 s^{-2}, a smaller value for Var_{v_h} than for the tower. The second flight leg has a deviation of ≈0.15 m^2 s^{-2}. The calculation of Var_{v_h} on the moving window shows a temporal increase during the second flight leg, concluding that the flow field is not stationary. The deviations can be partly explained by the strong gradient, as indicated with by the 10 min values of the tower ($\Delta\text{Var}_{v_h}/\Delta z$), as well as by the temporal and spatial variability. The data points of the variances of the vertical wind vector component Var_w agree very well with the tower measurements. This quantity is less subject to temporal change or the influence of gusts and transient motions on minute time-scales during the period of comparison, than Var_{v_h}. Although the 10 min values of the tower also indicate, with a changing offset between the height levels (gradients $\Delta\text{Var}_w/\Delta z$) between the first and the second group of values, that the state of the boundary layer changes.

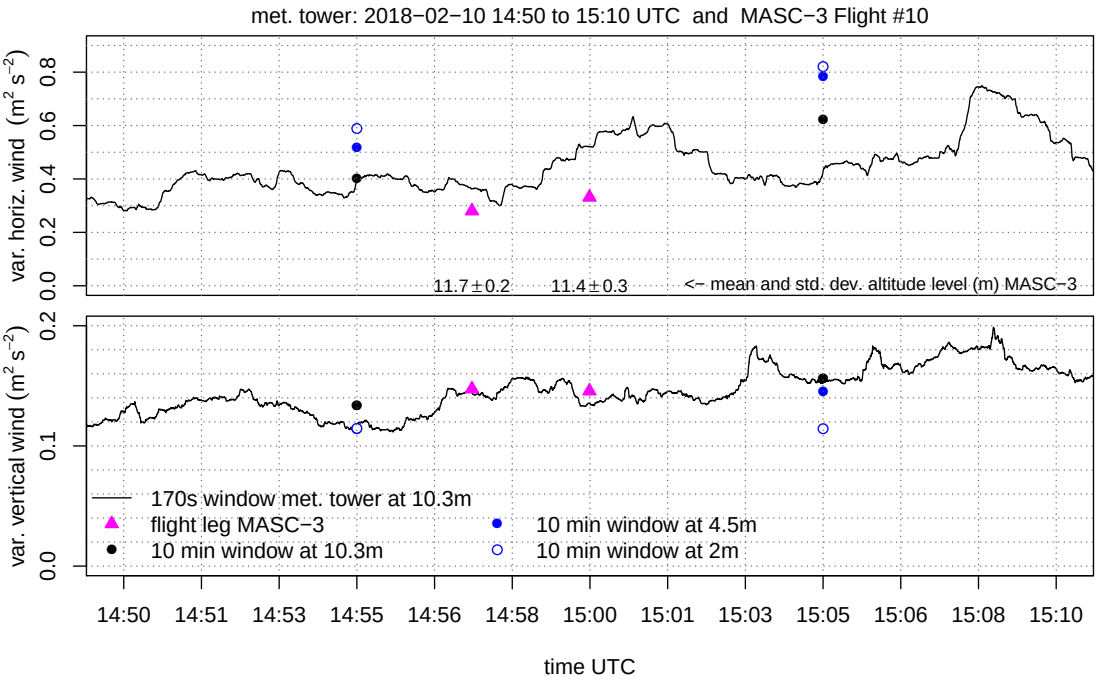

Figure 11. Time series of the tower with the corresponding leg averages of MASC-3 at the lowest flight levels for the variance of the horizontal wind Var_{v_h} (**top**) and the vertical wind component Var_w (**bottom**). The mean altitude and standard deviation of the individual flight leg is given for the MASC-3 data points. The data of the tower at 10.3 m is calculated on a moving window with a width of $\Delta t_{\mathrm{tower}} = 170$ s corresponding to the fetch of the MASC-3 flight legs with an average duration of $\Delta t_{\mathrm{UAS}} = 80$ s. Furthermore the neighboring ten minute averages of the tower at all height levels are given. The Var_w for the first ten minute interval of the tower at 10.3 m and 4.5 m lie on top of each other.

The turbulent kinetic energy TKE in Figure 12 also agrees very well between the measurement systems. The temporal evolution of the structure of the boundary layer is again visible in the gradients $\Delta\mathrm{TKE}/\Delta z$ of the 10 min tower measurements. The importance of applying adapted window lengths is evident, since the slight increase of TKE during the period of comparison is well represented by both systems and could not be addressed by only applying flux converged 10 min windows. This is even more important for the covariances of the vertical and horizontal wind component $\mathrm{Cov}_{wu_{rot}}$, since the variability is high. For both measurement systems, the coordinate systems was rotated into the mean wind direction so that the horizontal wind component u_h is aligned with the mean wind direction. The first flight leg does agree with the tower measurement for the moving window calculation and the 10 min value. The second leg has an offset of $\approx$0.02 m^2 s^{-2}. This correlates with the offset for Var_{v_h} in Figure 11 and can also be explained by the influence of gusts and transient motions on minute time-scales of the horizontal wind. Furthermore the spatial offset between the flight path and the measurement tower may cause these differences.

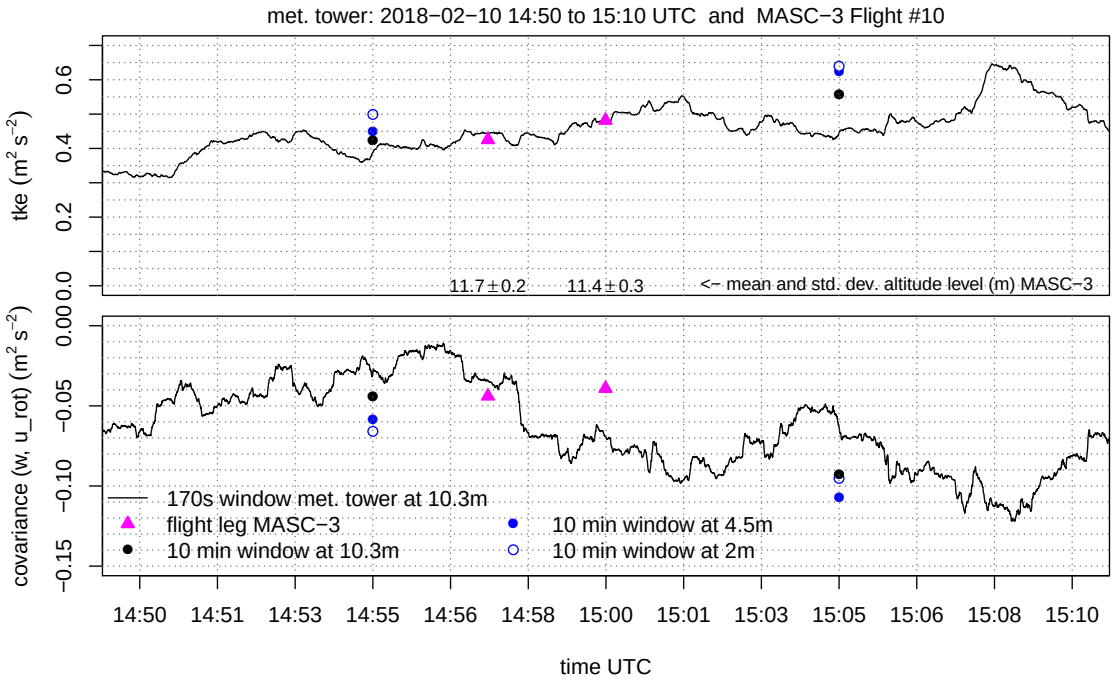

Figure 12. Time series of the tower with the corresponding leg averages of MASC-3 at the lowest flight levels for the turbulent kinetic energy (TKE) (**top**) and the covariance of the vertical and horizontal wind component $\mathrm{Cov}_{wu_{rot}}$ (**bottom**). By 2D double rotation for the tower and by coordinate transformation with the mean wind direction of the individual MASC-3 flight legs, u_{rot} was aligned with the mean wind direction. The mean altitude and standard deviation of the individual flight leg is given for the MASC-3 data points. The data of the tower at 10.3 m is calculated on a moving window with the length of $\Delta t_{\mathrm{tower}} = 170$ s corresponding to the fetch of the MASC-3 flight legs with an average duration of $\Delta t_{\mathrm{UAS}} = 80$ s. Furthermore the neighboring ten minute averages of the tower at all height levels are given.

The integral length scale of the horizontal $L(v_h)$ and vertical wind component $L(w)$ is given in Figure 13. The integral length scale can be interpreted as the biggest scales or eddies that are inherited in the measurement [68]. For the first flight leg, both systems give $L(v_h) \approx 15$ m but for the second flight leg, the time series of MASC-3 yields again 15 m and the tower 20 m. This offset for the second flight leg does correlate with the offsets in Var_{v_h} and $\mathrm{Cov}_{wu_{rot}}$ and leads back to previous explanation. It is remarkable, that the 10 min time series result in a negative gradient $\Delta L(v_h)/\Delta z$ for the first 10 min period and in a positive gradient for the second 10 min period, indicating again, that a temporal evolution of the boundary layer is present. Furthermore, the 10 min time series at the 10.3 m level do not agree with the smaller window of $\Delta t_{\mathrm{tower}} = 170$ s, indicating that the shorter time periods do not include the same spectrum of eddies. The integral length scale of the vertical wind component $L(w)$ agrees well between the measurement systems. For the same reasons than mentioned previously, the variability is less than for $L(v_h)$. Also the deviation between the 10 min time series and the shorter time period of $\Delta t_{\mathrm{tower}} = 170$ s of the tower measurements is smaller (1.5–2 m). Again, the comparison during the first leg agrees better than that of the second leg, where the evolution of $L(w)$ decreases before, during and after the comparison with the flight leg.

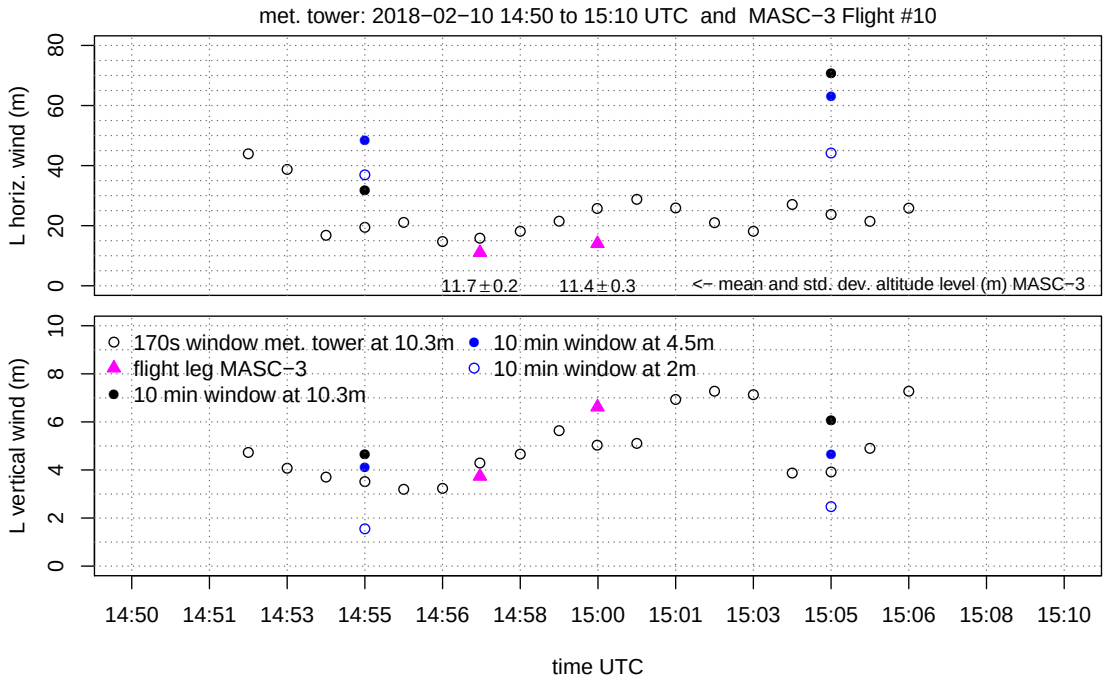

Figure 13. Integral length scales of the horizontal wind $L(v_h)$ (**top**) and the the vertical wind component $L(w)$ (**bottom**). For the tower at 10.3 m, several fractions of the time series with a duration of $\Delta t_{\text{tower}} = 170$ s, corresponding to the fetch of the MASC-3 flight legs with an average duration of $\Delta t_{\text{UAS}} = 80$ s, were used to plot the length scales alongside the values for the individual MASC-3 flight legs. The mean altitude and standard deviation of the individual flight legs are indicated. Furthermore, the integral length scales of the 10 min time series of the tower at all height levels are given.

It is concluded that the MASC-3 measurements of mean values and statistical moments of second order agree very well with the measurements of the meteorological tower. The comparison between the stationary tower and the moving UAS is best if the temporal fetch of both systems is considered. The structure functions and spectra in Figure 9 revealed, that the spatial and temporal resolution of MASC-3 is significantly higher than for the tower. This advantage is even more important if the mean wind speed is lower. In a stably stratified boundary layer, shorter averaging periods are applicable and may even be advantageous if the fast evolution of the boundary layer is of interest. Representative calculations of statistical moments of second order were given. Although the significance of only two legs is limited, the close analysis provides a first step towards validation of the 3D wind and turbulence measurements with MASC-3.

In order to summarize the persisting error sources and uncertainties for the presented comparison with the data of MASC-3 and to provide indications for future comparisons, the following list is given.

- The remaining spatial offset between the flight path and the tower, as well as differences of the footprint cause discrepancies.
- The temporal and spatial variability of the wind field and the questionable assumption of Taylor's hypothesis of frozen turbulence for the bigger scales of the wind field cause discrepancies.
- The measured quantities from MASC-3 do not represent the whole turbulence range and the measurements are influenced by a random error, which can be improved only by either having a larger ensemble of measurements or longer flight legs in horizontally homogeneous and stationary meteorological conditions.

- An error that is caused by the flight height persists. In sheared flow the changes in flight height and the associated changes of the turbulence regime may cause random error or bias. This depends on how the flight height changes during the flight leg and how strong the shear of the boundary layer is. If the flight height is constant on average but small variations in flight height are present, a random error must be expected. If there is a trend in flight height, or the flight height is clearly above the reference, a bias must be expected.
- Airspeed variations of MASC-3 and differences in the Reynolds number of the five hole probe's tip between the calibration in the wind tunnel and the measurement, influence the turbulence measurements [45].
- Airspeed variations of MASC-3 during the measurement cause an uneven sampling of the turbulent structures due to the acceleration and deceleration of the UAS, cf. References [69] and [37].
- The misalignment between the five-hole probe's orientation and MASC-3 requires three offset corrections. A forth correction factor for the norm of the true airspeed vector accounts for the differences between the airspeed of the calibration in the wind tunnel and during the measurements [45,47].
- The accuracy of the pressure and temperature sensors [47,59,60], as well as the accuracy of the INS, influence the results. The influence of the INS on the turbulence measurements with MASC-3 during dynamic motions of the UAS is especially very difficult to address and has not yet been analyzed sufficiently [45].

4.2. Profiles of the Atmospheric Boundary Layer with MASC-3

This section reverses the principle of the comparison and includes the temporally and spatially closest tower measurement periods into the height profiles of Flight #11. Figure 14 is also supplemented with the Sodar measurements and indicates the timestamps of the data of the three measurement systems. The Figures 14–16 inherit the tower measurements with the equivalent timestamps of the MASC-3 legs that are closest to the tower. MASC-3 ascended, descended and ascended for a second time during Flight #11. Two racetracks were conducted at every height level, resulting in two consecutive headwind legs at each height level. During the first ascent, the lowest flight level was approximately 14 m AGL and after descending and before ascending the second time, the lowest flight level was 25 m AGL. During these lowest flight legs, the corresponding time stamps for the tower data is used for calculating and plotting the data. With $\overline{v_h} = 6.3\ \mathrm{ms}^{-1}$, $|\overline{\vec{u}_a}| = 19.7\ \mathrm{ms}^{-1}$ and $\Delta t_{\mathrm{UAS}} = 55$ s for the first two legs of the first ascent, the duration of the considered time series of the tower is again $\Delta t_{\mathrm{tower}} = 170$ s. For the second ascent, where the lowest flight level was 25 m AGL, the corresponding period of the tower was also set to $\Delta t_{\mathrm{tower}} = 170$ s. The combined profiles of various quantities measured by the MASC-3 (triangles), the tower (circles), and Sodar (lines) are presented. Each profile took between 16 and 30 min to complete. The time difference between the first and the last triangle of a profile are summarized together with timestamp of the corresponding Sodar profile in Table 1. Each profile was flown with two racetracks, yielding two measurements per height. The first ascent started at 19:37 UTC, the descent at 20:09 UTC and the second ascent at 20:28 UTC.

Table 1. Timestamps (UTC) and duration of the profiles of MASC-3 and the corresponding timestamp of the Sodar measurement for Flight #11.

Flight #11	Start [hh:mm:ss]	End [hh:mm:ss]	Duration [mm:ss]	Sodar Profile [hh:mm]
ascent #1	19:37:05	20:07:04	29:59	19:45
descent #1	20:09:29	20:25:43	16:14	20:15
ascent #2	20:28:03	20:54:14	26:11	20:45 and 20:55

Figure 14 shows the averages of potential temperature, wind speed and wind direction. Potential temperature increases with height, that is, 1.2 K in the lower 50 m, indicating the presence of a weak surface-based inversion. The first two profiles, ascent #1 and descent #1, indicate that a stable stratification persists up to 140 m; whereas the third profile, ascent #2, indicates that the atmosphere has cooled and approaches neutral stratification above 50 m. Furthermore, in the lower 50 m all flight patterns show a decrease in wind speed with height of about 3 ms^{-1} together with a change in wind direction of about 40°. The first two MASC profiles agree well with the corresponding Sodar profiles of wind speed and direction at 19:45 UTC and 20:15 UTC, whereas ascent #2 reveals for the wind speed features of both the Sodar profiles taken at 20:45 UTC and 20:55 UTC. The MASC-3 data at levels below 80 m are closer to the Sodar profile from 20:45 UTC. Above this level data are in good agreement with the Sodar data profile from 20:55 UTC. This case indicates that what at first sight appears to be a jet like feature, observed during ascent #2, is in fact the result of a strong instationarity related to a decrease in wind speed during the time it took to complete the profile. The change in wind speed and wind direction occurred relatively sudden, which explains why the red triangles at 70 m are further apart from each other than at the other levels. The wind direction profiles of the Sodar measurements during ascent #2 deviate slightly more from the MASC-3 profiles than for ascent #1 and descent #1. Further, the turning of the wind direction measured by the tower and the lowest flight legs of MASC-3 between ascent #1 and ascent #2 was oppositely measured by the Sodar profiles above.

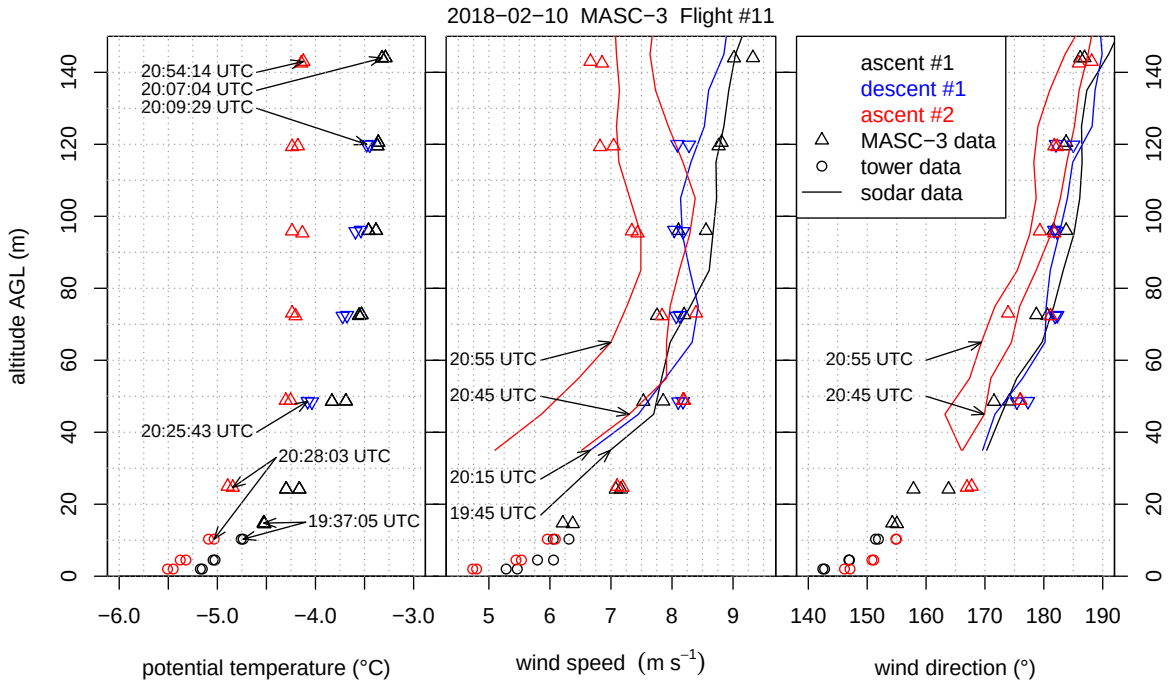

Figure 14. MASC-3 Flight #11 alongside the corresponding tower data and Sodar data as height profile for the potential temperature θ (**left**), the horizontal wind speed v_h (**middle**) and the wind direction ϕ (**right**). The time series of the tower data points have a duration of $\Delta t_{\text{tower}} = 170$ s, corresponding to the fetch of the MASC-3 flight legs at the lowest levels with an average duration of $\Delta t_{\text{UAS}} = 55$ s. The timestamps of the first measurement points of each profile and the timestamps of the Sodar profiles are given.

During the whole flight, a stable boundary layer was present, but surface observations reveal that turbulence conditions were not stationary. Around 18:30 UTC clouds enter the area. Long-wave incoming radiation increases from 220 W m^{-2} to 280 W m^{-2} around 19:00 UTC, and recovers to its original values just after 20:00 UTC. At the same time, the sensible heat flux at 2 m height increases

from -25 W m^{-2} at 18:00 UTC to 0 W m^{-2} at 19:00 UTC, and decreases to -20 W m^{-2} at 20:00 UTC. At 10 m height, the sensible heat flux also increased to 0 W m^{-2} at 18:00 UTC; but during the cloud free periods, the magnitude of the flux in 10 m height was about 5 W m^{-2} smaller than at 2 m height. Furthermore, stability at 2 m height was constant around 0.05 and, whereas at 10 m height values decreased from 0.4 at 18:00 UTC to 0.05 at 19:00 UTC, recovering to 0.4 at 20:00 UTC. Finally, the friction velocity, u_*, steadily decreased from 0.25 ms^{-1} to 0.16 ms^{-1} during this time period.

To get more insight in the atmospheric structure for this specific situation, the MASC-3 measurements allow to consider second-order moments as well. Figure 15 and 16 present variances of horizontal (Var_{v_h}) and vertical wind speed (Var_w), as well as turbulent kinetic energy (TKE) and the covariance of horizontal and vertical winds $\mathrm{Cov}_{wu_{rot}}$. Note that also these variables represent time averages for the tower data of $\Delta t_{\mathrm{tower}} = 170$ s. This is a rather short averaging interval for second-order moments but it contains 90% of the relevant information as shown by the Ogives in Figure 8 [70,71]. Furthermore, profile scaling functions of Var_w and $\mathrm{Cov}_{wu_{rot}}$ by Reference [72] are plotted. The scaling function for $\mathrm{Cov}_{wu_{rot}}$ is given by

$$\mathrm{Cov}_{wu_{rot}} = u_*^2 \left(1 - \frac{z}{h}\right)^{\frac{3}{2}} \tag{12}$$

and the scaling of the variance of the vertical wind vector component Var_w is given by

$$\mathrm{Var}_w = 1.96\, u_*^2 \left(1 - \frac{z}{h}\right)^{\frac{3}{2}} \tag{13}$$

where h is the estimated height of the boundary layer. For this situation, we used $u_* = 0.16$ ms^{-1} based on the tower data at 2 m and $h = 50$ m. The main assumptions for this model are a stationary boundary layer with constant Richardson and Richardson flux numbers [72].

Figure 15 shows that Var_{v_h} is 0.20–0.25 m^2 s^{-2} at the surface and decreases with height in the lower 60 m AGL. Above this level, the first two profiles show increasing Var_{v_h}, whereas the third profile remains constant with height. Also for Var_w an apparent difference between the first and the last profile exist. The first profile shows an increase in height in the lower 60 m AGL, whereas the third profile shows a decrease Var_w following the scaling function from Reference [72] presented in Equation (13). The profiles of TKE and $\mathrm{Cov}_{wu_{rot}}$ as shown in Figure 16 are consistent with this picture. In the last profile TKE decreases in the lower 60 m AGL, whereas in the first profile TKE increases. The $\mathrm{Cov}_{wu_{rot}}$, which is aligned in the mean wind and thus represents u_*, seems to follow the scaling profile of Nieuwstadt given in Equation (12) in all cases. Nevertheless, the first profile shows a greater spread between the two flight legs and suggests a maximum of $\mathrm{Cov}_{wu_{rot}}$ at about 70 m AGL.

These data show that during the cloudy atmospheric conditions the boundary layer is not in balance with the surface, that is, conditions are non-stationary. Ascent #1 took place in the period when the clouds were leaving the area. The radiative cooling starts to enhance the magnitude from the surface fluxes, but at greater heights turbulence is still more active due to the previously existent neutral conditions. One may argue that this profile suggests the existance of a so-called upside-down boundary layer, that is, a boundary-layer containing an elevated shear layer. The profile of Var_w shows a maximum at about 70 m [73] and TKE increases with height [52]. However, since conditions are non-stationary, we rather relate this elevated shear layer to the onset of radiative cooling at the surface than to an upside down boundary layer with an elevated source of turbulence cf. Reference [52,73].

Further scaling methods were not found to be applicable.

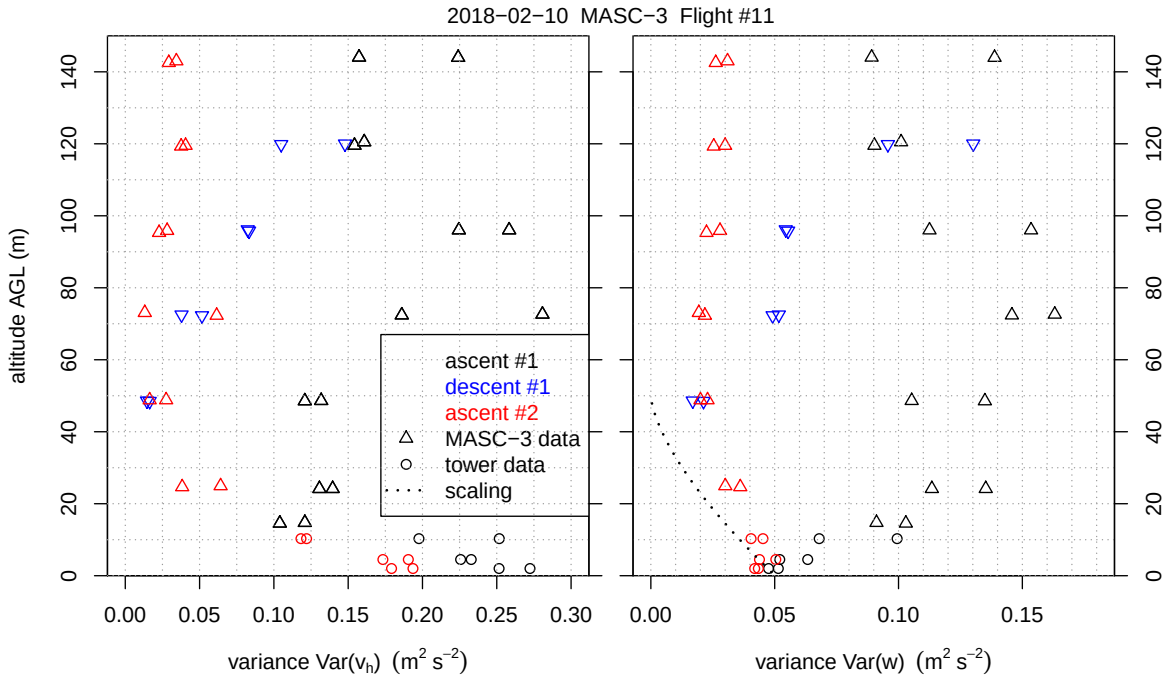

Figure 15. MASC-3 Flight #11 alongside the corresponding tower data as height profile for the variance of the horizontal wind speed Var_{v_h} (**left**) and the variance of the vertical wind speed Var_w (**right**). The time series of the tower data points have a duration of $\Delta t_{\mathrm{tower}} = 170$ s, corresponding to the fetch of the MASC-3 flight legs at the lowest levels with an average duration of $\Delta t_{\mathrm{UAS}} = 55$ s. The Var_w profile (**right**) inherits the scaling function.

After an hour without clouds, the situation has become more stationary and profiles suggest that turbulence is now mainly confined to the surface. The potential temperature approaches the neutral stratification at heights above 60 m [68]. Note that since the wind suddenly reduced during the measurements, there is no real jet, which explains why $\mathrm{Cov}_{wu_{rot}}$ is not >0 above 60 m for ascent #2 cf. Reference [74]. Furthermore, turbulence parameters follow the scaling laws from Reference [72] and TKE and Var_w are largest close to the surface [52,73]. As such, the boundary layer classification, may be considered a weakly stable boundary layer in the transition regime, that is, no constant flux layer and stability >0.1 [75].

We conclude that the MASC-3 measurements agree well with measurements of the meteorological tower and the Sodar and the combination of these measurement systems captures the interactive nature of the stable boundary layer well. The relatively long sampling time for a full ABL profile, consisting of several straight and vertically stacked legs, may however cause misleading interpretations when sampled under conditions with strong instationarity. For such cases, additional boundary layer remote sensing systems such as Sodar are highly valuable.

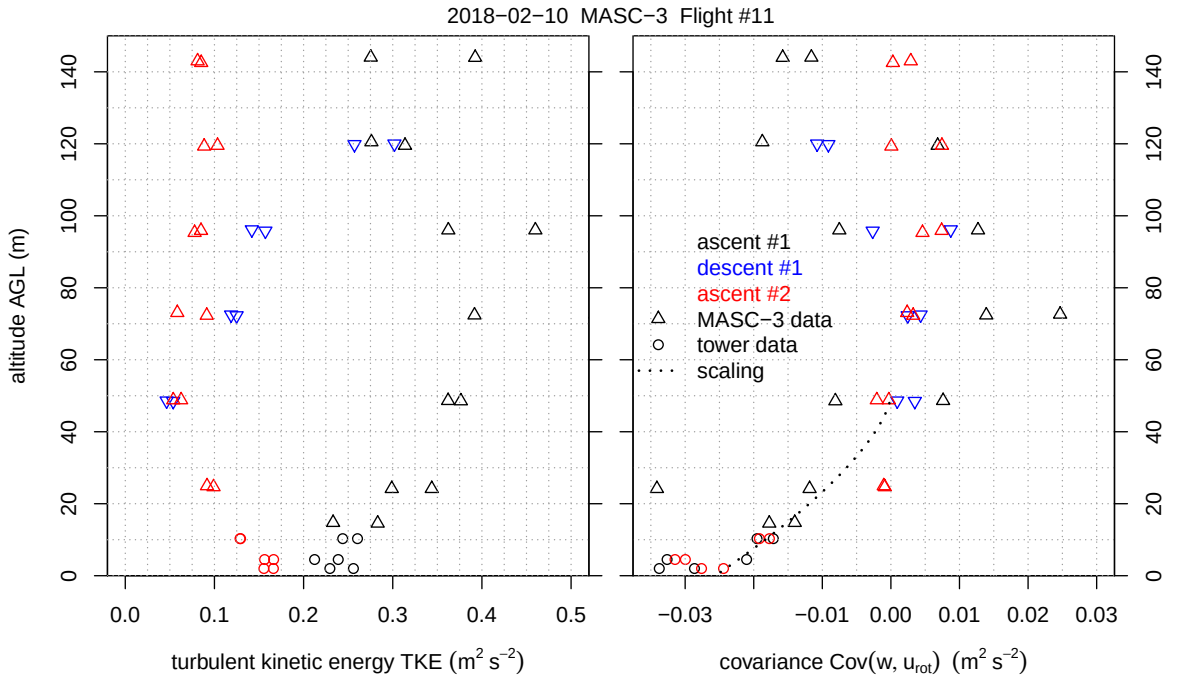

Figure 16. MASC-3 Flight #11 alongside the corresponding tower data as height profile for the TKE (**left**) and the covariance $\mathrm{Cov}_{wu_{rot}}$ (**right**) of the vertical wind w and the transformed vector component u_h which is aligned with the mean wind direction. The time series of the tower data points have a duration of $\Delta t_{\mathrm{tower}} = 170$ s, corresponding to the fetch of the MASC-3 flight legs at the lowest levels with an average duration of $\Delta t_{\mathrm{UAS}} = 55$ s. The $\mathrm{Cov}_{wu_{rot}}$ profile (**right**) inherits the scaling function.

5. Conclusions

The recent mark of the Multi-Purpose Airborne Sensor Carrier MASC-3 improved the turbulent 3D wind vector measurement and gained endurance, since the flight mechanical performance of the wing design with a high lift/drag ratio and the streamlined design is less susceptible to turbulence. The influence on the location of the sensors was minimized by locating the engine behind the tail unit. The fuselage and the installed sensor hat, as well as the modular software architecture of the data acquisition system, allow for different payloads and a variety of applications that can be supplemented to the turbulent 3D wind vector measurement. The autopilot system and the durable airframe can be deployed in polar conditions and provides manifold maneuverability including a multitude of flight patterns for different missions, as well as automatic landing. The precision and repeatability of the Pixhawk 2.1 autopilot ensures the quality of turbulence measurements in the atmospheric boundary layer. The telemetry of the autopilot and the sensor system, as well as the post-processing software MADA, provide insight of the prevailing conditions on sight and enable interactive and adjusted measurement campaigns. Two flight experiments in a SBL and a close comparison with a meteorological measurement tower, equipped with sonic anemometers, depicted the capabilities of MASC-3. Beside mean values, MASC-3 measurements allow second-order statistical moments, even suitable for estimating the turbulence regimes of SBL, where small differences distinguish between important characteristics of the SBL. The close comparison with the data of the measurement tower showed, that variances, covariances, turbulent kinetic energy and the integral length scale can be reliably estimated and agree well. With MASC-3 and its sensor system, the turbulent structure of the ABL can be sampled faster and with higher resolution than standard sonic anemometers mounted on a measurement tower. Considering the individual fetch of a stationary measurement system and a

moving UAS, the systems can be plotted together with continuous profiling systems, such as Sodar to depict fast evolving SBL. Due to the ability to transect the ABL, shorter averaging intervals for second-order moments are applicable when compared to stationary measurement systems, especially if the mean flow is weak and the advection over the stationary sensors is small. The temporal evolution and transition phases between turbulence regimes can be captured with higher resolution and thus, MASC-3 is a valuable addition to meteorological towers and Sodar measurements when investigating the interactive nature of the stable boundary layer.

Author Contributions: A.R. performed the analysis, created the figures and wrote the paper. M.S. contributed to the figures, the text and the interpretation of the results. K.z.B. contributed to the figures and the text. M.M. contributed to the text. P.M. contributed to the figures and the text. A.P. contributed to the text. B.v.K. contributed to the text and the interpretation of the results. I.S. contributed to the text, the figures, the data analysis and the interpretation of the results. S.K. contributed to the text, the data analysis and the interpretation of the results. J.B. provided guidance and advice on aspects of the study.

Funding: This research was funded by Norges Forskningsråd (the Research Council of Norway) grant number [251042/F20].

Acknowledgments: The Hailuoto-II campain was integral part of the ISOBAR project funded by the Research Council of Norway (RCN) under the FRINATEK scheme (project number: 251042/F20). The authors are grateful to all camapaign participants for their support during the field period, in particular: Joachim Reuder, Timo Vihma, for their contribution to the planning of the instrumental set up and measurement strategies; Joachim Reuder, Timo Vihma, Andrew Seidl, Line Båserud, Kristine Flacké Haualand, Heidi Golid, Elise Braaten for the installation of the 10 m weather tower and its maintenance during the period of operation; Anak Bhandari and Andrew Seidl for all the support in the preparation of the campaign and the organization of the transport of all equipment. Special thanks is given to Hannu, Sanna and Pekka from Hailuodon Majakkapiha for the provision of all required logistics, their hospitality, and the fantastic food that was essential to keep spirits up during the campaign.

Conflicts of Interest: The authors declare no conflict of interest. The founding sponsors had no role in the design of the study; in the collection, analyses, or interpretation of data; in the writing of the manuscript, and in the decision to publish the results.

References

1. Taylor, G.I. The spectrum of turbulence. *Proc. R. Soc. Lond. Ser. A Math. Phys. Sci.* **1938**, *164*, 476–490. [CrossRef]
2. Lumley, J. Interpretation of time spectra measured in high-intensity shear flows. *Phys. Fluids* **1965**, *8*, 1056–1062. [CrossRef]
3. Kaimal, J.C.; Finnigan, J.J. *Atmospheric Boundary Layer Flows: Their Structure and Measurement*; Oxford University Press: Oxford, UK, 1994.
4. Kolmogorov, A.N. The local structure of turbulence in incompressible viscous fluid for very large Reynolds numbers. *Dokl. Akad. Nauk SSSR* **1941**, *30*, 299–303. [CrossRef]
5. Cheng, Y.; Sayde, C.; Li, Q.; Basara, J.; Selker, J.; Tanner, E.; Gentine, P. Failure of Taylor's hypothesis in the atmospheric surface layer and its correction for eddy-covariance measurements. *Geophys. Res. Lett.* **2017**, *44*, 4287–4295. [CrossRef]
6. Wyngaard, J.; Clifford, S. Taylor's hypothesis and high–frequency turbulence spectra. *J. Atmos. Sci.* **1977**, *34*, 922–929. [CrossRef]
7. Suomi, I.; Gryning, S.E.; O'Connor, E.J.; Vihma, T. Methodology for obtaining wind gusts using Doppler lidar. *Q. J. R. Meteorol. Soc.* **2017**, *143*, 2061–2072. [CrossRef]
8. Samuelsson, P.; Tjernström, M. Airborne flux measurements in NOPEX: Comparison with footprint estimated surface heat fluxes. *Agric. For. Meteorol.* **1999**, *98*, 205–225. [CrossRef]
9. Lenschow, D.H.; Mann, J.; Kristensen, L. How Long Is Long Enough When Measuring Fluxes and Other Turbulence Statistics. *J. Atmos. Ocean. Technol.* **1994**, *11*, 661–673. [CrossRef]
10. Egger, J.; Bajrachaya, S.; Heinrich, R.; Kolb, P.; Lämmlein, S.; Mech, M.; Reuder, J.; Schäper, W.; Shakya, P.; Schween, J.; et al. Diurnal winds in the Himalayan Kali Gandaki valley. Part III: Remotely piloted aircraft soundings. *Mon. Weather Rev.* **2002**, *130*, 2042–2058. [CrossRef]
11. Egger, J.; Blacutt, L.; Ghezzi, F.; Heinrich, R.; Kolb, P.; Lämmlein, S.; Leeb, M.; Mayer, S.; Palenque, E.; Reuder, J.; et al. Diurnal circulation of the Bolivian Altiplano. Part I: Observations. *Mon. Weather Rev.* **2005**, *133*, 911–924. [CrossRef]

12. Spiess, T.; Bange, J.; Buschmann, M.; Vörsmann, P. First application of the meteorological Mini-UAV'M2AV'. *Meteorol. Z.* **2007**, *16*, 159–169. [CrossRef]
13. Reuder, J.; Brisset, P.; Jonassen, M.; Müller, M.; Mayer, S. The Small Unmanned Meteorological Observer SUMO: A new tool for atmospheric boundary layer research. *Meteorol. Z.* **2009**, *18*, 141–147. [CrossRef]
14. Reuder, J.; Jonassen, M.O.; Ólafsson, H. The Small Unmanned Meteorological Observer SUMO: Recent developments and applications of a micro-UAS for atmospheric boundary layer research. *Acta Geophys.* **2012**, *60*, 1454–1473. [CrossRef]
15. Chilson, P.B.; Gleason, A.; Zielke, B.; Nai, F.; Yeary, M.; Klein, P.; Shalamunec, W. SMARTSonde: A small UAS platform to support radar research. In Proceedings of the 34th Conference on radar meteorology, American Meteorological Society, Williamsburg, VI, USA, 5–9 October 2009; Volume 12.
16. Bonin, T.A.; Goines, D.C.; Scott, A.K.; Wainwright, C.E.; Gibbs, J.A.; Chilson, P.B. Measurements of the temperature structure-function parameters with a small unmanned aerial system compared with a sodar. *Bound.-Layer Meteorol.* **2015**, *155*, 417–434. [CrossRef]
17. Thomas, R.; Lehmann, K.; Nguyen, H.; Jackson, D.; Wolfe, D.; Ramanathan, V. Measurement of turbulent water vapor fluxes using a lightweight unmanned aerial vehicle system. *Atmos. Meas. Tech.* **2012**, *5*, 243–257. [CrossRef]
18. Wildmann, N.; Hofsäß, M.; Weimer, F.; Joos, A.; Bange, J. MASC—A small Remotely Piloted Aircraft (RPA) for wind energy research. *Adv. Sci. Res.* **2014**, *11*, 55–61. [CrossRef]
19. Altstädter, B.; Platis, A.; Wehner, B.; Scholtz, A.; Wildmann, N.; Hermann, M.; Käthner, R.; Baars, H.; Bange, J.; Lampert, A. ALADINA—An unmanned research aircraft for observing vertical and horizontal distributions of ultrafine particles within the atmospheric boundary layer. *Atmos. Meas. Tech.* **2015**, *8*, 1627–1639. [CrossRef]
20. Bärfuss, K.; Pätzold, F.; Altstädter, B.; Kathe, E.; Nowak, S.; Bretschneider, L.; Bestmann, U.; Lampert, A. New Setup of the UAS ALADINA for Measuring Boundary Layer Properties, Atmospheric Particles and Solar Radiation. *Atmosphere* **2018**, *9*, 28. [CrossRef]
21. de Boer, G.; Palo, S.; Argrow, B.; LoDolce, G.; Mack, J.; Gao, R.S.; Telg, H.; Trussel, C.; Fromm, J.; Long, C.N.; et al. The Pilatus unmanned aircraft system for lower atmospheric research. *Atmos. Meas. Tech.* **2016**, *9*. [CrossRef]
22. Witte, B.M.; Singler, R.F.; Bailey, S.C. Development of an Unmanned Aerial Vehicle for the Measurement of Turbulence in the Atmospheric Boundary Layer. *Atmosphere* **2017**, *8*, 195. [CrossRef]
23. Caltabiano, D.; Muscato, G.; Orlando, A.; Federico, C.; Giudice, G.; Guerrieri, S. Architecture of a UAV for volcanic gas sampling. In Proceedings of the 2005 IEEE Conference on Emerging Technologies and Factory Automation, Catania, Italy, 19–22 September 2005; Volume 1, p. 6.
24. Diaz, J.A.; Pieri, D.; Wright, K.; Sorensen, P.; Kline-Shoder, R.; Arkin, C.R.; Fladeland, M.; Bland, G.; Buongiorno, M.F.; Ramirez, C.; et al. Unmanned aerial mass spectrometer systems for in-situ volcanic plume analysis. *J. Am. Soc. Mass Spectrom.* **2015**, *26*, 292–304. [CrossRef]
25. Platis, A.; Altstädter, B.; Wehner, B.; Wildmann, N.; Lampert, A.; Hermann, M.; Birmili, W.; Bange, J. An Observational Case Study on the Influence of Atmospheric Boundary-Layer Dynamics on New Particle Formation. *Bound.-Layer Meteorol.* **2016**, *158*, 67–92. [CrossRef]
26. Schuyler, T.J.; Guzman, M.I. Unmanned Aerial Systems for Monitoring Trace Tropospheric Gases. *Atmosphere* **2017**, *8*, 206. [CrossRef]
27. Hobbs, S.; Dyer, D.; Courault, D.; Olioso, A.; Lagouarde, J.P.; Kerr, Y.; Mcaneney, J.; Bonnefond, J. Surface layer profiles of air temperature and humidity measured from unmanned aircraft. *Agron. Sustain. Dev.* **2002**, *22*, 635–640. [CrossRef]
28. Van den Kroonenberg, A.; Bange, J. Turbulent flux calculation in the polar stable boundary layer: Multiresolution flux decomposition and wavelet analysis. *J. Geophys. Res.* **2007**, *112*, 6112. [CrossRef]
29. Martin, S.; Bange, J.; Beyrich, F. Meteorological Profiling the Lower Troposphere Using the Research UAV 'M^{2}AV Carolo'. *Atmos. Meas. Tech.* **2011**, *4*, 705–716. [CrossRef]
30. Van den Kroonenberg, A.; Martin, S.; Beyrich, F.; Bange, J. Spatially-averaged temperature structure parameter over a heterogeneous surface measured by an unmanned aerial vehicle. *Bound.-Layer Meteorol.* **2012**, *142*, 55–77. [CrossRef]

31. Jonassen, M.O.; Ólafsson, H.; Ágústsson, H.; Rögnvaldsson, Ó.; Reuder, J. Improving high-resolution numerical weather simulations by assimilating data from an unmanned aerial system. *Mon. Weather Rev.* **2012**, *140*, 3734–3756. [CrossRef]
32. Reuder, J.; Ablinger, M.; Agústsson, H.; Brisset, P.; Brynjólfsson, S.; Garhammer, M.; Jóhannesson, T.; Jonassen, M.O.; Kühnel, R.; Lämmlein, S.; et al. FLOHOF 2007: An overview of the mesoscale meteorological field campaign at Hofsjökull, Central Iceland. *Meteorol. Atmos. Phys.* **2012**, *116*, 1–13. [CrossRef]
33. Bonin, T.; Chilson, P.; Zielke, B.; Fedorovich, E. Observations of the early evening boundary-layer transition using a small unmanned aerial system. *Bound.-Layer Meteorol.* **2013**, *146*, 119–132. [CrossRef]
34. Martin, S.; Beyrich, F.; Bange, J. Observing Entrainment Processes Using a Small Unmanned Aerial Vehicle: A Feasibility Study. *Bound.-Layer Meteorol.* **2014**, *150*, 449–467. [CrossRef]
35. Wildmann, N.; Rau, G.A.; Bange, J. Observations of the Early Morning Boundary-Layer Transition with Small Remotely-Piloted Aircraft. *Bound.-Layer Meteorol.* **2015**, *157*, 345–373. [CrossRef]
36. Wainwright, C.E.; Bonin, T.A.; Chilson, P.B.; Gibbs, J.A.; Fedorovich, E.; Palmer, R.D. Methods for evaluating the temperature structure-function parameter using unmanned aerial systems and large-eddy simulation. *Bound.-Layer Meteorol.* **2015**, *155*, 189–208. [CrossRef]
37. Braam, M.; Beyrich, F.; Bange, J.; Platis, A.; Martin, S.; Maronga, B.; Moene, A.F. On the Discrepancy in Simultaneous Observations of the Structure Parameter of Temperature Using Scintillometers and Unmanned Aircraft. *Bound.-Layer Meteorol.* **2016**, *158*, 257–283. [CrossRef]
38. Kral, S.T.; Reuder, J.; Vihma, T.; Suomi, I.; O'Connor, E.; Kouznetsov, R.; Wrenger, B.; Rautenberg, A.; Urbancic, G.; Jonassen, M.O.; et al. Innovative Strategies for Observations in the Arctic Atmospheric Boundary Layer (ISOBAR)—The Hailuoto 2017 Campaign. *Atmosphere* **2018**, *9*, 268. [CrossRef]
39. Båserud, L.; Flügge, M.; Bhandari, A.; Reuder, J. Characterization of the SUMO turbulence measurement system for wind turbine wake assessment. *Energy Procedia* **2014**, *53*, 173–183. [CrossRef]
40. Subramanian, B.; Chokani, N.; Abhari, R.S. Drone-based experimental investigation of three-dimensional flow structure of a multi-megawatt wind turbine in complex terrain. *J. Sol. Energy Eng.* **2015**, *137*, 051007. [CrossRef]
41. Wildmann, N.; Bernard, S.; Bange, J. Measuring the local wind field at an escarpment using small remotely-piloted aircraft. *Renew. Energy* **2017**, *103*, 613–619. [CrossRef]
42. Neumann, P.P.; Bartholmai, M. Real-time wind estimation on a micro unmanned aerial vehicle using its inertial measurement unit. *Sens. Actuators A Phys.* **2015**, *235*, 300–310. [CrossRef]
43. Brouwer, R.L.; De Schipper, M.A.; Rynne, P.F.; Graham, F.J.; Reniers, A.J.; MacMahan, J.H. Surfzone monitoring using rotary wing unmanned aerial vehicles. *J. Atmos. Ocean. Technol.* **2015**, *32*, 855–863. [CrossRef]
44. Palomaki, R.T.; Rose, N.T.; van den Bossche, M.; Sherman, T.J.; De Wekker, S.F. Wind estimation in the lower atmosphere using multirotor aircraft. *J. Atmos. Ocean. Technol.* **2017**, *34*, 1183–1191. [CrossRef]
45. Rautenberg, A.; Allgeier, J.; Jung, S.; Bange, J. Calibration Procedure and Accuracy of Wind and Turbulence Measurements with Five-Hole Probes on Fixed-Wing Unmanned Aircraft in the Atmospheric Boundary Layer and Wind Turbine Wakes. *Atmosphere* **2019**, *10*, 124. [CrossRef]
46. Lenschow, D.H. Aircraft Measurements in the Boundary Layer. In *Probing the Atmospheric Boundary Layer*; Lenschow, D.H., Ed.; American Meteorological Society: Boston, MA, USA, 1986; pp. 39–53.
47. Van den Kroonenberg, A.; Martin, T.; Buschmann, M.; Bange, J.; Vörsmann, P. Measuring the wind vector using the autonomous mini aerial vehicle M2AV. *J. Atmos. Ocean. Technol.* **2008**, *25*, 1969–1982. [CrossRef]
48. Rautenberg, A.; Graf, M.; Wildmann, N.; Platis, A.; Bange, J. Reviewing Wind Measurement Approaches for Fixed-Wing Unmanned Aircraft. *Atmosphere* **2018**, *9*, 422. [CrossRef]
49. Foken, T. 50 Years of the Monin–Obukhov Similarity Theory. *Bound.-Layer Meteorol.* **2006**, *119*, 431–447. [CrossRef]
50. Mahrt, L.; Vickers, D. Contrasting vertical structures of nocturnal boundary layers. *Bound.-Layer Meteorol.* **2002**, *105*, 351–363. [CrossRef]
51. Banta, R.M.; Pichugina, Y.L.; Newsom, R.K. Relationship between low-level jet properties and turbulence kinetic energy in the nocturnal stable boundary layer. *J. Atmos. Sci.* **2003**, *60*, 2549–2555. [CrossRef]
52. Banta, R.M.; Pichugina, Y.L.; Brewer, W.A. Turbulent velocity-variance profiles in the stable boundary layer generated by a nocturnal low-level jet. *J. Atmos. Sci.* **2006**, *63*, 2700–2719. [CrossRef]

53. Mauritsen, T.; Svensson, G. Observations of stably stratified shear-driven atmospheric turbulence at low and high Richardson numbers. *J. Atmos. Sci.* **2007**, *64*, 645–655. [CrossRef]
54. Tampieri, F.; Yagüe, C.; Viana, S. The vertical structure of second-order turbulence moments in the stable boundary layer from SABLES98 observations. *Bound.-Layer Meteorol.* **2015**, *157*, 45–59. [CrossRef]
55. Mahrt, L. Nocturnal boundary-layer regimes. *Bound.-Layer Meteorol.* **1998**, *88*, 255–278. [CrossRef]
56. Suomi, I.; Vihma, T. Wind gust measurement techniques—From traditional anemometry to new possibilities. *Sensors* **2018**, *18*, 1300. [CrossRef] [PubMed]
57. Brown, N. Position error calibration of a pressure survey aircraft using a trailing cone. *NCAR Tech. Note NCAR/TN-313STR* **1988**. [CrossRef]
58. Guinamard, A.; Ellipse, A.; Performance, I.H. *Miniature Inertial Sensors User Manual*; SBG Systems: Rueil-Malmaison, France, 2014.
59. Wildmann, N.; Ravi, S.; Bange, J. Towards higher accuracy and better frequency response with standard multi-hole probes in turbulence measurement with remotely piloted aircraft (RPA). *Atmos. Meas. Tech.* **2014**, *7*, 1027–1041. [CrossRef]
60. Wildmann, N.; Mauz, M.; Bange, J. Two fast temperature sensors for probing of the atmospheric boundary layer using small remotely piloted aircraft (RPA). *Atmos. Meas. Tech.* **2013**, *6*, 2101–2113. [CrossRef]
61. Platis, A. *Der Drohnenführerschein Kompakt. Das Grundwissen zum Kenntnisnachweis und Drohnenflug*; Motorbuch Verlag: Stuttgart, Germany, 2018; Volume 1.
62. Lenschow, D.H. *Probing the Atmospheric Boundary Layer*; American Meteorological Society: Boston, MA, USA, 1986; Volume 270.
63. Mahrt, L. Flux sampling errors for aircraft and towers. *J. Atmos. Ocean. Technol.* **1998**, *15*, 416–429. [CrossRef]
64. Lenschow, D.H.; Stankov, B.B. Length Scales in the Convective Boundary Layer. *J. Atmos. Sci.* **1986**, *43*, 1198–1209. [CrossRef]
65. Rotta, J. *Turbulente Strömungen: Eine Einführung in die Theorie und ihre Anwendung (Turbulent Flows: An Introduction to the Theory and Its Application)*; Teubner: Stuttgart, Germany, 1972.
66. Bange, J. *Airborne Measurement of Turbulent Energy Exchange Between the Earth Surface and the Atmosphere*; Sierke Verlag: Göttingen, Germany, 2009; ISBN 978-3-86844-221-2.
67. Foken, T.; Wimmer, F.; Mauder, M.; Thomas, C.; Liebethal, C. Some aspects of the energy balance closure problem. *Atmos. Chem. Phys.* **2006**, *6*, 4395–4402. [CrossRef]
68. Stull, R.B. *An Introduction to Boundary Layer Meteorology*; Springer Science & Business Media: Berlin, Germany, 2012; Volume 13.
69. Martin, S.; Bange, J. The Influence of Aircraft Speed Variations on Sensible Heat-Flux Measurements by Different Airborne Systems. *Bound.-Layer Meteorol.* **2014**, *150*, 153–166. [CrossRef]
70. Hartogensis, O.; De Bruin, H.; Van de Wiel, B. Displaced-beam small aperture scintillometer test. Part II: CASES-99 stable boundary-layer experiment. *Bound.-Layer Meteorol.* **2002**, *105*, 149–176. [CrossRef]
71. Foken, T.; Wichura, B.; Klemm, O.; Gerchau, J.; Winterhalter, M.; Weidinger, T. Micrometeorological measurements during the total solar eclipse of August 11, 1999. *Meteorol. Z.* **2001**, *10*, 171–178. [CrossRef]
72. Nieuwstadt, F.T. The turbulent structure of the stable, nocturnal boundary layer. *J. Atmos. Sci.* **1984**, *41*, 2202–2216. [CrossRef]
73. Mahrt, L. Stratified atmospheric boundary layers. *Bound.-Layer Meteorol.* **1999**, *90*, 375–396. [CrossRef]
74. Grachev, A.A.; Leo, L.S.; Sabatino, S.D.; Fernando, H.J.S.; Pardyjak, E.R.; Fairall, C.W. Structure of Turbulence in Katabatic Flows Below and Above the Wind-Speed Maximum. *Bound.-Layer Meteorol.* **2016**, *159*, 469–494. [CrossRef]
75. Grachev, A.A.; Fairall, C.W.; Persson, P.O.G.; Andreas, E.L.; Guest, P.S. Stable Boundary-Layer Scaling Regimes: The Sheba Data. *Bound.-Layer Meteorol.* **2005**, *116*, 201–235. [CrossRef]